The Chemo-dynamics and Origin of Extended Stellar Structures in Milky Way Dwarf Galaxy Satellites

by

Jaclyn Jensen
B.Sc., University of Denver, 2017
M.Sc., University of Victoria, 2020

A Dissertation Submitted in Partial Fulfillment of the
Requirements for the Degree of

DOCTOR OF PHILOSOPHY

in the Department of Physics & Astronomy

We acknowledge and respect the Lək̓ʷəŋən (Songhees and Xʷsepsəm/ Esquimalt) Peoples on whose territory the university stands, and the Lək̓ʷəŋən and W̱SÁNEĆ Peoples whose historical relationships with the land continue to this day.

The Chemo-dynamics and Origin of Extended Stellar Structures in Milky Way Dwarf Galaxy Satellites

by

Jaclyn Jensen
B.Sc., University of Denver, 2017
M.Sc., University of Victoria, 2020

Supervisory Committee

Dr. Alan McConnachie, Co-Supervisor
(Department of Physics & Astronomy)

Dr. Sara Ellison, Co-Supervisor
(Department of Physics & Astronomy)

Dr. Thomas Darcie, Outside Member
(Department of Electrical & Computer Engineering)

ABSTRACT

Dwarf galaxies are fundamental to our understanding of galaxy formation and evolution. As the most numerous galaxies in the Universe, they are the foundation of more massive systems (like the Milky Way) and are considered the foundation of galaxy formation. As they are accreted, the debris of these galactic building blocks is tidally stripped, leaving trails of stars throughout the host's stellar halo. Though much observational evidence of this hierarchical assembly exists in our own Galaxy, it remains uncertain whether dwarf galaxies themselves host extended haloes of previously accreted stars. Observing these low-density features is complicated by the dwarf's intrinsic faintness, particularly the lowest-mass systems such as ultra-faints. Though detection of dwarf stellar haloes is challenging (and remains largely unexplored territory), identifying and cataloguing these substructures holds significant promise to further our understanding of galaxy formation and small-scale cosmology.

This thesis investigates the detection and characterization of extended stellar substructure in dwarf galaxies, via the chemo-dynamical properties of their constituent stars. In these works, I study the sample of dwarf galaxy satellites in the Milky Way (MW) whose proximity allows us to explore a wide range of stellar masses (i.e., down to the faintest galaxies known) and furthermore provides us with astrometric data obtained from the space-based telescope, *Gaia*. In my PhD, I first addressed the detectability of these extended features in our MW dwarfs by updating an existing Bayesian-based algorithm that combines spatial, photometric, and astrometric information from *Gaia* to (i) characterize stellar memberships and (ii) identify extended stellar features in every MW dwarf. Applied to $\sim$60 systems, this method produced the first systematic census of extended structure in our nearby dwarf galaxies. Out of the entire sample, nine dwarfs were identified as exhibiting an extended stellar component.

Building on this foundation of this work, I then focused on one specific MW dwarf galaxy (Boötes 3) whose stellar density profile indicated an excess of stars in the dwarf's outskirts. Using our *Gaia*-selected members, new CaHK photometry taken at the Canada-France-Hawaii Telescope, and matched filter searches using photometric catalogues produced by the Sloan Digital Sky Survey (SDSS) and the DECam Local Volume (DELVE) survey, I aimed to characterize whether this stellar excess could be explained by tidal influence with the MW. Interestingly, and contrary to previous works, I do not find evidence of lengthy tidal tails in this system. However, the

dynamical analysis conducted in this work indicates that Boötes 3's orbit may be strongly influenced by MW tides. I argue that the appearance of lengthy tidal tails may be truncated by (i) the steep distance gradient of the dwarf's nearly radial orbit, and/or (ii) the dissipation of stars due to a recent interaction with the Galactic bar. This work highlights the necessity of combining astrometry, chemistry, and dynamics to confirm progenitor-stream associations.

A substantial outcome of this work, regarding the identification of candidate stars in each MW dwarf satellite, has been the science that has been enabled by these data. For every dwarf satellite observable by *Gaia*, I have produced target lists of stellar candidates for future follow-up programs. The observational campaigns that have been facilitated by my data include (i) smaller scale spectroscopic programs for one, or a few, dwarf galaxies, and (ii) selecting targets as part of commissioning the Gemini High-resolution Optical SpecTrograph (GHOST) at the Gemini South Observatory. These data also form the basis for a larger scale, homogeneous, high-resolution study of southern MW dwarfs as part of GHOst Ultra-faint Legacy Survey (GHOULS). Collectively, these programs underscore the broader scientific impact and lasting utility of the algorithm's candidate lists in future studies of MW dwarfs.

The outskirts of dwarf galaxies are not only key to understanding their individual evolutionary histories, but also serve as sensitive probes to small-scale cosmology. By cataloguing extended stellar features and constraining their likely origin with follow-up observations, this work provides crucial observations to better understand our cosmological perspective. The faintest systems are arguably the most useful to answer fundamental questions about the nature of dark matter, and their outskirts are key to understanding the smallest scales of galaxy formation.

Contents

List of Tables

List of Figures

Acknowledgements

I am forever grateful for the substantial support I have been privileged to receive, from friends, educators, and family. Above all, much thanks to:

Alan McConnachie & Kim Venn, for your supervision and mentorship throughout my years at UVic. Thank you for supporting me, providing constructive feedback, and for ultimately shaping me into the researcher that I have become. Thanks also to the **UVic Near-Field Cosmology group**, the **Streams community**, and fellow **Galactic Archaeologists** for the continuous academic support, intriguing discussions, and incredibly cool science.

The additional academic mentors that I have recently acquired, particularly **Nora Shipp, Maren Cosens, & Akshara Viswanathan**. Thank you for all your immensely helpful advice and continued guidance.

Fellow grad student cohorts and supportive friends, particularly **Katie Crotts, William & Natalie Thompson, Shoshannah Byrne-Mamahit, Anya Dovgal, Simon Smith, Clare Higgs, Ted Grosson, among so many others** for your emotional support and beer time.

And to **James, my parents, and my amazing in-laws** for their constant support that helped to get me this far in the first place.

The mind is not a vessel to be filled but a fire to be kindled.
Plutarch

Chapter 1

Introduction

1.1 Dwarfs: the Smallest Galactic Systems

Galaxies are self-gravitating systems consisting of stars, gas, dust, and dark matter. Trillions of galaxies exist in the observable Universe (Conselice et al. 2016) varying in morphology, brightness, colour, size, and masses, depending on their local environment and history. Statistically, the number density of these galaxies organized by their luminosity are well-described by the Schechter Luminosity Function (Schechter 1976) which − in log-log space − follows a steeply decreasing exponential cutoff for galaxies brighter than the Milky Way (MW) and a rising power-law towards fainter systems. As evidenced by this empirical relation, the most common type of galaxies in the Universe are also the smallest and faintest. These are considered dwarf galaxies (see examples provided in Figure 1.1; compiled in Mao et al. 2024).

Dwarfs are typically defined as galaxies whose stellar mass (M_*) is $\lesssim 10^9\ M_\odot$ (Bullock & Boylan-Kolchin 2017), though this threshold is arguably arbitrary. In many ways, dwarfs are similar to the rest of the galaxy mass spectrum: they have the same formation mechanisms, experience many of the same evolutionary processes, and are similarly dominated in total mass by dark matter (DM). Indeed, dwarfs differ from their more massive counterparts in that their total mass is significantly more dominated by DM, often by factors >100 (Simon 2019). For comparison, the factor of DM dominating the MW's mass is only on the order of $\sim 16 - 20$ (Bland-Hawthorn & Gerhard 2016). Although their DM haloes act as a protective shield to the baryonic matter contained within, their shallow gravitational potentials make dwarfs generally more susceptible to evolutionary and environmental effects. As a result, the

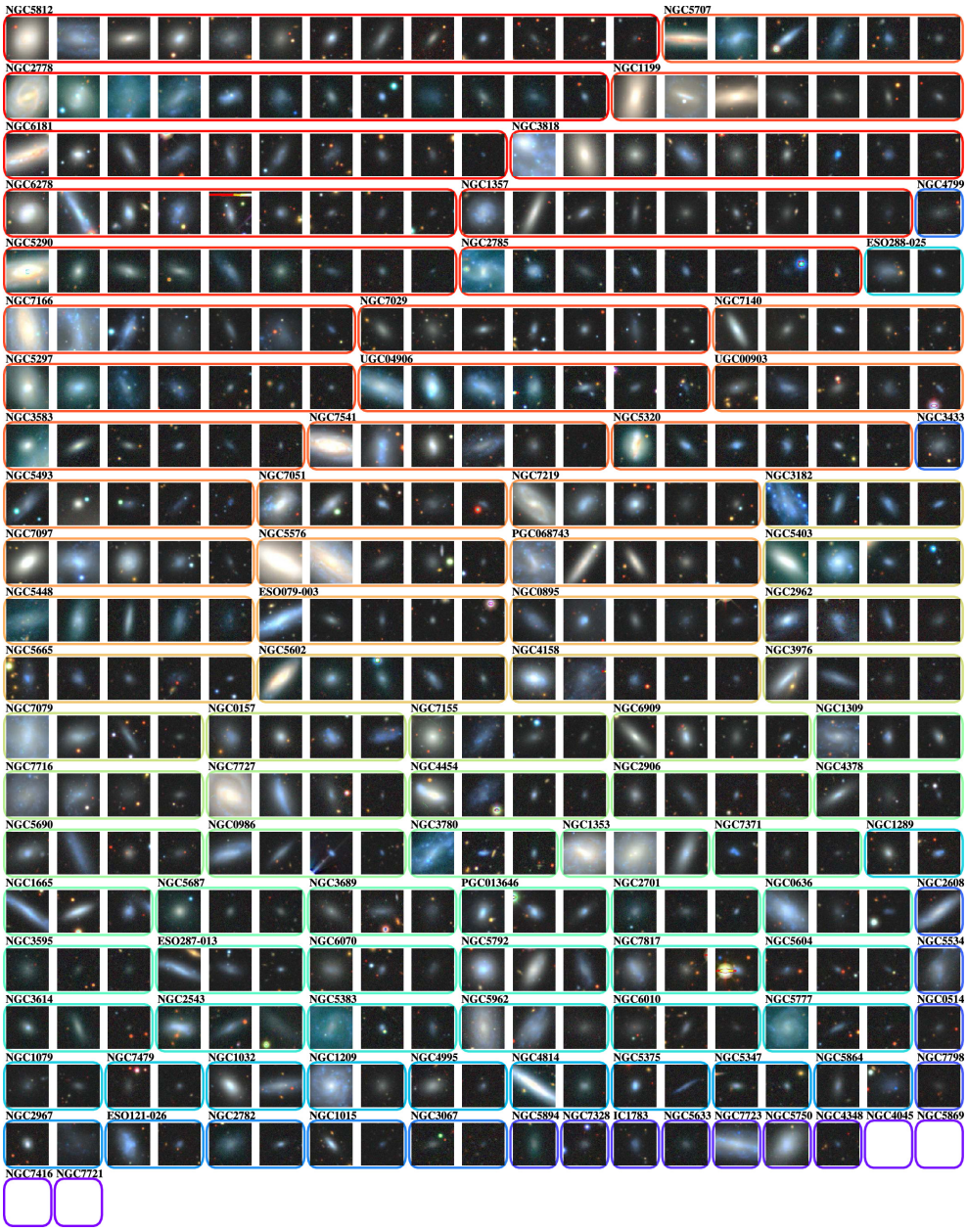

Figure 1.1: DESI imaging of dwarf galaxy satellites studied in the Satellites Around Galactic Analogs (SAGA) survey, to showcase the vast morphologies of dwarf galaxies. SAGA aims to study the dwarf satellite populations of 100 MW-like galaxies, specifically those outside of the Local Volume. Images here are organized by each host galaxy, where satellites associated to each host are indicated by similar colour. Labels of these hosts are provided for each coloured grouping, but images of the hosts are not. This figure is sourced directly from Mao et al. (2024).

observable properties of dwarf galaxies serve as sensitive tracers of their evolutionary history. Dwarfs are therefore particularly useful to understand evolutionary processes, particularly when the effects of one or a few mechanisms can be isolated and studied.

Though they are intrinsically faint systems, and therefore challenging to observe, the study of dwarf galaxies provides crucial context into multiple facets of astronomy. Given their substantial fraction of DM, it is argued that dwarfs themselves provide an observational window into the nature of the DM particle (Bullock & Boylan-Kolchin 2017). Dwarf galaxies also play an essential role in galaxy formation at all mass scales, serving as the fundamental building blocks from which larger systems are assembled (White & Rees 1978). Even just constraining the *number* of these low mass galaxies contained within some redshift (z) or (co-moving) volume is a useful metric to constrain the flavour of cosmology governing the Universe. Theoretical abundances of simulated DM subhaloes have been found to vary across cosmological models, as illustrated in the relative counts of DM subhaloes in Figure 1.2 for three different DM particle types (Cold, Warm, and Self-Interacting). The study of dwarfs therefore has profound implications not only for understanding the roots of galaxy formation, but also for constraining our underlying cosmology.

Though they potentially offer solutions to many cosmological questions, dwarf galaxies are also at the forefront of tensions between observations and theoretical predictions at the smallest scales. Large-scale hydrodynamical simulations are capable of reproducing statistical relations for systems whose total masses are $\gtrsim 10^{11}$ $M_{\odot}$ (e.g., see statistical comparisons provided in Somerville & Davé 2015), yet they often inadequately capture general properties of the smallest galaxies. These inconsistencies have given rise to three main problems in astrophysics:

- The "missing satellites" problem (Klypin et al. 1999; Moore et al. 1999): in the standard cosmological framework, simulations predict substantially more DM subhaloes orbiting a MW-like host than the numbers of dwarf galaxies we currently detect in our Galaxy. These predictions vary on the order of hundreds to thousands of "missing" low-mass galaxies in the MW.

- The "core-cusp" problem (de Blok 2010): these simulations also predict that the inner density profile of DM subhaloes are much higher (i.e., "cuspy") compared to observations, whose implied densities from stellar kinematics imply a more centrally flattened (i.e., "cored") profile.

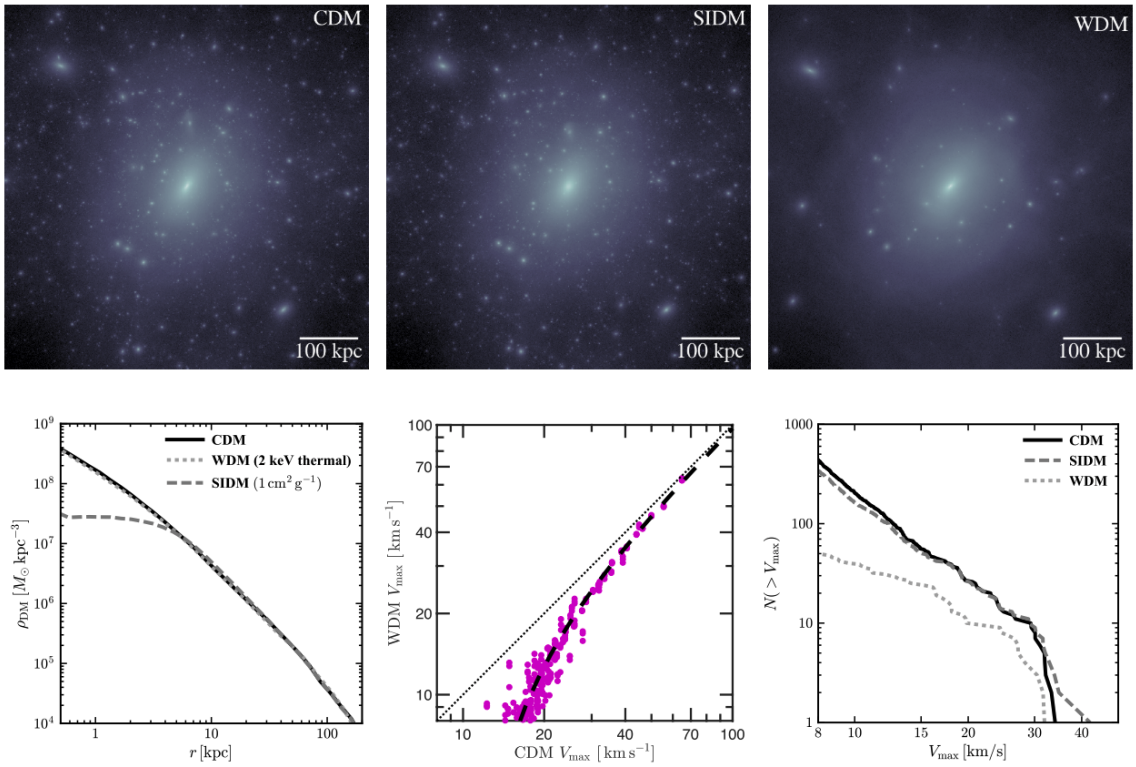

Figure 1.2: Simulations of a MW-size halo surrounded by accreted DM subhaloes in Cold, Warm, and Self-Interacting DM cosmologies, sourced from Bullock & Boylan-Kolchin (2017). Top panels represent images of the final simulation snapshot, while the bottom panels showcase the statistical differences between each cosmology. The bottom left panel indicates the DM density of each simulated MW halo, bottom middle indicates the differences in halo masses (represented by the maximum velocity of the halo's rotation curve, V_{max}) between Warm and Cold DM models, and the bottom right illustrates the relative counts of subhaloes in each MW-analogue (organized by mass, or again V_{max}).

- The "too-big-to-fail" problem (Boylan-Kolchin et al. 2011): simulations of MW-analogues predict several massive, dense subhalo satellites that exceed the masses of our own MW satellite population. The lack of these massive dwarfs in our observations alludes to the possibility that these haloes are dark, or failed to form stars. Given their more massive potentials, there is no clear justification as to why this would occur; thus these massive haloes are too big to have failed forming stars.

The solutions to some of these "problems" can arguably be solved by (i) increasing the resolution of the simulation, (ii) accounting for baryonic effects (e.g., star formation, supernovae feedback, active galactic nuclei, etc.), (iii) altering the type of DM in the cosmological model, (iv) exploring observational biases in our detection of our nearby dwarf galaxies, or (v) a combination of the above. However, tensions between observation and theory still remain for the galaxies at the faintest end of the luminosity function.

As previously discussed, dwarfs are not only significant in the formation of galaxies at all mass scales, but they are strongly influenced by evolutionary processes. In the following section, I discuss dwarf galaxies in a larger framework to underscore their importance in our understanding of galaxy formation and evolution overall.

1.2 Galaxy Formation and Evolution

1.2.1 Hierarchical Assembly

The overall formation process of galaxies in the Universe occurs within the larger context of cosmology, governed by dark energy and dark matter. The standard cosmological perspective is known as Λ Cold Dark Matter (ΛCDM; summarized efficiently in Mo et al. 2010 and Bullock & Boylan-Kolchin 2017). In brief, Λ represents the "negative pressure" that causes the Universe to accelerate in expansion, and "cold" refers to the low velocities of DM particles (i.e., significantly slower than the speed of light). The interactions of DM particles in ΛCDM are collisionless, such that no additional thermal energy is produced in the Universe which would cause an increase in temperature. In this cosmology, the only influence of DM is therefore caused by gravity.

A result of the expansion of the Universe post-Big Bang and the initial density field of baryonic (protons, neutrons, atomic nuclei) and non-baryonic (dark) matter,

was the formation of the cosmic web. Small fluctuations of mass in this initial density field would grow via gravity and eventually produce large cosmic filaments. Through the filaments, pristine gas (i.e., hydrogen and helium and no additional heavier metals) and DM were then funnelled into regions of higher density, forming the "seeds" of galaxies. Once these density "seeds" accumulate enough mass to become gravitationally self-bound, they are considered "proto-galaxies".

In order to then form stars, a DM halo must contain enough mass such that the accreted gas from cosmic filaments will be retained. Once the potential well is sufficiently deep enough, the gas cools and condenses towards the centre of the halo (Rees & Ostriker 1977). This occurs due to radiative processes that allow the gas to lose thermal energy (e.g., atomic line cooling, metal-line cooling, and molecular cooling; see Benson 2010). The collapsed gas then fragments into dense molecular clouds, collapsing into stellar cores, and finally igniting nuclear fusion and giving rise to the first generation of stars and thus, forming a galaxy.

In this cosmological regime, the dominant force impacting the growth of galaxies is gravity. A natural consequence of this paradigm is hierarchical assembly – or broadly, the accretion of smaller galaxies into larger, more massive systems (White & Rees 1978; Frenk et al. 1988). The top panels of Figure 1.2 highlight an example of this process, as each panel represents a theoretical host halo populated by a significant number of smaller DM subhaloes that have been accreted by the more massive system. Though the overall number of DM subhaloes varies between the different flavours of DM (Cold, Warm, and Self-Interacting) in each panel, we note that the mechanism of halo growth (i.e., accretion of smaller haloes) ultimately does not.

Hierarchical assembly for galaxy growth is shown to occur at all mass scales, and across all cosmologies. Smaller satellite systems are subsumed into larger host galaxies, accreting the satellite's stars, gas, dust, and DM as it is stripped apart by tidal forces. Scattered debris of these mergers is strewn about the host's diffuse, extended stellar outskirts: i.e., the *stellar halo*. Typically populated by old, metal-poor stars, a galaxy's stellar halo is essentially a galactic graveyard where signatures of past accretion events are preserved (see review by Belokurov 2013). At large distances from the host's centre, the satellite's disrupted material becomes part of the more massive galaxy and can retain a coherent structure (e.g., stellar streams) for many Gyrs. In this way, the stellar halo represents a galaxy's "fossil record" of its accretion history.

Figure 1.3 showcases an example of the of the NGC 474 galaxy's stellar halo,

Figure 1.3: An example of substructure in the stellar halo of NGC 474 observed with the Canada-France Hawaii Telescope (CFHT). The outskirts of this system are populated by both trailing streams of stars (i.e., stellar streams) and shell-like annuli of stars, most likely from a previous merger on a radial orbit. To the right of NGC 474 is a nearby spiral galaxy. Source: Galaxy NGC 474: Shells and Star Streams | CFHT Astronomy Image Of The Month (July 2013). Image credit: CFHT, Coelum, MegaCam, J.-C. Cuillandre at CFHT & G. A. Anselmi at Coelum.

in which we observe the galaxy surrounded by substructures in its outskirts. These structures can take the form of shells or stellar streams, depending on the mass ratio and orbit of the merger event. These remnants, located in the host's outskirts, are signatures of its past interactions. A galaxy's stellar halo is therefore a particularly valuable region to uncover information about its formation. It remains speculated, however, if dwarf galaxies themselves host stellar haloes of accreted matter (Deason et al. 2022) or what the frequency of mergers in dwarf galaxies even is.

1.2.2 The Forces that Shape Galaxies

Dwarf galaxies are a powerful population for studying the processes that drive galaxy evolution, as their low masses make them especially sensitive to a variety of influences. The morphologies and properties of these systems arise from a complicated interplay between internal mechanisms (e.g., feedback) and external forces (depending on their environment). The following section summarizes several of the primary internal and external effects acting to shape the present-day appearance of dwarf galaxies.

Internal Effects

Owing to their inherently shallow potential wells, dwarf galaxies can lose gas relatively easily. Feedback processes limit the system's available gas used in star formation (SF), thereby altering the system's star formation history (SFH) and stellar chemistries. Ultimately, the gas may fall back onto the galaxy's halo at a later time. In galaxies, feedback occurs via two main sources: through its massive stars, and its active galactic nuclei (AGN; if applicable).

Stellar feedback has two primary mechanisms that can affect the SF of galaxies. The first is from its Asymptotic Giant Branch stars, whose stellar winds inject energy and momentum into the galaxy's interstellar medium (ISM). This same sort of effect can be similarly achieved from supernovae (SNe; Dekel & Silk 1986). This process can suppress or even fully quench SF, leaving behind ancient stellar populations while also enriching the ISM with heavy elements. In the smallest dwarfs, a few SNe may be sufficient to unbind much of the cold gas, thereby strongly shaping their SFH and chemical evolution.

AGN feedback is another mechanism by which a galaxy's SF is affected. Galaxies often host a centrally located black hole (BH) that actively accretes nearby gas.

In some cases, powerful jets of gaseous material are ejected perpendicular to the accretion disk from the BH itself. Similar to stellar/SNe feedback, this process can expel substantial gas and affect the system's SF. However, it is rare to observe an AGN in dwarf galaxies (Reines et al. 2013).

External Effects

A major influence in dwarf galaxies and their gas is believed to be due to the residual effects of cosmic reionization (Bullock et al. 2000). After the first stellar population (Pop III) formed in the Universe, UV radiation emitted from these massive stars ionized and heated gas in the intergalactic medium. These high energy photons not only increased the temperature of the gas above the SF threshold such that stars in haloes could not form, but also this process prevented low-mass haloes from continuing to accrete gas from the cosmic filaments. Observations of SFHs from the Local Cosmology from Isolated Dwarfs project show that, after quenching from reionization, isolated systems with $M_* \gtrsim 10^6\ M_\odot$ were able to re-initiate their SF around z $\sim$ 6 (e.g., Monelli et al. 2010; Hidalgo et al. 2011; Skillman et al. 2014; also corroborated by simulations in Benítez-Llambay et al. 2015).

Another key process that affects the SF of dwarfs is ram pressure stripping, which occurs when a smaller satellite (initially, with gas) moves through the hot halo of a galaxy, group, or cluster (Gunn & Gott 1972). As the satellite travels through the medium, a force from the medium is imparted on the satellite similar to a strong wind. This force acts to remove the gas from the satellite, and is yet another mechanism that can quench a galaxy's SF.

Two final processes are linked to gravitational effects and the nature of hierarchical assembly. The first, is the process of tidal stripping. As a smaller system orbits a larger host, the host imparts a gravitational force that acts to strip away mass from the satellite. The disrupted satellite's debris is scattered in trails of stars within the stellar halo of the host galaxy, forming lengthy tidal tails (also known as a stellar stream). Over time, the satellite will inevitably become completely destroyed and phase-mixed into the host (e.g., see simulated examples of tidal disruption studies from from Read et al. 2006, Peñarrubia et al. 2008, and Johnston et al. 2008).

The second gravitationally-motivated process is mergers, or in the case of low-mass systems, dwarf-dwarf mergers. As with more massive systems, dwarfs are assumed to form hierarchically, though it remains an open question as to what the smallest galaxy

that can form is or how many mergers a dwarf galaxy experiences. In simulations of merging satellite dwarfs in a Local Group analogue, Deason et al. (2014) estimated that 10% of satellites with $M_* > 10^6\ M_\odot$ should have experienced a major merger since z $\sim$ 1. Similar to their larger counterparts, the accreted component of dwarf-dwarf mergers are anticipated to form an extended stellar halo. The shape and physical extent of this feature depends on the mass ratio of the merger, where the accretions from lower mass ratio mergers (i.e., 1:2) sink to the centre due to dynamical friction (e.g., see dwarf-dwarf merger simulations in Deason et al. 2022). The accreted debris from more intermediate (1:5) and low (1:10) mass ratios is much more likely to be found at larger radii, in the dwarf's outskirts.

1.3 The Importance of the Local Group

The morphologies of dwarf galaxies are shaped by a wide array of internal and external processes that give rise to the diversity we observe today (e.g., see SAGA dwarfs in Figure 1.1). To understand the impact of these processes on galaxy evolution as a whole, we must be able to disentangle their relative influence on our observations. This can be achieved by targeting specific dwarf populations, where some of these influences can be minimized. To focus on the influences of dwarf-dwarf mergers for instance, we can study populations where SF feedback is minimized, such as quenched dwarf satellites or the smallest (i.e., ultra-faint) dwarf regimes. Fortunately, the best laboratory for such research is also the nearest; i.e., our galaxies in the Local Group.

The Local Group describes the group of galaxies that are mutually gravitationally bound with the MW, shown in the artist's rendering in Figure 1.4. The most massive systems are the MW and M31/Andromeda, and each of these spiral galaxies contains a multitude of smaller dwarf galaxy satellites that are gravitationally bound to either host. Most satellites are devoid of gas and active SF[1] (therefore they are considered *quenched*). In addition, such systems generally have a more elliptical-shaped structure that is maintained by pressure and not rotation (i.e. a rotating, gaseous disk). These are considered the dwarf spheroidal (dSph) population. Outside of $\sim$400 kpc of both M31 and the MW are the "isolated" dwarfs, which are assumed to currently not be influenced by either spiral's environment (such that they might be quenched of gas,

[1] A handful of larger satellites in the Local Group have been able to retain their gas and are *not* quenched, allowing them to continue actively forming stars. These are the Magellanic Clouds and Leo T in the MW, and M33/Triangulum in Andromeda. They are not considered dwarf spheroidals.

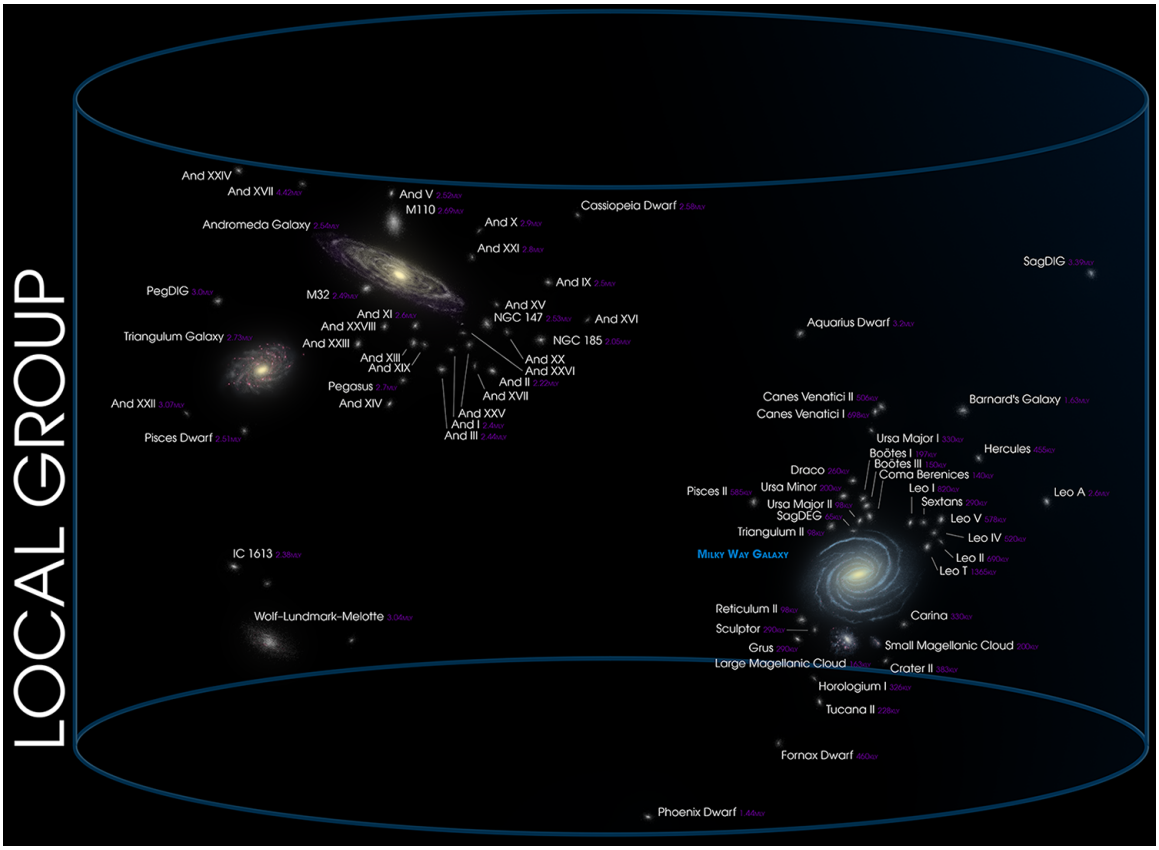

Figure 1.4: Artist's rendering of the galaxies located within the Local Group, including some satellites of both large spirals and isolated dwarfs. Source: Wikimedia Commons. Image credit: Andrew Z. Colvin

for example).

The galaxies of the Local Group are an excellent database to study the intrinsic nature of dwarf galaxies. Firstly, we have access to individual resolved stars of these dwarfs, which can yield information about the dwarf's SFH, chemical evolution, gas mixing, etc. in detail. And secondly, the Local Group dwarfs are the most metal-poor and old (>10 Gyrs) systems known (Tolstoy et al. 2009), owing to their loss of gas at early times via environmental effects (e.g., ram pressure stripping and reionization). This means that many dSphs (particularly the ultra-faint dwarf population; $M_* \approx 10^{2-5}\ M_\odot$) are considered chemically primitive and a window into the early formation of galaxies.

While both the MW and M31 host valuable satellite populations, the MW's satellites are an arguably better resource. For one, the proximity of these dwarfs allows us to resolve stars over a broader stellar mass range than currently available with M31's satellites. We illustrate this in Figure 1.5, which shows the size-luminosity (or, half-light radius r_h, vs absolute magnitude M_V) and stellar mass of dwarf galaxies compiled in the Local Volume Database (Pace 2024). Here, we observe the vast range of MW satellite stellar masses (shown as blue points) in comparison to those of the M31 population (orange points) that indicates an abrupt luminosity cutoff at $M_V \approx -6.0$ mag due to observational detection limits. It is apparent that the MW dwarfs in contrast provide a wider sample of masses and sizes, allowing us to study the faintest (and smallest) dwarf galaxies ever discovered.

Secondly, MW-focused studies benefit from all-sky astrometric data from the era of *Gaia*. *Gaia* is a space-based telescope whose science goals are to obtain five-parameter astrometry (positions, proper motions, and parallaxes) for 1% of stars in the MW (equivalent to ∼1 billion stars; Gaia Collaboration et al. 2016). For many of the nearest MW dwarfs, these data have enabled measurements of bulk transverse motions and, when combined with radial velocities and an assumed MW gravitational potential, orbit integrations. This kinematic information allows for detailed orbital and dynamical studies that remain unattainable for the more distant satellites in M31. For context, transverse kinematics of dwarf satellites were limited to the brightest MW systems prior to the arrival of *Gaia* DR2. With the most recent *Gaia* Data Release (DR3; Gaia Collaboration et al. 2023), orbital properties for all dwarf satellites with complete velocity information (i.e., proper motions and radial/line-of-sight velocities) are now readily available in the literature (McConnachie & Venn 2020b; Pace et al. 2022; Battaglia et al. 2022).

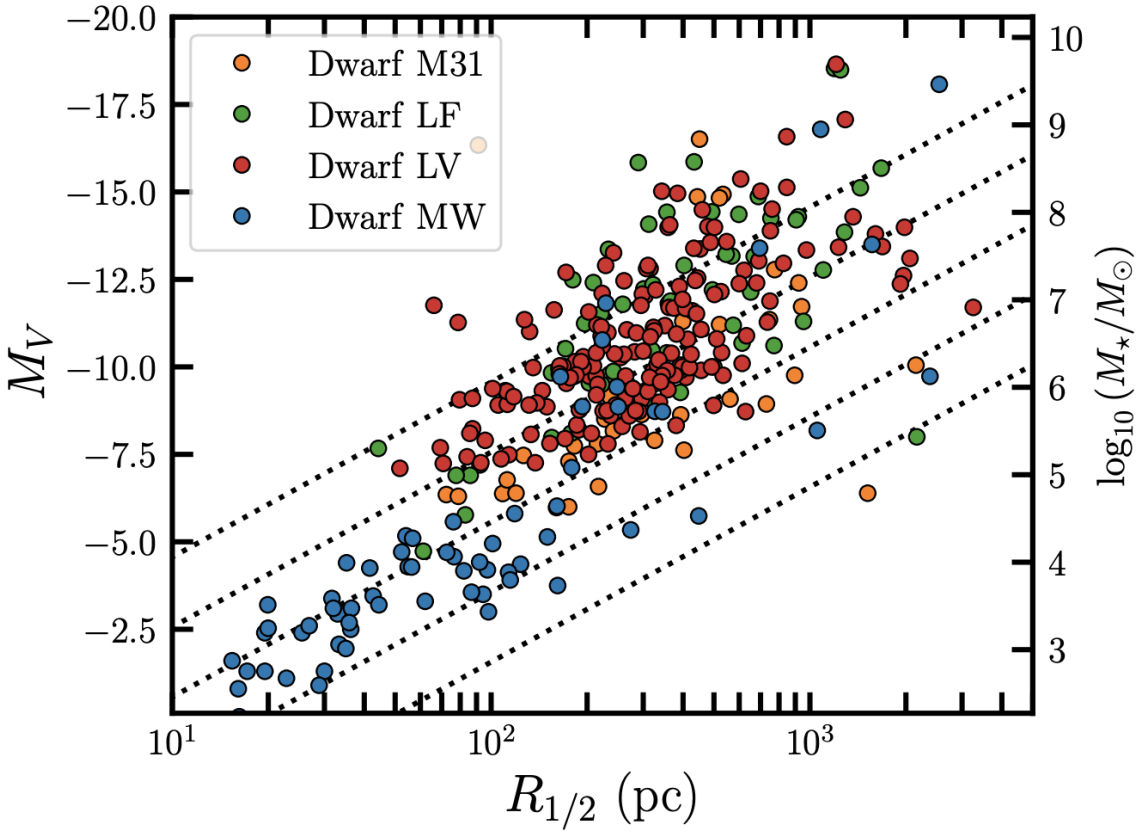

Figure 1.5: Size-luminosity plane of our nearby dwarf galaxies, sourced from Pace (2024) using the Local Volume Database. We note the stark difference in range between the MW (blue) and M31 (orange) satellites, where there is clear observational limitations in the M31 sample.

The advent of *Gaia* has ignited a new era of Galactic Archaeology. It has enabled substantial new discoveries, such as (i) the detection of newly discovered stellar streams (e.g., STREAMFINDER; Malhan & Ibata 2018; Malhan et al. 2018; Ibata et al. 2019), (ii) updated orbits for globular clusters (e.g., Baumgardt et al. 2019), (iii) estimates of the MW's total mass (e.g., Wang et al. 2022; Ibata et al. 2024), (iv) kinematic evidence of the last major merger in the MW (e.g., Belokurov et al. 2018; Helmi et al. 2018), and (v) proper motion (PM) estimates for a multitude of dwarf galaxy satellites (Pace et al. 2022; Battaglia et al. 2022; McConnachie & Venn 2020b,a) among other exciting findings (also see Helmi 2020 for an excellent review of *Gaia*'s discoveries, and references therein). *Gaia*'s influence cannot be overstated, and as a dataset whose astrometric measurements will continue to increase in accuracy with each new data release, it will continue to remain a benchmark for MW studies for years to come.

1.4 The Extended Outskirts of Dwarf Satellites: A Probe of Galaxy Formation at the Smallest Scales

As discussed in the previous section, galaxies form via accretion of smaller systems, and observational evidence of this hierarchical assembly is present as substructure throughout our own MW. As satellites orbit, the tug of tidal forces from the host acts to strip stars and DM from the smaller system. The debris of these interactions approximately follows the orbit of the disrupted satellite and are located in the host galaxy's stellar halo. In a MW-sized galaxy, these remnants can survive as coherent structures for billions of years, given their large distances from Galactic centre (and therefore also, their large dynamical timescales). Our own Galaxy's stellar halo is populated with $\sim$65 (and counting) surviving dwarf galaxies (McConnachie 2012), some of which exhibit evidence of this disruption in the form of stellar streams across the Galaxy (see Grillmair & Carlin 2016 and Helmi 2020 for recent reviews, and Mateu 2023 for the most up-to-date compilation of known stellar streams in the MW halo).

While hierarchical assembly does apply to smaller scale systems, very little observational evidence for stellar haloes of dwarf galaxies currently exists (Deason et al. 2022) and their observational study is complicated by their intrinsically low masses. Furthermore, separating the influence of internal and external effects in these feeble

systems is complex, and both can obscure the origin of stars in a dwarf's outskirts.

Given that the majority of MW satellite dwarfs are presently devoid of gas and formed most of their stars ∼10 Gyrs ago (prior to z ∼ 2; Weisz et al. 2014) the processes that can affect their present-day morphologies may be somewhat limited, compared to isolated systems. For example, in a dwarf galaxy with active star formation, stellar feedback may act to "puff up" a dwarf. However, the dwarf's SFH would have to be particularly bursty in order to push stars radially outward (see arguments in Chiti et al. 2023) and change the overall morphology. Recent work from Kado-Fong et al. (2022) found that dwarfs in the FIRE simulation suite ($M_* \approx 10^{8.5-9.6}\ M_\odot$) can have extended stellar haloes formed from in-situ stars. However, these stars' outward migration is due to the presence of a rotationally-supported thick disk, and the MW dSph population are all pressure-supported systems lacking this feature.

It can be therefore postulated that stars in the outskirts of dwarf galaxy satellites (specifically, dSphs) may in fact be displaced there largely as a result of external, gravitational influence. In this scenario, two competing theories are at play:

1. Tidal stripping: the host galaxy (i.e., the MW) imparts a differential gravitation force on the smaller accreted system. This tidal force acts to remove both DM and stellar mass from the dwarf. As stars are stripped, those located at higher potential energies (i.e., located at farther Galactocentric radii) trail behind the satellite, while those at lower potentials (closer Galactocentric radii) increase in speed and orbit ahead of the satellite. Once the stars are unbound from their dwarf and begin to orbit around the host instead, these stars are considered members of a stellar (or tidal) stream.

2. Dwarf-dwarf mergers: mergers of dwarf galaxies may produce extended morphology in satellites that remains observable at present-day. In simulations by Deason et al. (2022) and Goater et al. (2024), the authors both found that "tidally isolated" dwarfs (i.e., not in a tidal influence of a host galaxy) can host extended substructure as a result of a late-time merger. In particular, Deason et al. (2022) found that dwarf merger ratios between 1:5 and 1:2 can produce a more radially extended, lower density outer component in the stellar density profile. In these simulations, the fraction of stars in the outskirts are accreted in origin, and dominate the stellar distribution at large radii (with respect to the dwarf's centre). The results of this work suggest that we may be better suited to observe the remnants of dwarf-dwarf mergers in the radially distant

outskirts of dwarf galaxies.

In the first case, there already exists direct observational evidence of the tidal stripping of MW satellites. A well-known example is the Sagittarius stellar stream (Ibata et al. 2002; Majewski et al. 2003), whose tidal tails wrap twice around the Galaxy (though smaller scale examples with dwarf galaxy progenitors also have been identified, e.g. Tucana 3; Drlica-Wagner et al. 2015; Li et al. 2018b). By definition, the MW satellite population is in some stage of accretion with the MW; the implication is that there may be some traceable evidence of tides in these dwarfs, even if only marginally. Largely, the strength of observed tidal disturbances depends on the dwarf's orbit in the MW and the internal kinematics/DM content of the satellite.

Observational evidence of the second scenario, in comparison, is particularly lacking in the Local Group. Presently, only three dwarfs in the total M31-MW satellite population are reported to have substructure indicative of a past merger; these systems are the MW satellites Tucana 2 (Chiti et al. 2021) and Sextans (Cicuéndez & Battaglia 2018; Roederer et al. 2023), and the M31 satellite Andromeda 2 (Amorisco et al. 2014). Statistical studies of external dwarf galaxies (i.e., not in the Local Volume; between $0.005 < z < 0.07$) in the TiNy-Titans survey (Stierwalt et al. 2015) have reported a multitude of interacting dwarf galaxy pairs and suggest that dwarf-dwarf mergers are indeed drivers of dwarf galaxy evolution. This finding is corroborated by Deason et al. (2014), who estimate that 10% of MW dwarfs have experienced a major merger since $z \sim 1$. It is therefore very possible that additional evidence of merged dwarfs exist in our nearby galaxies.

Both instances of gravitational interactions are particularly interesting for large-scale studies of the MW. Stellar streams in the Galaxy, particularly those with evident progenitors, are one of the most accessible methods to constrain the mass and potential of the DM halo. Increasing the number of systems that exhibit evidence of tidal disturbances (throughout the MW) may allow for a more continuous DM halo profile to be developed, while also potentially creating a consensus regarding its shape. At present, simulations predict that DM haloes of MW-sized galaxies are triaxial (Navarro et al. 1996); however, when baryonic physics is included, these haloes may become more round and axisymmetric (e.g., DeBuhr et al. 2012). Generally, there remains no true consensus on the shape of our own Galaxy's DM halo (e.g., Law et al. 2009 fit a triaxial DM halo to Sagittarius stellar stream, but Palau & Miralda-Escudé 2023 find that the best fit halo to the NGC 3201, M68, and Palomar 5 stellar streams

is oblate), but the disruptions of dwarf galaxy satellites may be useful to gaining closer agreement.

Furthermore, identifying evidence of dwarf-dwarf mergers in the Local Group will aid in pushing the limits of current knowledge in the realm of galaxy formation in the smallest scales. Though the case of dwarf-dwarf mergers are seemingly rare in observation, creating a census of these systems will allow us to better constrain the frequency of dwarf-dwarf mergers in MW-like galaxies. Ultimately, the identification of systems with this evidence may prove useful to disentangling the flavour of cosmology that dictates the Universe, as predictions from Deason et al. (2022) show that the frequency of dwarf-dwarf mergers in simulations are suppressed in Warm Dark Matter cosmologies. Therefore, the study of extended substructure in these systems is promising for future science, and important to the community of Galactic Archaeology.

1.4.1 Observational Signatures of Tides and Mergers

Satellite systems often experience strong enough MW tides such that their stars unbind and form stellar streams across the Galaxy. This phenomenon is particularly well-documented in globular clusters (GCs; bound stellar systems containing $\sim 10^{4-6}$ stars but unlike dwarfs, are not bound by a DM halo). There are $\sim$150 known globular clusters in the Galaxy today (Harris 2010) compared to $\sim$60 dwarf galaxies. In the literature, there are so far:

- 9 globular clusters reported to have tidal tails, extending multiple degrees beyond their estimated tidal radii (Mateu 2023);
- $\gtrsim$10 globular clusters with so-called "extra-tidal" stars (see discussion in Sollima 2020);
- Nearly 100 stellar streams in the Galaxy (Mateu 2023), many of which may have fully disrupted progenitors (dwarf galaxies or globular clusters) that are no longer discernible. It is unknown how many are truly from dwarf galaxy progenitors, though dwarf galaxy streams are argued to be much wider and have larger velocity/metallicity dispersions.

Compared to the number of (partially) disrupted globular cluster systems, there are only three MW dwarf galaxies exhibiting clear evidence of a stellar stream from a

dwarf galaxy progenitor. These are Sagittarius (Ibata et al. 2002; Majewski et al. 2003), Tucana 3 (Li et al. 2018b), and Boötes 3 (assuming it is indeed related to the Styx stellar stream; Grillmair 2009; Carlin et al. 2009).

Even with obvious tidal tails extending from the progenitor, the origin of stars in a dwarf's outskirts may not be tidal in nature. For example, the Engineering Dwarfs at Galaxy Formation's Edge (EDGE) cosmological simulation suite reported that dwarf-dwarf mergers in a "tidally isolated" (as in, not contained in a larger MW-type halo) system may exhibit extended features similar to tidal tails (Goater et al. 2024). In the literature, there exist a few observables and arguments that may suggest tides are the most logical scenario. These are discussed below.

Morphology

Aside from clear evidence of a stellar stream where stars are found some degrees beyond the dwarf's King tidal radius (King 1962), tidally disturbed systems may show evidence of the initial stages of disruption in their morphology. As a satellite orbits the host galaxy, gravitational forces between the host potential and the satellite act to strip mass from the smaller body. In a simplistic two-body system with spherical potentials, the mass is lost from the L1 and L2 Lagrange points of the satellite; these are specifically locations where the centripetal force equals the gravitational forces between the satellite and host (shown in Figure 1.6). Stars removed from the L1 Lagrange point are closer to Galactic centre, and once removed from the satellite, will orbit the MW on lower potential orbits (thereby increasing in kinetic energy to maintain conservation of energy). These stars will form the leading arm of the stream, while the stars at L2 will fall behind in velocity (with respect to the dwarf) and form the trailing arm. The initial stripping of stars at these particular locations may create an "s-shaped" morphology in the satellite. Additionally, it follows that the stars stripped from the satellite (now orbiting the MW) will coincide with an elongation in the direction of orbit.

Velocity Gradient

In stars that have been tidally stripped, there may be an appreciable velocity gradient as stars become unbound from the satellite. This is again due to the removal of stars into lower and higher potential energy orbits.

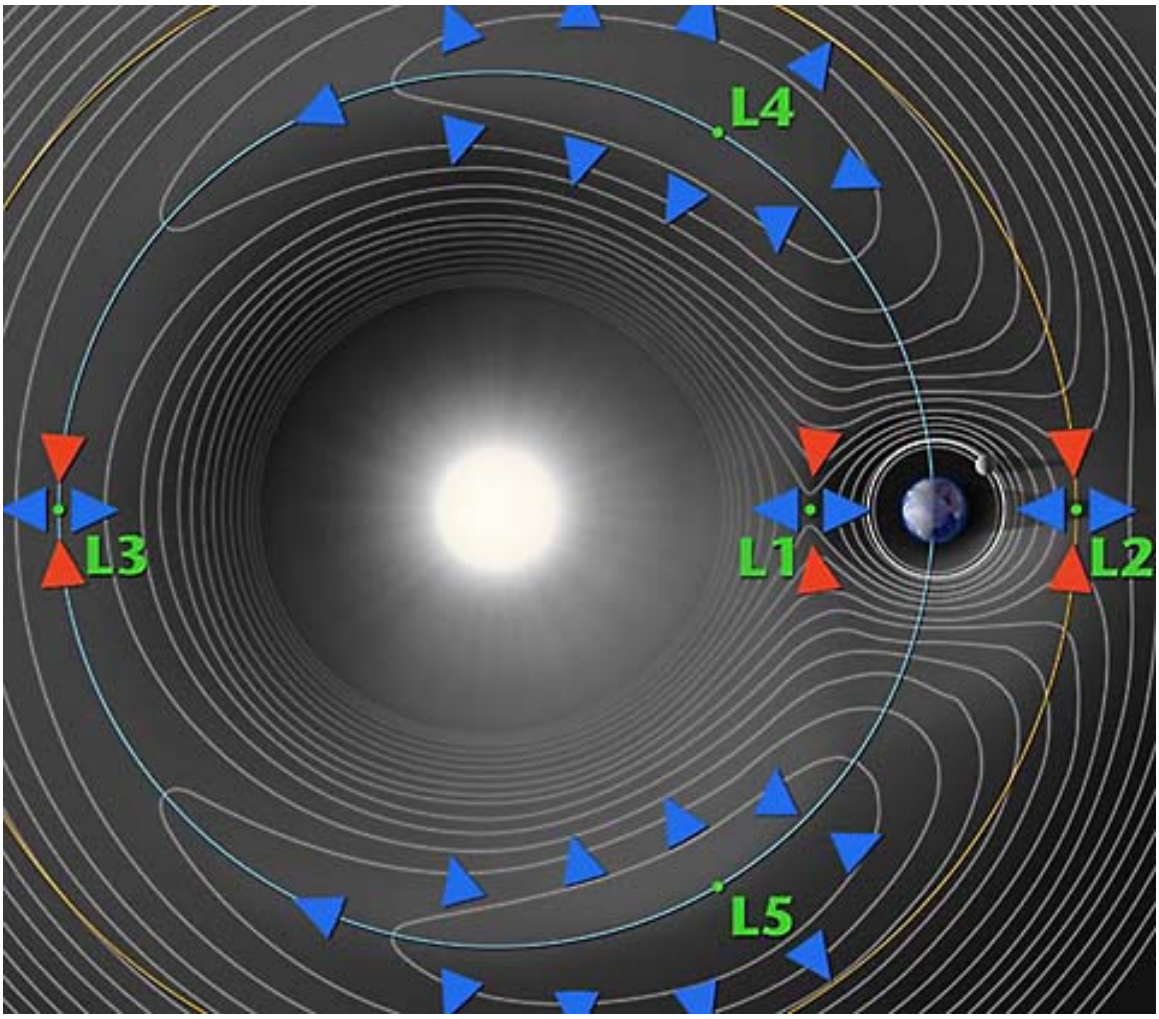

Figure 1.6: Contour plot of the effective potential in a two-body system. In a tidally disrupting system, stars will escape the satellite at the L1 and L2 Lagrange points indicated in the figure, where the superposition of the potentials of the two bodies are stable saddle points. Source: Lagrange Points of the Sun-Earth system, with Gravity Field | NASA.

Orbit

Systems whose pericentre is relatively near the Galactic Centre ($r_{peri} < 20$ kpc) are more likely to be tidally influenced (Read et al. 2006). This is largely because a satellite's maximum mass loss occurs at pericentre, due to two processes at play. Firstly, tidal stripping is naturally strongest where the host's gravitational force is largest (i.e., r_{peri}). Secondly, the system experiences disequilibrium due to tidal shocking (also at r_{peri}). This occurs when the the timescales of the gravitational interaction are much shorter than the dwarf's internal dynamics (specifically at close Galactocentric distances or through the Galactic disk) causing a net impulse in the system. As the kinetic energy changes, the potential energy remains the same. To compensate, the system will increase in size to return to virial equilibrium. The satellite's stars will migrate to physically larger distances in the dwarf, thereby allowing them to become unbound. In N-body simulations from Read et al. (2006), the authors found that tidal shocking was negligible for systems at distances >35 kpc from Galactic centre.

Density Ratio

Recently, Pace et al. (2022) presented a compelling argument as to whether a system may have experienced strong tidal disruption. This proxy utilizes relatively simple logic and can be applied to any system for which we have a constructed orbit as well as structural information of the dwarf. The authors first claim that situations of "strong disruption" would occur under the assumption that the tidal radius of a dwarf is approximately equal to the half-light radius (also found in simulations by Peñarrubia et al. 2009). The tidal radius (often approximated as the Jacobi radius) is essentially the distance from the centre of the satellite where the gravitation of the MW equals that of the satellite. Beyond this radius, the MW is able to capture satellite stars. The equation for the tidal radius is given as:

$$r_t = R(\frac{m}{2M(< R)})^{\frac{1}{3}} \tag{1.1}$$

where R is the satellite's distance from Galactic centre, m is the satellite's total mass, and $M(< R)$ is the enclosed mass of the MW at R. Assuming the situation for strong disruption occurs when the tidal radius is approximately equal to the half-light radius (r_h) of the dwarf, the mass m can first be approximated using the dynamical mass of the system (Wolf et al. 2010):

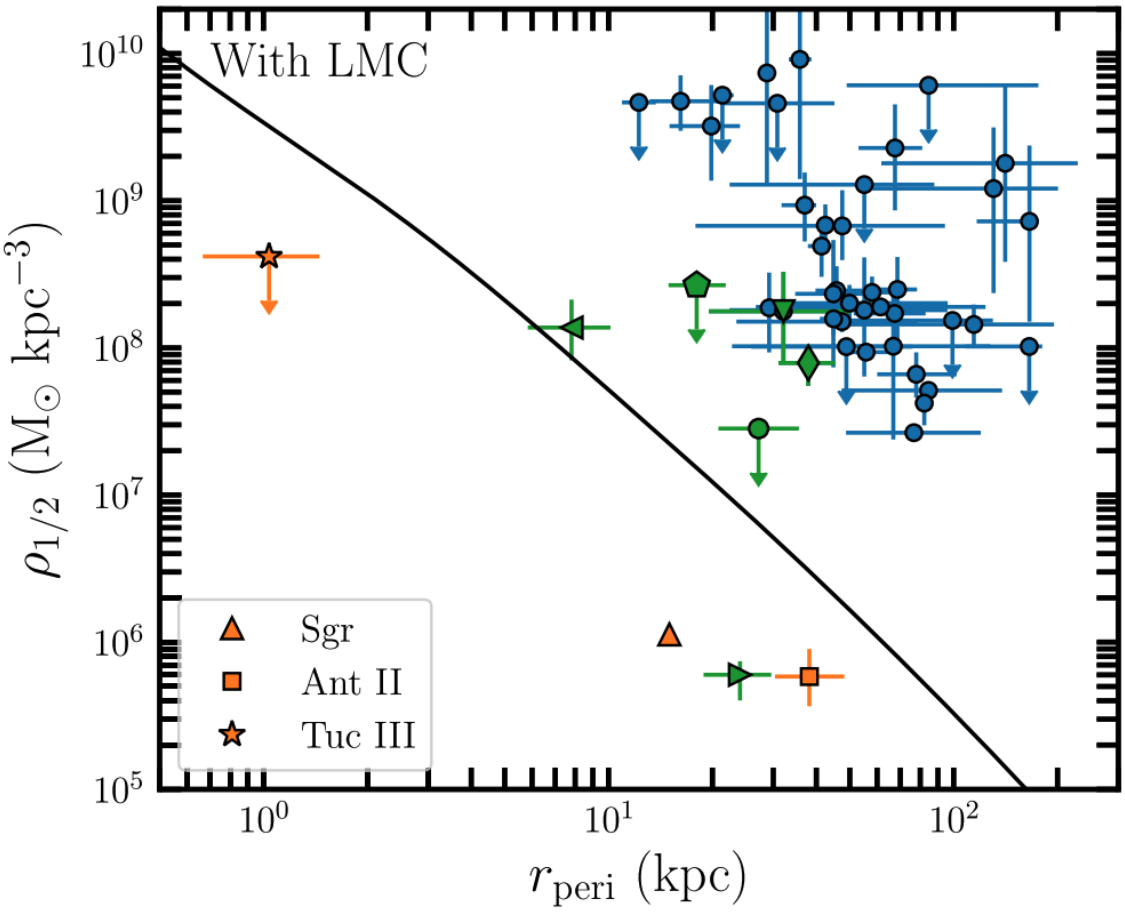

Figure 1.7: Density ratio argument presented for MW satellites, sourced directly from Pace et al. (2022). The black function represents 2× the density of the MW (in their assumed MW potential) as a function of radius. Therefore, systems below or at this line are suggested to have strong tidal influence. All orbits in the figure account for the time-varying potential in the presence of the orbiting LMC.

$$m(< r_h) = \frac{3\sigma^2 r_h}{G} \tag{1.2}$$

where σ represents the dwarf's line-of-sight velocity dispersion. Recalling that the highest rate of mass-loss occurs at pericentre, Equation 1.1 can be re-written as:

$$\frac{2M(< R_{peri})}{R_{peri}} \gtrsim \frac{m(< r_h)}{r_h^3}. \tag{1.3}$$

The final condition from Pace et al. (2022) then relates the density of the MW to that of the central mass of the dwarf by:

$$\rho(< r_h) \lesssim 2\rho_{MW}. \tag{1.4}$$

Figure 1.7 is a presentation of the density ratio argument, where the y-axis is the density within the half-light radius (note that $\rho(< r_h) = \rho_{1/2}$ in Figure 1.7) versus pericentre for all MW satellites with orbit information. The black trendline here represents $2\times$ the density of the MW (ρ_{MW}) as a function of radius. Systems plotted below this line are therefore suggested to be strongly tidally disturbed. Indeed, the three MW satellites with reported stellar streams are located at or under this region (Sagittarius, Tucana 3, and Boötes 3 plotted as the orange triangle, orange star icon, and green left-pointing triangle icon, respectively). Additionally, the low densities of Antlia 2 (orange square) and Crater 2 (green right-pointing triangle) fall in this regime; indeed, these systems have recently been proposed to have been influenced by tides (Ji et al. 2021).

Chemically Similar Trends

In a dwarf galaxy, stars that formed in-situ are expected to follow the same underlying chemical abundance sequence, albeit with a modest metallicity ([Fe/H]) dispersion. One such example is seen in the chemical trends of the [α/Fe]-[Fe/H] plane, which is often used to examine the chemical evolution history of a given galaxy by tracing the abundances of elements formed from Type II (core-collapse; α-elements) and Type Ia (white dwarf binary; iron peak elements) SNe. The trends observed in this plane are characteristic of a given galaxy, as they reflect the system's mass, ability to retain gas, and chemical enrichment. Assuming the system is well-mixed, chemical trends such as these should be consistent across all in-situ stars (even for those later displaced by tidal stripping), preserving a recognizable chemical signature of their

shared origin. Conversely, if a dwarf has undergone a past merger, stars originating from progenitors of different masses may retain distinct chemical-evolution tracks – potentially including multiple or offset [α/Fe]-[Fe/H] "knees" – that reflect their separate enrichment histories. However, the Ultra-Faint Dwarf (UFD) population are often considered pristine systems and therefore may have much less variance between chemical trends in their stars. The exception is cases of inhomogenous mixing, which may explain a large scatter in overall chemical trends. Evidence of inhomogeneous mixing was found in the r-process enhanced stars in Reticulum 2 (e.g., Ji et al. 2016b; Hayes et al. 2023), for example.

Contrarily, simulations conducted in Benítez-Llambay et al. (2016) found that dwarf-dwarf mergers may leave the remaining satellite with a metallicity (and age) gradient due to "outside-in" formation. In this scenario, the older population is metal-poor ([Fe/H] ~ -2.0) and formed similarly and at all radii due to early mergers. Subsequently, SF ceases due to stellar feedback and reionization. The dwarf's gas (not removed from the galaxy entirely, but is heated) is later able to cool and condense during a late-time merger, thereby initiating a second burst of SF. Energy from the merger then causes the older population to physically expand the system and populate a lower density halo, surrounding the more metal-rich in-situ population. This process introduces a metallicity and age gradient in the dwarf. In a satellite with a less active merger history, there may not be a resolved gradient in metallicity.

Stellar Density Profile (and Its Derivative)

Tidal influence can also change the distribution of stars in the outskirts of satellites. Numerical simulations by Peñarrubia et al. (2008, 2009) showed that stars in dwarfs experiencing tidal perturbations may gain energy in their internal orbit, thereby moving to larger apocentric radii, with respect to stellar orbits *within* the dwarf. This process can create an outer "excess" of stars in the dwarf's stellar density profile, or Σ(r).

Furthermore, there are signatures that should also be observed in the derivative of this function, or Γ(r). In the Peñarrubia et al. (2008, 2009) simulations, the original stellar distribution is assumed to be a King sphere embedded in a DM halo (Γ in the initial case is a steeply decreasing function). The system is allowed to orbit once past pericentre and continues to apocentre, where it is allowed to relax dynamically. In the final stellar density distribution, Peñarrubia et al. (2008, 2009) show that stars

will diverge from a linear dependence in Γ at a so-called "kink" radius. At larger radial distances where dwarf stars are migrating to very loosely bound orbits, a tidal model will then approach a power-law slope of $\Gamma \approx -4$. If there is enough data in the most distant radial bins, one may also observe a "break" radius in this profile, where Γ approaches 0.

1.5 Thesis Outline

This thesis investigates the chemo-dynamics and origins of extended stellar structures in MW dwarf galaxy satellites, with the central aim of identifying such structures and disentangling whether they arise from (i) tidal disruption by the Galaxy or (ii) the accretion of smaller dwarfs themselves. In this work, I focus primarily on the MW dSph population, as their quenched SFHs naturally minimizes the effects of SF-related processes on the stellar density in the outskirts. The proximity of these systems also enables the use of *Gaia*, whose all-sky astrometry provides the means to resolve individual member stars, examine their transverse motions, and effectively filter out the contaminating MW foreground. By combining spectroscopic (chemo-) data with astrometric (dynamic) catalogues, I aim to detect and characterize these faint outer features to disentangle their origin.

This thesis is organized as follows: in Chapter 2, I present the work of Jensen et al. (2024) where I enhanced an existing Bayesian-based algorithm to identify extended stellar substructure in MW dwarf satellites. This method combines spatial, colour-magnitude, and proper motion information from *Gaia* to construct the first systematic census of outer structure across ∼60 MW dSphs. I identified nine MW dSph satellites that exhibit evidence of extended stellar components. One of these systems, Boötes 3, forms the basis of the follow-up studies in Chapter 3. Here, I aim to characterize the extended stellar features observed in Jensen et al. (2024) for this system, using *Gaia*-selected members, new CFHT CaHK photometry, and matched filter searches in SDSS and DELVE photometric catalogues. This follow-up study explores only a small fraction of the science possible with the target lists provided in Jensen et al. (2024). In Chapter 4, I describe the collaborative follow-up efforts of our group and the science that has been enabled by my data, in which these follow-up spectroscopic observations probe the chemo-dynamical nature of dwarf galaxies. Finally, Chapter 5 summarizes these results and provides context for current and future studies.

Chapter 2

Detecting the Extended Substructure of our Dwarf Galaxy Satellites

This chapter presents the work of Jensen et al. (2024) in which I enhanced an existing Bayesian-based algorithm (based on that of McConnachie & Venn 2020b) to detect extended stellar components in the outskirts of Milky Way (MW) dwarf galaxy satellites. The algorithm combines spatial, colour-magnitude, and proper motion information to identify stars belonging to individual dwarf galaxies, using the all-sky photometric and astrometric data from *Gaia*. This method, applied to ∼60 dwarfs, is the first systematic census of outer substructure in our MW dwarf galaxy satellites. I identified nine dwarfs that appear to host extended stellar structure. Some of these detections have been previously reported in the literature as systems that are being tidally stripped, or are systems that appear to host a stellar halo of accreted stars. Here, I present the results of this work which lays the scientific foundation for the subsequent chapters. The candidate catalogues produced here have already enabled multiple spectroscopic campaigns and ongoing studies of tidal disruption and chemical evolution, which are discussed in later chapters.

This chapter is originally published as Jensen et al. (2024), and the majority of this paper is my own work, analysis, and scientific writing. The algorithm itself is based on a previous version from McConnachie & Venn (2020b) that I have enhanced in this work, as described in the text. The compilation of cross-matched data between Gaia stars and previous spectroscopic surveys in the literature presented in Table 2.1 were initially compiled by Dr. Alan McConnachie. I appended a few additional cross-matches for additional systems (e.g., Boötes 1, Boötes 3, and Sculptor) and also

cross-matched all Gaia fields used in this work to APOGEE. For stars with more than one existing radial velocity measurement, I calculated the weighted mean and standard deviation and saved these data in the final dataset. I created all figures in the final manuscript. Co-authors assisted in providing comments/edits to the final manuscript.

This work is originally published in Monthly Notices of the Royal Astronomical Society, Volume 527, Issue 2, p. 4209 – 4233 (2024), titled "Small-scale stellar haloes: detecting low surface brightness features in the outskirts of Milky Way dwarf satellites". Authors: Jaclyn Jensen, Christian R. Hayes, Federico Sestito, Alan W. McConnachie, Fletcher Waller, Simon E. T. Smith, Julio Navarro, and Kim A. Venn

2.1 Introduction

The early stages of galaxy formation involve the accumulation of baryonic and non-baryonic matter at conjunctions of the cosmic web, where the first proto-galaxies are suggested to have formed (Mo et al. 2010). Baryons are accreted into dark matter haloes, and these halos grow hierarchically (White & Rees 1978; Frenk et al. 1988). This general framework applies to galaxies of all sizes, including typical galaxies like the Milky Way (MW; $M_* \approx 5 \times 10^{10} M_\odot$) and Andromeda (M31), down to the least massive systems (ultra-faint dwarfs, UFDs; $M_* \lesssim 10^{2-5} M_\odot$; Simon 2019).

The debris of past accretions can be traced in the stellar haloes of galaxies, where gravitational accelerations are low and dynamical timescales are long. Substantial observational evidence of accreted substructures is present in our own MW, as our stellar halo is populated with a multitude of surviving dwarf galaxies (∼60 to date; McConnachie 2012) and disrupted satellites in the form of stellar streams (see Grillmair & Carlin 2016 and Helmi 2020 for recent reviews, and Mateu 2023 for the most up-to-date compilation of known stellar streams in the MW halo).

While these hierarchical processes are also expected to apply to smaller scale systems, little observational evidence for stellar haloes around dwarf galaxies currently exists (Deason et al. 2022), and their observational study is complicated by their intrinsically low masses. They are particularly feeble systems: their shallow potential wells are sensitive to a multitude of internal (star formation, stellar feedback) and external processes (mergers, ram pressure stripping, tidal stripping) that can strongly influence their individual morphologies (e.g., see discussion in Higgs et al. 2021). Over a dwarf's lifetime, these environmental and internal factors make it difficult to disentangle the origin of the stars which are present in the dwarf's outskirts. In addition, the intrinsic faintness of dwarfs means observations of the extended substructure in the dwarf's outskirts are challenging, especially when viewed against the dominant MW foreground populations.

With the advent of the *Gaia* satellite (Gaia Collaboration et al. 2016) and its wealth of kinematic data for ∼1.5 billion stars in the most recent data release (DR3; Gaia Collaboration et al. 2023), major progress has been made to study the individual resolved stars of MW dwarf galaxy satellites. A significant challenge when studying MW satellites is the ability to effectively and appreciably remove MW foreground contamination. However, *Gaia* proper motions provide one way of overcoming this challenge, as stars moving with the bulk proper motion of the dwarf galaxy can be

separated from MW stars moving in the foreground. Recent works using Bayesian techniques (applied to *Gaia* photometry and astrometry) have found high success in obtaining dwarf member samples, thereby enabling the measurement of systemic proper motions for most of these dwarf galaxies (e.g., Pace & Li 2019, McConnachie & Venn 2020b,a, Pace et al. 2022, Qi et al. 2022, and Battaglia et al. 2022).

In some of these Bayesian framework examples, a primary assumption for the dwarf model is the spatial distribution of stars. In most cases, the stellar density of the dwarf is assumed to be an exponentially decaying function (e.g., McConnachie & Venn 2020b; Battaglia et al. 2022; Pace et al. 2022). However, as the stellar distribution in the outskirts of dwarf galaxies remains unknown, this presumption may unduly restrict the detectability of stars in the dwarf's stellar halo, should one exist. For example, satellite systems (as a consequence of their accretion into the MW's halo) are under the influence of the MW potential and susceptible to tidal forces, which can act to strip stars from the dwarf satellite. Additionally, recent simulations conducted by Goater et al. (2024) and Deason et al. (2022) showed that dwarf-dwarf mergers may exhibit a secondary, extended radial profile beyond the primary component of the dwarf galaxy. The extended secondary component in this case (depending on the mass ratio of the merger itself) may contain a large fraction of stars which originated from a past accretion event and may even exhibit lengthy stellar distributions similar to tidal tails.

Recently, an exciting observation was made by Chiti et al. (2021) who uncovered evidence of an extended stellar halo in the MW satellite, Tucana 2 (Tuc2). Spectroscopically confirmed members of this UFD were identified out to significantly large radial distances ($\sim$9 circularized half-light radii, equating to a physical distance of 1 kpc). Given (i) the outskirt stars' lower metallicity compared to stars in the main body of the dwarf, (ii) a lack of a velocity gradient across the body of Tuc2, and (iii) the extended orientation of stars which are perpendicular to Tuc2's orbit, the authors argue that these radially distant stars are likely evidence of a past accretion event (i.e., dwarf-dwarf merger).

Motivated by this recent discovery, I initiated a search using *Gaia* to hunt for evidence of extended stellar structures around all of the known MW dwarf galaxies (and candidate systems). In this work, I expand the Bayesian methods of McConnachie & Venn (2020b, hereafter MV20a) to include extended multi-component substructure in the membership criteria, thus enabling the detection of members at much larger radii than in previous studies.

2.2 Data

I target all Milky Way (MW) dwarf galaxy satellites and likely candidates, as maintained in the tables originally published in McConnachie (2012)[1]. However, I intentionally exclude the relatively massive Magellanic clouds, as well as the Sagittarius (Sgr) dwarf galaxy whose outskirts are so extended that they form the basis of an extensive literature by themselves (for the most recent *Gaia*-based work, see Gaia Collaboration et al. 2018c and Kallivayalil et al. 2013 for the Magellanic systems, and Ibata et al. 2020 and Ramos et al. 2022 for Sgr). The dwarf inventory is therefore all other systems out to Leo T (heliocentric distance of ∼450 kpc), including a handful of recently discovered dwarfs. Newly discovered systems I include are: Boötes 5 (Smith et al. 2023, Cerny et al. 2023b), DELVE J0155-6815 (Cerny et al. 2021a), Eridanus 4 (Cerny et al. 2021b), Leo Minor and Virgo 2 (Cerny et al. 2023b), and Pegasus 4 (Cerny et al. 2023a). In Figure 2.1, I show the positions of all the candidate and confirmed dwarfs studied in this work in Galactic coordinates, and I list their names and positions in Table 2.1.

For each dwarf, I use the measured structural properties, distances, radial velocities, and metallicities as provided in the updated tables of McConnachie (2012), with some exceptions. For the newly added systems, I use parameters as reported in the relevant detection papers. I also updated parameters for Boötes 3 and Grus 1, both of which have recent structural measurements/updates (Moskowitz & Walker 2020 and Cantu et al. 2021, respectively). The parameters used for the newly added and updated systems are reported in Table 2.2.

While all dwarfs have measured distances and half-light radii, not all have measured ellipticities, position angles, radial velocities (RVs) and/or metallicities. I use all the aforementioned information for these systems, when available, to create the model likelihoods (discussed in Section 2.3) which represent the dwarf galaxy as a whole. For all dwarf parameters used in this work (structural parameters, positions, distance moduli, RVs, and metallicities) with the exception of updates/new dwarfs listed in Table 2.2, I refer the reader to Table 1 of MV20a.

My analysis is based on the data available in *Gaia* early Data Release 3 (eDR3; Gaia Collaboration et al. 2021). Specifically, I use stellar sources with all five astrometric solutions (positions, parallaxes, and proper motions) and photometry (G, B_P, and R_P magnitudes). For most dwarfs, I select all such sources within 2° of the

[1] https://www.cadc-ccda.hia-iha.nrc-cnrc.gc.ca/en/community/nearby/

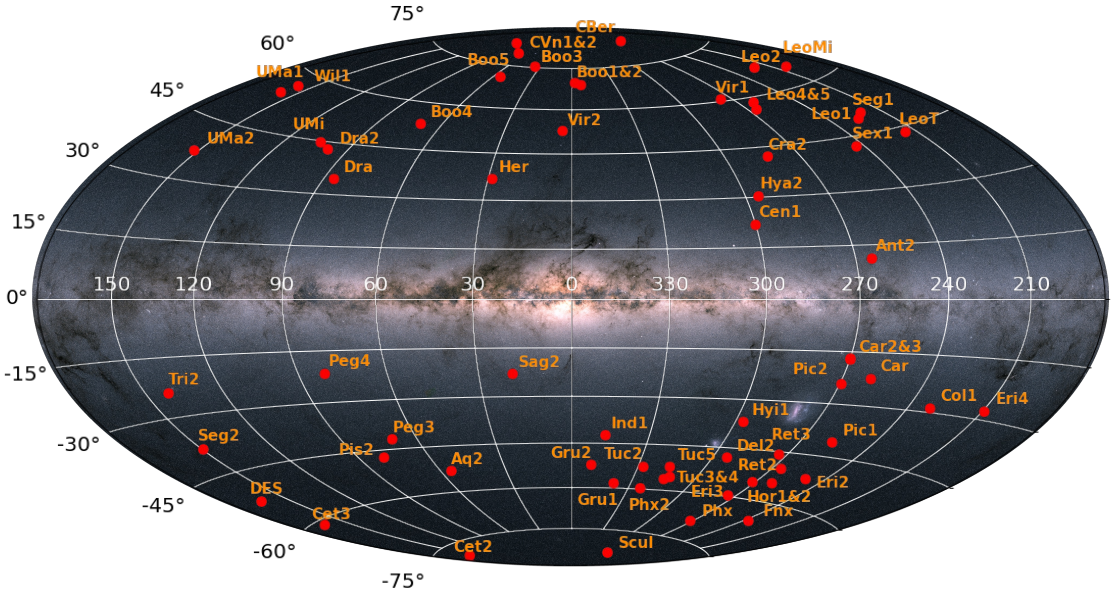

Figure 2.1: Galactic coordinates of the MW dwarf galaxy satellites used in this work, overlaid on the *Gaia* stellar density map. Image credit: ESA/*Gaia*/DPAC.

centre of the dwarf, which corresponds to on-sky distances well beyond 10 half-light radii for any dwarf. However, for larger systems (Antlia 2, Boötes 3, Carina, Crater 2, Fornax, Sculptor, Sextans 1, and Ursa Minor), I use a larger selection radius of 4° − 9° to better capture any distant members.

To select stars with reliable photometry and astrometry in *Gaia* eDR3, I require that they pass the same criteria discussed in McConnachie & Venn (2020a, hereafter MV20b). Specifically, the sources must have high-quality astrometry (`ruwe` < 1.3), as given by Lindegren et al. (2018) and Lindegren et al. (2021a). I de-redden the photometry using the dust maps in Schlegel et al. (1998) and relevant extinction coefficients (see Equation 1 of Gaia Collaboration et al. 2018b). I then correct the parallaxes of the stellar sources by the global zero-point of -0.017 mas (Lindegren et al. 2021b). As part of the membership selection algorithm, I filter the parallaxes to only select stars in the field that are at broadly consistent distances to the dwarf (i.e., stars whose 3-σ parallax uncertainty places them within the 3-σ range of the dwarf, inferred from the distance modulus).

Following MV20a and MV20b, I do not *require* stellar radial velocities (RVs) to identify members. However, I later use these data to validate the method and estimate contamination fractions (Section 2.4.2) when RVs are available. The radial velocities used in this work are from:

(i) the APOGEE Survey (Majewski et al. 2017) using the 17th data release of the Sloan Digital Sky Survey (SDSS; Blanton et al. 2017; Abdurro'uf et al. 2022). The APOGEE instruments (Wilson et al., 2019) are located on the 2.5-m SDSS and 2.5-m DuPont telescopes (Bowen & Vaughan, 1973; Gunn et al., 2006) providing dual-hemisphere coverage of Milky Way dwarf galaxies, whose targeting is described in Zasowski et al. (2013, 2017), Beaton et al. (2021), and Santana et al. (2021). In this work we use the radial velocities from the APOGEE survey which are measured as described in Nidever et al. (2015) and Holtzman et al. (in prep). These exist for a limited subset of the dwarfs. The number of APOGEE stars within the *Gaia* field of each dwarf are reported in the sixth column of Table 2.1;

(ii) a compilation of surveys targeting individual dwarf galaxies. The number of stars per *Gaia* field from these surveys are reported in the seventh column of Table 2.1. These data specifically have been largely compiled by Dr. McConnachie, with only a few exceptions.

In practice, for stars with more than one RV measurement, I take the weighted mean and weighted standard deviation of the multiple RV measurements.

2.3 Methods

The methodology is an extension of MV20a (inspired by Pace & Li 2019; see other similar implementations in Pace et al. 2022, Qi et al. 2022, and Battaglia et al. 2022), to which I direct the reader for specifics in the approach of the analysis. In summary, it is assumed that every star in a given field is a member of one of two populations: (a) the satellite, or (b) the MW foreground. A star's total likelihood is therefore given as:

$$\mathcal{L} = f_{sat}\mathcal{L}_{sat} + (1 - f_{sat})\mathcal{L}_{MW} \tag{2.1}$$

where $\mathcal{L}_{MW}$ and $\mathcal{L}_{sat}$ are the likelihoods of the MW and dwarf models respectively, and f_{sat} represents the fraction of stars in the dataset that are members of the dwarf. In this Bayesian framework, the two likelihoods in Equation 2.1 are based on three main components: (i) the stellar colour and apparent magnitude ($\mathcal{L}_{CMD}$); (ii) the radial distance of the star from the dwarf's centre ($\mathcal{L}_S$); (iii) the stellar proper motions ($\mathcal{L}_{PM}$), such that:

$$\mathcal{L}_{sat} = \mathcal{L}_{CMD}\mathcal{L}_{PM}\mathcal{L}_S \tag{2.2}$$

The three likelihood functions $\mathcal{L}_S$, $\mathcal{L}_{CMD}$, and $\mathcal{L}_{PM}$ are constructed for both the satellite and MW foreground populations. The final probability of a star being a member of a dwarf is therefore:

$$P_{sat} = \frac{f_{sat}\mathcal{L}_{sat}}{f_{sat}\mathcal{L}_{sat} + (1 - f_{sat})\mathcal{L}_{MW}}. \tag{2.3}$$

For each aforementioned likelihood function, I map each as a 2-D "look-up map". The method to create the look-up maps for the MW foreground models are the same as in MV20a. However, the current methodology for the dwarf model varies from the original implementation. In the following subsections, I highlight the differences between the MV20a paper and this approach. All dwarf parameters that are used in the satellite model are adopted from Table 1 in MV20a, with the exceptions of the new and updated systems described in Section 2.2 and listed in Table 2.2.

Table 2.1: The Milky Way dwarf satellites explored in this work (1; marked with * if no systemic RV is reported for the dwarf) and their equatorial positions in the sky (2, 3). Galactic coordinates are included in (4, 5). Provided also are the number of stars in a given dwarf field that contain RV information from APOGEE DR17 (6), as well as the number of stars with RVs available in focused dwarf studies (7; compiled primarily by Dr. McConnachie). Relevant references for (7) are listed in the final column (8).

Galaxy	R.A. (°)	Dec (°)	ℓ (°)	b (°)	No. APOGEE RVs	No. Survey RVs	Spec. Follow-up References
Antlia 2 (Ant2)	143.887	-36.767	264.895	11.248	1374	221	Torrealba et al. (2019)
Aquarius 2 (Aq2)	338.481	-9.328	55.107	-53.009	616	11	Torrealba et al. (2016)
Bootes 1 (Boo1)	210.025	14.500	358.082	69.624	237	282	Muñoz et al. (2006)
							Martin et al. (2007)
							Norris et al. (2008)
							Norris et al. (2010)
							Koposov et al. (2011)
							Waller et al. (2023)
Bootes 2 (Boo2)	209.500	12.850	353.694	68.871	103	8	Koch et al. (2009)
Bootes 3 (Boo3)	209.300	26.800	35.405	75.353	1483	20	Carlin & Sand (2018)
*Bootes 4 (Boo4)	233.689	43.726	70.682	53.305	524	–	
*Bootes 5 (Boo5)	213.911	32.912	55.661	70.916	–	–	
Canes Venatici 1 (CVn1)	202.015	33.556	74.305	79.822	217	145	Simon & Geha (2007)
Canes Venatici 2 (CVn2)	194.292	34.321	113.577	82.703	146	42	Martin et al. (2007)
							Simon & Geha (2007)
Carina (Car)	100.403	-50.966	260.112	-22.223	260	1855	Walker et al. (2009a)
Carina 2 (Car2)	114.107	-57.999	269.982	-17.140	62	283	Li et al. (2018a)

Table 2.1 – continued

Galaxy	R.A. (°)	Dec (°)	ℓ (°)	b (°)	No. APOGEE RVs	No. Survey RVs	Spec. Follow-up References
Carina 3 (Car3)	114.630	-57.900	270.006	-16.846	32	283	Li et al. (2018a)
*Centaurus 1 (Cen1)	189.585	-40.902	300.265	21.902	–	–	
*Cetus 2 (Cet2)	19.470	-17.420	156.465	-78.531	–	–	
*Cetus 3 (Cet3)	31.331	-4.270	163.810	-61.133	116	–	
Columba 1 (Col1)	82.860	-28.030	231.621	-28.879	–	49	Fritz et al. (2019)
Coma Berenices (CBer)	186.746	23.904	241.889	83.611	155	47	Simon & Geha (2007)
							Waller et al. (2023)
Crater 2 (Cra2)	177.310	-18.413	282.908	42.028	621	404	Caldwell et al. (2017)
*DESJ0225+0304 (DES)	36.427	3.069	163.582	-52.201	25	–	
Draco (Dra)	260.052	57.915	86.367	34.722	1246	1420	Walker et al. (2009a)
Draco 2 (Dra2)	238.198	64.565	98.294	42.880	43	45	Martin et al. (2016a)
							Longeard et al. (2018)
Eridanus 2 (Eri2)	56.088	-43.533	249.781	-51.646	–	44	Li et al. (2017)
*Eridanus 3 (Eri3)	35.690	-52.284	274.960	-59.599	–	–	
*Eridanus 4 (Eri4)	76.438	-9.515	209.499	-27.772	–	–	
Fornax (Fnx)	39.997	-34.449	237.103	-65.652	263	2486	Walker et al. (2009a)
Grus 1 (Gru1)	344.177	-50.163	338.679	-58.245	–	79	Walker et al. (2016)
Grus 2 (Gru2)	331.020	-46.440	351.143	-51.939	234	256	Simon et al. (2020)
Hercules (Her)	247.758	12.792	28.728	36.872	99	81	Simon & Geha (2007)
							Adén et al. (2009)
							Deason et al. (2012)

Table 2.1 – continued

Galaxy	R.A. (°)	Dec (°)	ℓ (°)	b (°)	No. APOGEE RVs	No. Survey RVs	Spec. Follow-up References
Horologium 1 (Hor1)	43.882	-54.119	271.388	-54.733	–	19	Nagasawa et al. (2018)
Horologium 2 (Hor2)	49.134	-50.018	262.472	-54.137	–	92	Fritz et al. (2019)
Hydra 2 (Hya2)	185.425	-31.985	295.617	30.464	–	19	Kirby et al. (2015a)
Hydrus 1 (Hyi1)	37.389	-79.309	297.416	-36.746	–	139	Koposov et al. (2018)
*Indus 1 (Ind1)	317.205	-51.166	347.156	-42.071	–	–	
Leo 1 (Leo1)	152.117	12.306	225.986	49.112	223	382	Mateo et al. (2008)
Leo 2 (Leo2)	168.370	22.152	220.168	67.231	275	220	Spencer et al. (2017)
Leo 4 (Leo4)	173.238	-0.533	265.442	56.515	239	27	Simon & Geha (2007)
Leo 5 (Leo5)	172.790	2.220	261.862	58.537	246	122	Walker et al. (2009b)
*Leo Minor (LeoMi)	164.261	28.875	202.232	64.750	–	–	
Leo T (LeoT)	143.722	17.051	214.853	43.660	–	42	Simon & Geha (2007)
Pegasus 3 (Peg3)	336.094	5.420	69.852	-41.813	–	–	Kim et al. (2016)
*Pegasus 4 (Peg4)	328.539	26.620	80.797	-21.403	–	–	
Phoenix (Phx)	27.776	-44.445	272.160	-68.949	–	118	Kacharov et al. (2017)
Phoenix 2 (Phx2)	354.997	-54.406	323.687	-59.749	–	75	Fritz et al. (2019)
*Pictor 2 (Pic2)	101.180	-59.897	269.633	-24.052	1150	–	
*Pictoris 1 (Pic1)	70.948	-50.283	257.299	-40.645	–	–	
Pisces 2 (Pis2)	344.629	5.952	79.206	-47.106	78	7	Kirby et al. (2015a)
*Pictor 2 (Pic2)	101.180	-59.897	269.633	-24.052	1150	–	–
*Pictoris 1 (Pic1)	70.948	-50.283	257.299	-40.645	–	–	–
Pisces 2 (Pis2)	344.629	5.952	79.206	-47.106	78	7	Kirby et al. (2015a)

Table 2.1 – continued

Galaxy	R.A. (°)	Dec (°)	ℓ (°)	b (°)	No. APOGEE RVs	No. Survey RVs	Spec. Follow-up References
Reticulum 2 (Ret2)	53.925	-54.049	266.296	-49.736	–	59	Koposov et al. (2015a)
							Simon et al. (2015)
							Walker et al. (2015)
Reticulum 3 (Ret3)	56.360	-60.450	273.878	-45.648	–	45	Fritz et al. (2019)
Sagittarius 2 (Sag2)	298.169	-22.068	18.936	-22.898	–	121	Longeard et al. (2020)
							Longeard et al. (2021)
Sculptor (Scl)	15.039	-33.709	287.535	-83.157	248	1462	Tolstoy et al. (2004)
							Walker et al. (2009a)
Segue 1 (Seg1)	151.767	16.082	220.478	50.426	21	327	Simon et al. (2011)
							Norris et al. (2010)
							Geha et al. (2009)
Segue 2 (Seg2)	34.817	20.175	149.433	-38.135	–	219	Belokurov et al. (2009)
							Kirby et al. (2013)
Sextans 1 (Sex1)	153.262	-1.615	243.498	42.272	1517	914	Walker et al. (2009a)
Triangulum 2 (Tri2)	33.322	36.178	140.899	-23.822	435	28	Kirby et al. (2015b)
							Martin et al. (2016b)
							Kirby et al. (2017)
Tucana 2 (Tuc2)	342.980	-58.569	328.086	-52.325	–	95	Walker et al. (2016)
							Chiti et al. (2021)
Tucana 3 (Tuc3)	359.150	-59.600	315.376	-56.184	–	675	Simon et al. (2017)
							Li et al. (2018b)

Table 2.1 – continued

Galaxy	R.A. (°)	Dec (°)	ℓ (°)	b (°)	No. APOGEE RVs	No. Survey RVs	Spec. Follow-up References
Tucana 4 (Tuc4)	0.730	-60.850	313.287	-55.292	–	81	Simon et al. (2020)
Tucana 5 (Tuc5)	354.350	-63.270	316.310	-51.892	–	29	Simon et al. (2020)
UrsaMajor 1 (UMa1)	158.720	51.920	159.431	54.414	100	106	Kleyna et al. (2005)
							Martin et al. (2007)
							Simon & Geha (2007)
UrsaMajor 2 (UMa2)	132.875	63.130	152.464	37.443	86	42	Martin et al. (2007)
							Simon & Geha (2007)
Ursa Minor (UMi)	227.285	67.222	104.965	44.801	273	958	Spencer et al. (2018)
*Virgo 1 (Vir1)	180.038	0.681	275.852	60.827	330	–	–
*Virgo 2 (Vir2)	225.059	5.909	4.067	52.754	–	–	–
Willman 1 (Wil1)	162.337	51.050	158.577	56.780	375	97	Martin et al. (2007)
							Willman et al. (2011)

Table 2.2: Relevant structural parameters, radial velocities, and metallicities for the newly discovered MW satellites. Updated parameters for Boo3 and Gru1 are additionally provided. Galaxies are marked with * if no systemic RV is reported for the dwarf. Citations: (1) Moskowitz & Walker (2020), (2) Smith et al. (2023), (3) Cerny et al. (2023b), (4) Cerny et al. (2021a), (5) Cerny et al. (2021b), (6) Cantu et al. (2021), (7) Cerny et al. (2023a).

Galaxy	RA (°)	DEC (°)	$(m-M)_0$	r_h (arcmin)	$e = 1 - \frac{b}{a}$	θ°	$v_h(kms^{-1})$	$\sigma_v(kms^{-1})$	$< [Fe/H] >$	Refs.
Boo3	209.300	26.800	$18.34^{+0.09}_{-0.10}$	33.03 ± 2.50	0.33 ± 0.09	-81.0 ± 8.0	197.5 ± 3.8	14.0 ± 3.2	−2.1 ± 0.2	(1)
*Boo5	213.911	32.912	$20.0^{+0.40}_{-0.48}$	$0.92^{+0.26}_{-0.19}$	$0.35^{+0.17}_{-0.21}$	$29.8^{+22.8}_{-21.8}$	–	–	–	(2); (3)
*DELVE2	28.772	-68.253	19.26 ± 0.1	$1.02^{+0.18}_{-0.15}$	$0.03^{+0.15}_{-0.03}$	74^{+84}_{-40}	–	–	–	(4)
*Eri4	76.438	−9.515	$19.43^{+0.1}_{-0.2}$	$4.9^{+1.1}_{-0.8}$	$0.54^{+0.10}_{-0.14}$	$65.0^{+9.0}_{-8.0}$	–	–	–	(5)
Gru1	344.177	−50.163	$20.4^{+0.2}_{-0.2}$	$4.16^{+0.54}_{-0.87}$	$0.44^{+0.08}_{-0.1}$	$153.0^{+8.0}_{-7.0}$	$-140.5^{+2.4}_{-1.6}$	<9.8	$-1.42^{+0.55}_{-0.42}$	(6)
*LeoMi	164.261	28.875	$19.56^{+0.11}_{-0.19}$	$1.09^{+0.37}_{-0.35}$	–	–	–	–	–	(3)
Peg4	328.539	26.620	19.77 ± 0.1	$1.6^{+0.29}_{-0.25}$	–	–	$-273.6^{+1.6}_{-1.5}$	$3.3^{+1.7}_{-1.1}$	$-2.63^{+0.26}_{-0.25}$	(7)
*Vir2	225.059	5.909	19.3 ± 0.22	$0.74^{+0.13}_{-0.11}$	–	–	–	–	–	(3)

2.3.1 Inclusion of the Horizontal Branch to $\mathcal{L}_{CMD}$

The implementation for the CMD satellite model is a likelihood function consisting of two separate likelihood maps: one for the red giant branch (RGB) and one for the horizontal branch (HB). The creation of the RGB likelihood map is performed in the same manner as in MV20a. I additionally include a model for the HB, which was not available in MV20a or MV20b. The HB implementation is simplified compared to the RGB, since the synthetic populations that fit the RGB well do not describe the HB population to a sufficient accuracy. In particular, the synthetic HB does not generally extend as blue as necessary to match the data, nor does it reproduce the observed HB shape[2]. This is highlighted in the central panel of Figure 2.2, which shows the positions on the CMD for stars in the field of Sculptor and the PADOVA isochrone (Girardi et al. 2002; converted to *Gaia* photometric bands using Weiler 2018 corrections) that best matches the RGB.

For the HB likelihood function, I chose to represent the HB as a constant value in G-magnitude, ranging between the blue end set by $(\mathrm{B}_P - \mathrm{R}_P) = -0.25$, and a red end extending to the RGB isochrone. This constant magnitude corresponds to the mean magnitude of an old (12 Gyr) and very metal-poor ([Fe/H] $= -2.19$) isochrone that is shifted by the dwarf's distance modulus.

In a similar manner to the implementation of the RGB, the likelihood function of the HB is essentially a Gaussian whose sigma is two factors added in quadrature. The first is an inherently assumed width of the stellar population; for the HB, the approximate width is assumed to be 0.1 mag in *Gaia* G. The second is the mean errors in $(\mathrm{B}_P - \mathrm{R}_P)$, to account for the errors in magnitude.

After the RGB and HB models are created, they are merged to create one likelihood map, such that each pixel in $\mathcal{L}_{CMD}$ is the maximum likelihood from either HB or RGB model. Then, the map is normalized such that the integral of the entire likelihood function ($\mathcal{L}_{CMD} = \mathcal{L}_{RGB} + \mathcal{L}_{HB}$) is equal to 1.

The left panel of Figure 2.2 shows an example of the constructed CMD likelihood for our example dwarf, Sculptor. The right panel shows the Sculptor stars whose probabilities obtained in the algorithm correspond to likely members ($P_{sat} \geq 20\%$) in green. The HB model, though certainly simplistic, effectively identifies probable HB

[2]In addition to synthetic isochrones not reproducing the HB's shape appropriately, there is also the "second parameter problem" (as seen in globular clusters; e.g., Moehler et al. 2003) that dictates how stars are distributed along the HB. These differences in similar metallicity systems are not well captured in synthetic stellar populations; nonetheless, these observed effects need to be accounted for.

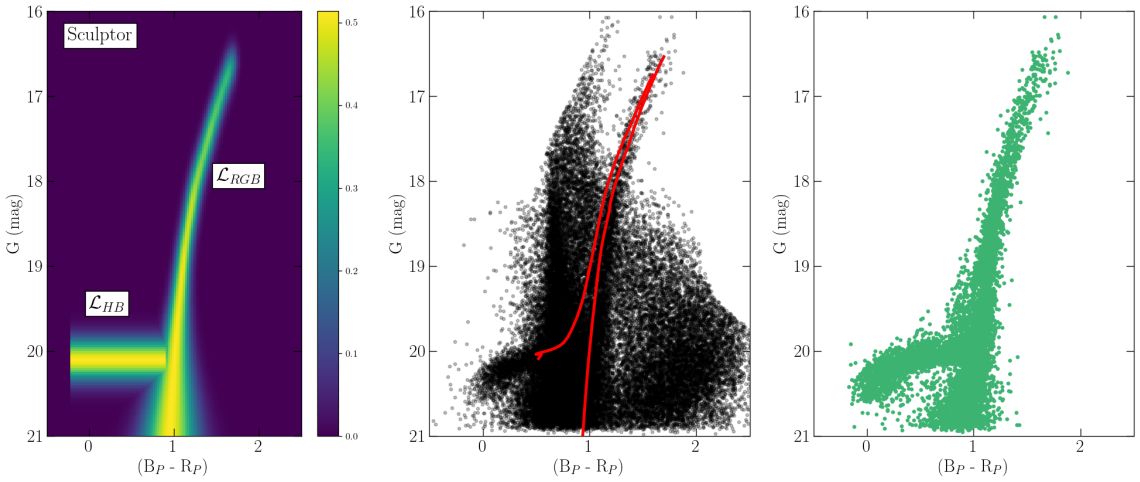

Figure 2.2: An example of the CMD likelihood ($\mathcal{L}_{CMD}$) calculated for the Sculptor dwarf galaxy. The left panel shows the CMD likelihood map, consisting of two models: one for the horizontal branch ($\mathcal{L}_{HB}$) and another for the red giant branch ($\mathcal{L}_{RGB}$), as described in the text. The middle panel is the CMD of Sculptor field stars, with the corresponding PADOVA isochrone overlain in red. The RGB of this model approximates the data well; however it is clear that the HB does not extend as blueward, and misses many Sculptor HB stars. Stars in the right panel are those with $P_{sat} \geq 20\%$, using the CMD likelihood map in the left panel, which clearly captures the full extent of the HB and exhibits little contamination.

members of the dwarf.

2.3.2 Spatial Likelihood Modifications to Identify Distant Members

For the dwarf spatial likelihood model, the original approach in MV20a is to create a look-up map, by co-adding many realizations of a 2-D exponential elliptical profile to approximate the dwarf's shape and stellar distribution. Each realization is created by randomly sampling the structural parameters of the dwarf (position angle, ellipticity, and half-light radius) using Gaussian uncertainty distributions, or assuming a circular profile shape if not all structural information is available.

In contrast, the approach used in this work assumes that there are two spatial components to every dwarf. The first ($\mathcal{L}_{S,inner}$) represents the main body, and corresponds to an exponential stellar density profile accounting for the structural parameters of the dwarf from the literature (similar to the methods of MV20a). Here, I expand this expression to include a secondary profile ($\mathcal{L}_{S,outer}$) which represents a putative outer, extended component. I chose to model this as an additional exponential profile with two unknown parameters. The first is the normalization (B) and the second is its scale radius (r_s). The overall spatial likelihood is therefore given by:

$$\mathcal{L}_S \propto \exp[\frac{-r}{r_e}] + B \exp[\frac{-r}{r_s}] \tag{2.4}$$

where r is the distance of the star from the dwarf's centre (accounting for position angle and ellipticity), r_e is the exponential scale radius of the dwarf (derived from the literature value of the half-light radius, r_h, such that $r_h \simeq 1.68 r_e$), B is the normalization of the outer component to the inner component (such that $0 \leq B < 1$), and r_s is the exponential scale radius of the putative outer component (such that $r_s > r_e$). If the preferred value for a dwarf is $B = 0$, this implies that no outer component is necessary in order to explain the data. In addition to requiring $r_s > r_e$, I set a weak prior on r_s such that it must be smaller than the radius of the field.

The implementation used in this work allows for a complete census of every dwarf, and the spatial likelihood specifically can determine which of these prefer outer profile to exist in order to explain the data (i.e., $B > 0$). However, it is important to not make strong assumptions about the shape of such an extra component, should it exist. Tidal tails can be very long and extended in specific directions (i.e., along the

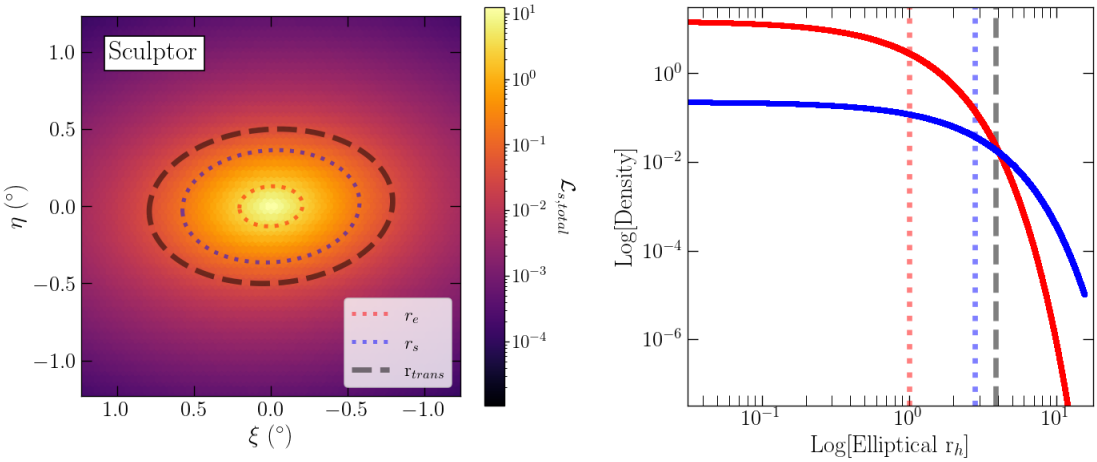

Figure 2.3: An example of the spatial likelihood ($\mathcal{L}_S$) for the Sculptor dwarf galaxy when assuming an elliptical outer profile. The 2-D spatial likelihood in the tangent plane is calculated using the values (B and r_s) solved for by the algorithm (see values in Table 2.3). The inner half-light exponential radius (r_e, red dotted), the outer scale radius (r_s, blue dotted), and the transition radius designating the approximate radii where the fraction of starlight is dominated by the secondary outer profile (r_{trans}, black dashed) are shown for comparison in both panels. The right plot shows the 1-D spatial likelihood for the inner (red line) and outer (blue line) spatial likelihood profiles.

dwarf's orbit); alternatively, there may be an "excess" of stars at all position angles around the dwarf due to an extended halo. To approach the problem agnostically, I adopt two simple assumptions and run the algorithm using both in order to check for consistency. The first is that the projected shape (i.e., ellipticity) of the outer profile is the same as the main body of the dwarf; the second is that the outer component is spherical. For the first, $r_{s,ell} = \sqrt{\xi_{rot}^2 + (\frac{\eta_{rot}}{1-ell})^2}$ where (ξ_{rot}, η_{rot}) are the tangent plane positions (ξ, η) of a star, whose axes have been rotated by the position angle. For the circular outer profile, $r_{s,circ} = \sqrt{\xi^2 + \eta^2}$.

In contrast to MV20a, the spatial likelihood function for the dwarf now contains unknown parameters. This means that look-up maps for the spatial likelihood cannot be easily constructed as was done previously, but instead the spatial likelihood function needs to be calculated from Equation 2.4 for each realization. While this allows the easy addition of a second spatial component, it does not allow the inclusion of the uncertainties in the measured parameters for the inner profile. I comment further on the influence of the spatial uncertainties in Section 2.5.10.

In Figure 2.3, I show an example of the spatial likelihood implementation for the Sculptor dwarf galaxy using an elliptical outer profile. The left panel shows a 2-D tangent plane map colour-coded by the total spatial likelihood ($\mathcal{L}_S$) and the right represents the likelihood in 1-D as a function of elliptical half-light radius. The relevant scale radii of the two components are shown as dotted lines, where the scale radius of the inner profile (r_e) is shown in red and the best-fit scale radius of the outer profile (r_s) is shown in blue for comparison. In the 1-D panel on the right, the relative densities for the inner (red) and outer (blue) components are plotted, where the outer profile is scaled by the algorithm's estimate for B. The associated scale radii are shown as vertical dotted lines in this panel. For dwarfs where the algorithm identifies an outer profile (i.e., B is non-zero), the approximate location where the outer profile begins to dominate over the inner profile can also be estimated. I refer to this boundary as the "transition radius" (r_{trans}), and for the Sculptor dwarf this boundary is highlighted as a black dashed line in Figure 2.3. Stars beyond this boundary will primarily belong to the outer component, and may have a particularly interesting physical origin.

To confirm internal consistency when using the 2-component $\mathcal{L}_S$ model to the previous work in MV20a and MV20b, I additionally compare these results to what will be referred to as the "1-component" model. In this version, the the $\mathcal{L}_S$ model is simply fixed per dwarf as was done in the preceding works (i.e., errors in struc-

tural parameters are accounted for, and only one exponential is used to describe the dwarf's density). The difference here is the addition of the HB from Section 2.3.1 to the CMD model. For internal consistency, it is necessary to compare both the 1- and 2-component models; these comparisons are discussed further in the following subsection.

2.3.3 Proper Motion Estimates and Added Prior

In the original implementation of MV20a and MV20b, the spatial likelihood model per dwarf was fixed, and so only three unknowns were to be solved for. These parameters being: the dwarf's systemic PMs in both directions, and the fraction of stars in the satellite. With the addition of an outer component whose unknowns describe the structure of the outer profile, the 2-component model now has five total variables to be estimated. In this version, note that the requirement to solve for the systemic PM of the dwarf is still maintained as part of the code, as it provides an additional method of verification of the method.

For the 1-component runs, I first confirm that the addition of the HB in $\mathcal{L}_{CMD}$ does not change the results of the proper motion estimate. Figure 2.4 compares the relative measurements and 1-σ errors of these estimates in the 1-component model (black) to the reported PMs in MV20b (grey dashed) and Battaglia et al. (2022, blue square). For the more recently discovered systems mentioned in Section 2.2, I also plot the reported PM estimates from each dwarf's respective detection papers (pink triangle). For nearly all systems with previous measurements, the PMs estimated in this work show consistency to past works within 1- to 2-σ.

In both versions of the 2-component runs (elliptical and circular outer profiles), I found that 51 out of the 64 satellites also have consistent PM estimates to MV20b. The 13 systems that fail the 2-component model do not produce consistent PM estimates due to an inability to converge in the spatial parameters B and r_s. I found that these particular systems have two properties in common: firstly, these dwarfs are of the smallest UFDs, such that the 1-component model only identifies $\lesssim$5 member stars within $6r_h$. And secondly, these small systems have substantially higher MW contamination fractions within the same area, such that the fraction of members within $6r_h$ is $\lesssim$20%. This means that the MW contamination is significantly higher than the signal of the satellite within those radii (a MW fraction of $\gtrsim$80%). Figure 2.5 shows this trend, with the systems that perform poorly highlighted in red text.

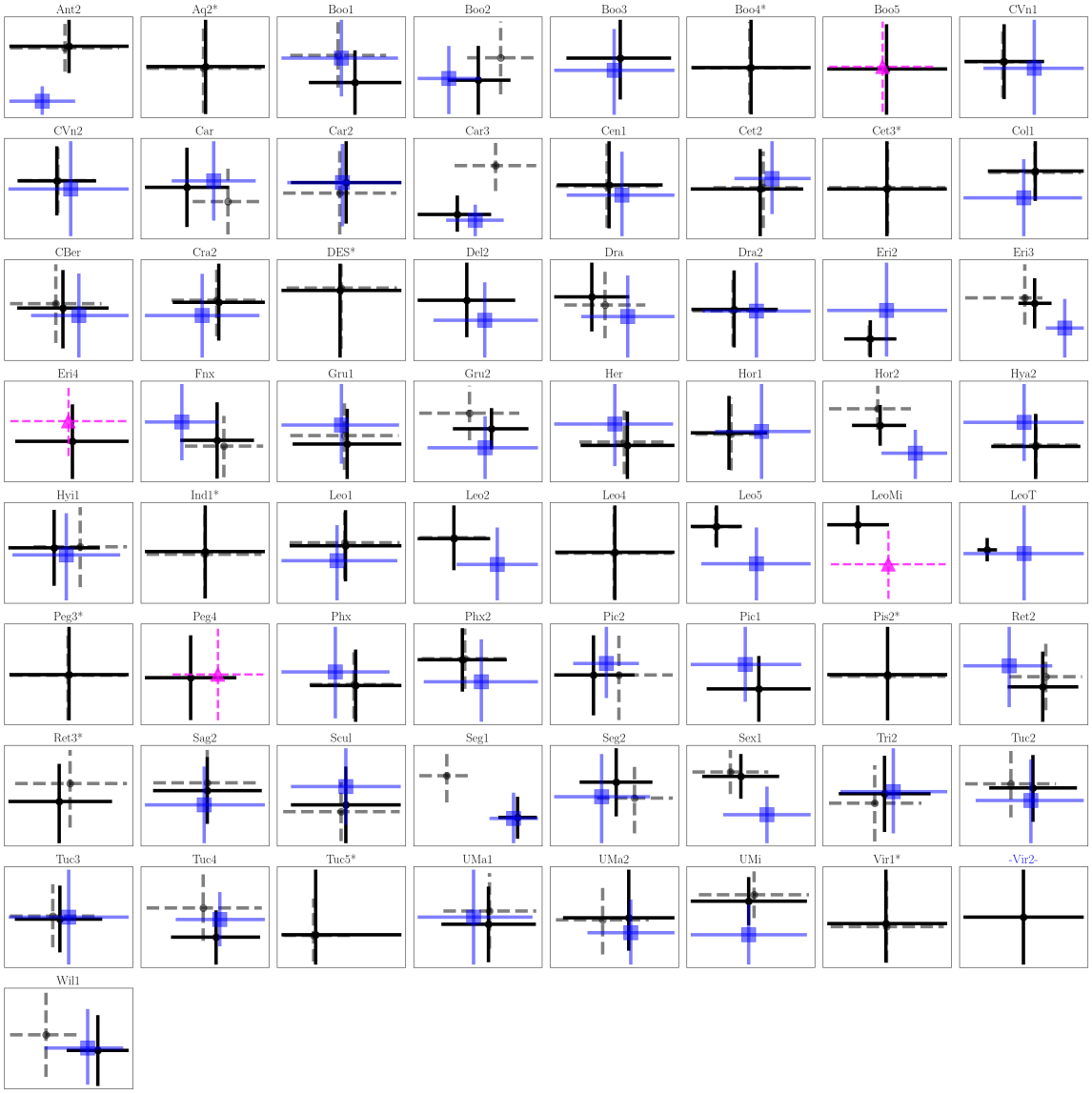

Figure 2.4: Comparison of the estimated proper motions of each dwarf used in this paper. To confirm internal consistency, the 1-component PM estimates from this work (black) are compared to those reported in MV20b (grey dashed) and to estimates from Battaglia et al. (2022) (blue square). All measurements show good consistency, and are within 3-σ. All errors in figure are reported as 1-σ errors. Some systems that are excluded from the Battaglia et al. (2022) dataset are those reported to have poor PM estimates (provided with a '*' in the title). For the recently discovered systems which have independently established proper motion estimates, the PM measurements from their relevant discovery paper (pink triangle) are also added.

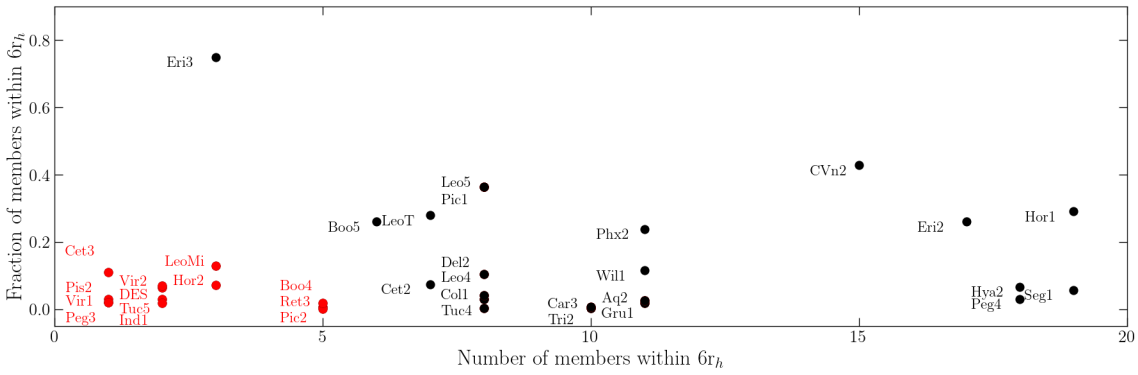

Figure 2.5: A comparison of the dwarf signal versus the MW foreground contamination, for systems with less than 20 high probability members ($P_{sat} > 50\%$) in the 1-component runs. The addition of free-parameters in the spatial likelihood results in a failure to converge in the 2-component runs due to a) the small number of member stars to begin with ($\lesssim$5), and b) the signal in the field dominates by a factor of >5. The systems where the 2-component algorithm fails are highlighted in red text. These dwarfs are excluded from the rest of the analysis.

Given this issue, a loose PM prior was adopted to better constrain $\mathcal{L}_{PM}$ in the 2-component spatial mode. In this version, the proper motion estimate must be within 5-σ of the PM of the dwarf derived in the single component case (accounting also for systematic errors; Lindegren et al. 2021a). Even with the addition of the PM prior, I find that these same 13 systems are unable to converge on any preferred values for the secondary component. These systems are: Boo4, Cet3, DES, Hor2, Ind1, LeoMi, Peg3, Pic2, Pisc2, Ret3, Tuc5, Vir1, and Vir2. It is unsurprising that the algorithm fails in these cases, as it is attempting to fit five parameters to less than 10 stars and is thus unable to resolve the dwarf's signal against the presence of the MW foreground. For the remainder of this work, these systems are removed from any further analysis.

2.3.4 A Note on Reported Parameters

Using the three likelihood functions ($\mathcal{L}_{CMD}$, $\mathcal{L}_{S}$, and $\mathcal{L}_{PM}$) for both the MW foreground and satellite models, the algorithm searches over parameter space for the combination that maximizes the total likelihood for a given dwarf. The estimated parameters are the following 5 variables: $\mu_{\alpha*}$, μ_{δ}, B, r_s, and f_{sat}. These parameters are determined using the `python` package `emcee` (Foreman-Mackey et al. 2013). The algorithm is applied to all *Gaia* fields obtained for the dwarfs listed in Table 2.1.

Typically, the parameters for the outer profile have asymmetric posterior distributions. Therefore, I opted to report the values corresponding to the mode of the posterior distribution. The mode is determined by creating a histogram of the posterior using very fine, equally spaced bins.

The uncertainties on this estimate are then reported as the high and low bounds of the highest density interval (HDI). The HDI is defined as the shortest interval in a posterior distribution that contains a specified credible mass. Consequently, the mode is always contained within the credible region of the PDF. I use a credible mass of 68%, which is essentially the Bayesian equivalent to $\overline{x} \pm 1\sigma$, or the 68% confidence interval in frequentist statistics.

2.4 Results & Validation

The algorithm's best-fit estimates for the spatial parameters (B and r_s) utilize the data to identify dwarfs whose outer profile solutions are non-zero. That is, in the ∼60 dwarfs explored in this work, I find a total of nine that are suggested to host extended

stellar substructure. In both of the 2-component runs, I find that the inventory of dwarfs where B is non-zero is the same between both assumed outer profile shapes. These dwarfs are: Boötes 1, Boötes 3, Draco 2, Grus 2, Sculptor, Tucana 2, Tucana 3, and Ursa Minor. The preferred parameter values for their outer stellar component in both the elliptical and circular runs are given in Table 2.3.

A natural consequence of the existence of an outer spatial profile is the transition at which the secondary component dominates the fraction of starlight. Largely, the location of this transition depends on the outer profile parameters, B and r_s. The location of this transition can be estimated empirically using the spatial likelihood function, and can then be used as a modest proxy to highlight stars that may be considered to be outskirt members. I reference this feature as the "transition boundary" (r_{trans}). In Table 2.3, I report the angular and physical semi-major axis of this transition, as well as the ellipticity of the transition boundary ellipse. For all systems, the position angle of this boundary is the same as that assumed for the dwarf itself (as in Table 1 of MV20a).

Prior to discussing the dwarfs that appear to host outer profiles in detail, I first explore the differences in the probability of membership between the two outer component shape assumptions in the following subsection. I then conduct an analysis to validate these methods using stars with RVs, when available.

2.4.1 Elliptical and Circular Outer Profiles

The main rationale of this work is to determine, with high fidelity, which dwarf galaxy systems host outskirt stellar substructures. However, it is not known *a priori* what the properties of the putative outer component may be. With respect to the projected shape of this component, the strategy has been to adopt two different shapes (one the same shape as the inner regions, i.e. elliptical, while the other is circular) and compare the resulting datasets for one system.

As reported in Table 2.3, the set of dwarfs that the algorithm identifies as having two components is the same for both outer profile runs. The conclusion that these dwarfs have more stars in the outskirts than expected from a simple exponential, is apparently robust to the assumed shape of the outer profile shape.

Figure 2.6 shows the differences in probabilities ($P_{Ell} - P_{Circ}$) between these two datasets as a function of r_h. For clarity, stars with $P_{sat} \geq 20\%$ in at least one of these datasets are plotted. Those with P_{sat} above this threshold in *both* datasets are shown

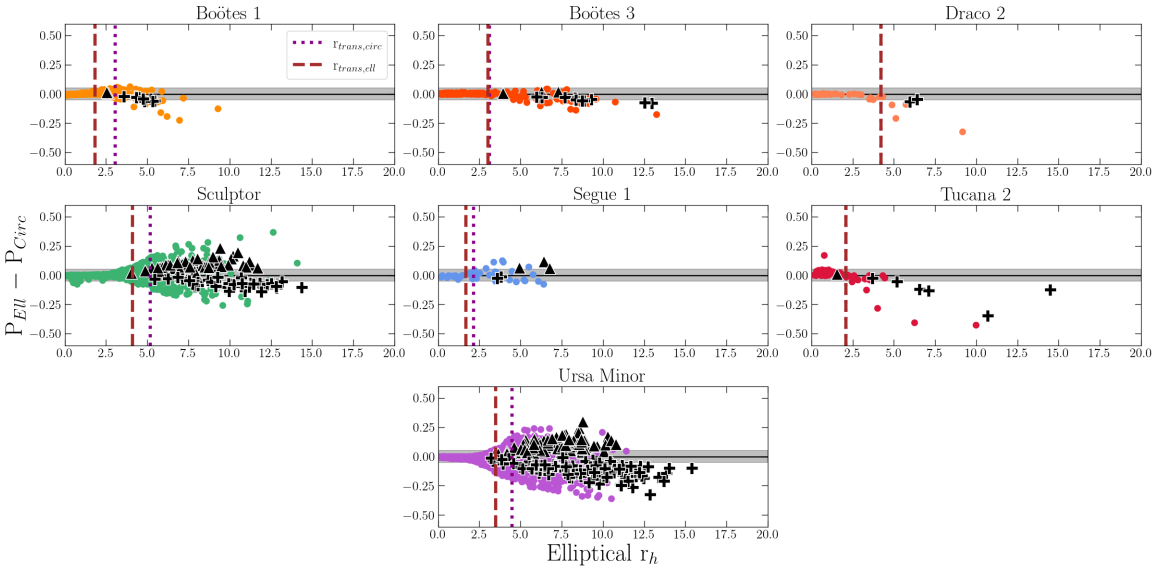

Figure 2.6: Differences between calculated probabilities in the elliptical and circular 2-component runs, for dwarfs with detectable outer profiles. In all panels, three subsets of the data are shown: stars which appear only in the elliptical dataset are shown as black triangles ($P_{ell} > 20\%$), stars which are only in the circular dataset are shown as black + icons ($P_{circ} > 20\%$), and stars in common between both profile runs are highlighted as coloured points (both P_{ell} and $P_{circ} > 20\%$). Over 90% of the data shown here have minimal changes in probabilities ($\pm 5\%$) between elliptical and circular models (highlighted by the grey region in each panel). The vertical magenta dotted and brown dashed lines are the transition radii solutions for the circular and elliptical profiles, respectively. Gru2 and Tuc3 are not included in the figure, since their structural parameters are assumed to be circular and there is no difference in probabilities between either 2-component run.

as filled circles. Stars whose probability is $\geq$20% in one set but not the other are plotted as black triangles (elliptical set only) and black + icons (circular set only).

Figure 2.6 shows that, for stars interior to the transition boundaries, the choice of an elliptical or circular outer profiles does not significantly change the probabilities. To emphasize this, each panel also shows a grey highlighted region, corresponding a change in probability of $\pm$5% between the two runs. In this figure, >90% of the overall data are found within these bounds.

As seen at larger radii, the greatest probability differences occur at farther radial distances. I find that these differences are a result of the outer profile shape: for example, when examining the majority of the data which appear in only one set versus the other (all black icons), the positive y-axis consists only of the "elliptical only" set, while the negative y-axis are those of the "circular only" set. The differences seen in Figure 2.6, whereby some stars are more likely to be members in one realization than the other, is a result of the stars' angle from the major axis. This concept is further corroborated when examining the tangent plane positions of these same stars in Figure 2.7. As shown in the figure, stars in these mutually exclusive sets are located along the dwarf's major axis ("elliptical only") and minor axis ("circular only"). As a final confirmation, I further examined the residuals of the tangent plane spatial likelihoods ($\mathcal{L}_{S,Ell} - \mathcal{L}_{S,Circ}$) and found the major and minor axes are enhanced in their respective model.

At this time, it is not obvious which model best fits these outer profile dwarfs as the structure will no doubt be linked to the stars' physical origin. However, the approach in this study is not to define the shape of dwarf galaxy outskirts explicitly, but instead is to identify whichever stars plausibly belong to these systems (of course, particularly those at large radii). Given these overall motivations, I remain agnostic about which shape should be utilized, and instead assume that any star with a reasonably high probability should be considered a member. For this reason, the possibility of membership is taken as the maximum probability (P_{max}) per star, between all three runs (the single and the two 2-component versions – i.e, elliptical and circular outer profiles). As evidenced by the data presented here, member stars may be overlooked when assuming one model over the other. Using the maximum probability of the three runs ensures that all plausible stars are accounted for. Future spectroscopic follow-up for these candidates will not only be necessary to confirm that a star is a member of its nearby satellite, but also to confirm their origin (accreted or tidal) and in turn derive the dwarf's stellar halo shape.

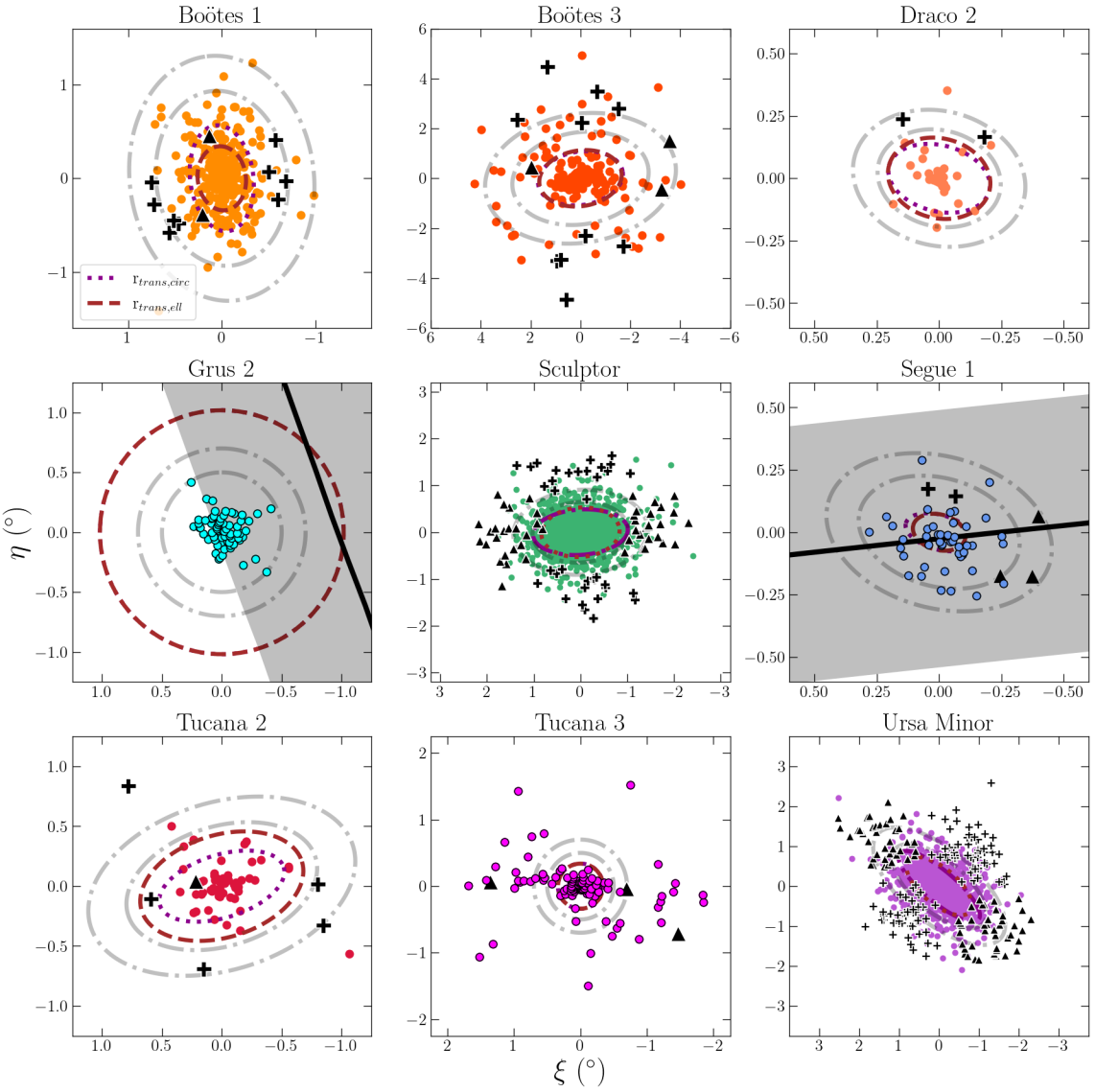

Figure 2.7: Tangent plane plots for all dwarfs with identified outer profiles. The relevant radii representing the transition boundary solutions ($r_{trans,circ}$ and $r_{trans,ell}$), and the three subsets of data (elliptical only, circular only, and stars in common) are represented the same as in Figure 2.6. The 5 and $7r_h$ ellipses for each system are additionally plotted in grey. For direct comparison to the incidence of the Orphan/Chenab stream to Gru2, and the 300 km s^{-1} stream to Seg1, the approximate stream position is included (black line; from the `python` package `galstreams`; Mateu 2023) and the grey highlight indicates the approximate width ($\sigma = 1°$ for Orphan/Chenab, and 0.4° for the 300 km s^{-1} stream).

Table 2.3: Dwarfs with secondary outer profiles, as determined in both the elliptical and circular runs. The transition boundary (r_{trans}, see text) is defined as the approximate boundary where the outer profile dominates the total fraction of starlight. The parameters describing this boundary by the semi-major axis and ellipticity of the best-fit ellipse are also provided here.

	Elliptical					Circular				
Galaxy	B	$r_{s,ell}$	$r_{trans,ell}$		Ellipticity	B	$r_{s,circ}$	$r_{trans,circ}$		Ellipticity
		($^\circ$)	($^\circ$)	(pc)			($^\circ$)	($^\circ$)	(pc)	
Boo1	$0.245^{+0.151}_{-0.35}$	$0.206^{+0.021}_{-0.036}$	0.34	400	0.25	$0.086^{+0.058}_{-0.098}$	$0.217^{+0.029}_{-0.055}$	0.57	660	0.41
Boo3	$0.015^{+0.006}_{-0.025}$	$1.901^{+0.554}_{-1.841}$	1.66	1350	0.33	$0.014^{+0.006}_{-0.021}$	$1.805^{+0.585}_{-1.53}$	1.71	1390	0.38
Dra2	$0.019^{+0.018}_{-0.148}$	$0.069^{+0.016}_{-0.05}$	0.21	80	0.23	$0.026^{+0.023}_{-0.198}$	$0.063^{+0.018}_{-0.031}$	0.21	80	0.36
Gru2	$0.004^{+0.002}_{-0.002}$	$0.088^{+1.704}_{-2.912}$	1.02	940	0.0	–	–	–	–	–
Scl	$0.015^{+0.004}_{-0.004}$	$0.317^{+0.022}_{-0.022}$	0.84	1260	0.37	$0.013^{+0.003}_{-0.003}$	$0.356^{+0.021}_{-0.048}$	1.06	1520	0.52
Seg1	$0.174^{+0.082}_{-0.562}$	$0.108^{+0.029}_{-0.022}$	0.11	40	0.34	$0.165^{+0.109}_{-0.507}$	$0.081^{+0.013}_{-0.029}$	0.14	60	0.50
Tuc2	$0.009^{+0.007}_{-0.219}$	$0.284^{+0.087}_{-0.187}$	0.70	700	0.39	$0.037^{+0.035}_{-0.201}$	$0.244^{+0.07}_{-0.104}$	0.54	540	0.51
Tuc3	$0.005^{+0.002}_{-0.004}$	$0.889^{+0.369}_{-0.954}$	0.34	150	0.0	–	–	–	–	–
UMi	$0.015^{+0.005}_{-0.004}$	$0.619^{+0.056}_{-0.063}$	1.00	1320	0.55	$0.022^{+0.00.}_{-0.006}$	$0.356^{+0.021}_{-0.048}$	1.29	1710	0.70

2.4.2 Examination of Purity Fractions and Contamination

In the Bayesian framework presented here, a typical method to classify data as a member of one population or the other is to select a decision boundary for the probabilities. Generally, a reasonable boundary is 50%, where >50% implies a dwarf member, and <50% is of the MW population. In this work, I instead chose to adopt a boundary that is inferred from the most likely members, by confirming their membership via radial velocity information (when available), to better interpret a reasonable limit. This approach also allows for an internal consistency check by comparing the samples of true MW foreground and true spectroscopically confirmed members to their associated probability (i.e., P_{max}).

This is done by first calculating what I refer to as the "purity fraction". For each star in a given field with spectroscopic data, I determine whether its measured RV is consistent with being a member of the dwarf. A star is considered a true member if its individual RV is within 3-σ of the satellite's RV, accounting for the dwarf's velocity dispersion, the star's individual RV error, and the dwarf's systemic RV error in the calculation. RV, errors, and dispersion of the dwarf are taken directly from Table 1 of MV20a or from the updated systems listed in Table 2.2. The purity fraction is defined as the fraction of stars per probability interval that have RVs consistent with membership of the dwarf, specifically in each probability bin from 0 to 1 (0% to 100%). Note that ∼3 out of every 100 stars may have an RV more than 3-σ from the satellite, but still be a genuine member, although it will end up classified as a non-member based on its RV.

An example of this validation test as applied to the Sculptor dwarf galaxy is highlighted in Figure 2.8. The RVs are taken as the weighted mean of APOGEE DR17 and individual survey measurements, if either exist for a given dwarf (listed in Table 2.1). For Sculptor, all stars in the field from Gaia eDR3 with no known spectroscopic data (at the time of this publication) are plotted in grey in the tangent plane (left) and CMD (centre) panels. Coloured symbols show stars with RV data separated by probability of membership to Sculptor; stars with $P_{max} > 10\%$ (dwarf members) are shown as red points, while those with $P_{max} < 10\%$ (MW foreground) are marked as blue **x** icons. The right panel shows individual star velocities as a function of elliptical half-light radii (in units of r_h), where the dwarf's systemic RV is highlighted as the black horizontal line.

The overwhelming fraction of stars flagged as members by this probability division

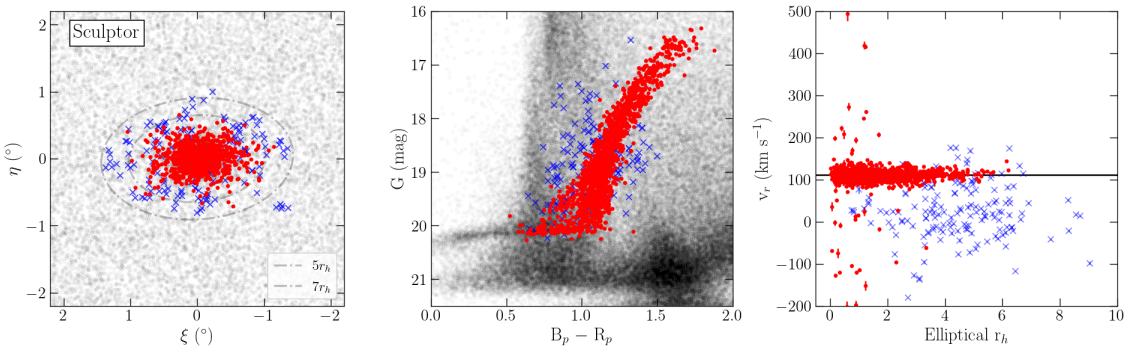

Figure 2.8: An example of the radial velocity purity test, for the Sculptor dwarf. Grey points in the tangent plane (left) and CMD (middle) represent all field stars analyzed in this work. Stars with radial velocity information available are shown as coloured points in all three panels; red indicates stars which are considered dwarf members ($P_{max} > 10\%$) are marked as points, while foreground MW contamination ($P_{max} < 10\%$) are shown as faint x's. The right panel shows these radial velocities as a function of distance, where Sculptor's systemic radial velocity is represented as the black horizontal line for comparison.

Probability bin	No. RV stars	No. Consistent	Fractional Purity
$0.0 \leq P_{max} < 0.1$	166	35	0.21 ± 0.08
$0.1 \leq P_{max} < 0.2$	2	2	1.00 ± 0.71
$0.2 \leq P_{max} < 0.3$	2	1	0.50 ± 0.70
$0.3 \leq P_{max} < 0.4$	1	1	1.00 ± 1.0
$0.4 \leq P_{max} < 0.5$	N/A	N/A	N/A
$0.5 \leq P_{max} < 0.6$	4	4	1.00 ± 0.50
$0.6 \leq P_{max} < 0.7$	5	5	1.00 ± 0.45
$0.7 \leq P_{max} < 0.8$	9	8	0.89 ± 0.33
$0.8 \leq P_{max} < 0.9$	18	17	0.94 ± 0.24
$0.9 \leq P_{max} \leq 1.0$	1781	1731	0.97 ± 0.02

Table 2.4: Purity fraction estimates for the Sculptor dwarf, as described in the text. Each probability bin is in increments of approximately 10%. Note that there are no stars in the sample found in the $0.4 \leq P_{max} < 0.5$ bin (i.e., no data with measured RVs are assigned probabilities in this range).

(red points in Figure 2.8) exhibit RVs that are consistent with the dwarf satellite. This remains true, and is particularly apparent, for stars found out to large distances where the MW foreground population dominates the total number of stars in any radial annulus. This result is particularly encouraging, as the kinematic model for the dwarf (i.e., the PM likelihood and its associated priors) is independent of RV considerations.

I then estimated the level of contamination in the Sculptor sample by determining its purity fractions. Per probability bin (in steps of 0.1, or 10%), I determine the number of RV stars which are consistent to dwarf membership, divided by the total number (N) of RV stars in that bin. Errors for the purity fraction are reported as $\frac{\sqrt{N}}{N}$ to account for Poisson statistics. Sculptor's purity fraction (and relative number of stars to obtain this statistic) are reported in Table 2.4.

Largely, the fractional purity for Sculptor across all P_{max} bins >10% is high (though, small number statistics in multiple bins suggest rather large errors), and a significant number of RV members are successfully identified with the highest probabilities (1731 member stars out of 1781, in the >90% bin). Note that in the >90% bin, there are 50 or so stars which are not members based on their RVs, yet their probabilities in the algorithm are high. These ∼50 stars are all located in the innermost regions of Sculptor (i.e., <2 r_h; shown as the red points in the RV panel of Figure 2.8). Though they indeed have inconsistent RVs to the dwarf, we note that these particular stars are all a) towards the centre of the dwarf, b) have consistent proper motions to Sculptor, and c) overlap the same region of the CMD as other Sculptor stars. Given that the model would therefore indicate that these stars are indeed members based on these three criteria, it is anticipated that they would be ascribed high probabilities (>95%, in fact). As evidenced by the purity fraction estimates in Table 2.4, these data represent the 3% of stars which contaminate the largest probability bin. This type of contamination is expected, and at close elliptical distances it is reasonable to have a larger *number* of stars with inconsistent RVs (though the *fraction* of contamination remains low).

This process is repeated for every dwarf which has a measured systemic RV. After obtaining the relative numbers of true members and the total per probability bin, the purity is expressed as a function of probability by marginalizing the data over all satellites. This "purity curve" (as it is hereafter titled) is essential to determining an appropriate decision boundary for dwarf membership based on the probability assigned, with the idea in mind to retain the most complete member sample out to

large radii.

Figure 2.9 shows, for all stars with a radial velocity, the fraction of stars that are RV confirmed members as a function of P_{max}. The first panel shows this for all dwarfs (with measured systemic RVs), the middle panel for dwarfs with $M_V \lesssim -8$ mag, and the right panel for dwarfs with $M_V \gtrsim -8$ mag.

In the idealized case, one might expect that the probability of membership is synonymous with the purity fraction, such that the correlation between purity and probability is one-to-one. However, all panels of Figure 2.9 show that the P_{max} estimated from the algorithm is in fact conservative. For example, ∼60% of stars with $P_{max} = 20\%$ are shown to be members (whereas, it would be expected that only 20% are members). I find that the traditional limit of $P_{max} = 50\%$ actually results in membership fractions of >85%.

It should also be stressed that the unequal distribution of the number of stars in each P_{max} bin results in vastly different errors between the intermediate bins versus the first and last ones (corresponding to the <10% and >90%, respectively; also seen in Table 2.4). This observation continues across all three dwarf galaxy groupings. It is first obvious that most stars in the field are not members of dwarfs, and so the lowest bin therefore contains a large number of stars (thereby resulting in small errors). Secondly, most spectroscopic member stars are correctly flagged in the algorithm as members with high P_{max} (such that the purity fraction is 0.97 for $P_{max} > 0.9$). For comparison, the raw number of RV stars whose probabilities are intermediate (i.e., $0.1 \leq P_{max} < 0.9$) is ∼620 stars, while the first and last bins contain ∼3360 and ∼6670, respectively. Given the corresponding purity fractions in the first and last bins (0.09 and 0.97, respectively), I conclude that the algorithm appropriately identifies the majority of MW and dwarf member stars in a given field, with very little contamination at high P_{max}.

2.5 Discussion

In this section, I conduct a detailed review of each dwarf for which an outer profile has been detected in this work. For each dwarf, I searched the literature for three main findings: (1) what is the most distant stellar member observed to date, and how far does each work trace each system; (2) do any previous works observe a break or transition in the stellar density profile, and if so, how do their results directly compare; and (3) what evidence (if any) is there in the literature to argue for/against

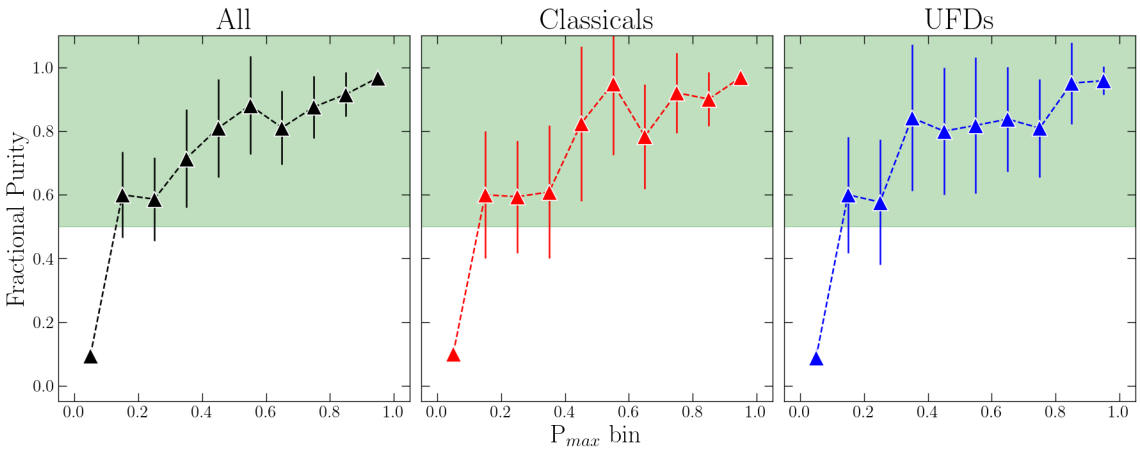

Figure 2.9: The fractional purity curves provided by the radial velocities of stars observed each dwarf, compiled together for both of the 2-component runs. These curves have been compiled for (a) all dwarfs, (b) classicals only, and (c) ultra-faints only. Green shading highlights the fractional purity regimes where statistically, at least 1 in 2 stars is correctly identified as a member (>50% fractional purity).

the dwarf's disruption via tidal influence imparted by the MW?

Throughout this discussion, I note whether previous works find evidence for a bump or break in the stellar density profiles of these nine systems, and compare their findings to the estimated transition boundaries from Table 2.3. For easy comparison, Figure 2.10 shows the surface number density profiles (constructed by taking candidate members stars whose $P_{max} \geq 10\%$) of these dwarfs. To highlight the benefit of the 2-component model and the detectability of radially distant stars, an exponential function is included in each panel (red) for reference.

Additionally, I report the number of "outskirt" candidate members; these are defined as stars whose radial distances place them farther than the transition boundary in Table 2.3, and are brighter than *Gaia* $G \leq 19.5$ mag. The spread of members radially and in magnitude are shown in Figure 2.11, where each point is colour-coded by P_{max}. For each dwarf, the transition boundaries (r_{trans}) in each panel are highlighted as arrows to show the approximate "outskirt" region.

The following section contains common themes and questions for each dwarf. Complementing figures for this section are Figure 2.7, Figure 2.10, and Figure 2.11.

2.5.1 Boötes 1

Boo1 is one of the most luminous ($M_V \approx -6.3$ mag; $L_V \approx 2.9 \times 10^4$ $L_\odot$; Muñoz et al. 2018) and relatively nearby (66 kpc; Dall'Ora et al. 2006) UFDs. With a physical half-light radius of ∼200 pc (10′, or 0.17°; Longeard et al. 2022), it is comparable in r_h to other MW classical systems. Boo1 has been the subject of many recent studies, resulting in a significant number of spectroscopic members (>70 stars; see compilation in Waller et al. 2023). While its size and chemical trends [α/Fe]-plane suggest it is a more massive UFD, Frebel et al. (2016) determined Boo1's abundances of neutron-capture elements are much lower than observed in MW halo stars − a trait unique to UFDs (Frebel & Norris 2015).

Of these spectroscopic data in the literature, the most distant, confirmed members of Boo1 have been traced out to ∼$4r_h$ (Longeard et al. 2022; Waller et al. 2023). Filion & Wyse (2021) also obtained photometric candidate members by probing the nearby blue horizontal branch (BHB) population, and found these BHBs occupy an extended outer envelope of the dwarf. For comparison, I detect 61 stars on the HB, and find the spatial distribution of these stars largely resembles that of Boo1 as presented in Filion & Wyse (2021) (see their Figure 6). The farthest BHB in their study was located at

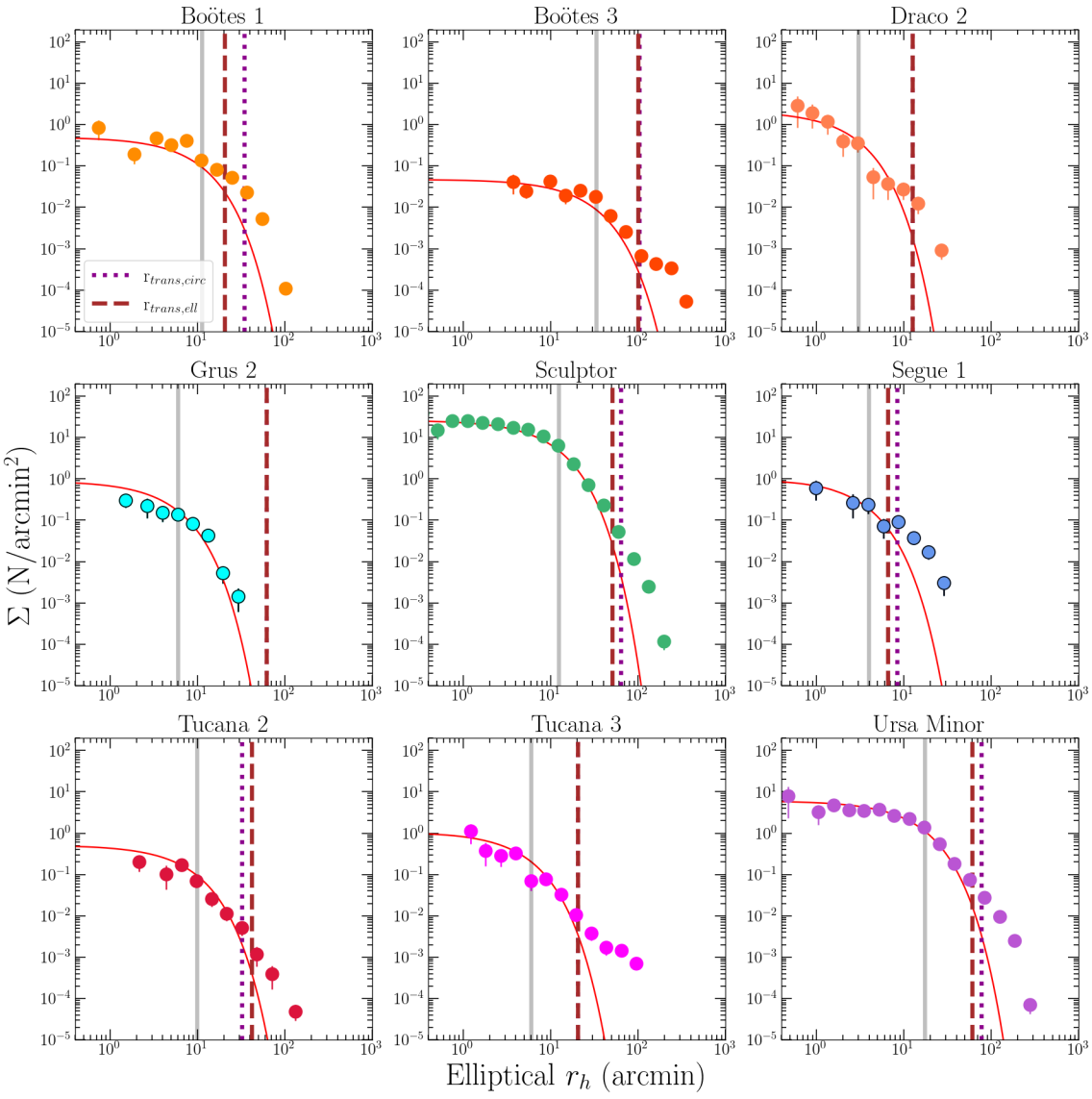

Figure 2.10: Stellar density profiles for all dwarfs with identified outer profiles. Each plot is made with stars whose $P_{max} \geq 10\%$. Vertical lines represent important radii: grey is each dwarf's half-light radius, and magenta dotted and brown dashed represent the transition radii ($r_{trans,circ}$ and $r_{trans,ell}$, respectively). For comparison, the 1-component exponential function for each dwarf is plotted in red to highlight the excess of stellar members detected in the 2-component model.

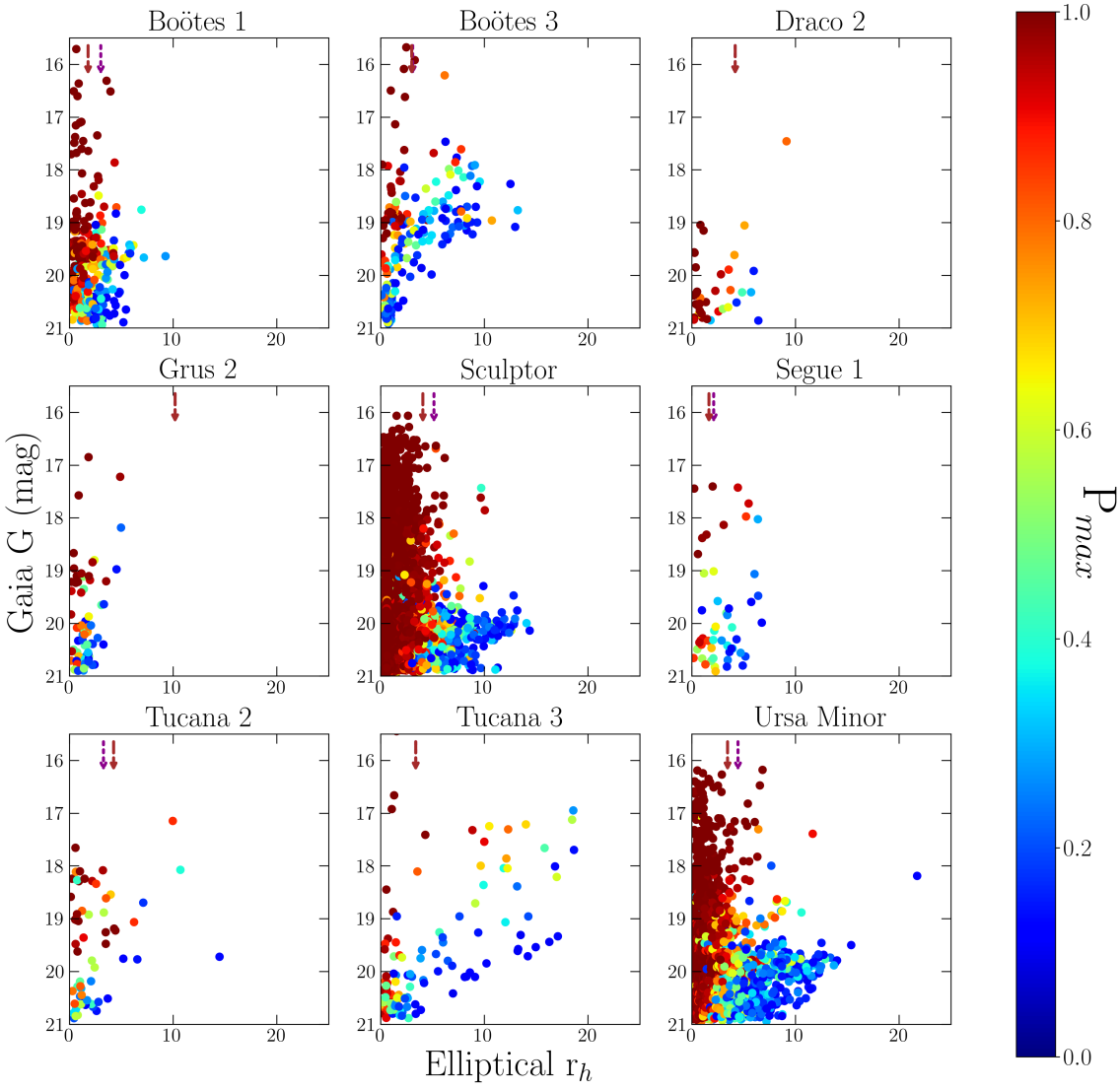

Figure 2.11: Magnitude versus distance for dwarf member stars with $P_{max} > 10\%$. Arrows in each panel represent r_{trans} to highlight the outskirts, and are colour-coded the same as Figure 2.7.

a radial distance of $\sim 10 r_h$, though this star does not have consistent proper motions to the dwarf and does not appear as a member according to this current work. It is confirmed that all 29 spectroscopic members from Longeard et al. (2022) are correctly identified as members in the algorithm, and with high probabilities of membership ($P_{max} > 50\%$). For comparison to previous works, the most distant member identified via the algorithm is located at an elliptical radius of $\sim 9 r_h$ from the centre of Boo1, and does show consistent PMs to other spectroscopically confirmed members of Longeard et al. (2022).

As reported in Table 2.3, there are two possible solutions for the transition boundary in the elliptical ($r_{trans,ell}$) and circular ($r_{trans,circ}$) 2-component models. These values correspond to $r_{trans,ell} = 0.34°$ ($\sim 1.8 r_h$) and $r_{trans,circ} = 0.57°$ ($\sim 3 r_h$), respectively. Multiple works have previously reported transitions in Boo1's stellar components. Koposov et al. (2011) probed stars in the inner half-light radius and detected two separate kinematically "hot" and "cold" samples. The authors suggest the nature of these two samples are clearly segregated by different velocity dispersions and metallicities in each population. In a more extended spectroscopic study, Longeard et al. (2022) claim there is evidence of a break in the velocity dispersion and metallicity profiles. This break is located at $\sim 2 r_h$, which corresponds to our solution for $r_{trans,ell}$. As evidenced by the stellar density plot in Figure 2.10, Boo1's stellar density profile breaks from the exponential at approximately this same position.

The tidal influence of Boo1 has been suspected in multiple previous works, such as Roderick et al. (2016) who observed a distinct overdensity near Boo1's estimated tidal radius (reported as 0.54° and approximated via a King density profile). Note that this particular report also coincides with the solution for $r_{trans,circ}$. However, recent works in Battaglia et al. (2022) and Pace et al. (2022) have concluded that the orbit of Boo1 has as pericentre of $\sim$35 kpc, and N-body simulations from Read et al. (2006) have found that tidal shocking and stripping may be negligible for systems whose pericentres are >35 kpc. It is therefore questionable if tides are afflicting the morphology of Boo1.

At present, no work has confirmed if Boo1 is actively disrupting. Considering that (1) the spectroscopic data in Longeard et al. (2022) shows a moderate velocity gradient, (2) studies argue for a relatively small pericentre, and (3) the dwarf's elongation aligns with the direction of orbit (Pace et al. 2022), a natural conclusion is that tides could have affected the distribution of the outermost stars in Boo1.

However, there is some evidence favouring the alternative model (an extended

stellar halo induced by a merger), or even a combination of the two scenarios. Firstly, Longeard et al. (2022) report a metallicity gradient for Boo1, which has only ever been observed in one other UFD (Tucana 2, see below). Pace et al. (2022) also argue that MW dwarfs with appreciably low central densities within the half-light radius, compared to the average density of the MW at the dwarf's pericentre, can be used as a proxy to identify likely disrupting dwarfs. The authors report that Boo1's density ratio is larger than that of known disrupting systems (Ant2, Boo3, Tuc3, and Sagittarius), placing it more in accordance with other typical MW satellites. And finally, abundances from Waller et al. (2023) showed that the outer stars (selected via the algorithm and shown to have consistent RVs to Boo1) have the same chemical properties as inner ones. This result may indicate that stars from the inner regions of Boo1 have been stripped to the outskirts, but additionally it cannot rule out a scenario where these stars were contributed from a chemically similar dwarf.

It is unclear at present if the outskirt members of Boo1 are due to the effect of tides, accreted members, or both. To conclude that Boo1's halo is more consistent with one scenario over the other would require ruling out the possibility of an extended halo from a contributing accretion, via evidence of a separate lower mass galaxy (e.g. a lower [α/Fe] knee). Therefore, more spectroscopic observations with detailed abundances will be necessary to conclude the dynamics in this intriguing UFD. For future campaigns of outer profile stars, I identify 34 outskirt candidates whose magnitudes are $G \leq 19.5$ mag and radial distance is greater than r_{trans}. Only nine of these stars have reported RVs in the literature.

2.5.2 Boötes 3

Boo3 was first identified in SDSS by Grillmair (2009); yet since its discovery, it has remained relatively unstudied. Compared to other UFDs, it is very typical in absolute magnitude ($M_V \approx -5.75$ mag; Correnti et al. 2009) and luminosity ($L_V \approx 1.74 \times 10^4$ $L_\odot$). However, it is a particularly diffuse and large ($r_h = 33.03' = 0.56°$; Moskowitz & Walker 2020) system. At a distance of ∼46 kpc (Carlin & Sand 2018), its physical half-light radius (∼450 pc) is relatively extensive for a UFD. Boo3's faint luminosity and diffuse nature in part explains the lack of substantial literature on this dwarf.

Since its discovery, Boo3 has been argued to be the progenitor (or at a minimum, associated with) the Styx stellar stream (Grillmair 2009; Carlin et al. 2009; Carlin &

Sand 2018). A number of results support this conclusion: firstly, Styx overlaps with Boo3 in the matched filter map of Grillmair (2009) at a distance corresponding to ∼45 kpc (i.e., the same distance of Boo3; Grillmair 2009). And secondly, Boo3 appears misshapen, double-lobed, and very diffuse (Grillmair 2009). These morphological characteristics suggest that the system is not in dynamic equilibrium and is being actively disrupted.

Currently, there are no publications that report any positions or kinematics of resolved stars in Styx. Only the distance to the stream and its length on the sky have been estimated, while orbit properties of Boo3 have been established and used for comparison to the stream's path. Grillmair (2009) first attempted to constrain the orbit of Styx (via an orbit-fitting method applied to the on-sky path), and was able to give first estimates for the PMs of Styx stars at the position of Boo3. This requires the assumption of either prograde or retrograde motion for the stream, but recent proper motion estimates of Boo3 in Pace et al. (2022) and Battaglia et al. (2022) would be consistent with Styx if the stream is in a retrograde orbit, providing further evidence that Boo3 may be the progenitor of Styx.

The updated orbit of Boo3 provided by Pace et al. (2022) and Battaglia et al. (2022) also strongly supports a disrupted dwarf. Both studies find Boo3's orbit to be highly eccentric ($\epsilon \approx 0.85$ and 0.95, respectively) and to have a small pericentre distance ($7 - 9$ kpc). It is important to note that only two MW dwarfs are known to have pericentric orbits of <10 kpc. Aside from Boo3, Tuc3's pericentre is also extremely close to Galactic centre, and is the only UFD known to be tidally disrupting (Li et al. 2018b). Boo3 allegedly recently passed pericentre (∼140 Myrs ago; Carlin & Sand 2018) and, according to Pace et al. 2022, does have a relatively low density ratio (on the order of Sagittarius and Tuc3), which they argue is in favour of a tidal disruption scenario.

At such a moderate distance, it is surprising that no resolved Styx members have yet been identified and kinematically associated to Boo3, though the evidence appears to favour that Boo3 is likely a disrupting dwarf. The most distant spectroscopic member of Boo3 to date is located at $2.56r_h$ (Carlin et al. 2009; Carlin & Sand 2018), which falls within the estimated transition boundaries of $r_{trans,ell} = 3.02r_h$ and $r_{trans,circ} = 3.11r_h$. All spectroscopic members reported in Carlin & Sand (2018) are successfully identified via the algorithm, save for 2 stars whose updated proper motions in *Gaia* eDR3 suggest they are not consistent with membership to Boo3. Though the globular clusters M3 and NGC 5466 (and its stream; see Jensen et al.

2021) are close to Boo3 in projection, there is no evidence of contamination from these systems as their proper motions and CMDs are unequivocally distinct from Boo3 stars.

At present, the outskirts of Boo3 remain largely unexplored. In this work, I report 65 candidate stars (with no known spectroscopic follow-up) whose distances are greater than r_{trans} and have magnitudes $\leq$19.5 mag.

2.5.3 Draco 2

Dra2 is a very small and nearby collection of stars whose estimated distance and brightness is $\sim$21 kpc and $L_V \approx 180$ $L_\odot$ ($M_V \approx -0.8$ mag; Longeard et al. 2018) respectively. With a half-light radius of a mere 3′ (0.05°, or $\sim$20 pc) and a sufficiently low (marginally resolved) velocity dispersion ($\lesssim$6 km s^{-1} at the 95% confidence interval), it has been a subject of controversy as to whether it is a true, dynamically cold UFD, or alternatively, a star cluster.

Though Dra2 is very nearby, spectroscopic follow-up of this intriguing system has been fairly limited due to a lack of bright ($g < 19$ mag) stars. First discovered in the Pan-STARRS 1 (PS1) 3π survey (Chambers et al. 2016) by Laevens et al. (2015), only two works have published further results on the system. Martin et al. (2016a) and Longeard et al. (2018) obtained a total of 14 spectroscopic members reported for Dra2. Of these stars bright enough to be included in *Gaia* eDR3, the algorithm successfully identifies all 12 spectroscopic members.

The true nature of Dra2 is still largely speculated. Longeard et al. (2018) suggest that Dra2 seemingly conforms with other UFD trends in its absolute magnitude, metallicity, and larger size than most globular clusters, but ultimately it lies on the boundary between either object. Given the small number statistics, Longeard et al. (2018) are unable to deduce a metallicity dispersion for Dra2 which would yield further evidence towards a dwarf scenario. In addition, the marginally resolved velocity dispersion is very cold for a UFD, but is still comparable to other known dwarf systems like Boo1 (2.4 km s^{-1}; Koposov et al. 2011) and Seg1 (3.7 km s^{-1}; Simon et al. 2011).

If Dra2 is indeed a cluster, the approximate Jacobi tidal radius is only 10 pc (according to Longeard et al. 2018 and assuming the mass is solely stellar), suggesting that the stars I find at many half-light radii would be members that have migrated to significant distances as a result of tides. However, as shown in Figure 2.7, the sample

of outer members from the algorithm are largely perpendicular to Dra2's elongation (also perpendicular to the direction of Dra2's orbit). This particular situation is contrary to the expected distribution of tidal tails, and therefore not likely to be initiated from a tidal stream.

However, multiple studies argue that Dra2 could be in the midst of tidal disruption. Namely, Pace et al. (2022) and Longeard et al. (2018) conclude that it is currently at pericentre (∼21 kpc), or close enough to experience tidal disturbance from the MW. Without a resolved velocity dispersion, Pace et al. (2022) note that the central density ratio argument (as suggested for Boo1) cannot be utilized for Dra2. However, they note that if the velocity dispersion is sufficiently low (∼1 km s^{-1}), Dra2's morphology is likely caused by tidal disruption.

Currently, the most distant spectroscopic member of Dra2 is located at $2.6r_h$ (∼8′; Longeard et al. 2018). In the work presented here, I identify members up to $9.15r_h$ and, contrary to past works, I identify an additional, bright (G-band = 17.5 mag) RGB star at this large elliptical distance. This particular star was not identified in the 1-component runs, suggesting that the spatial likelihood without the free parameters of an outer profile was too restrictive to obtain a complete sample. Follow-up of this individual star may lead to a better understanding of Dra2, as it is located perpendicular to the system's orbit (as in the stellar features of Tuc2, see below). Further, if this most distant star is bound to the system, it could be argued that Dra2 (under the assumption of a dwarf galaxy nature) could have a sizable DM halo.

Regardless, Dra2 lacks a substantial sample of bright enough RGBs for spectroscopic follow-up (save the one most radially distant example), as many would-be targets in the outskirts lie at G-band > 19 mag. In this work, I only find 4 stars brighter than $G \leq 19.5$ mag, and only 2 of these are beyond the estimated $r_{trans} = 0.21°$ ($4.2r_h$, or 80 pc).

2.5.4 Grus 2

Gru2 was first discovered in the Dark Energy Survey (DES; Drlica-Wagner et al. 2015). It is a moderately distant system (∼55 kpc; Martínez-Vázquez et al. 2019), whose luminosity is consistent to other UFDs ($L_V \approx 3150$ $L_\odot$). Though a resolved velocity dispersion has not yet been determined for this system, it is classified as a dwarf galaxy, mainly based on its absolute magnitude ($M_V \approx -3.9$ mag), metallicity ([Fe/H] = −2.51; Simon et al. 2020) and relatively large physical size ($r_h = 5.9′ =$

0.1°, or ∼95 pc).

Gru2 is located behind a more metal-rich and diffuse substructure, known as the Orphan/Chenab (OC) stream (Grillmair & Dionatos 2006; Belokurov et al. 2007b; Shipp et al. 2018). Koposov et al. (2019) first reported on these incident structures, finding the proper motions were similar (particularly at stream longitude position of Gru2, or $\phi_1 = 66.1°$) and suggested that these structures may be linked. However, there is strong evidence to suggest that Gru2 is not the stream's progenitor, as it differs in heliocentric distances by ∼10 kpc (Martínez-Vázquez et al. 2019) and it's heliocentric RV is offset by ∼90 km s^{-1} (and Gru2's Galactocentric RV $v_{GSR,Gru2} \approx -131$ km s^{-1}, while $v_{GSR,OC} \approx -200$ km s^{-1}; Erkal et al. 2019; Koposov et al. 2019).

As shown in Figure 2.7, the OC stream clearly overlaps Gru2 (grey highlight), but additionally the calculated transition boundary reaches the stream's centre. Given that the algorithm's method relies on proper motions, but not parallaxes/distances or RVs, it is very likely that the OC stream affects our determination of an outer profile for Gru2. It can also be noted that Gru2 is the only dwarf with no stars beyond our calculated r_{trans}.

Though Gru2's outer profile detection may be compromised by an unrelated structure in the field, the algorithm appears to identify only member stars out to $5r_h$ (all of which are also members in the 1-component model). In comparison, previous work in Simon et al. (2020) estimated a tidal radius for Gru2 to be roughly 300 pc, or $\sim 3r_h$. According to the central density to MW pericentre density ratio calculated in Pace et al. (2022), Gru2 is potentially tidally disrupting. The spectroscopic members traced in Simon et al. 2020 extend out to $2r_h$, and so it is possible that some radially distant stars are evidence of this disruption. However, given the OC stream's width and overlap with these stars, it is certainly possible that the outer stars identified here are indeed members of the OC stream and not Gru2.

In dynamical models constructed in Koposov et al. (2023), the authors claim that, while Gru2 itself is not the progenitor of the OC stream, its orbit coincides with recent interactions with the OC progenitor. These close passages suggest that Gru2 may have been accreted with the OC progenitor, which is more similar in mass to a classical dwarf system. Determining the influence of tides on Grus2 is complicated by the interplay with not only the OC stream, but additionally the LMC. Orbit projections in Battaglia et al. (2022) suggest that, while Gru2 was not accreted with the LMC, it has been interacting/potentially captured by the Magellanic group within the past 200 Myrs. This is further corroborated by results in Santos-Santos et al. (2021)

who reported that Gru2 is a potential associate of the LMC. Given the relatively close pericentres ($24 - 31$ kpc) determined by Pace et al. (2022) and Battaglia et al. (2022) and the dwarf's low central density, tides may have been important in shaping this system. Suffice to say, the complicated interplay of Gru2, the LMC, and the OC stream make for intriguing future work.

2.5.5 Sculptor

Of the many MW satellites, Scl was the first dwarf spheroidal (dSph) discovered (Shapley 1938), thereby earning its title as a classical dwarf. It is the fourth brightest dSph at $M_V \approx -10.82$ mag ($L_V \approx 1.8 \times 10^6$ L$_\odot$; Muñoz et al. 2018), preceded only by Fornax, Leo1, and Sagittarius. It is a typical-sized system with a physical half-light radius of $\sim$310 pc ($r_h = 12.33' = 0.21°$) and a large velocity dispersion ($\sigma_{RV} \sim 9.2$ km s^{-1}; Walker et al. 2009a) indicative of the presence of dark matter.

Given the brightness and angular size of this system, Scl's resolved stellar populations have long been studied, yielding a wealth of information and detail into this particular system. Multiple studies have explored the chemo-dynamics of Scl and concur that it consists largely of old (>10 Gyrs) metal-poor ([Fe/H] $= -1.8$ dex; Tolstoy et al. 2023) stars with well-mixed enrichment (e.g., Hill et al. 2019). Star formation in Scl is proposed to have had one epoch which ceased $8 - 10$ Gyrs ago and lasted $\lesssim$1.4 Gyrs (Bettinelli et al. 2019); de los Reyes et al. 2022). Much like Boo1 and UMi (see below), Scl's innermost regions ($<2r_h$) are composed of a metal-rich and kinematically cold population that transitions to a metal-poor, kinematically hot population (e.g., Tolstoy et al. 2004; Battaglia et al. 2008). The transition from the inner to the outer population occurs at $\sim$0.2° ($\sim 0.95 r_h$), and is potentially a result of outside-in star formation.

Regarding kinematic details, little evidence has been found to suggest that Scl is in the process of losing stellar mass via tides. For example, both Pace et al. (2022) and Battaglia et al. (2022) find large pericentric distances for Scl, in the range of $45 - 65$ kpc, depending largely on the assumed MW mass. Additionally, Tolstoy et al. (2023) recently consolidated archive spectra for Scl RGBs out to the nominal tidal radius ($\sim 6.2 r_h$ via a King density profile; Irwin & Hatzidimitriou 1995) and did not resolve an RV gradient (see also Martínez-García et al. 2023). At a heliocentric distance of 86 kpc (Muñoz et al. 2018), MW tidal influence is not purportedly large enough to strongly distort Scl's morphology. Recent simulations from Iorio et al. (2019) show

that the stellar component of Scl is not obviously affected by tides, but up to 60% of the DM halo may have been stripped by present-day.

In comparison, recent work by Sestito et al. (2023a) utilized my Scl candidate members and obtained spectroscopic follow-up for the 2 most radially distant (out to $10r_h$) and relatively bright stars in the sample. The authors confirm that these distant stars are *bona fide* members of Scl based on their metallicities and RVs. As this finding expands the radial stellar distribution of Scl out to ∼3 kpc, the authors also explored the stellar density profile and its derivative – $\Gamma(r_{ell})$ – using the full sample of candidates that I provided and compared them to a tidal disruption simulation from Peñarrubia et al. (2008). With my candidate members, Sestito et al. (2023a) report a sharp deviation from an exponential profile in the stellar density in Scl (also shown in this work in Figure 2.10), located at about 25′. According to the tidal model of Peñarrubia et al. (2008), tides can be responsible for an outer excess over the initial exponential profile, also called at a "kink" radius. This is followed by a region where $\Gamma(r_{ell})$ approaches a power-law with a slope of -4, before flattening back to ∼0. The second change in $\Gamma(r_{ell})$ occurs where the local crossing time of stars in the dwarf exceeds the time since the last pericentric passage, and is referred to as a "break". Remarkably, the Peñarrubia et al. (2008) tidal model matches well with the observed Scl data. The conclusion of work done in Sestito et al. (2023a) is that the extended profile in Scl is indeed indicative of tidal disturbance.

The "kink" in $\Gamma(r_{ell})$ is located at ∼25′ (∼$2r_h$), corresponding with a profile excess also seen in the density profiles of Irwin & Hatzidimitriou (1995) and Figure 2.10. In this present work, the transition boundary solutions are $r_{trans,ell} = 0.84°$ (∼$4r_h$) and $r_{trans,circ} = 1.06°$ (∼$5.1r_h$). These are much larger than the "kink" radius from Sestito et al. (2023a), yet are less than the nominal tidal radius from Irwin & Hatzidimitriou (1995) and less than the "break" radius from Sestito et al. 2023a (which was found to be ∼80′ = $6.5r_h$). Seemingly, the proposed values of r_{trans} do not correspond to these other estimates.

Prior to Sestito et al. (2023a), the most distant spectroscopic member was $6r_h$, which now expanded out to $10.1r_h$. Not including those already observed by Sestito et al. (2023a), I find 48 outskirt ($> r_{trans}$) candidates for spectroscopic follow-up (G ≤ 19.5 mag).

2.5.6 Segue 1

At a heliocentric distance of 23 kpc (Belokurov et al. 2007a), Seg1 is one of the nearest dwarf galaxies. Its size is relatively compact ($r_h = 3.95' = 0.07°$, or ∼30 pc; Muñoz et al. 2018) and similar in luminosity to other MW UFDs ($M_V \approx -1.5$ mag; $L_V \approx 340$ $L_\odot$; Martin et al. 2008). In the discovery paper of Belokurov et al. (2007a), this system was proposed as a globular cluster containing very few stars. However, spectroscopic follow-up conducted by Geha et al. (2009) and Martinez et al. (2011) suggested that Seg1's internal kinematics are consistent with a dwarf galaxy. The former determined that Seg1 has an exceptionally large dark matter content ($M/L \approx 1340 - 2440$ $M_\odot/L_\odot$) while the latter claimed this system may be one of the highest DM density systems in the Local Group.

As the focus of many individual spectroscopic studies, Seg1 has consistently proven to be a particularly unique system. In addition to its high M/L ratio, Seg1 is one of the most metal-poor dwarfs in the MW ([Fe/H] = −2.7; Frebel et al. 2014; Norris et al. 2010), comparable to other UFDs like Tuc2, Hor1, and Boo2 (Simon 2019). Intriguingly, Frebel et al. (2014) observed a large metallicity dispersion in this system ($\sigma_{[Fe/H]} = 0.95$), yet all stars were found to have high α-enhancement regardless of metallicity (see also Vargas et al. 2013). Given the high [α/Fe] ratios across all measured stars in this study, the authors deduced that Seg1 lacks enrichment from Type Ia supernovae (SNe) which pollute the dwarf's ISM with iron over time, and that its star formation must have only lasted for a few hundred Myrs. Enriched only by the core-collapse of massive stars, Seg1's exceptionally distinctive chemical trends suggest it is a candidate "first galaxy" (Webster et al. 2016), or one that experienced a short burst of star formation, and has remained since unchanged.

Seg1 is located in a particularly advantageous position for spectroscopic study. Its close proximity, in addition to its high Galactic latitude (+50°) means that a) stars down to ∼1 mag below the main sequence turn-off are accessible for spectroscopic follow-up (Frebel et al. 2014), and b) contaminating MW foreground stars can be effectively removed. As such, previous work by Simon et al. (2011) obtained a fairly complete sample of radial velocity measurements for 98.2% of candidate member stars within 10′ (or $\sim 2.5 r_h$) of Seg1. In an independent study, Norris et al. (2010) targeted stars out to $\sim 9 r_h$ in the g-band range of [17, 21.4] mag. Additionally, Seg1's field was partially covered by APOGEE DR17. The relatively large number of stars with radial velocities in and around the dwarf (348 stars in total; see Table 2.1) alongside the

high completeness achieved in previous studies for the inner regions of Seg1 provides us with a more complete dataset to test the robustness of our algorithm detection.

To examine the consistency of the algorithm with previous works, I compared the probabilities of stars in my sample to the spectroscopically-confirmed members identified in Norris et al. (2010) and Simon et al. (2011). For the Simon et al. (2011) sample, of which 30 stars are bright enough to be in *Gaia* eDR3 and the most distant member is located at $2.9r_h$, all stars have consistent membership probabilities. The Norris et al. (2010) sample shows similar consistency in membership, such that all but two of their stars are indeed members according to the algorithm. These two remaining cases were found in this work to have inconsistent PMs to the rest of Seg1, and thus have been flagged as non-members.

Thus far, the most radially distant spectroscopic member of this system is $5.25r_h$. For comparison, the most distant member (with no present spectroscopic follow-up) is located at $6.8r_h$. The radius of the transition boundary for Seg1 is $r_{trans,ell} = 0.11°$ ($\sim 1.57r_h$) and $r_{trans,circ} = 0.14°$ ($\sim 2r_h$) in the elliptical and circular cases, respectively. For this well-studied system, I only identify 2 candidates beyond r_{trans} with $G \leq 19.5$. These are located at $r_{ell} = 5.5$ and $6.3r_h$, and $G = 17.7$ and 18.0 mag respectively.

Though Seg1 has been extensively studied, it is at present unclear if it is currently undergoing tidal disruption. A photometric study conducted by Niederste-Ostholt et al. (2009) claimed to have found a 1° extension of stars they deemed "tidal debris". However, a more detailed analysis in Geha et al. (2009) reports no kinematic tracers nor any other clear evidence of tidal disruption from their sample. Geha et al. (2009) also determine a Jacobi radii of 220 pc (or 7.4_h) where stars in Seg1 are likely to be unbound. Here, I confirm that no member stars (in *Gaia* eDR3) are located beyond this radius.

Searching for tidal signatures in Seg1 is further complicated by the multitude of stellar streams intersecting in the field of the dwarf. These are: Slidr, Sagittarius, Gaia-10, Orphan/Chenab, and the 300 km s^{-1} stream (Mateu 2023; see Figure 2.7). In this less than fortunate circumstance, there are potential sources of contamination from these substructures. Six stars with measured RVs are flagged as Seg1 members, but their origin is clearly the 300 km s^{-1} stream (at 18 kpc in heliocentric distances, and approximately the same proper motions; Frebel et al. 2013; Fu et al. 2018) while eight more originate from a lower RV structure (likely Sagittarius, see Geha et al. 2009). However, I find that the algorithm performs well at minimizing the number of false negatives, though there is contamination of false positives from other

substructures (especially when they have similar proper motions to the dwarf) than would be ideal. Given the detailed spectroscopic follow-up thus far of the system, it is indeed impressive that only a few interlopers from these stellar streams managed to contaminate the sample.

2.5.7 Tucana 2

Upon first glance, Tuc2's characteristics are fairly typical compared to other UFDs. Its intrinsic brightness ($M_V \approx -3.9$ mag; $L_V \approx 3150$ $L_\odot$) and physical size ($r_h = 9.83' = 0.16°$, or ∼160 pc; Bechtol et al. 2015) places it squarely in the locus of other MW satellites in the size-luminosity relation (see Figure 2 of Simon 2019 and Figure 3 of Bechtol et al. 2015). Velocity dispersion measurements also support Tuc2's classification as a dwarf galaxy ($\sigma \sim 3.8$ km s^{-1}; Chiti et al. 2023), and its mean metallicity falls well below the proposed "metallicity floor" for most MW globular clusters (Harris 1996, 2010 version; Wan et al. 2020 and references therein). A somewhat unique characteristic is its low metallicity, suggesting Tuc2 is one of the most metal-poor systems in the MW ([Fe/H] = −2.71 dex; Ji et al. 2016c; Chiti et al. 2018), on average.

Despite these parallels to other UFDs, Tuc2 has been shown to be a particularly interesting dwarf. In 2021, Chiti et al. searched the outskirts of Tuc2 for spectroscopic members and reported two compelling results. Firstly, they detected the most radially distant Tuc2 member, located at 1.1 kpc ($10.71r_h$ in elliptical radii). This observation was (at the time) the most distant star in a UFD, preceded only by spectroscopic members of other dwarfs up to $4r_h$ (Frebel et al. 2016; Norris et al. 2010). Secondly, the authors identified 7 RGBs in Tuc2's outskirts, located at distances $>2r_h$. The authors suggested these stars were members of an extended stellar component which originated from the dwarf. As to the physical motivation for these stars to be displaced to such large radii, Chiti et al. (2021, 2023) argue that their location conflicts with tidal stripping. Instead, Chiti et al. (2021, 2023) suggest that this structure is a result of an early galactic merger, whose remnant accreted stars remain in the outskirts of Tuc2 (corroborated by the outside-in formation scenario in dwarf-dwarf mergers; Benítez-Llambay et al. 2016). This initial discovery is significant to our understanding of dynamics of stars in low-mass systems, particularly as we do not yet have a census of dwarfs whose outskirts show evidence for this type of scenario.

Chiti et al. (2021, 2023) propose three main possibilities for the extended sub-

structure in Tuc2. One hypothesis is that Tuc2's structure could be the result of bursty feedback or energetic SNe. By comparing the innermost stellar chemistries to outskirt members, Chiti et al. (2023) found that the metallicities and chemical abundances are similar to other UFDs. While UFDs in their formation may have experienced early bursty feedback (e.g., Wheeler et al. 2019), the conclusion that Tuc2 seems to have had similar enrichment compared to other UFD systems suggests that the energies of past SNe would make the extension in Tuc2 a much more common feature than currently observed. In agreement with this conclusion, the authors find that the chemical abundance trends favor a low mass progenitor, and therefore does not suggest particularly energetic SNe that could act to displace these stars.

The second (and most common conclusion) is a tidal scenario. However, the authors' observations find no conclusive evidence for tides. When modelling its tidal disruption, Chiti et al. (2021) determined that Tuc2's tidal debris would be observed following the direction of orbit, as is typical for many other dwarf and globular cluster streams. Even when including the time-varying potential of the LMC in their orbits, they find that Tuc2's observed stellar extension is indeed located perpendicular to the proposed direction of tidal debris. The authors further confirmed in later high-resolution spectroscopic studies that there is no clear RV gradient in Tuc2 that would be indicative of disruption (Chiti et al. 2023).

Also contrary to tides is Tuc2's current distance (58 kpc; Bechtol et al. 2015), but most importantly, its orbit places its pericentre between ∼35 kpc (Battaglia et al. 2022) and ∼45 kpc (Pace et al. 2022), depending on the model for MW mass (both including the LMC). In either case, this pericentre is not particularly small, and indeed Pace et al. (2022) do not find a particularly large density ratio for this system that would suggest it is actively tidally disrupting.

The lack of evidence for both the previous scenarios (i.e., tidal origins or expulsion due to energetic SNe) led Chiti et al. (2021, 2023) to this final hypothesis: that Tuc2's morphology and steep metallicity gradient could be the remnants of an ancient merger. Simulations of a UFD (similar to Tuc2) in Tarumi et al. (2021) showed that the early (first ∼100s Myrs) merging of two galaxies can produce extended features in the direction of the merger, which could explain the perpendicular stellar extension in Tuc2. These simulations also showed that accreted stars from the merger can be deposited in the outskirts of the central dwarf, as the central dwarf is dynamically heated which forms an extended stellar distribution. Similarly, simulations by Benítez-Llambay et al. (2016) find that mergers in dwarfs can induce metallicity (and

age) gradients in the surviving dwarf galaxy. Arguably, this could be why Chiti et al. (2023) observed a metal-poor inner component ([Fe/H] = −2.71 dex) yet an even lower metallicity outer component (>$2r_h$, [Fe/H] = −3.02 dex) in Tuc2.

The nullification of the previous two hypotheses presents a strong case for the dwarf-dwarf merger remnant scenario, though direct observational evidence is clearly difficult to ascertain. Nonetheless, in the methods presented here, all literature spectroscopic members are successfully identified as members of Tuc2. I find only one velocity-confirmed member star with a particularly low probability (7%); however, this star is evidently an AGB, and considering that the AGB is not explicitly included in the CMD likelihood, $\mathcal{L}_{CMD}$ is particularly low for this individual star.

Given the expansive work conducted by previous studies, very few Tuc2 stars are candidates for follow-up. The most radially distant star identified is the same as Chiti et al. (2021), located at a distance of $r_{ell} = 10.71r_h$. Considering that the transition boundaries are $r_{trans,ell} = 0.70°$ (∼$4.38r_h$) and $r_{trans,circ} = 0.54°$ (∼$3.38r_h$), there are only four candidates in the outer profile regime which have not yet been observed. Note that three of these stars are HBs.

2.5.8 Tucana 3

Tuc3 is a fairly small ($r_h = 6' = 0.1°$, or ∼45 pc) and faint ($L_V \approx 800$ $L_\odot$; $M_V \approx -2.4$ mag; Drlica-Wagner et al. 2015) collection of stars located near the LMC. Discovered in DES alongside Gru2, the first observation of the dwarf was reported simultaneous to the ∼4°-long tidal tails emanating from the dwarf's centre. Besides the aforementioned Dra2 and Seg1 dwarf galaxies, Tuc3 is also one of the closest dwarfs (∼25 kpc). Its proximity has enabled multiple high-resolution spectroscopic studies such that its stellar stream and chemical trends have been studied in detail (e.g., Simon et al. 2017; Hansen et al. 2017; Li et al. 2018b; Marshall et al. 2019).

Though the presence of tidal tails is a strong indication of tidal disruption, the velocity dispersion of Tuc3 is smaller than typically associated with dwarf galaxies (an upper limit reported as $\sigma_{RV} \sim 0.1$ km s^{-1} in Simon et al. 2017). However, Simon et al. (2017) argued that the low velocity dispersion could have resulted from the removal of stars which then acts to decrease the velocity dispersion in the system. Indeed, Marshall et al. (2019) observed a metallicity dispersion in Tuc3 − a result in favour of a dwarf galaxy origin since the potential wells in globular clusters are not typically large enough to retain the gas ejected from SNe. At present, its dwarf

nature is not ultimately confirmed but certainly likely.

From these spectroscopic studies, it has also been found that Tuc3 is one of only two r-process enhanced UFDs in the MW (Hansen et al. 2017). Marshall et al. (2019) showed that this enhancement must have occurred before Tuc3's most recent pericentric passage, as these same enrichment features are observed in the core and most distant stars in the tails.

Most spectroscopic members of Tuc3 are successfully identified using the algorithm. However, there are seven members with substantially low probabilities that are not included in the member lists. Given their proper motions and position on the CMD, they indeed appear to be consistent with membership to Tuc3. However, these seven stars are the most radially distant of the sample which results in their low spatial probabilities. Indeed, this inconsistency is due to the reliance on a centrally concentrated outer component, rather than having a prior that would be more consistent to a longer stream structure. Nonetheless, I find that the most distant spectroscopic member within the probability limit is at $14.25r_h$, though the actual most distant spectroscopic member to date is located at $16.63r_h$.

The reported transition boundary for Tuc3 is $r_{trans} = 0.34^\circ = 3.4r_h$. Though Tuc3 is known to be tidally disrupting, it is unclear if this boundary is physically motivated. Close inspection of the stellar density profile in Figure 8 of Drlica-Wagner et al. (2015) shows a break at this radius, which at minimum appears to be a transition from the Tuc3 core to the tidal tails. However, it should be noted that a break can also be observed in Tuc3's stellar density profile in Figure 2.10. Given the transition boundary, I identify 18 stars (five of which are HBs) in the outskirts with reasonable magnitudes that have not been already spectroscopically observed.

Pace et al. (2022) and Battaglia et al. (2022) updated kinematic information for Tuc3 and both reported very small pericentre distances ($\sim 1 - 4$ kpc), a very radial orbit, and high eccentricities ($\approx 0.85 - 0.95$). Pace et al. (2022) additionally note that Tuc3 is a system whose central density ratio is indicative of likely tidal influence. Interestingly, Tuc3 has also been proposed to be intertwined with the LMC system, as Erkal et al. (2018) reported that Tuc3 passed within tens of kpcs to the LMC some $\sim$75 Myrs ago.

2.5.9 Ursa Minor

The final system where the algorithm identifies evidence for an outer profile is the classical system, UMi. UMi resides at a relatively large heliocentric distance (∼76 kpc; Bellazzini et al. 2002), yet it was one of the first discovered MW satellites (Wilson 1955), owing largely to its luminosity, $M_V \approx -9.03$ mag ($L_V \approx 3.6 \times 10^5$ $L_\odot$; Muñoz et al. 2018). It is a sufficiently large system ($r_h = 17.32' = 0.28°$ or 380 pc; Muñoz et al. 2018) with a large velocity dispersion (8.6 km s^{-1}; Spencer et al. 2018) similar to other classical dwarfs.

It has been speculated in many studies that tides may affect UMi; this was concluded from (i) morphological asymmetries, (ii) a relatively large ellipticity ($\epsilon = 0.55$; Muñoz et al. 2018), and (iii) stellar clumps that are offset from the dwarf's centroid, and appear aligned with UMi's orbital direction (e.g., Olszewski & Aaronson 1985; Irwin & Hatzidimitriou 1995). To better constrain the stellar density of UMi out to its nominal tidal radius, Palma et al. (2003) conducted a large-area (∼3° radius) photometric survey of UMi, and confirmed two main results: the first being that UMi's isocontours appear S-shaped rather than elliptical (see also Irwin & Hatzidimitriou 1995), and the second was that UMi has two main peaks in stellar densities which are offset from the dwarf's centre. Though the photometric data do not confirm if the most distant stars are bound or unbound to UMi, the authors propose their presence and UMi's morphology are likely as a result of tides.

Multiple properties of UMi that would be further indicators of tidal influence remain speculated. For example, UMi's most recent orbit estimates seemingly do not suggest a substantially close pericentre such that tides can strongly affect the dwarf (see simulations in Read et al. 2006). Pericentres estimated from Pace et al. (2022) and Battaglia et al. (2022) range from $35 - 55$ kpc, depending on the potential used. Secondly, UMi's Jacobi tidal radius[3] estimates range from ∼76′ (1.3°, or ∼500 pc; Palma et al. 2003; Piatek et al. 2005) up to 4.4° (or 6 kpc; Pace et al. 2020). Furthermore, Pace et al. (2022) do not find a substantially low central density ratio such that UMi is a tidal candidate. Though a velocity gradient in UMi has been detected in multiple studies (e.g., Hargreaves et al. 1994), the trend is identified along the minor axis, suggesting a modest internal rotation and not necessarily tides.

[3]The derivation for this tidal radius assumes that the system is in dynamical equilibrium. In the case of UMi, it has been suggested that the dwarf recently passed apocentre (see Sestito et al. 2023b and Figure 6 in Martínez-García et al. 2023) and may be reasonably relaxed such that the tidal radius could be useful.

Spectroscopic study of UMi's outskirts is already in progress. Sestito et al. (2023b) obtained spectroscopic follow-up for five of the most distant and bright stellar candidates identified in this work, ranging from distances of 5.1 to 11.7r_h, confirming that all targets are indeed UMi members. According to previous studies, the most distant member was located at 6.8r_h; with this work, the outskirts of UMi are extended from ∼2.6 kpc out to ∼4.4 kpc. There is virtually no contamination in this sample, as I find *only* four contaminants in the RV sample (i.e., they show inconsistent RVs but are flagged as members in the algorithm). The contamination rate for UMi is only four stars out of the total 436 that have RV measurements.

The transition boundaries in UMi are equal to $r_{trans,ell} = 1°$ (or 3.46r_h) and $r_{trans,circ} = 1.29°$ (or 4.47r_h). Note that the circular solution coincides not only with a previous estimate for the tidal radius (from Piatek et al. 2005 and Palma et al. 2003 at 1.3°) but also to a break in the outskirts of the stellar density profile in Palma et al. (2003), located at ∼80′ (see their Figure 14, and UMi's stellar density profile in Figure 2.10). In comparison, Sestito et al. (2023b) report the "kink" radius for UMi is ∼30′ (or 1.7r_h) while the "break" is ∼225′ (or 13r_h).

Aside from the five candidates in Sestito et al. (2023b), I find that there are 29 candidate outskirt ($> r_{trans}$) members with no current spectroscopic follow-up.

2.5.10 Additional Considerations

The algorithm has proven to be robust in identifying (i) candidate members of MW dwarf galaxies and (ii) systems that exhibit evidence of outer substructure, in agreement with much of the literature. In this section, I emphasize three main considerations:

- The nine systems identified in this work may not be the only systems in the sample with two components, but they are the only systems where the second component is identifiable using this technique with *Gaia* data.

- There are many systems with stars at relatively large radii (>5r_h) that do not require two components to explain the overall stellar distribution.

- I have determined that the detection of an outer profile in the nine systems is robust against uncertainties in the structural parameters (ellipticity, position angle, and half-light radius). I have confirmed that all systems use the most recent updates in structural parameters.

To address the first of these points, note that the detection of an outer profile in each dwarf is limited by the density and physical extent of the structure. For example, it will be more difficult to detect a secondary component around small systems that contain only a handful of stars. As such, it cannot be said that there exist *only* nine systems with extended stellar features. In the future, the total number of dwarfs with outer profiles will likely increase with upcoming *Gaia* data releases and future large-sky surveys like LSST.

The second consideration relates to the fact that stars can exist at large radius from the host galaxy without requiring the galaxy to have a secondary component. For example, recent follow-up by Roederer et al. (2023) identified five member stars in Sextans at distances between $3.5 - 10r_h$. In comparison, the 1-component model of Sextans does similarly identify distant candidate members, but only out to $6.8r_h$. This is also the case in Fornax for which it finds candidate members out to $\sim 7r_h$ (2.1°), or the same radial distance as stars reported in Yang et al. (2022). In these cases, a secondary component is not necessary to find member out to beyond $5r_h$, and the existence of members at these radii is consistent with these systems having a single structural component.

And finally, I consider the limitations of the outer component as it relates to the assumed structural parameters. As discussed in Section 2.3.2, a consequence of the 2-component spatial model is that the likelihood map cannot easily account for uncertainties in the dwarf's spatial parameters. A particular case arose with Gru1, as recent structural parameters for this system have been significantly changed. Specifically, Gru1's new r_h is in fact 2.5 times larger, and the position angle is now rotated into the next quadrant (i.e., it now is oriented West of North instead of East of North) resulting in a vastly different orientation and size in the likelihood model. In using the previous values for Gru1, the algorithm determined that Gru1 had an outer profile, albeit the transition boundary was only slightly larger than the new measurement for Gru1's half-light radius. Additionally, the scale of the outer profile (B) was found to be much larger than in any of the other detections.

Determining the stability of the outer profile is an important outcome of this work, and so I thoroughly examined the list of outer profile systems to confirm that these detections are not hindered by large structural uncertainties. In doing so, I verified that:

1. The uncertainties in position angle, ellipticity, and half-light radius are all suffi-

ciently smaller than the changed percent error in Gru1 (or for position angle, a small enough change such that the orientation is not in the opposing quadrant);

2. If updated structural information exists, I confirmed that using these new values do not produce a different membership list for these dwarfs, even if the individual probabilities may be different; and

3. The updated values do not invalidate the detection of an outer profile.

Of the dwarfs where outer profiles were detected, the only systems with recently updated spatial parameters were Boo1 and Gru1. I found no change in Boo1's results when using the updated parameters in Longeard et al. (2022).

2.6 Summary & Conclusions

In this chapter, I presented an updated algorithm for the detection of dwarf galaxy stellar members using *Gaia* eDR3 photometry and astrometry. This application differs from previous works in that the method allows for the detection of an outer component in the stellar distribution (if there is one), enabling a census of dwarfs which likely host extended structure to be developed. I applied the algorithm to all known MW dwarf galaxy satellites (and dwarf candidates). Of these, I detect outer profiles in a total of nine systems; these are: Boo1, Boo3, Dra2, Gru2, Seg1, Scl, Tuc2, Tuc3, and UMi.

I have shown that the presence of an extended profile in this model does successfully acquire additional members in the outskirts of these dwarfs. Many of these stars would have likely been missed without this change, as evidenced by the excess of stars seen in the stellar density profiles of Figure 2.10. The inclusion of these distant members indicates a divergence from the fiducial 1-component exponential function and at distances $> r_{trans}$. The only exception is Gru2, which I found is limited by the presence of the OC stream that overlaps the dwarf in projection (and inconveniently has the same proper motions as Gru2).

For systems with an extended profile, I note that the addition of a secondary component does not change the vast majority of stellar members in the interior ($< r_{trans}$). Primarily, the change is evident in the outskirts where it is shown that the 1-component case restricts the detectability of distant members. Using my membership lists for Scl and UMi, Sestito et al. (2023a,b) showed that the 1- and 2-component

data produce exceptionally similar inner stellar density profiles, save for the evident truncation of stars in more distant radial bins. As the 1-component model has been shown to limit these detections, I find that these adjustments merely allow for the inclusion of additional stars at large radii. In doing so, the algorithm is able to probe further into the outskirts of these satellites.

Of the systems that are identified as having extended structure, a handful in the literature have already been reported as possibly disrupted systems (Boo1, Boo3, Tuc3, Scl, UMi; see references for each in Section 2.5). Encouragingly, I also find evidence of an extended feature in Tuc2. Conclusively, the algorithm performs well at locating systems with extended haloes and tidal disturbances. However, note that I remain agnostic regarding the origin of these outer features, and that it will be up to future follow-up campaigns to make this conclusion.

An additional concept I report here is the boundary at which the spatial likelihood transitions from the inner exponential to the outer, which may prove to be an interesting feature. This feature corresponds to known breaks/bumps in the stellar density profiles of other works as explored in Section 2.5. As Figure 2.10 shows, the transition boundary nicely corresponds with the divergence of the stellar density from a singular exponential. In some clear cases (like Boo3 and Tuc3), I find that the substantial excess of stars beyond this boundary appears as a stellar density bump. Indeed, it may be a useful limit to examine the central dwarf members compared to the stellar halo outskirt stars for exploration in future works.

I also showed in this work that the algorithm performs exceptionally well at removing MW foreground contamination from the dwarf candidate samples. By comparing my membership probabilities to the RV-confirmed dwarf members for which there is data, I confirmed that the algorithm obtains reasonable purity down to $P_{max} \geq 10\%$ and determined that a purity of >85% can be obtained for stars with $P_{max} \geq 50\%$. However, in fields where the MW foreground contamination dominates significantly and the system in question is particularly small, the algorithm is unable to effectively converge on spatial parameters for the outer profile (see Section 2.3.4).

This algorithm proves to be very efficient at detecting true members of dwarf galaxies, even those at large radial distances. Already, my source list of individual resolved members has proven useful for detailed study of these interesting dwarfs (Boo1, UMa1, and ComaBer in Waller et al. 2023; Boo5 in Smith et al. 2023; Ret2 in Hayes et al. 2023; Scl in Sestito et al. 2023a; and UMi in Sestito et al. 2023b). With the availability of deeper photometric campaigns (e.g., LSST) paired with the

impressive precision and increasing accuracy of *Gaia* kinematics in each new data release, detectability of dwarf stellar haloes will be exceptionally promising in the near future. Specifically, our group is looking forward to disentangling the origins of these extended features, with the advent of the Gemini High-resolution Optical SpecTrograph (GHOST; Pazder et al. 2016) at the Gemini South Observatory.

Chapter 3

Characterizing the Stellar Debris of the Boötes 3 Dwarf Galaxy

This chapter presents new observations and analysis of the Boötes 3 (Boo3) dwarf galaxy, a large (half-light radius = 33′) and diffuse system that has long been suspected of being tidally disrupted. Since its discovery, which was simultaneous to a coincident 50°-long stellar stream known as Styx, it has been argued to be the progenitor of this stream. However, this association has remained unconfirmed.

In Chapter 2, I identified Boo3 as a system whose stellar distribution appeared to have an extended stellar component − a finding that may corroborate the presence of tidal tails in Boo3. To investigate further, I first combined my *Gaia*-selected stellar candidates from Jensen et al. (2024) with new CaHK photometric observations from CFHT/MegaCam. From these observations, I derived photometric metallicities of stars central to Boo3 and re-analyzed its mean metallicity and metallicity dispersion. Using these new estimates, in conjunction with other properties central to Boo3 (e.g., systemic proper motion and distance), I probed catalogues of stellar tracers (blue horizontal branch and red giant branch stars) to search for extended stellar debris. Upon finding no link between stars in the inner regions ($<5r_h$) to a coherent stream structure, I then conducted a large-sky search for Boo3's putative stream using a matched filter technique applied to multiple photometric catalogues.

Despite its apparent susceptibility to tides, I identify no significant stellar debris at large radius and find no kinematic link between Boo3 and Styx. These results suggest either that Boo3's extended substructure is too diffuse to be detected with current data, or that a more complex dynamical process (such as interaction with the

Galactic bar) has dispersed stars in Boo3's stellar stream. This work highlights the necessity of obtaining follow-up observations for photometrically-identified substructures, particularly as even fainter accretion remnants across the Galaxy are uncovered with next-generation surveys.

This work is currently in preparation for submission. The majority of this chapter is my own work, analysis, and scientific writing. The observations taken at CFHT are part of a joint Canada-France observing proposal to target the largest of the smallest galaxies, in which I am a Principal Investigator on the Canadian side. The France PI was Dr. Raphaël Errrani, who contributed to this work by creating Figure 3.4 to highlight the proposed observed fields of Boo3. The proposal is titled, "Small but large: tides and their role in shaping the structures of the most puzzling Milky Way satellites" (CFHT 22AC17 and 22AF17).

The initial calibration of the observations (flat-field corrections and bias subtraction) were performed by the observing team at CFHT. The fields were stacked by France collaborator Dr. Nicolas Martin, who also created the catalogue of sources and magnitudes using `DAOPHOT`*. All additional data corrections (zero-point offsets and photometric metallicity calibrations) were conducted by myself.*

3.1 Introduction

In the prevailing ΛCDM cosmological model, galaxies like the Milky Way are assembled hierarchically through the accretion and merging of smaller systems (White & Rees 1978; Frenk et al. 1988). Dwarfs − the most numerous type of galaxy in the Universe − are considered the fundamental building blocks of larger galaxies as their stars and dark matter directly contribute to the growing haloes of their host (Bullock & Johnston 2005; Cooper et al. 2010). As these low-mass satellites fall into the gravitational potential of a massive galaxy like the Milky Way, they experience tidal forces imparted by the host that act to gradually strip away mass. Over time, this process results in the decimation of a satellite, whose mass is strewn across the host in the form of lengthy tidal tails until the disrupted system becomes completely phase-mixed and assimilated into the more massive galaxy.

The stellar halo of our own Milky Way (MW) is similarly populated by substructures in various stages of disruption (Shipp et al. 2025), ranging from intact satellites (dwarf galaxies and globular clusters; McConnachie 2012; Harris 1996), to partially disrupted systems (stellar streams, with and without clear progenitors; Mateu 2023), and fully decimated, phase-mixed debris that may only retain chemical or kinematic signatures of their origin (e.g., Helmi et al. 1999, 2018; Naidu et al. 2020). Studying these structures not only reveals our own Galaxy's accretion history and the underlying influence of the MW potential, but furthermore can inform on the resilience of accreted dwarf galaxies within their own DM haloes, thereby offering insight into the nature of dark matter and small-scale galaxy formation.

Boötes 3 (Boo3) is one such dwarf galaxy that is currently believed to be undergoing the final stages of tidal disruption. Photometric observations indicate that Boo3 is particularly diffuse, large (half-light radius of 33.03′; Moskowitz & Walker 2020), and morphologically, appears double-lobed and misshapen (see Figure 10 in Grillmair 2009) which may indicate that the system is not currently in dynamical equilibrium. Its on-sky position also lies coincident to a $\sim 50^{\circ}$-long structure, known as the Styx stellar stream, that was simultaneously discovered with Boo3 in Grillmair (2009). These initial observations have led to the conclusion that Boo3 is the progenitor (or at minimum, associated with) Styx. However, both of these structures have remained largely unstudied since their original detection, in part due to the faint ($M_V = -5.75$ mag; Correnti et al. 2009) and diffuse nature of Boo3 making follow-up observations challenging.

In previous work by Jensen et al. (2024, presented in Chapter 2), Boo3 was identified as one of nine dwarf galaxies in the MW (out of the ∼60 studied) that exhibit evidence for an extended stellar distribution. Boo3's stellar distribution indicated an excess of stars beyond ∼3 half-light radii (r_h) that extends out to large radial distances (∼$14r_h$). This outer component, as discussed in the previous chapter, is argued to originate due to external factors (i.e., MW tides acting to radially migrate *in situ* stars outwards, or a previously accreted system populating an accreted stellar halo). As these previous findings indicate there is an extended stellar population in the outskirts of Boo3, I aim to explore in this work whether this feature is tidal in origin.

Despite the lack of recent studies, a number of previous results indeed suggest that Boo3 is tidally disrupting. Recent constraints of Boo3's kinematics, such as proper motion (Carlin & Sand 2018; Pace et al. 2022; Battaglia et al. 2022) and radial velocity (Carlin et al. 2009), suggest a very small pericentre of only $7 - 9$ kpc (Pace et al. 2022; Battaglia et al. 2022) which may signify strong tidal influence from the MW. This conclusion is further in agreement with Boo3's substantial velocity dispersion ($\sigma_{RV} \sim 14$ km s^{-1}; Carlin et al. 2009) which may have been inflated substantially as the system loses mass (Errani & Navarro 2021; Errani et al. 2022).

Though there is substantial evidence to support the disruption of this dwarf, it remains true that (i) no extended stellar debris of Boo3 has been catalogued or reported in the literature and (ii) no link between Boo3 and Styx has been officially confirmed. This work aims to closely inspect the Boo3 dwarf with an intent to detect its presumed tidal debris. Assuming the system's outer profile can be explained by MW tides, this work will finally confirm or deny its association to Styx. If Boo3 is shown to possess a stream, it will join the exceedingly small sample of (two other) dwarf galaxy progenitors that are reported to have lengthy (> multiple degree-long) tidal tails. This putative verification could yield interesting results for future dynamical studies exploring the underlying mass and shape of our Galaxy's dark matter halo.

3.2 Modeling the Dynamics of Boötes 3

To help guide the search for a coherent structure from Boo3, I first computed the satellite's orbit in addition to the positions and velocities of its alleged debris. However, note that these models are not relied upon in the selection of candidate

Parameters	Symbol	Value	Reference
RA, Dec (°)	(α, δ)	(209.30, 26.80)	(1)
Distance (kpc)	R_{helio}	46.56 ± 0.25	(2)
Half-light radius (arcmin)	r_h	33.03 ± 2.50	(3)
Physical half-light radius (pc)		447 ± 2	(4)
Position Angle (°)	PA	−81 ± 8.0	(3)
Ellipticity	ϵ	0.33 ± 0.09	(3)
Absolute magnitude (mag)	M_V	−5.74 ± 0.5	(5)
Metallicity	[Fe/H]	−2.1 ± 0.2	(6)
		−2.1 ± 0.1	This work
Metallicity dispersion	$\sigma_{Fe/H}$	0.6 ± 0.2	(6)
		0.2 ± 0.1	This work
Proper motion in R.A. (mas yr^{-1})	$\mu_{\alpha*}$	−1.160 ± 0.037	(4)
Proper motion in dec (mas yr^{-1})	μ_δ	−0.88 ± 0.035	(4)
Radial velocity (km s^{-1})	RV	197.5 ± 3.8	(6)
RV dispersion (km s^{-1})	σ_{RV}	14.0 ± 3.2	(6)

Table 3.1: Observational properties of Boo3 relevant to this work. Citations: (1) Grillmair (2009), (2) Carlin & Sand (2018), (3) Moskowitz & Walker (2020), (4) Jensen et al. (2024), (5) Correnti et al. (2009), (6) Carlin et al. (2009).

stream stars, but instead serve to independently compare expected trends of *bona fide* stream members. This first section presents the initial conditions and adopted parameters used in this dynamical analysis. I summarize the dynamical methods in which I adopt two complementary approaches. These involve (i) determining Boo3's point-mass orbit to observe the trajectory of the satellite, and (ii) using a "particle-spray" technique (Fardal et al. 2015) where massless particles are "ejected" at specified timesteps along the system's orbit and integrated forward in time, thus illustrating the phase-space distribution of putative debris. In both methods, the observed differences when assuming a static versus a time-evolving potential (i.e., one that included the influence of a massive LMC) are compared. Note that Boo3's point-mass orbit will appear later in Sections 3.5.1 and 3.5.2, and that a thorough discussion of Boo3's dynamics is reserved for Section 3.6.

3.2.1 Initial Conditions

To estimate Boo3's orbit and create a particle-spray model representing its debris, orbit integrations are calculated within the Galactic dynamics `AGAMA` (Vasiliev 2018) framework. Initial conditions for Boo3 are determined using the present-day observations of the system, summarized in Table 3.1. Unit conversion between Galactic and Equatorial coordinates are conducted using `astropy` (Astropy Collaboration et al. 2013, 2018), where I assume a right-handed Galactocentric Cartesian coordinate (X, Y, Z) system. In this frame, the Sun is located at $(-8.122, 0.000, 0.025)$ kpc (Gravity Collaboration et al. 2019; Jurić et al. 2008) with a circular velocity of 229 km s^{-1} (Eilers et al. 2019). To convert from the Local Standard of Rest to Galactocentric frame of reference, the Solar peculiar motion is assumed to be $[U, V, W]_{\odot} = [11.1, 12.24, 7.25]$ km s^{-1} (Schönrich et al. 2010).

To explore the impact of the LMC in Boo3's trajectory, I use both a static and time-evolving potential. Both MW potentials consist of three main components: a spherical bulge, an exponential disk, and a triaxial dark matter halo. The static potential, modelled after that of Thomas & Battaglia (2022), is a composite whose parameters (scale lengths, densities, and axis ratios) have been tuned to best replicate the observed MW rotation curve (Eilers et al. 2019). For the evolving potential, I utilize the pre-set triaxial model developed by Vasiliev et al. (2021) which has been calibrated to match the MW rotation curve and provides an excellent fit for the Sagittarius stream. The evolving potential includes the orbit and gravitational wake

of a massive LMC (1.5×10^{11} $M_{\odot}$) which varies the MW potential over time. The LMC in this model is on first infall, entering the MW only 1.6 Gyrs ago.

Figure 3.1 shows that the rotation curves of both the static (green) and evolving (orange) potentials are consistent to the observed MW rotation curve (cyan error bars) and fit the circular velocity of the Sun (grey cross-hairs) sufficiently. Although these potentials differ in construction, the enclosed masses for each MW component are broadly consistent to observed estimates. These values are provided in Table 3.2 for reference, and include the ranges of reported literature values for comparison.

3.2.2 Satellite Orbit & Phase-Space of Stream

The orbit of Boo3, represented by a point-mass, is then calculated in both the static and evolving potentials. In the pre-set model from Vasiliev et al. (2021), the MW's potential over each timestep is represented by snapshots that were taken from a more detailed `AGAMA` N-body simulation. While using this version of the evolving potential is more accessible and takes less computation time than a full N-body simulation, the Vasiliev et al. (2021) evolving potential does not currently include the orbit of the LMC in timesteps past the present day. As such, the orbit of this model is only integrated backwards in time by 5 Gyrs, in timesteps of 5 Myrs. As the static potential does not vary with time, the orbit of this model is integrated both forwards and backwards in time (i.e., $\pm$5 Gyrs) in timesteps of 5 Myrs.

The resulting orbits are shown in Figure 3.2 in Galactocentric coordinates. It is particularly apparent in the bottom panel that Boo3 experiences more frequent pericentric passages in the evolving potential, and indeed this detail may prove relevant for future N-body simulations of Boo3's disruption. A more detailed discussion of these implications will be presented in Section 3.6.

For both potentials, both orbits' equatorial coordinates and kinematics are practically identical within $\sim$20° of Boo3 such that either result can be used to examine the satellite's on-sky trajectory. In Sections 3.5.1 and 3.5.2, the observational results are compared to solely the orbit from the static potential for simplicity. A further discussion of the differences regarding the evolving potential will be presented later in Section 3.6 with the particle-spray analysis.

To explore the positions and velocity of Boo3 debris, I also approximate a "particle-spray" model (Fardal et al. 2015) using the `AGAMA` framework. For this, the Galactocentric positions and velocities of the dwarf are first calculated at a given timestamp

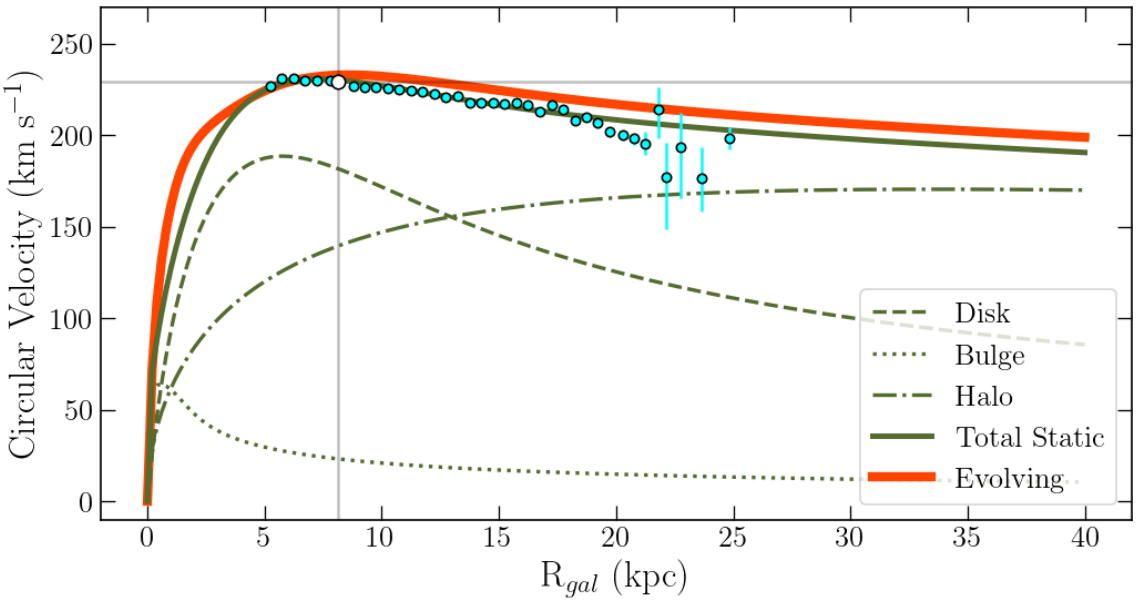

Figure 3.1: Rotation curves for the total static potential (consisting of a composite 3-component disk, a bulge, and a DM halo) in olive and a time-evolving potential (including the LMC) in orange. There is good agreement between both models compared to the MW's observed rotation curve (Eilers et al. 2019; cyan error bars), and also note that both models accurately reproduce the circular velocity of the Sun at $v_{circ}(R_\odot) = 229.0$ km s^{-1} (grey cross-hairs).

Component	Static	Evolving	Observations	Refs.
Disk	6.5×10^{10}	5.0×10^{10}	$(4.6 - 5.7) \times 10^{10}$	(1); (2); (3)
Bulge	1.0×10^{9}	1.2×10^{10}	$(0.9 - 2.2) \times 10^{10}$	(2); (4); (5)
Halo	0.7×10^{12}	0.88×10^{12}	$M_{200} \sim (0.8 - 1.3) \times 10^{12}$	(6); (7); (8)
LMC	–	1.5×10^{11}	$(1.3 - 1.9) \times 10^{11}$	(9); (10); (11)

Table 3.2: Enclosed masses for MW components used in the static and evolving potential, compared to current literature estimates. All values are given in units of solar masses ($M_\odot$). Citations: (1) Bovy & Rix (2013), (2) Licquia & Newman (2015), (3) McMillan (2017), (4) Valenti et al. (2016), (5) Portail et al. (2017), (6) Callingham et al. (2019), (7) Cautun et al. (2020), (8) Deason et al. (2021), (9) Erkal et al. (2019), (10) Vasiliev et al. (2021), (11) Shipp et al. (2021).

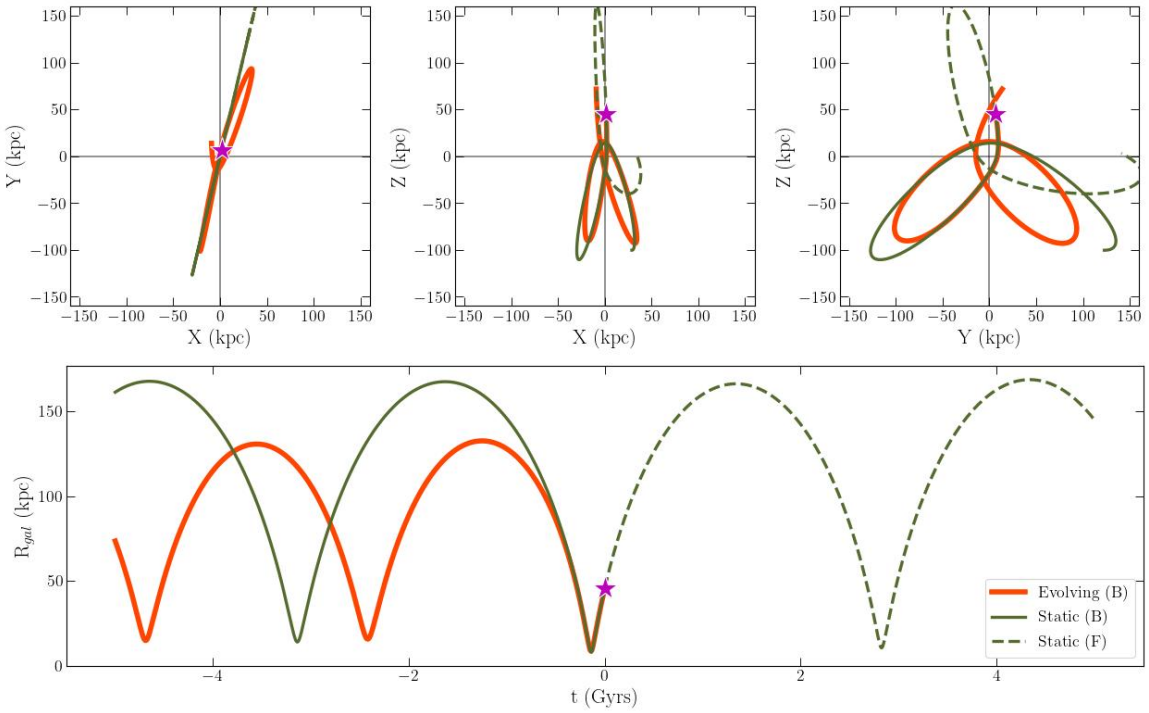

Figure 3.2: Orbit trajectories for both the static (olive) and time-evolving (orange) potentials. In both potentials, Boo3's orbit is integrated backwards by 5 Gyrs (shown as the solid lines). For the static potential only, the orbit is also integrated forward by 5 Gyrs (dashed line). The initial conditions of Boo3 are indicated as a magenta star.

to set as the initial conditions for the progenitor. Here, the integration is initiated 3 Gyrs ago in the orbit. At timesteps of 5 Myrs along the orbit, two massless particles are seeded at the satellite's Lagrange points and are assigned a typical escape velocity (derived from the self-gravity of Boo3, assuming a Plummer spherical potential; Plummer 1911). Thus the particles' velocities and positions account for both the orbit of the system at that timestep, in addition to the velocities imparted by the dwarf's own potential. These escaped particles are then integrated forward to the present day. The resulting distribution of particles produces an approximate stream model, thereby illustrating the approximate spatial and kinematic distribution of tidal debris without performing a full N-body simulation.

3.3 Data

As discussed in Section 3.1, Boo3 was previously identified as a dwarf in which an outer excess of stars in *Gaia* was detected by the algorithm (presented in Chapter 2). Here, the first dataset used to study Boo3 and its putative stream is the list of stellar candidates identified in Jensen et al. (2024). To explore this (relatively unstudied) system in further detail, I obtained follow-up observations of Boo3 using the narrow-band CaHK filter centred on the inner regions ($<3r_h$) of the dwarf. These observations enable the derivation of photometric metallicities across multiple fields, and as such provide substantially more stars with metallicity information than was previously obtained in spectroscopic studies. To conduct a wide-field search for individual stream members, I also use catalogues of stellar tracers (specifically, blue horizontal branch and red giant branch stars). Finally, I revisit the original matched filter evidence for stellar debris in the vicinity of Boo3 by exploring additional photometric catalogues (SDSS and DELVE). These various data and catalogues are discussed in detail below.

3.3.1 *Gaia* Members from Jensen et al. (2024)

In Jensen et al. (2024, Chapter 2), I applied a Bayesian-based algorithm to identify all likely stellar sources – for *all* MW dwarf spheroidals – observed in *Gaia*'s early Data Release 3 (eDR3; Gaia Collaboration et al. 2021). The first dataset used in this work is thus the candidate list of Boo3 stars from Jensen et al. (2024).

It was shown in Chapter 2 that, for stars with radial velocity measurements as an independent metric to confirm sample purity, the algorithm performs exceptionally

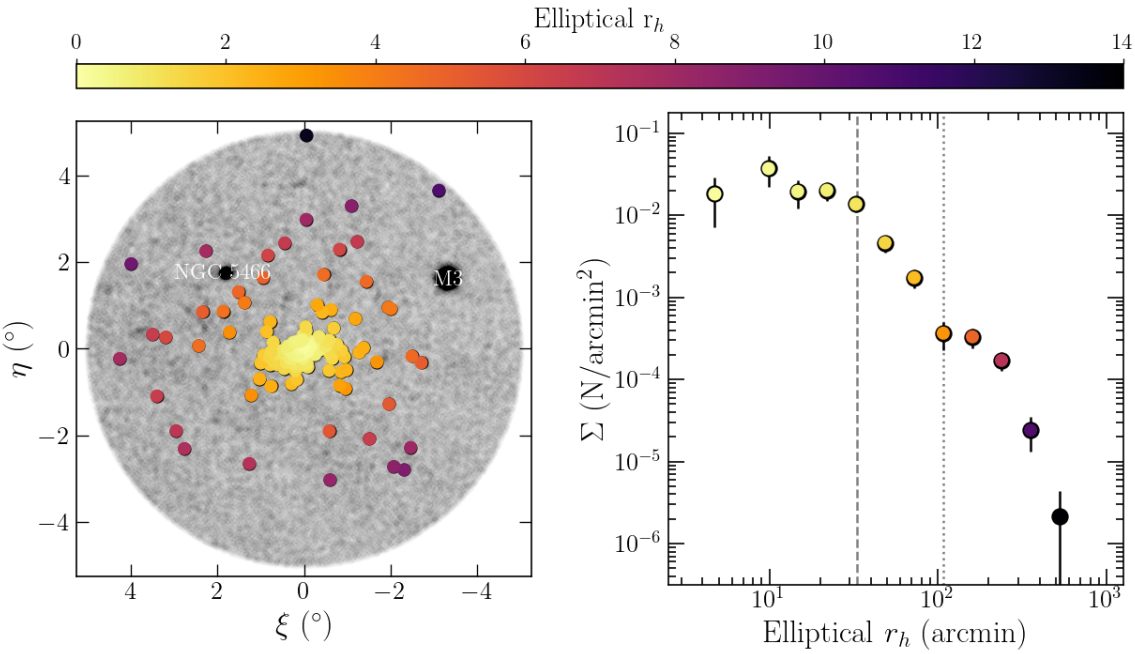

Figure 3.3: *Gaia* candidate stars of Boötes 3 derived in Jensen et al. (2024). Data are coloured according to their radial distance from the centre, in units of elliptical half-light radii (r_h). **Left:** Tangent plane projection of candidates, overlain on MW field stars (grey). Globular clusters within the field are labelled in white text. **Right:** Stellar density profile of candidates as a function of elliptical r_h in units of arcmin. For reference, r_h and the transition radius (r_{trans}; from Jensen et al. 2024) are indicated as the dashed and dotted vertical lines, respectively.

well at removing contamination by assigning appropriately low membership probabilities ($\lesssim$5%) to MW foreground stars. The dataset of stellar sources used in this present work are thus a subset of this catalogue, where the data are restricted to membership probabilities greater than 20% ($P_{max} \geq 20\%$). Figure 3.3 showcases the physical extent of these Boo3 candidates in the tangent plane and stellar density profile (left and right panels, respectively). As indicated by the range of the colour bar, these data span a significant radial distance (up to $14r_h$) despite the algorithm not requiring radial velocity information to identify members.

3.3.2 Follow-Up CaH&K Photometry of Boötes 3

Tidal interactions in dwarf galaxies are most clearly evident as morphological disturbances in the outskirts of their stellar distributions. However, these substructures are usually considerably lower in surface brightness than the main body of the progenitor (e.g., see the density profile of Pal-5 and its stream in Bonaca et al. 2020 and simulated profiles of the disruption of Sagittarius in Niederste-Ostholt et al. 2012) such that the signal of a stellar stream can be washed out by the dominating MW foreground. While the previous work in Jensen et al. (2024) revealed the presence of an extended stellar population observed in *Gaia*, confirming stellar memberships ideally requires spectroscopy to measure each star's radial velocity (RVs) and metallicity ([Fe/H]) to verify consistency to the progenitor. However, spectroscopic follow-up is observationally expensive as it requires substantially more observing time than photometric observations. Given the limited literature on Boo3 (e.g., Grillmair 2009; Carlin et al. 2009; Correnti et al. 2009; Carlin & Sand 2018), where even its half-light radius was only recently estimated (Moskowitz & Walker 2020) and its other structural parameters are not well-constrained, I pursued an alternative approach to study this system. Specifically, I obtained narrow-band Calcium H&K (CaHK) photometric observations which can be utilized to calibrate photometric metallicities. By providing a cost-effective way to determine metallicity information across multiple fields, this particular filter offers a powerful method to distinguish Boo3 members from the more metal-rich MW foreground with less required overall observing time.

These observations were obtained as part of a semester-long imaging program with CFHT. As shown in Figure 3.4, the proposed field patterning would provide complete photometric coverage of Boo3 (red central fields) and ideally some coverage of any extended tidal debris. However, only six central fields ($<3r_h$) were observed

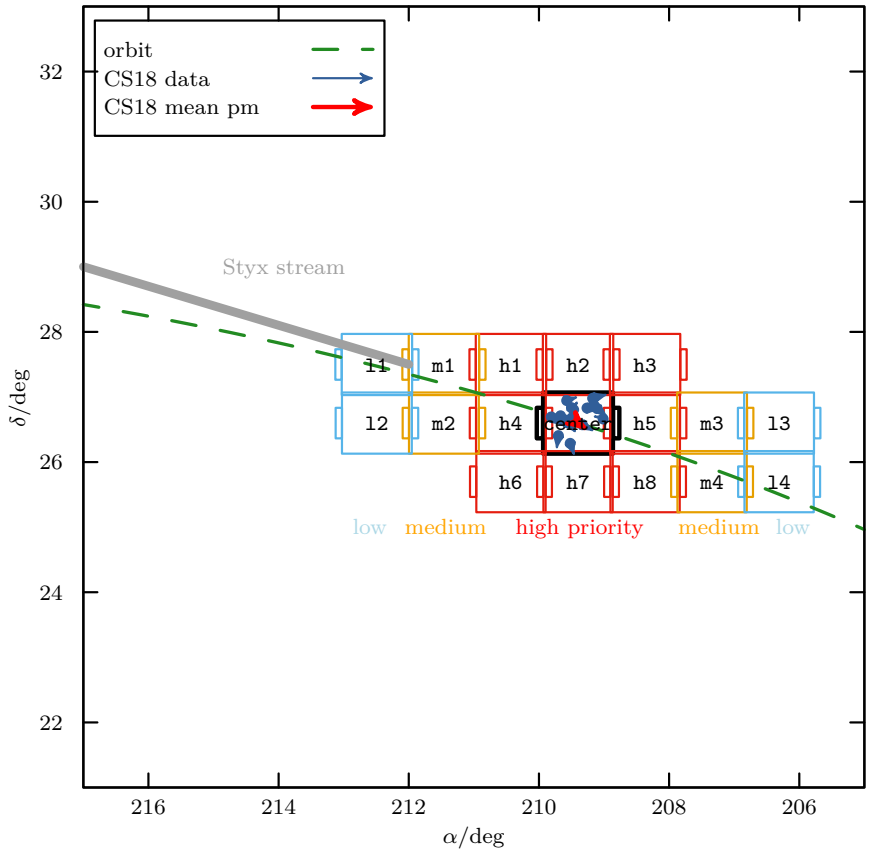

Figure 3.4: Proposed fields for observation in and around the Boötes 3 dwarf. Only the "center", "h1", "h2", "h3", "h4", and "h5" fields were observed as the observations were not completed during the 2022A semester. The orbit of Boötes 3 (green dashed) and the approximate position of the Styx stellar stream (grey) are shown for reference. This figure was created by Dr. Errani during the Phase 2 observing preparations.

due to inclement weather. To calibrate these observations and obtain photometric metallicities, the data were calibrated using the methods of the "Pristine dwarf galaxy" program (e.g., Longeard et al. 2018, 2020, 2022, 2023 to name a few). This program is a subset of the larger-scale *Pristine* collaboration. In the following section, I briefly summarize the goals and methods of *Pristine* as applicable to this work.

Pristine: Survey & Collaboration

The *Pristine* collaboration is an international consortium dedicated to studying the most metal-poor and chemically pristine stars in and around the Galaxy (Starkenburg et al. 2017). A star's metallicity ([Fe/H]) directly reflects the metals present in the environment from which it was formed, thus the oldest, most metal-poor stars provide insight into the early conditions of the MW (see related reviews by Belokurov 2013 and Helmi 2020). By identifying the most metal-poor ([Fe/H] < -3.0) stars in the Galaxy's halo and bulge, *Pristine* aims to use these stars to uncover the early evolution of the MW.

Cataloguing the most metal-poor stars presents an observational challenge, as these sources are exceptionally rare. In a typical MW halo field, only about 1 in every $\sim$2,000 stars with $14 < V < 18$ has [Fe/H]< -3.0 dex (Robin et al. 2003; Youakim et al. 2017). Furthermore, obtaining reliable metallicities through spectroscopy requires long exposure times to achieve sufficient signal-to-noise ratios (SNR), making a wide-field survey of these stars prohibitively expensive. Wide-field spectroscopic facilities may mitigate these issues in the future; however, there are only a limited number (e.g., WEAVE, 4MOST) that currently exist. As a result, these combined challenges significantly hinder our ability to identify and study the most metal-poor stars in the MW.

To overcome these limitations, *Pristine* employs a technique to photometrically calibrate metallicities, using the CaHK narrow-band (100 nm wide) filter at the 3.6-meter Canada-France-Hawaii Telescope (CFHT). This filter, centred on the Ca H&K absorption lines (393.3 and 396.9 nm), is particularly sensitive to a star's metallicity. Figure 3.5 shows the throughput of the filter over the CaH&K spectral lines (left panel) and illustrates the dependence of these features on a star's intrinsic properties (right panel). As seen on the right, the absorption features are weakest for the most metal-poor stars, regardless of temperature or surface gravity. By construction, this filter is capable of efficiently detecting metal-poor stars from the more metal-rich

MW foreground. Additionally, the ∼1 square degree field-of-view (FOV) of CFHT's MegaCam imager enables efficient coverage over large areas of sky.

The *Pristine* calibration method (originally presented by Starkenburg et al. 2017) infers a star's photometric metallicity by exploiting empirical relationships between broad-band colours (i.e., a star's temperature) and CaHK magnitudes. Because weaker CaHK absorption produces brighter narrow-band magnitudes, metallicity can be estimated from flux differences between CaHK and broad-band filters. Polynomial relations in colour–colour space are able to sufficiently separate stars of different metallicities into distinct loci. This approach allows *Pristine* to efficiently estimate metallicities photometrically across wide regions of sky, achieving results at a fraction of the cost and observing time required for spectroscopy.

In the collaboration's on-going self-titled long-program, the *Pristine* survey is working to obtain large-sky CaHK observations, primarily at high Galactic latitudes ($b > 30°$) with more recent efforts extending into the Galactic bulge (Starkenburg et al. 2017; Martin et al. 2024). Their methodology has proven highly effective, as photometric metallicities derived using CaHK data show excellent agreement with spectroscopic measurements of both individual stars (Youakim et al. 2017) and globular clusters (Figure 19 in Martin et al. 2024). While this survey has greatly expanded the census of metal-poor stars in the Northern hemisphere, its current footprint (∼6100 square degrees) does not presently have coverage near Boo3. To enable all-sky coverage, Martin et al. (2024) generated a synthetic CaHK catalogue by deriving CaHK magnitudes from *Gaia* XP spectra (Gaia Collaboration et al. 2023) to then calibrate all-sky photometric metallicities. This *Pristine*-*Gaia* synthetic catalogue contains metallicity information for nearly ∼219 million stars. However, since *Gaia*'s low-resolution BP/RP spectra are limited to bright, high-SNR sources, this catalogue does not contain a substantial number of red giant branch stars and is thus also insufficient to study Boo3.

Therefore, I opted to obtain independent CaHK observations in order to similarly capitalize on the efficiency of CFHT's CaHK filter. To calibrate these data, I implement the same methodology as the *Pristine* collaboration. Deriving photometric metallicities for stars in and around Boo3 enables the (i) verification of Boo3's previous metallicity estimate, and (ii) individual confirmation of membership to the dwarf. These metallicity estimates are particularly useful for distinguishing Boo3 members, as Boo3 is a much more metal-poor system (−2.1 dex; Carlin et al. 2009) than the more metal-rich MW disk ([Fe/H] ~ -0.5 dex, albeit with considerable spread; Helmi

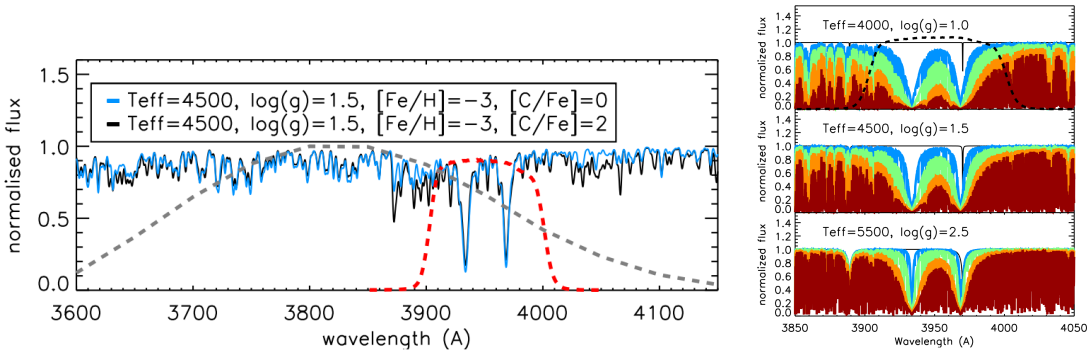

Figure 3.5: **Left**: Example throughput curves of the narrow-band CaHK filter (red) used in this work. Synthetic model spectra in blue and black show the Ca H&K absorption lines, efficiently covered by the Pristine filter. **Right**: Synthetic spectra of 3 different RGB stars of varying metallicities: [Fe/H] = 0.0 in red, −1.0 in orange, −2.0 in green, and −3.0 in blue. Black line shows a comparison model spectrum with no metals. Throughput curves of the CaHK filter (black dashed) are only shown in the top panel. Sourced directly from Starkenburg et al. (2017).

2020).

Observation Strategy & Data Calibration

In the 2022A semester, I was awarded time at CFHT for a total of nine hours under good seeing conditions (>0.8″) using the MegaCam imager. The full target area is shown in Figure 3.4. To ensure complete sky coverage of our target area, each field was overlaid by 0.1° to account for the "ears" of MegaCam, which are essentially a set of protruding CCDs on the East and West sides of the camera. To achieve similar depths as *Gaia* across as many fields as possible, each observation consisted of a single 912-second exposure per field.

Due to poor observing conditions, only 4.5 hours of observations were taken over the course of 4 nights (February 25, February 26, August 2, and August 3, 2022). The final observed fields for the semester were "center", "h1", "h2", "h3", "h4", and "h5" as indicated in Figure 3.4. Despite the limited observing time, the region spans slightly more than three times the half-light radius ($3r_h$) and at minimum fully encapsulates the central regions of Boo3. In Jensen et al. (2024), I estimated that the radius at which the outer profile dominates the total fraction of starlight in Boo3's stellar density profile (r_{trans}) is $\sim 1.7r_h$. Therefore the photometric observations should also cover Boo3's putative stellar debris. The raw data were then processed using CFHT's `elixir` pipeline (Magnier & Cuillandre 2004) to conduct bias subtraction and apply flat-field corrections on the images.

In a recent *Pristine* publication, Martin et al. (2024) discuss two essential calibration steps required prior to converting observed CaHK magnitudes into photometric metallicities. The first step addresses zero-point magnitude variations related to a star's position within the telescope's FOV, referred to here as the offset per pixel in $(x,\ y)$ for a given exposure sequence (j). This offset is denoted as $FOV_j(x,\ y)$. The second necessary calibration addresses the overall zero-point offsets caused by varying observational conditions, referred to as the zero-point offset per image (i) or $zp(i)$. The combined magnitude calibration for these effects (CaHK_{calib}) are represented in the following equation from Martin et al. (2024):

$$CaHK_{calib} = CaHK_{uncalib} + zp(i) + FOV_j(x,\ y) \tag{3.1}$$

where the raw magnitudes from our observed fields are given as $\mathrm{CaHK}_{uncalib}$, $zp(i)$ are the median offsets per field (i), and the calibrated magnitudes accounting for FOV

offsets in a given observing run j (determined in `PhotCalib`, discussed below) are $FOV_j(x,\ y)$.

As highlighted by previous works (e.g., Ibata et al. 2017; Martin et al. 2024), zero-point variations not only differ across the telescope's FOV but also fluctuate slightly between observing runs − typically occurring once or twice a month when MegaCam is reinstalled on the telescope. To correct for these systematic spatial and temporal variations, Martin et al. (2024) developed a specialized calibration algorithm named `PhotCalib`. This algorithm uses a neural network trained on *Pristine* data gathered over multiple semesters, spanning from 2015A to 2022B. The training dataset includes the observed star positions, raw CaHK magnitudes ($\mathrm{CaHK}_{uncalib}$), and synthetic magnitudes (CaHK_{syn}) obtained from the *Pristine-Gaia* synthetic photometric catalogue. The output from `PhotCalib` provides precise CaHK magnitude corrections as a function of pixel position $(x,\ y)$ across the entire FOV of the image. Martin et al. (2024) demonstrate that `PhotCalib` reduces residual calibration uncertainties down to approximately 13 mmag − a level of precision crucial for obtaining accurate photometric metallicities from CaHK magnitudes. Figure 3.6 illustrates the effectiveness of this algorithm for a representative observing run. The top panels show the remaining magnitude offsets between the single ground-based exposure at CFHT ($\mathrm{CaHK}_{uncalib}$) versus the all-sky synthetic magnitudes from the *Pristine-Gaia* catalogue (CaHK_{syn}), accounting for the median zero-point offset of the image due to observing conditions ($zp(i)$). It is clear that the fluctuations across the FOV are non-negligible, and in fact are greatly improved in the residuals when using the `PhotCalib` method (bottom right panel).

Even though the *Pristine-Gaia* catalogue is insufficient to study Boo3 directly, the all-sky capabilities of the dataset means the data can be calibrated for clear zero-point offsets between images/fields. First, the observations were cross-matched to the *Pristine-Gaia* synthetic catalogue. `PhotCalib` was then applied to each image (for either the j = 22Am02 or 22Am07 observing run) and the $FOV_j(x,\ y)$ offsets per pixel was obtained through `PhotCalib`. Though the FOV calibration from the neural network is estimated using a selection of stars common to both observed and synthetic catalogues, the derived corrections broadly apply to all stars within the field. Irrespective of their magnitude, the $FOV_j(x,\ y)$ correction is applied for all stars in the image (i) for a given observing run (j).

The second necessary calibration addresses the overall zero-point offsets caused by varying observational conditions, or the zero-point offset per image ($zp(i)$). Following

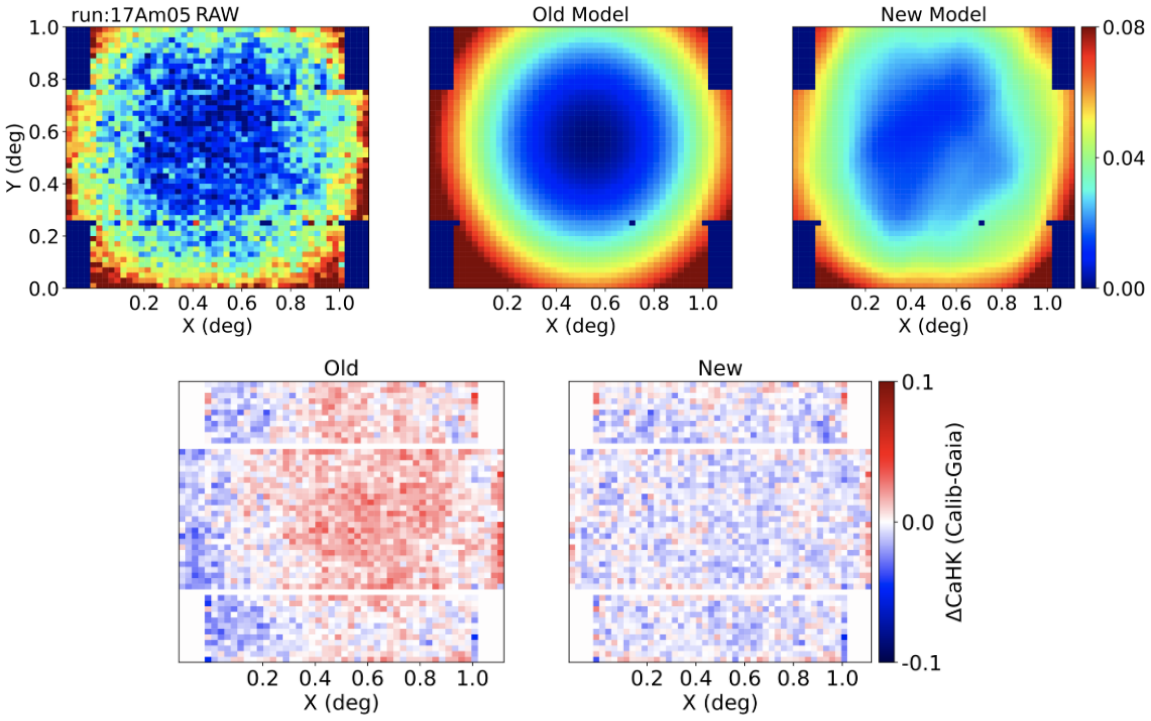

Figure 3.6: An example of the FOV corrections for observing run j = 17Am05, sourced from Martin et al. (2024). **Top:** The difference between uncalibrated and *Pristine-Gaia* synthetic magnitudes, accounting for the zero-point offset of the image ($\mathrm{CaHK}_{uncalib} + zp(i) - \mathrm{CaHK}_{syn}$). The middle and right panels indicate the residuals across the image due to the stars' position in MegaCam's FOV (for the old and new model respectively), while the left indicates the raw measurements. Note that the new method using `PhotCalib` better reflects the non-linear fluctuations across the FOV when compared to the raw residuals. **Bottom:** Median residuals between the calibrated and synthetic magnitudes ($\mathrm{CaHK}_{calib} - \mathrm{CaHK}_{syn}$) for the old and new models. Note the improved smoothness of the residuals in the `PhotCalib` run.

the methodology outlined in Martin et al. (2024), this offset is given as the median difference between observed stars within each field and their corresponding CaHK_{syn} magnitudes from the *Pristine-Gaia* synthetic catalogue. Corrections for extinction of these data are handled within *Pristine*'s newly updated data processing pipeline (Martin et al. 2024; see also Ardern-Arentsen et al. 2025). This step is explained in more detail in Section 3.4.

3.3.3 Tracer Stellar Populations Derived from the Ultraviolet Near-Infrared Optical Northern Survey

In this work, I search for Boo3's putative stellar debris at large separations from the satellite by probing catalogues of stellar tracers. These datasets consist of specific stellar populations − blue horizontal branch (BHB) and red giant branch (RGB) stars − that have been identified with photometry from the Ultraviolet Near-Infrared Optical Northern Survey (UNIONS; Gwyn et al. 2025). Every stellar source in the catalogues possesses well-constrained photometric distances, and (when paired with *Gaia*) enable the tracing of coherent kinematic signals across large Galactocentric distances.

Figure 3.7 shows the spatial footprint of the BHB (blue) and RGB (red) samples used in this study. Note that there are indeed differences in coverage between the two catalogues, due to the on-going survey of the u-band observations between their publication in 2018 and 2019. Jointly however, the two datasets provide sufficient coverage of Boo3 (highlighted in the figure with a magenta star) in addition to a substantial area surrounding the system where tidal debris may be located.

The utility of these catalogues to trace MW substructure has already been demonstrated with the kinematic detection of the NGC 5466 stellar stream in Jensen et al. (2021). These catalogues originate from early observations contributing to UNIONS, specifically the u-band from the Canada-France Imaging Survey (CFIS; Ibata et al. 2017). At the time of observation, the CFIS u-band was combined with the Pan-STARRS 3π (PS1 3π) $griz$-bands (Chambers et al. 2016) and *Gaia*'s second data release (DR2; Gaia Collaboration et al. 2018a). When combined with other photometric bands, the u-band enables the (i) determination of stellar populations (in certain scenarios where differences in u-band magnitudes may trace spectral features, such as the Balmer jump) and thus, estimate absolute magnitudes to calibrate photometric distances, and (ii) assessment of photometric metallicities (due to the numerous

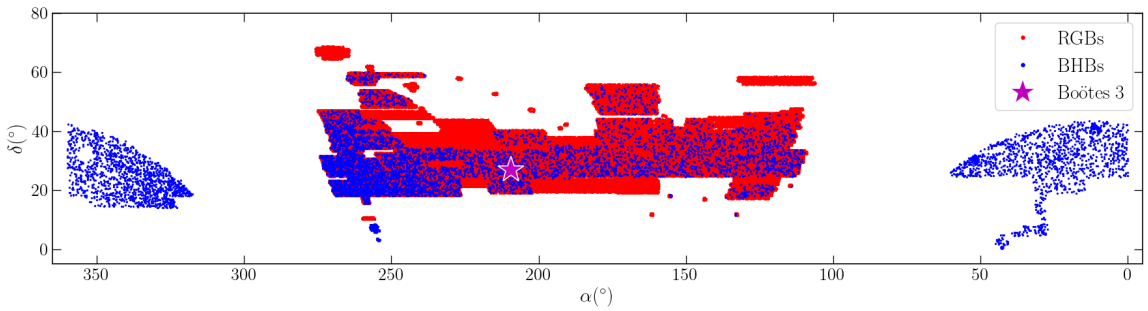

Figure 3.7: Positions of UNIONS blue horizontal branch (BHB; blue points) and red giant branch (RGB; red points) stellar population catalogues, plotted in equatorial coordinates. The location of Boo3 is indicated with a magenta star icon.

metal lines at the UV-blue end of the spectrum). In what follows, I briefly describe the tracer catalogues employed in this study and how their photometric properties were derived.

Blue Horizontal Branch (BHB) Sample

The first stellar population used in this work is the sample of blue horizontal branch (BHB) stars from Thomas et al. (2018, hereafter T18). BHBs are A-type giants with relatively stable absolute magnitudes ($M_g \sim 0.5 - 0.7$ mag; Deason et al. 2011), making them excellent standard candles with well-constrained distance uncertainties ($\sim$10%). Their intrinsic brightness allows them to be detected at large distances (>100 kpc), making them valuable tracers of Milky Way substructure.

Traditionally, BHBs are identified spectroscopically. Balmer line profiles can distinguish BHBs from similarly hot A-type stars (i.e., blue stragglers) due to their difference in surface gravity, which are lower for BHBs (Xue et al. 2011). In lieu of costly spectroscopic observations, recent studies have demonstrated high success in identifying BHBs by leveraging u-band photometry (e.g., Yanny et al. 2000; Sirko et al. 2004; Deason et al. 2011). These photometric approaches enable a wider and deeper census of these rare − yet extremely valuable − tracers. However, these samples face contamination from blue straggler stars which share similar photometric properties.

In a more advanced approach to identify BHBs photometrically, T18 applied a machine learning technique known as Principal Component Analysis (PCA) to isolate BHBs from blue straggler stars. Their algorithm relied on the comprehensive optical coverage provided by the CFIS u- and PS1 3π $griz$-bands to correctly label the stellar populations of A-type stars. After training the PCA on a sample of SEGUE (Yanny et al. 2009) spectroscopically confirmed BHBs and blue stragglers, the algorithm identified the most significant colour combinations to distinguish these populations.

T18 then developed a function, based on these principle components, to classify each A-type star as either BHB or blue straggler. This analysis was then applied to the full CFIS–PS1 3π catalogue, resulting in a final sample of $\sim$10,200 BHBs. Based on close inspection of the training sample in globular clusters, T18 estimated the rate of contamination in this sample to be below 25%.

Heliocentric distances for these BHBs are then computed using the distance modulus, with absolute magnitudes calibrated from photometric relations provided in

Deason et al. (2011). Typical uncertainties for these distances are estimated to be on the order of ∼10%, and extend to nearly ∼220 kpc in the MW halo.

Though BHBs are a powerful tracer to explore MW substructure, they are an intrinsically rare stellar population. To increase sample density, this dataset is supplemented with the UNIONS "Dwarfs/Giants" catalogue of Thomas et al. (2019).

Red Giant Branch (RGB) Sample

The second tracer population used in this work is a catalogue of red giant branch (RGB) stars from Thomas et al. (2019, hereafter T19). For this dataset, T19 classified ∼12.8 million stars in the the CFIS-PS1 3π footprint as either "dwarf" (main sequence population) or "giants" (primarily RGB) using machine learning techniques. This work again leveraged complete optical coverage of CFIS-PS1 3π in addition to *Gaia* B_P and R_P broadband photometry. Here, the combination of optical filters with the u-band enables estimates for both absolute magnitudes and photometric metallicities.

To derive photometric metallicities and absolute magnitudes, T19 trained a two-step machine learning pipeline on a sample of spectroscopically confirmed dwarfs and giants in SEGUE, where the inputs to the algorithm were each star's CFIS-PS1 3π-*Gaia* photometry. The first stage of the algorithm categorized each star into the "dwarf" or "giant" stellar population using a Random Forest Classifier (RFC), based on the star's colours. The RFC provided a probability of membership to either population where, $P_{dwarf} + P_{giant} = 1$. Then, a set of Artificial Neural Networks (ANNs), trained on the "dwarf" and "giant" populations separately, predicted each star's photometric metallicity ([Fe/H]) and absolute magnitude (M_G) based on these initial categorizations.

Using these methods, T19 report a sample completeness of more than 70% for metal-poor giants ([Fe/H] < -1.2) in the SEGUE training set, with photometric metallicities accurate to ∼0.2 dex. T19 also claim that their derived distances in this catalogue are valid out to ∼80 kpc and achieve typical uncertainties of $\lesssim$25%. While these RGBs do not extend to such large distances as the BHB catalogue, they are a far more numerous tracer population and provide substantial complementary spatial coverage. Furthermore, the photometric metallicity estimates are an added benefit to help discriminate Boo3 members from the more metal-rich foreground.

When applied to the entire cross-matched catalogue, T19 identify nearly 136,000 giants and 11.2 million dwarfs. For this work, I select a subsample of likely gi-

ants ($P_{giant} > 50\%$) and apply additional quality cuts recommended from T19. To remove extended sources (e.g., background galaxies), only point-sources satisfying $|r_{PSF} - r_{ap}| < 0.05$ mag (also recommended in Farrow et al. 2014) are retained. Following T19's recommendation to remove more metal-rich stars that are misclassified in the RFC, the sample is also restricted to only stars with good photometric errors by taking $\delta M_{G,pred} \lesssim 0.5$ mag (where $\delta M_{G,pred}$ includes the photometric and systematic errors of each star, added in quadrature).

The original datasets in T18 and T19 utilized the second data release from *Gaia* (Gaia Collaboration et al. 2018a), and therefore already contain proper motion and parallax information. Though the photometric measurements between data releases does not vary significantly, both a star's parallax and proper motion are greatly enhanced with additional observation epochs such that newer data releases will continue to increase in *Gaia*'s accuracy. For this reason, both the BHB and RGB samples are cross-matched to *Gaia*'s third data release (DR3; Gaia Collaboration et al. 2023). To avoid nearby disk stars (Lindegren et al. 2018) and simultaneously account for *Gaia*'s systematic parallax offset (-0.017 mas; Lindegren et al. 2021b), the following cut to both the BHB and RGB datasets is also applied:

$$\frac{1}{\pi + 0.03}$$

mas > 5

kpc. (3.2)

This restriction ensures all stars with distances of < 5 kpc, or within the Solar neighbourhood, are removed from the dataset.

3.3.4 Matched Filter Searches Using SDSS and DELVE Photometric Catalogues

This work will also rely on data from additional photometric catalogues. These will be used to conduct a matched filter (MF) analysis applied to the area of sky surrounding Boo3. Using the MF method (explained in more detail in Section 3.5.2) is largely to achieve two goals; these are (i) to attempt to replicate results of the initial detection and compare to the observations in this work, and (ii) to independently characterize the dwarf and/or its stream. Furthermore, by applying this analysis to

multiple photometric catalogues, it should be possible better inspect observational artifacts that may have resulted in spurious detections.

The first catalogue we will use is photometry from the Sloan Digital Sky Survey (SDSS). Both Boo3 and Styx were originally discovered in SDSS by Grillmair (2009); here, I revisit the detection by conducting my own MF analysis applied to a later SDSS data release. I also conduct the same MF analysis using the (slightly deeper) DECam Local Volume (DELVE) photometric catalogue. Unfortunately, the UNIONS catalogue cannot be used here, as Boo3 lies outside the main multi-band survey footprint and currently only has u-band coverage. For both catalogues, I queried the respective databases for stars located in a substantial area surrounding Boo3 corresponding to $154° \leq \mathrm{RA} \leq 230°$ and $+7° \leq \mathrm{Dec} \leq +43°$. This region encompasses most of the area included in the original detection, but not entirely. Given that the field becomes overwhelmed by the Sagittarius stream in the West (RA below $\sim$190°), extending this area is not necessary.

Below, I discuss the catalogues used in the MF analysis and what calibrations I applied to these datasets.

SDSS

The Sloan Digital Sky Survey (SDSS; York et al. 2000) is a large-scale astronomical survey that has been continuously operating since first light in 1998. As of 2017, SDSS now achieves dual-hemisphere coverage via two 2.5-meter telescopes – the Sloan Foundation telescope at Apache Point Observatory in New Mexico, and the du Pont telescope at Las Campanas Observatory in Chile – covering the northern and southern celestial spheres, respectively. SDSS employs a unique observational technique in that it images in continuous, narrow (2.5°-wide) "stripes" across the sky. Each stripe imaged by SDSS takes simultaneous observations in all five of its optical filters (*ugriz*) in one continuous pass. This approach guarantees efficient and uniform sky coverage over extensive sky regions, although this results in shallower photometric depths in bluer filters compared to other bands.

For this work, SDSS is used in order to replicate the first detection of the Boo3 and Styx substructures originally identified in Grillmair (2009). I acquired photometric data covering a broad area from the most recent SDSS data release, DR17 (Abdurro'uf et al. 2022), using the `CasJobs` SQL interface. Photometric measurements in the g-, r-, and i-bands and their associated errors were downloaded for wide field of

northern sky from SDSS DR17's `star` catalogue, which comprises high-confidence stellar sources identified internally by SDSS. To ensure good quality photometry, stars were removed that are flagged with poor measurements (magnitude or magnitude error $= -9999.0$). The catalogue is limited further by determining a photometric depth in each filter, and retaining only data whose magnitudes are less than these limits. This is done by determining the median photometric error in each band as a function of magnitude, and interpolating this function to find at what magnitude the median photometric error is equal to a threshold of 0.2 mag. In practice, this means that SDSS' 5-σ depths in gri-bands are 23.2, 22.8, and 22.3 mag, respectively. Finally, these data are corrected for extinction using the extinction coefficients from Schlafly & Finkbeiner (2011) and the `python`-wrapped package `dustmaps` (Green et al. 2024).

DELVE

The DECam Local Volume (DELVE; Drlica-Wagner et al. 2022) survey is an optical photometric catalogue focused on obtaining $griz$-band photometry for sources in the southern hemisphere (declinations below $< 30°$, excluding the Galactic disk). Taken using the 4-meter Blanco Telescope at Cerro Tololo Interamerican Observatory in Chile, this imaging survey aims to uncover newly discovered faint MW satellites and establish their observational properties (e.g., Mau et al. 2020; Martínez-Vázquez et al. 2021; Cerny et al. 2021a,b). DELVE's median 5-σ depth is slightly deeper than SDSS: in gri the limits are are 24.3, 23.9, and 23.5 mag, respectively. Compared to the shallower limits of SDSS (23.2, 22.8, and 22.3 mag), DELVE provides an independent dataset to confirm these structures, as well as to assess artificial/spurious features in the matched filter density maps.

For this analysis, I downloaded a dataset of g- and r-band sources from the second DELVE data release (DR2; Drlica-Wagner et al. 2022). While it would be beneficial for the MF method to also use DELVE's i-band, these observations are not continuous this far north. It is for this reason only the g- and r-band magnitudes from DELVE are utilized. To ensure the dataset consists only of the most reliable stellar sources, I followed several criteria recommended in Drlica-Wagner et al. (2022) for DELVE DR2:

- The total sample is first limited to sources where `extended_class` ≤ 1. This flag indicates the confidence of a source to be a star ($\leq$1) or galaxy (>1), as identified using `SourceExtractor`.

- Stars with poor photometric measurements are removed by limiting the sample to those with `mag_PSF` < 99 and `magerr_PSF` < 99. This flag indicates sources with poor photometry (and uncharacterized photometric errors) according to the DELVE collaboration.

- The catalogue is then limited by my own estimates for the photometric depths in each band. Given the 5-σ depths we calculate, DELVE's g- and r-bands are limited to 24.0 and 23.3 mag, respectively.

Finally, the DELVE g- and r-band observations are corrected for reddening using the extinction coefficients in Abbott et al. (2018) and the `dustmaps` package. These processed data now provide a catalogue of robust, extinction-corrected (g_0 and r_0) stellar sources suitable for further photometric analysis.

3.4 Analysis of the Main Body of Boötes 3

3.4.1 Calibrating Photometric Metallicities

To establish a relationship between a star's temperature, brightness in CaHK, and its metallicity, Starkenburg et al. (2017) first studied the distribution of a model population of stars (using the Besançon MW statistical model; Robin et al. 2003) in colour-colour space using a narrow-band colour, $(\mathrm{CaHK} - g) - 1.5(g - i)$ on the y-axis, versus a broad-band colour, $(g - i)$ on the x-axis. Magnitudes for this representative sample were derived from a grid of synthetic stellar spectra that covered a range of stellar parameters including surface gravity ($\log(g)$), effective temperature (T_{eff}), and metallicity ([Fe/H]). The top panels of Figure 3.8 illustrate this calibration process to obtain photometric metallicities from the SDSS-CaHK colour-colour plane. The right panel shows the simulated halo population (black points) while the overlain grey boxes indicate *Pristine*'s spectral grid where the synthetic magnitudes are derived. The right panel presents the *Pristine* colour-colour plane, highlighting the efficient separation of more metal-poor (bluer icons) to more metal-rich (redder icons) stars. Trend lines in this figure represent the calibration curves derived by Starkenburg et al. (2017) to estimate photometric metallicities. As clearly shown in the bottom panel, these calibration curves demonstrate excellent agreement to observation when compared to a spectroscopic sample of stars in SDSS/SEGUE, particularly for more metal-poor stars. By positioning observed stars within this

empirically-calibrated framework, this method is efficient at calibrating photometric metallicities, especially for large datasets.

The broad-band filters utilized in this first work relied on those of SDSS (in particular, g- and i-band), though *Pristine*'s more recent work is now optimized to use *Gaia* magnitudes (Martin et al. 2024). Here, I derive photometric metallicities from CaHK magnitudes using the newest version of the *Pristine* pipeline and *Gaia* broad-band magnitudes. The general approach of this pipeline is summarized below.

In *Pristine*'s newest generation of photometric metallicity calibration, Martin et al. (2024) estimate photometric metallicities from *Gaia*'s low-resolution BP/RP spectro-photometry (DR3; Gaia Collaboration et al. 2023) to leverage the satellite's all-sky coverage. This work relies on *Gaia*'s blue prism (BP) spectra, which includes the Calcium H&K absorption region, allowing the derivation of synthetic CaHK magnitudes. To then estimate photometric metallicities using *Gaia*, Martin et al. (2024) generally follow the same implementation as Starkenburg et al. (2017) by first generating a grid of synthetic stellar spectra from which both broad-band (*Gaia* G, B_P, R_P) and narrow-band (CaHK) magnitudes are computed. The algorithm is calibrated to real data, specifically spectroscopic samples from SEGUE and APOGEE. The model then derives the *Pristine* colour-colour plane empirically from these data by plotting them and segmenting the plane into a grid. Each cell of the grid is then assigned a metallicity mean [Fe/H] of the stars within it. The mapped space is then smoothed, and from it, the algorithm can now link a star's location in colour-colour space to its photometric metallicity.

An important step of this calibration is the correction for extinction, which requires a more sophisticated approach when using *Gaia* magnitudes. For these broader passbands, the extinction of a star in a given filter (A_f) not only varies with the star's position on the sky, but also as a function of its underlying properties (temperature, $\log(g)$, and metallicity). Martin et al. (2024) address this issue by deriving the extinction iteratively within the algorithm. Using the synthetic *Gaia* magnitudes from their stellar spectral grid, the authors first establish the relationship between the extinction coefficients (k_f, where $A_f = R_f \times \mathrm{E}_{(B-V)}$ and R_f is a function of k_f) depending on a star's effective temperature (T_{eff}) and metallicity ([Fe/H]) in the *Gaia* magnitudes. To determine the extinction of an individual star where both T_{eff} and [Fe/H] are determined by A_f, the pipeline first calibrates A_f provided (i) the star's reddening ($\mathrm{E}_{(B-V)}$) from Schlegel et al. (1998) dust maps, and (ii) T_{eff} from observed ($\mathrm{B}_P - \mathrm{R}_P$) colours. The algorithm provides a first guess for the photometric metallicity, and

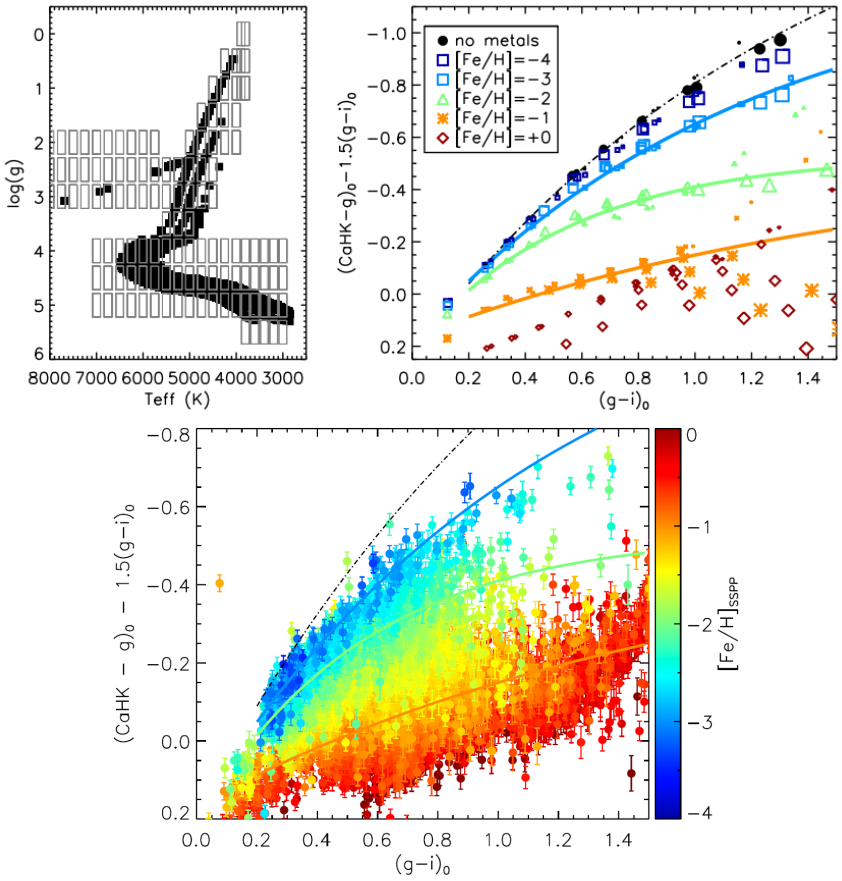

Figure 3.8: All panels are replicated from Starkenburg et al. (2017). **Top left**: Surface gravity log(g) vs effective temperature for simulated halo stars (black) overlain with the spectral synthesis grid (grey boxes) used in Starkenburg et al. (2017). All simulated stars are matched to the most representative spectra from the grid, and ascribed SDSS colours accordingly. **Top right**: Pristine calibration to obtain photometric metallicity estimates using their polynomial fits in colour-colour space, applied to the synthetic stellar populations in the left panel. Coloured lines are the polynomial fits used to relate the star's colour-colour magnitudes to photometric metallicities. Relative sizes of icons (colour-coded by actual metallicity) highlight the inverse log(g) of different stellar populations: smaller icons represent main sequence stars, and larger represent RGB. **Bottom**: Colour-colour space of (actual) stars observed in SDSS/SEGUE and CaHK magnitudes. As shown in the colour-coded metallicities from SDSS, the CaHK metallicity functions have excellent consistency to observations, and are an effective method to remove the more metal-rich foreground population.

the process is repeated with the updated [Fe/H] estimate. This process is repeated iteratively until the values converge.

The final parameters provided from the algorithm are then k_f, T_{eff}, and $[Fe/H]_{phot}$ for each star. Uncertainties for the photometric metallicity are determined through a Monte Carlo (MC) simulation, where 100 samples are drawn from each star's photometric uncertainties. The final photometric metallicity is then reported as the median of this estimate, with errors corresponding to the 16^{th} and 84^{th} percentiles of the probability density function.

To calibrate the photometric metallicities for the Boo3 observations using the updated *Pristine* pipeline, the CaHK photometry are first cross-matched to broad-band magnitudes from *Gaia* DR3. Specifically because the resulting dataset is identical to the sample from Jensen et al. (2024), differing only in that it is over a smaller area of sky, I chose to cross-match to the Jensen et al. (2024) catalogue for Boo3 in order to include membership probabilities. Initially, this dataset includes CaHK-derived metallicities for 13,258 stars across all six observed fields.

To retain only the most reliable of these data, several quality cuts recommended by Martin et al. (2024) are then applied. Stars with metallicities at the edges of the synthetic grid are removed first so that only those within $-4.0 < [Fe/H] \leq 0.0$ are retained. Additionally, the sample is limited to stars whose MC sampled photometry remains largely within the colour-colour space of the metallicity model (`mcfrac_Pristine` ≥ 0.8). Following *Gaia* quality criteria, the sample is further restricted to sources with reliable astrometric and photometric measurements, specifically requiring `ruwe` < 1.4 (or flagged by `F_BEST` $= 1$ as done in Jensen et al. 2024). These criteria yield a final sample of 2,040 stars.

3.4.2 Comparison of Jensen et al. (2024) Members

Given that the previous estimate of Boo3's metallicity dispersion is particularly wide for a dwarf galaxy ([Fe/H] $= -2.1$ and $\sigma_{[Fe/H]} = 0.6$; Carlin et al. 2009), selecting a sample of Boo3 stars based solely on a range of photometric metallicities was found to be insufficient to effectively discriminate dwarf galaxy membership. Out of the current sample, there are 661 stars whose metallicities are contained with in 1-σ of Boo3's range (-2.7 to -1.5 dex). Therefore, I incorporated an additional membership criterion ($P_{max} \geq 0.2$) from Jensen et al. (2024), narrowing the sample to 39 stars consistent with membership to Boo3. The final sample of Boo3 stars with

CaHK-derived photometric metallicities are indicated with cyan open circles in Figure 3.9. For comparison, all cross-matched *Gaia* stars in the 6 observed fields appear in grey, while stars specifically from Jensen et al. (2024) with consistent membership probabilities are indicated in black. Also indicated as green plus (+) icons are spectroscopic members identified in Carlin et al. (2009), cross-matched to the Jensen et al. (2024) *Gaia* catalogue.

The differences between the Jensen et al. (2024) Boo3 data (black) and the photometric metallicity sample (cyan) in Figure 3.9 arise due to three factors. As shown clearly in the rightmost panel, the metallicity sample from this work are strictly limited to the RGB, but are also very sparsely populated at faint magnitudes. This first difference is due solely to the *Pristine* CaHK magnitude calibration. CaH&K absorption lines are inherently weaker in bluer stars due to the temperatures at which calcium becomes ionized, and so consequently, the *Pristine* pipeline only derives photometric metallicities for stars between $0.5 < (\mathrm{B}_P - \mathrm{R}_P)_0 < 1.5$. This limitation therefore excludes the entirety of the horizontal branch from the CaHK photometric metallicity sample. Regarding the sparse sampling of stars at $G > 20$ mag, these stars are excluded due to the recommended limit on `mcfrac_Pristine`, indicating these stars all have photometric MC samples that are located outside the colour-colour space grid. The third difference between the samples is the presence of a bright RGB star in Jensen et al. (2024) but not in our CaHK data (indicated as the only black RGB with no surrounding cyan icon). This star was excluded from the calibration pipeline due to its location precisely on a CCD chip gap in the MegaCam imager during observations, and so, there is no CaHK observations of this particularly RGB.

Previous spectroscopic observations of Boo3 by Carlin et al. (2009) yielded metallicities and radial velocities for 193 stars in the vicinity of the dwarf, with 20 stars flagged as members based on similar radial velocities. After cross-matching with *Gaia*, 16 of these remain and are marked as green + icons in Figure 3.9. However, two of these stars have membership probabilities inconsistent with Boo3 due to discrepant proper motions (visible as outliers in the central panel), and an additional seven HB stars are excluded due to the aforementioned colour limitations for the *Pristine* algorithm. This leaves only seven spectroscopic RGB members for direct comparison to the *Pristine* photometric metallicities.

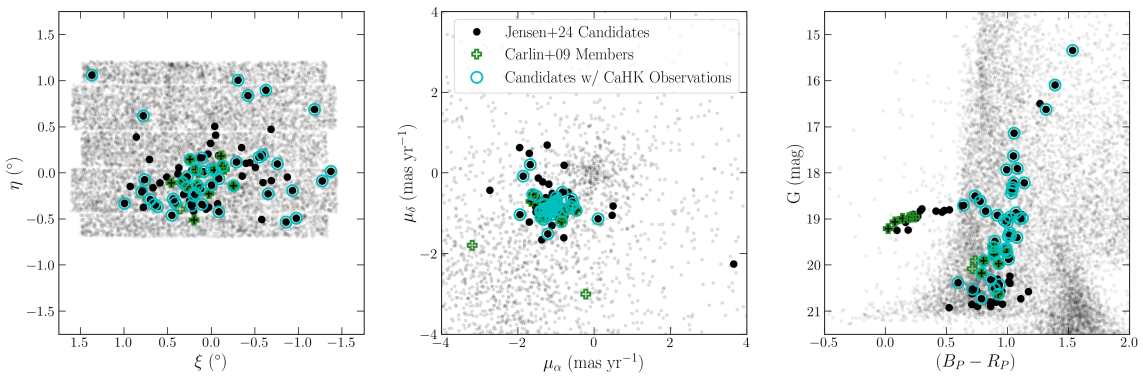

Figure 3.9: Tangent position centred on Boötes 3 (left), proper motions (centre), and CMD (right) of stars from the observing runs. Black points in this figure indicate the *Gaia* candidate members (as in Figure 3.3), but only those within the same region of sky as the targeted fields. Cyan circles highlight the *Gaia* candidate members with new CaHK observations. For comparison, the Carlin et al. (2009) spectroscopic members are also plotted as green plus (+) icons. The remaining foreground observations are represented in grey.

3.4.3 Boötes 3's Metallicity Distribution Function

Given the broad metallicity range and lack of recent spectroscopic follow-up for Boo3, I independently estimated the dwarf's mean metallicity ([Fe/H], or $\langle x_{\rm Fe/H} \rangle$) and metallicity dispersion ($\sigma_{\rm Fe/H}$) from the photometric metallicity sample, which is $\sim$2$\times$ larger than the original spectroscopic dataset. Adopting an approach similar to Walker et al. (2006), Maximum Likelihood Estimation in a Markov Chain Monte Carlo (Hastings 1970; MCMC) framework is used to derive the best-fit parameters provided the observations and their associated errors. The log-likelihood function to be maximized is defined as:

$$\ln(\mathcal{L}) = -\frac{1}{2}\sum_{i=1}^{N}\ln(\sigma_i^2 + \sigma_{Fe/H}^2) - \frac{1}{2}\sum_{i=1}^{N}\frac{(x_i - \langle x_{Fe/H}\rangle)^2}{\sigma_i^2 + \sigma_{Fe/H}^2} - \frac{N}{2}\ln(2\pi) \tag{3.3}$$

where x_i and σ_i represent each star's observed photometric metallicity and uncertainty, respectively. The MCMC then solves for the combination of $\langle x_{\rm Fe/H} \rangle$ and $\sigma_{\rm [Fe/H]}$ that maximizes the log-likelihood function above, using the `emcee` (Foreman-Mackey et al. 2013) `python` package. The only priors placed on the posterior distributions are that the metallicity must only range from $-4.0 < \langle x_{\rm Fe/H} \rangle \leq 0.0$ and the dispersion must be greater than 0 dex.

The resulting posterior distribution functions (PDFs) are presented in the top panel of Figure 3.10. For the mean metallicity and dispersion of the system, the MCMC estimates $\langle {\rm Fe/H} \rangle = -2.1 \pm 0.1$ and $\sigma_{\rm Fe/H} = 0.2 \pm 0.1$, respectively.

From this analysis, there is indeed agreement between the mean metallicity derived from the CaHK-derived sample and previous spectroscopic measurements. However, the newly derived dispersion is significantly smaller – approximately three times lower than reported by Carlin et al. (2009). In direct comparison with the subset of seven spectroscopically confirmed RGBs from Carlin et al. (2009), I find broad consistency between metallicity estimates within 1-σ, though it should be noted that the errors on the photometric metallicities are substantially larger than the spectroscopic sample. The inflated uncertainties for these stars arise due to their faint magnitudes ($G > 19.5$ mag) and inherently larger photometric errors, which propagates to the CaHK-derived metallicities. Nevertheless, many of the CaHK sample have much smaller errors overall and furthermore are robust members due to their derived probabilities from Jensen et al. (2024).

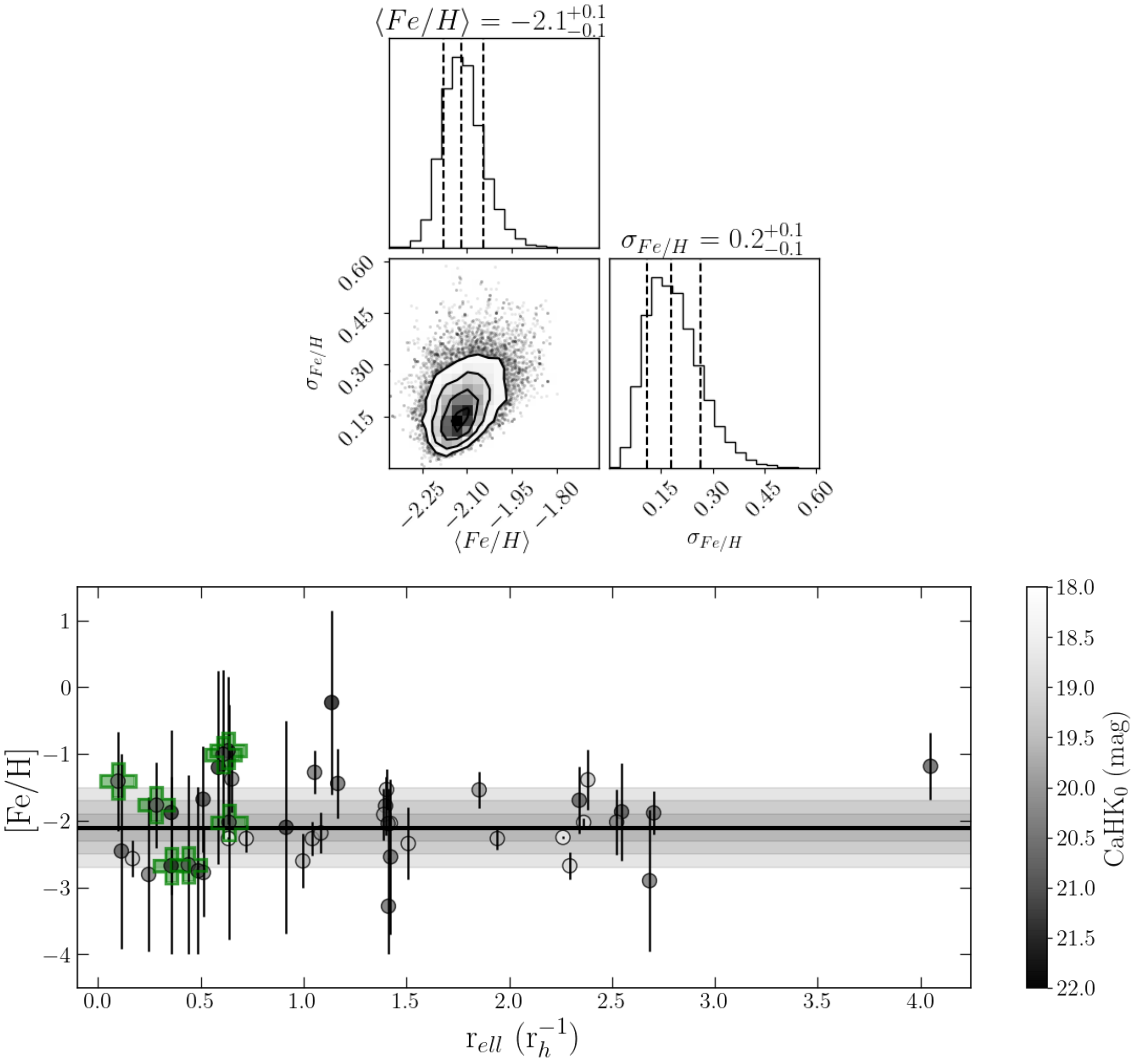

Figure 3.10: Photometric metallicities and errors for stars that are candidate members of Boötes 3 (probabilities $> 20\%$) as a function of elliptical half-light radius (r_h). Each star is shaded corresponding to its CaHK magnitude, and previous spectroscopic members of Boo3 from Carlin et al. (2009) are indicated as green + icons. To showcase the spread in metallicity of these observations compared to our MCMC estimates for the dwarf, Boo3's mean metallicity ([Fe/H]) estimate is also shown here as the black horizontal line, as well as the ranges indicated by 1×, 2×, and 3× the MCMC's estimate for the metallicity dispersion ($\sigma_{[Fe/H]}$) shaded in the grey bands. Note that these new estimates for $\sigma_{[Fe/H]}$ are only 0.2 dex and rely on photometric metallicities of 39 total stars, while the previously reported estimate of 0.6 dex relied on only 20 (Carlin et al. 2009).

The bottom panel of Figure 3.10 illustrates these findings, displaying CaHK-derived photometric metallicities as a function of elliptical half-light radius. The black horizontal line indicates the mean metallicity derived via the MCMC analysis, with grey shaded regions indicating 1×, 2×, and 3× the dispersion. The CaHK dataset significantly expands the available metallicity information, reaching distances up to $4r_h$. The estimate for the metallicity and dispersion appear to be robust and reliable for subsequent analyses. In the next section, I leverage this updated information (specifically $\sigma_{[Fe/H]}$) to investigate the stellar tracer catalogues for Boo3 debris where the updated metallicity dispersion will provide better constraints on the selection of RGB candidates.

3.5 Pushing Out to Large Radius: Searching for Boötes 3's Stellar Debris

The goal of this section is to utilize various observational catalogues to search for stellar debris associated with Boo3. Section 3.5.1 first discusses the methods and results in probing the BHB and RGB datasets for stream candidate members. Section 3.5.2 follows with a presentation of the matched filter method (replicated from Grillmair 2009) where I explore a much larger area of sky for evidence of a stream-like structure using the SDSS and DELVE photometric catalogues.

3.5.1 Kinematic Detection Method for Stream Identification

This section discusses the first search for extended debris of Boo3 using the BHB and RGB stellar tracer catalogues discussed in Section 3.3.3. To identify putative substructure of the dwarf, I first took a subsample of giants whose properties are broadly consistent to that of the progenitor, and then probed this data for kinematic signatures identified as a continuous trend across the sky. Trends in proper motions (and distances) are a useful indicator of a shared dynamical origin and may uncover hidden substructures such as a coherent stellar stream. For this analysis, I utilized the same sigma-clipping routine from Jensen et al. (2021) to identify candidate stream stars. The benefit of this method over selecting stars by eye is that the detection remains independent of prior knowledge, such as Boo3's orbit or the reported location of Styx in Grillmair (2009), which may unintentionally bias the detection.

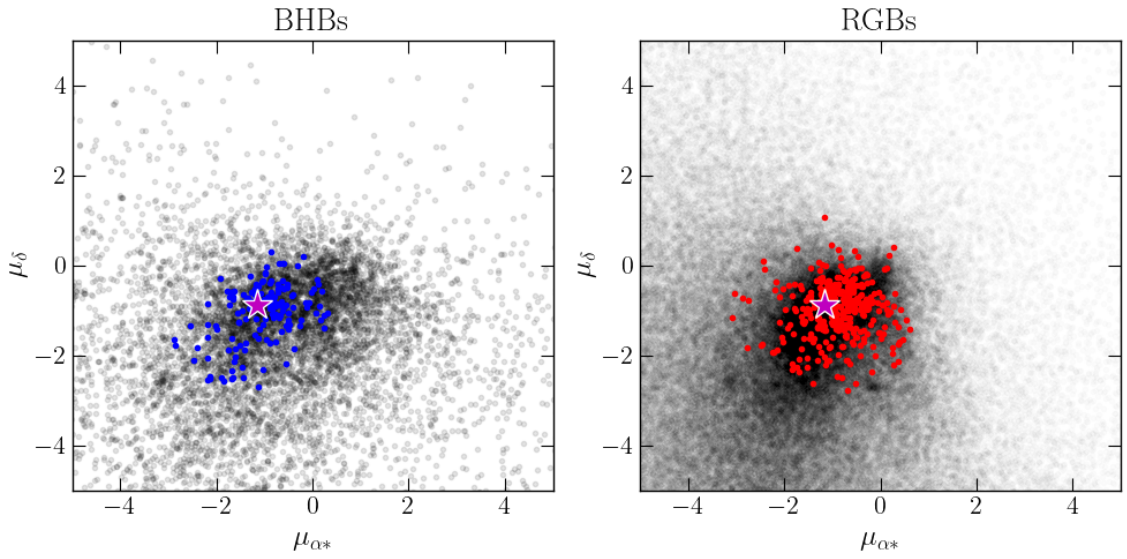

Figure 3.11: Proper motion space of the T18 (left panel) and T19 (right panel) catalogues represented as grey points. The data from these catalogues that are retained for the sigma-clipping routine are indicated by their respective colours (blue for the BHB sample and red for the RGBs). The systemic motion of Boo3 is indicated as the magenta star icon.

To first isolate stars consistent with being members of Boo3, the following restrictions are applied uniformly to the BHB and RGB catalogues. The data are first spatially limited to a region of sky between $200° \leq \text{RA} \leq 220°$ and $+18° \leq \text{Dec} \leq +35°$. This boxed area mainly serves to ensure the coverage between the catalogues is approximately continuous (see the area in Figure 3.7 surrounding Boo3), while also encompassing a large enough area around the dwarf to detect any lengthy substructure. Data from this set are excluded if their proper motions significantly vary from Boo3, by only keeping stars whose PMs are within a radius of 2 mas yr^{-1} to that of the dwarf. This measure serves to remove many MW disk stars that are inconsistent with membership based on their kinematics, as shown in Figure 3.11. The last shared restriction is that the data are limited to only stars with heliocentric distances between 35 and 80 kpc. This range would allow for hypothetical debris at or near the distance of Boo3 to be retained, while also being inclusive of a putative stream with a potential distance gradient.

The RGB catalogue includes an additional parameter than that of the BHBs, which are photometric metallicities. For this dataset, the RGBs are also limited to a range of metallicities consistent to Boo3 using the updated metallicity dispersion from Section 3.4. The final sample is restricted to $-2.3 < [\text{Fe/H}]_{phot} < -1.9$ dex, corresponding to the mean metallicity of Boo3 ± 1-$\sigma_{Fe/H}$.

The next stage of this analysis is to apply the sigma-clipping routine from Jensen et al. (2021) to isolate a subset of stars whose kinematics and positions are consistent with Boo3 debris. If a coherent structure is present in the data, this procedure should yield a sample of extended Boo3 stars indicative of a stellar stream. The steps of the routine are as follows:

(i) The first step of the algorithm is to plot the proper motion in RA ($\mu_{\alpha*}$) versus RA (α) for the dataset. A simple linear fit is applied to the data, where the weights of this fit are the errors in each star's proper motion in RA;

(ii) Next, the routine identifies all stars in the subsample whose $\mu_{\alpha*}$ measurements are 3-σ within this fitted line. A new linear fit is then generated to this smaller subsample;

(iii) The one-degree polynomial fit from the previous step is then compared again to the total dataset of stars we initially put into the algorithm. The routine then retains a new subsample of stars whose $\mu_{\alpha*}$ are consistent with this new fit (within 3-σ);

(iv) Step (iii) is repeated until convergence, such that the generated fit and sample of stars retained no longer vary;

(v) For the subsample of stars that survive the sigma-clipping in $\mu_{\alpha*}$ vs α, the process is repeated but now using the proper motion in Declination (μ_δ) vs α[1].

Applying this method to the sample relies heavily on each star's proper motions and their errors. Given that the distances of this data are intentionally chosen to be rather large ($35 - 80$ kpc), the sample's proper motion errors overall tend to also be large (e.g., nearly 20% of the sample have have errors >100%). When the routine was initially ran, the fits were dominated by the stars with the closest distances due to their generally lower errors in proper motions. This is evidenced by two factors in the weighted trendlines: (i) the direction of the trends were in complete opposition (i.e., perpendicular) to what direction would be anticipated given the proper motions of Boo3, and (ii) the fit did not pass through the position of Boo3 in (α, μ_α). In order to ensure that the trendlines indeed remain consistent to that of Boo3 in the presence of substantial foreground contamination and high proper motion errors, the fit is stabilized by generating 10,000 MC sampled "stars" to represent the dwarf. Thee positions of stars are randomly sampled within $3r_h$ and are provided with proper motions sampled under the 1-σ uncertainties of Boo3 (see Table 3.1). These mock stars are appended to the BHB + RGB sub-sample prior to running the routine, which serves to anchor the fit based on observations of Boo3.

The subsample of RGBs and BHBs totals 166 sources, and after the sigma-clipping routine, it is limited to 103 stars across the $\sim 20^\circ \times \sim 20^\circ$ field. Figure 3.12 presents the positions and kinematics of the subsample (coloured red and blue in the left panels; represented as grey squares in the right) prior to applying the routine, while green data in the right panels indicate the remaining sample.

Encouragingly, there is an apparent grouping of stars coinciding with the position of Boo3 in the upper right panel of Figure 3.12 that survive the sigma-clipping routine. These, upon further inspection, all have consistent proper motions and distances to that of Boo3 and are very likely *bona fide* members as they are located within $5r_h$. However, the other stars surviving the sigma-clipping routine appear to have a nearly isotropic spatial distribution, which does not appear to favour a coherent

[1]Previously in Jensen et al. (2021), I conducted this second sigma-clipping routine in μ_δ vs Declination (δ). However, Boo3's orbit in μ_δ vs δ is more complex than can be described with a simple linear fit. For this reason, I opted to change the x-axis to α for the second round of sigma-clipping.

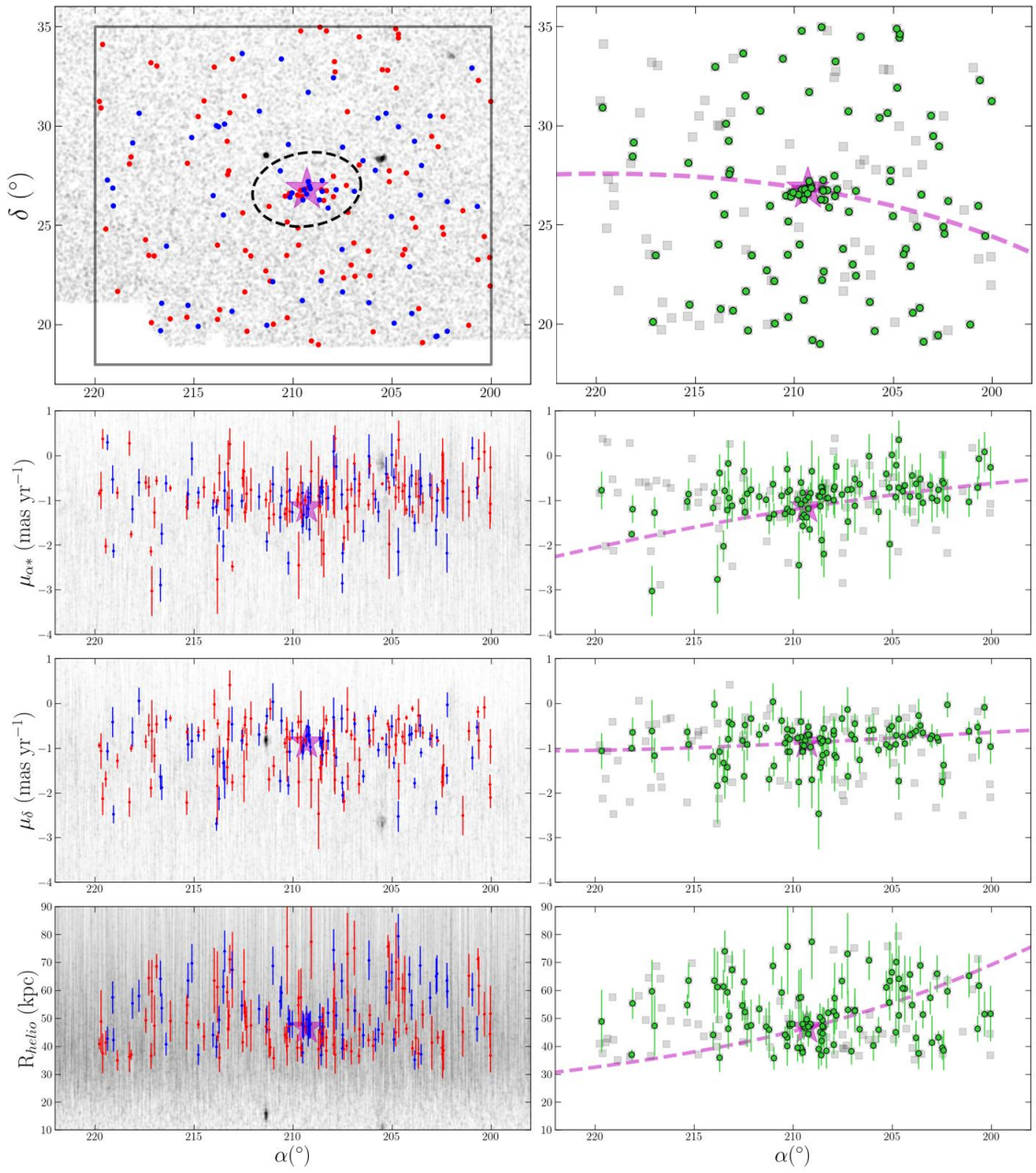

Figure 3.12: Equatorial positions, proper motions, and heliocentric distances of the BHB + RGB sample. The left panels show the subset of data used in the routine (BHBs in blue, RGBs in red) compared to the total catalogues in grey. The right panels showcase the sample surviving the routine in green points against the original BHB + RGB subsample (now presented as grey squares). Though it is not used as part of the selection, the expected orbit of Boo3 is also plotted here in the magenta dashed tracks on the sky (in proper motions and distances) for direct comparison to the data. Boo3's parameters are indicated as the magenta star.

and lengthy stream. The proper motion panels of Figure 3.12 show that, while these surviving stars indeed are approximately within to 3-σ to the orbit (shown as the dashed pink lines), many stars in this sample survive the routine due to their large proper motion errors. The bottom panel of this figure further indicates this, as a substantial number of surviving stars are inconsistent with the heliocentric distances predicted by the orbit. Note that distances were excluded from the sigma-clipping routine; as such, they can be used as a sanity check to confirm the presence of an underlying substructure in the remaining data.

To clean the sample of potential outliers, and determine whether these remaining stars are actually consistent with membership to Boo3, I conducted a brief sanity check. For every star surviving the sigma-clipping routine, its true tangential motion is calculated and plotted as a vector to indicate its motion on the sky. Note that the true tangential motion is essentially the star's proper motion vector, corrected for solar-reflex motion (which relies on each star's proper motion and photometric distance). If the star's vector appears to be moving in the same direction as the satellite, and its distance is also consistent to that of the orbit at that location on the sky, then it may be considered a star originating from Boo3.

Figure 3.13 shows the on-sky positions and corrected proper motion vectors (multiplied by a factor of 2 for better visibility) of the remaining stars in the sample. Boo3's solar-corrected proper motion vector is also highlighted in magenta, centred on the position of the dwarf and scaled by $\times 10$. As shown in the figure, very few stars outside of $5r_h$ (black dashed ellipse) have motions consistent to that of Boo3's orbit. These are a small collection of three or so stars at approximately at (RA, Dec) = (216°, 29°). Upon further inspection however, the distances to these stars are substantially different than the distances predicted by the orbit, and so these are not likely stellar debris of Boo3.

3.5.2 Matched Filter Analysis

This section details the continued search for a stream in the vicinity of Boo3 using the same matched filter (MF) technique described in Grillmair (2009). This method, which is optimized to search for substructures over large areas of sky, ultimately constructs a map where stellar streams and satellites can be identified by eye. MW substructures appear as over-dense regions of the map, where the density of these objects are higher than the background. Matched filters have shown success in many

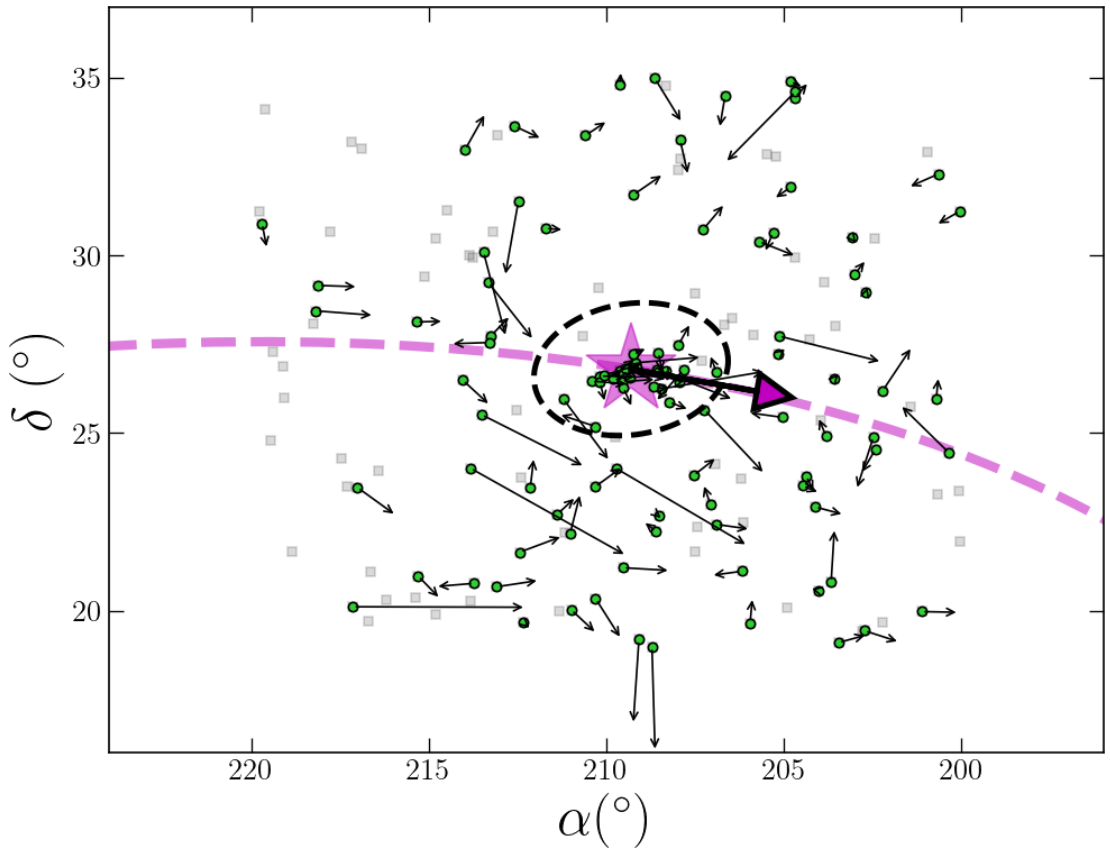

Figure 3.13: On-sky positions of the BHB + RGB sub-sample (grey squares) compared to the sample remaining after the sigma-clipping routine (green). Vectors on these data represent the solar-corrected proper motions. As noted in the text, stars stripped from Boo3 should have similar proper motions to that of the dwarf (magenta arrow), yet only a small fraction of stars moving in the same direction are found.

works to detect numerous MW stellar streams (e.g., Belokurov et al. 2006; Shipp et al. 2018; Ferguson & Shipp 2025) including the work conducted in Grillmair (2009). Applied here, I attempt to replicate the results in Grillmair (2009) in SDSS to re-examine the detection of Styx and Boo3. Subsequently, I also apply the MF to the (slightly deeper) DELVE catalogue to test the robustness of the Grillmair (2009) detection. Using both photometric surveys with the same detection method provides a sanity check that any faint or ambiguous features identified the MF maps are not spurious detections or due to observational artifacts.

This section briefly summarizes the similarities in method used in Grillmair (2009) and this present work. Essentially, the MF constructs a weighted density map in which each star is assigned a likelihood of membership to an assumed stellar population (in this case, representative of Boo3 itself), according to its consistency in colour and magnitude. The map is then smoothed to remove small-scale fluctuations, and later enhanced by subtracting a modelled background density. This method successfully improves the detection of satellites and streams by increasing the contrast between underlying structures and the MW foreground.

In this current implementation, the weights to each star are calculated from a likelihood function that is modelled after both the satellite and a background CMD. These functions describe a star's likelihood of association to Boo3 or the MW foreground based on its colour and magnitude. I choose to represent these functions as "lookup maps" – similar to the method described in McConnachie & Venn (2020b) and Jensen et al. (2024) – wherein one can simply "look up" an individual star's likelihood by locating its colour and magnitude on this map. Each pixel in this map is 0.025 mag wide in colour and magnitude.

The satellite CMD map is modelled after an old (12 Gyr) Padova isochrone (Girardi et al. 2002, converted to *Gaia* magnitudes using the corrections from Weiler 2018) assuming a metallicity of [Fe/H] $= -2.1$. The likelihood of membership on the CMD is derived from a Gaussian PDF, whose mean is centred on the isochrone and whose width extends in colour for a given bin in g. The width and amplitude of this Gaussian accounts for (i) the uncertainties of Boo3's distance modulus, (ii) photometric errors as a function of magnitude, and (iii) the relative number of expected stars in a given population along the isochrone. To accomplish this, a random sample is taken of Boo3's distance modulus within 1-σ (see Table 3.1) and shifted the isochrone to this magnitude. The distribution of stars anticipated per evolutionary phase is accounted for by providing weights to the amplitudes, according to a Kroupa

initial mass function (Kroupa 2001). The σ of the Gaussian PDFs are essentially the photometric errors as a function of g added in quadrature to a fixed intrinsic width of the RGB in colour (0.1 mag). For 1,000 individual Monte Carlo samples of the distance modulus, this process is repeated in order to create a series of 1,000 likelihood maps. These maps are then summed together and normed such that the final CMD satellite map integrates to unity.

In contrast, the foreground CMD likelihood map is constructed entirely empirically. To develop this lookup map, a region of sky that distant to Boo3 and does not contain large-scale known substructure (e.g., the Sagittarius stream) is taken as data that represents the background. This region is indicated as $214° \leq \mathrm{RA} \leq 225°$ and $+7° \leq \mathrm{Dec} \leq +16°$. The colours and magnitudes of stars within this region are then binned into a similar CMD pixel grid as the satellite CMD likelihood map. A bivariate Gaussian kernel is applied to the likelihood map in order to account for individual photometric uncertainties. The final background CMD likelihood map is then similarly normed such that it integrates to unity.

Finally, the total CMD likelihood map (i.e., the MF template) is constructed by dividing the satellite CMD map by that of the background. Figure 3.14 shows examples of these lookup maps, where the rightmost panel indicates the total CMD likelihood map used in this work.

To create the matched filter density map, the weighted counts are computed by looking up each star's likelihood in the MF template and summing the total counts per 0.1° pixel in tangent plane coordinates. For both surveys, the matched filter map is created using g vs $(g-r)$ colour-magnitudes. The MF map using SDSS additionally benefits from continuous coverage of the i-band, and so a second matched filter map is made using g vs $(g-i)$. As conducted in Grillmair (2009), these two maps are summed together to make the final image. This is only conducted for the SDSS map as the current survey footprint in DELVE lacks uniform i-band coverage this far north. Each band of each catalogue is limited in magnitude by the 5-σ point source depths discussed in Section 3.3.4. In creating the MF maps, both the SDSS and DELVE maps appeared largely the same in using their respective magnitude limits. To enhance the contrast of the MF maps, a final broad limit of $15 \leq g \leq 22.5$ mag is taken for both maps. Note that this final step was also applied in Grillmair (2009).

Smaller-scale density fluctuations are removed by smoothing the image with a Gaussian kernel of 0.2°. As a final step to enhance contrast, a background density map modelled after a 5^{th}-degree polynomial surface (after masking known globular

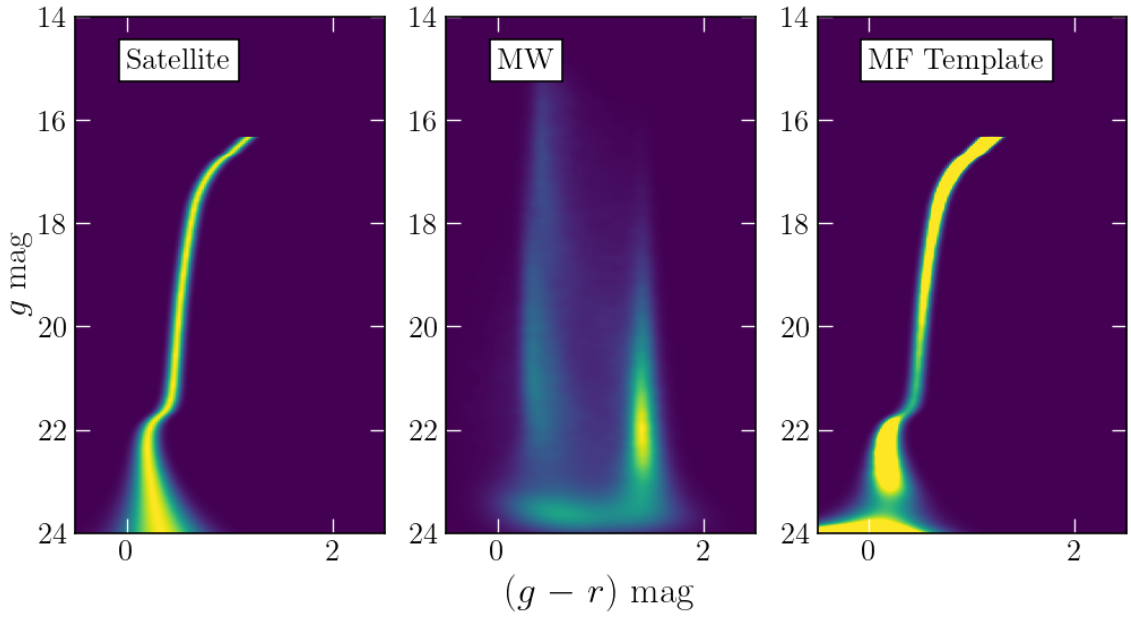

Figure 3.14: Example of the CMD "lookup maps" used to estimate a star's likelihood of association to Boo3. The final likelihood function in the rightmost panel represents the matched filter template used to create the density map.

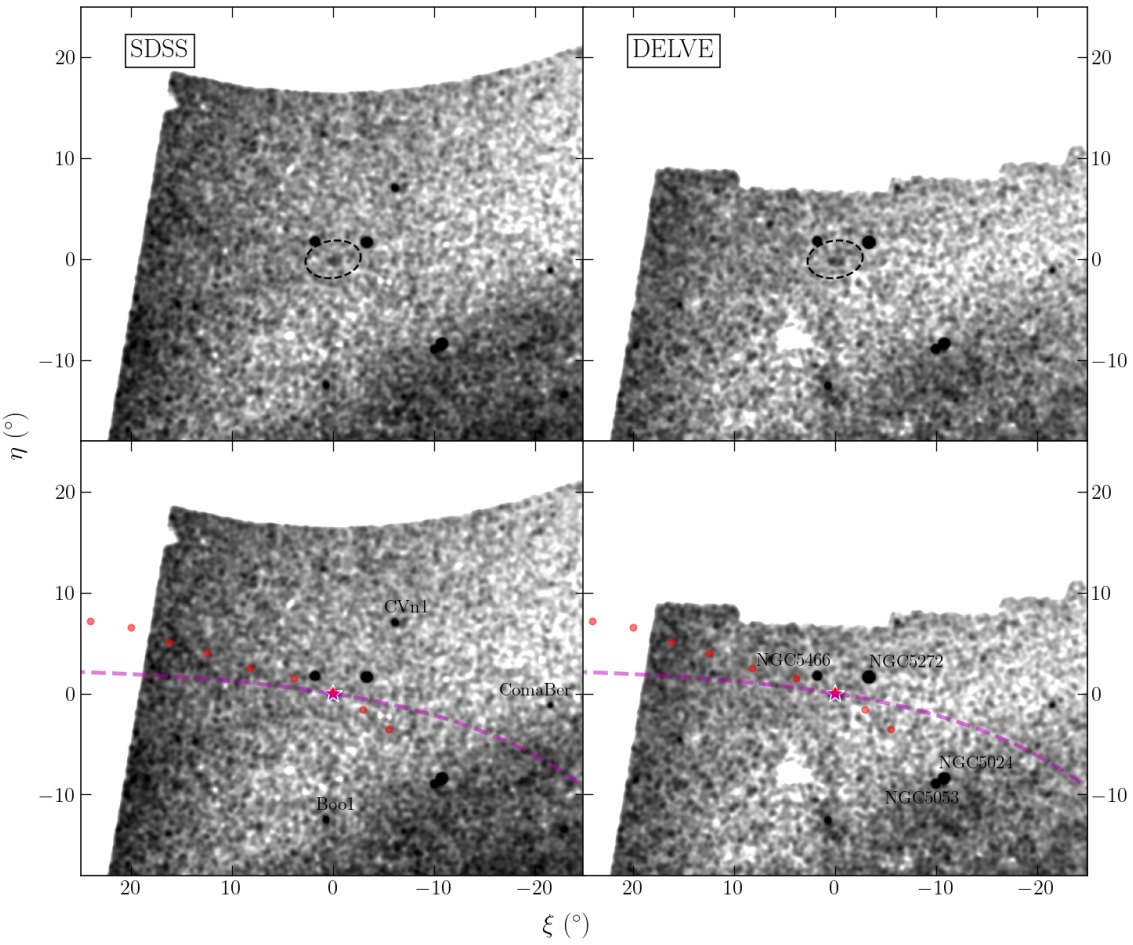

Figure 3.15: Tangent plane projections of the matched filter maps produced using SDSS (left panels) and DELVE (right panels). The top and bottom panels are the same maps, with added annotations. Boo3, located at (0, 0), is highlighted with the magenta star. To indicate the differences between Boo3's trajectory and the approximate location of Styx, both the expected orbit of Boo3 (magenta dashed line) and a range of nodes along the position of Styx (red points) are plotted for comparison. Note that these nodes, originally in SDSS survey coordinates, have been converted to equatorial coordinates and then into the tangent plane projection. For a distance comparison, the black dashed ellipse indicates $5r_h$ in the top panels. Known satellites (dwarf galaxies and globular clusters) observable in these maps are also annotated.

clusters and dwarf galaxies) is also subtracted. The final matched filter maps for both SDSS (left) and DELVE (right) in a tangent plane projection are presented in Figure 3.15.

As shown in all panels of Figure 3.15, all previously reported globular clusters and dwarf galaxies within the field are recovered (labelled in the bottom right and left panels, respectively). This includes the faint and diffuse Boo3 dwarf centred at the origin. As expected, the matched filter maps indeed look very similar between SDSS and DELVE, with some minor differences in sky coverage and overall footprint. As an aside, it should be noted that the maps also include the Sagittarius stream (shown as the overdensity in the bottom right of each panel) though these zoomed-in panels do not highlight it sufficiently. A better view of the entire field, including the Sagittarius stream, is provided in Figure A.1 in the appendix for both catalogues.

Though Boo3 is observed in both catalogues, there is not sufficient evidence for extended tidal tails emerging from the dwarf. In the SDSS panel, there appears to be a small streak to the upper right of Boo3 within $5r_h$ (indicated by the black dashed ellipse in the top panel). However, this feature is not observed in the accompanying DELVE map, and furthermore is perpendicular to the orbit trajectory and putative path of Styx (discussed further in Section 3.6). It is likely that this feature is an artifact of the SDSS observing strategy, which surveys the sky in striping patterns along great circles. This argument is further demonstrated in Figure A.2 in the Appendix A, where stars down to magnitudes of $g = 24$ are plotted with the matched filter technique. Given the streak around Boo3 in both the absolute density (left) and the MF (right), it appears that the small-scale fluctuations produced by the observation patterns may in fact grow in size and sum together once smoothed by the Gaussian kernel.

As a final sanity check, the reported location of Styx (as identified in the original detection) is also plotted in the bottom panels of Figure 3.15 as a series of red nodes. These represent the approximate locations of Styx in SDSS survey coordinates $(\lambda, \eta)_{SDSS}$. To plot their location in the tangent plane, I first identified a series of nodes on the original MF map from Grillmair (2009), where each node is roughly centred on the position of Styx. I then manually converted their SDSS coordinates in $(\lambda, \eta)_{SDSS}$ to equatorial coordinates using the transforms provided in Stoughton et al. (2002) (equations are reproduced in Appendix A). These coordinates are then converted from (α, δ) to the tangent plane (ξ, η) where the origin is centred on Boo3. As shown in Figure 3.15, the nodes do intersect with Boo3. However, they appear to

not follow the trajectory of the satellite given by its orbit.

In viewing the matched filter maps, there is not sufficient evidence for either (i) extended structure (i.e., beyond $5r_h$) of Boo3, or (ii) Styx itself, even with the replication of analysis from the original detection of these features. In the following section, I discuss implications for these results when examining the dynamical properties derived for Boo3.

3.6 Discussion

After probing multiple stellar tracer catalogues for samples of co-moving stars and photometric surveys in search of true substructures presenting themselves as stellar overdensities, the detection of *any* extended debris of Boo3 $>5r_h$ cannot be confirmed in this work. This null results appears to conflict with previous findings regarding the satellite. As discussed in Section 3.1, Boo3 is an extremely diffuse and sizable dwarf whose large velocity dispersion implies it is *not* a system in dynamic equilibrium. Even in this current work, it appears that Boo3 may be strongly affected by MW tides given the proximity of its $2-3$ most recent pericentres ($<$20 kpc, which is argued to be enough to disrupt a typical dwarf; see N-body simulations and relevant arguments by Read et al. 2006). Furthermore, its orbit is very eccentric (0.88) and polar (yet slightly retrograde) which may additionally play a role in the level of observed disruption. Why then, are Boo3's tails unable to be observed here?

Some initial insight into this question can be interpreted from the phase-space distribution of the particle-spray model. In Figure 3.16, the locations of Boo3's putative debris is plotted in various on-sky observables (equatorial and Galactic coordinates, proper motions, heliocentric velocities, and distances) versus their on-sky positions in α and colour-coded by the host potential. For comparison, the present-day observables of Boo3 are highlighted with a magenta star and grey dashed crosshairs. As observed in each panel, the overall trends between the static and evolving potentials are largely similar with minor offsets in the trailing arm. The continuity of these trends, which are similar in *both* potentials, imply that it *should* have been possible to observe a coherent stream structure if indeed there is a continuous distribution of Boo3 debris. Certainly, it is logical to assume there *should* be debris closest to the system itself in the stellar tracer catalogues, if Boo3 is indeed disrupting.

On closer inspection however, Boo3's debris is predicted to exhibit a steep distance gradient as shown in the bottom right panel. To showcase the extent of this gradient,

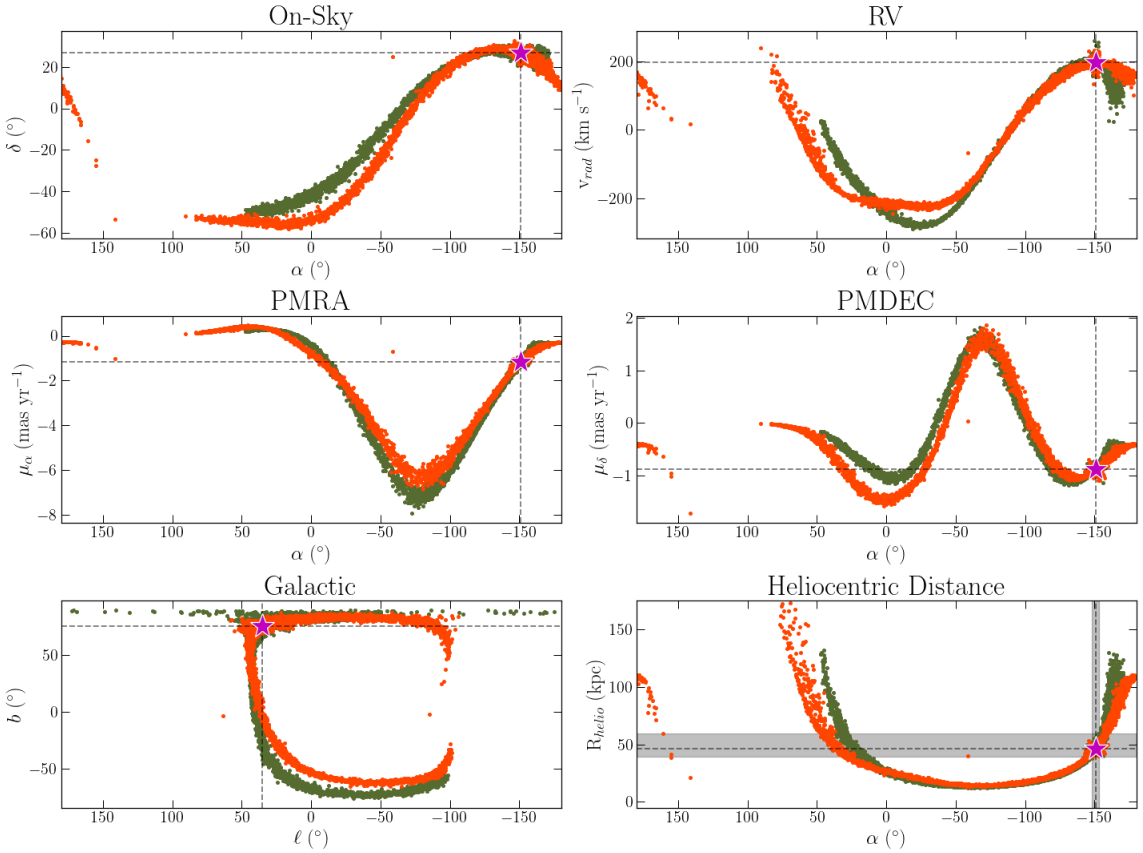

Figure 3.16: Distribution of simulated particles in various observables versus their on-sky position in RA (α) or Galactic longitude (ℓ). The phase-space trends of sprayed particles for both the static (olive) and evolving (orange) potentials are largely similar, including the significant heliocentric gradient of the leading arm ($-180 \lesssim \alpha \lesssim -150°$). For comparison, the location of Boo3 is indicated in each observable as the magenta star, further highlighted by the grey dashed cross-hairs.

I highlight the range of distances spanning area on the sky equal to $5r_h$ ($\pm 2.5°$; slightly larger than the CaHK footprint of Figure 3.9) around Boo3 in grey vertical and horizontal bands. The particles in both models are shown to span distances of $\sim$39 kpc in the trailing arm and out to $\sim$60 kpc in the leading arm, within 5° in RA of Boo3. This indicates that Boo3's putative debris may be experiencing a substantial distance gradient such that our view of the stream may be obscured. Even so, the distance moduli corresponding to these distances are actually within the 1-σ errors of Boo3's estimated distance modulus, indicating that the likelihood maps used to construct the MF would include stars at these distances. Thus, if there was indeed a structure located here, it would still have been detected as an overdensity in the MF maps.

A truncated view of the leading arm due to this distance gradient is certainly a feasible reason as to the lack of observed Boo3 debris. However, the heliocentric distance trends of the trailing arm does suggests that there may be a portion of Boo3's debris that is orbiting at much closer distances. The closest extension, ranging from $10 - 20$ kpc, is predicted to occupy a large area of the sky from $245° \lesssim \mathrm{RA} \lesssim 340°$ and $-47° \lesssim \mathrm{Dec} \lesssim +25°$. In an attempt to link a previous detected stream to Boo3, I also searched the `galstreams` compilation of MW stellar streams (Mateu 2023) for any previously reported structure matching these broad criteria. Unfortunately, no such feature in this area of sky (whose distances are also broadly within the ranges of the models) has yet been catalogued. Given the relatively nearby proximity of Boo3's trailing debris, it is indeed surprising that no structure in this vicinity has yet been reported.

Another possible explanation for the absence of Boo3's tidal tails could be explained by an interaction with the Galactic bar. Recent studies have demonstrated that bar-induced perturbations on stream stars can affect the stream's overall morphology, particularly for systems with pericentres $\lesssim$10 kpc (Bonaca & Price-Whelan 2025). For example, simulations by Pearson et al. (2017) found that the dispersal of stars in the Pal 5 stream may be explained by torques imparted by the bar at pericentre. In this scenario, Pearson et al. (2017) argue that the additional torque (either positive or negative, depending on the bar's orientation) increases/decreases the star's angular momentum and therefore also its orbital energy. If these perturbations *add* torque, L_z increases, total E becomes less negative, and star particles migrate to orbits at larger radii and orbit the MW at slower speeds. The inverse is true if the added torque is negative: the star's orbit becomes shorter and its velocity

increases to be pulled ahead. Thus the influence of the Galactic bar can result in the dispersal of stream stars, vastly decreasing the overall density along the stream.

Other studies of the Ophiuchus stream have shown that bar-driven morphological changes could explain its interesting structure, such as shortening/lengthening of its tails due to bar resonances ("shepherding"; Hattori et al. 2016) or dispersal of its stream stars due to the progenitor's chaotic orbit ("chaotic fanning"; Price-Whelan et al. 2016). In the latter scenario, Price-Whelan et al. (2016) argue that the bar's influence may force disrupted stream stars into chaotic regions of E and L_z. This process results in a dramatic drop in stream density, such that only the most recently disrupted material will be detected as a coherent structure. Given the simplicity of the models used in this present work, in which we do not include a rotating central bar, it is currently not possible to test if chaotic fanning could affect Boo3's debris. However, a detailed study of Boo3's disruption and potential interaction with the bar may be an intriguing investigation for future works.

In the case of the Boo3 dwarf, it is possible that the satellite has experienced a close enough pericentre such that the bar's influence may be considered non-negligible. For both the static and evolving potentials, Boo3's closest pericentre is ∼8 kpc (congruent to findings from Battaglia et al. 2022 and Pace et al. 2022). However, this most recent pericentre (∼140 Myrs ago) is the *only* instance in Boo3's orbit where its stream may have been affected by the bar. In the past 5 Gyrs of its orbit, the pericentres of Boo3 are nearly *double* this value (on the order of ∼16 kpc). Therefore, *if* the bar has had any interaction with Boo3's stream, it *must* have occurred only recently and, prior to this incident, the putative stream was likely unaffected by the bar. At this time, a more sophisticated analysis of Boo3's disruption is left to future works.

In summary, no clear evidence of extended Boo3 debris ($>5r_h$) can be observed in the various datasets used in this work. Furthermore, I am unable to detect the Styx stellar stream in any of these searches. Even if Styx is a real structure, its reported orientation does not align with Boo3's orbit as shown in the bottom panels of Figure 3.15. This means Styx, if it exists, is unlikely to originate from Boo3. Moreover, if Boo3 is indeed tidally disrupting, its tails may have been dispersed by the most recent interaction with the Galactic bar. This conclusion would indicate that the surface brightness of these tails falls below our current detection limits. A detailed study of this dwarf's stellar debris will be more feasible with the completion of deep photometric surveys such as UNIONS, whose data (when observations are complete) will achieve similar depths to the first data release of the Rubin Observatory's *Legacy*

Survey of Space and Time (Ivezić et al. 2019; Bianco et al. 2022).

Chapter 4

Applications of the Algorithm: Follow-Up Science and Impact

Detecting extended substructure around our Milky Way (MW) dwarf galaxies remains a challenge in Galactic Archaeology. This is in part due to the inherent faintness of these systems, but it is also difficult to discern even fainter underlying signals from the overwhelming MW foreground. Chapter 2 presented my solution to these observational limitations, in which I developed a Bayesian-based framework to efficiently remove the contaminating MW population from samples of dwarf galaxy candidate stars. As a result of this work, I have access to individual stellar candidates for every system studied in Jensen et al. (2024).

A substantial outcome of this work are the follow-up programs and scientific endeavours that our group at the University of Victoria have conducted, which were been enabled by the identification of these stellar candidates. In this chapter, I will discuss the investigations and observational campaigns that have been facilitated as a direct result of Jensen et al. (2024). These include (i) spectroscopic follow-up programs using major facilities, such as the Gemini Observatories (using both the GRACES and GHOST instruments) and (ii) second-hand confirmation of newly detected MW satellites in UNIONS. For these cases, I outline the scope of the follow-up project, summarize key findings, and clarify my contributions to these publications.

This chapter summarizes work conducted in various papers written by members of our group at the University of Victoria, of which I am a listed co-author. In all of these works, I am also listed as a co-Investigator for the corresponding follow-up proposals. The papers presented here are the following:

1. Hayes et al. (2023), published in The Astrophysical Journal, Volume 955, Issue 1, id. 17 (2023), titled "GHOST Commissioning Science Results: Identifying a New Chemically Peculiar Star in Reticulum II". Authors: Hayes C. R., Venn K. A., Waller F., Jensen J., et al.

2. Zaremba et al. (2025), published in The Astrophysical Journal, Volume 987, Issue 2, id. 217 (2025), titled "GHOST Commissioning Science Results. IV. Chemodynamical Analyses of Milky Way Satellites Sagittarius II and Aquarius II". Authors: Zaremba D., Venn K., Hayes C. R., Errani R., Cornejo T., Glover J., Jensen J., et al.

3. Sestito et al. (2023a), published in Monthly Notices of the Royal Astronomical Society, Volume 523, Issue 1, p. 123-131 (2023), titled "Stars on the edge: Galactic tides and the outskirts of the Sculptor dwarf spheroidal". Authors: Sestito F., Roediger J., Navarro J. F., Jensen J., et al.

4. Sestito et al. (2023b), published in Monthly Notices of the Royal Astronomical Society, Volume 525, Issue 2, p. 2875-2890 (2023), titled "The extended 'stellar halo' of the Ursa Minor dwarf galaxy". Authors: Sestito F., Zaremba D., Venn K. A., D'Aoust L., Hayes C., Jensen J., et al.

5. Smith et al. (2023), published in The Astronomical Journal, Volume 166, Issue 2, id. 76 (2023), titled "Discovery of a New Local Group Dwarf Galaxy Candidate in UNIONS: Boötes V". Authors: Smith S. E. T., Jensen J., Roediger J., Sestito F., et al.

6. Smith et al. (2024), published in The Astrophysical Journal, Volume 961, Issue 1, id. 92 (2024), titled "The Discovery of the Faintest Known Milky Way Satellite Using UNIONS". Authors: Smith S. E. T., Cerny W., Hayes C. R., Sestito F., Jensen J., et al.

4.1 Commissioning & Follow-Up Campaigns with the Gemini High-resolution Optical SpecTrograph (GHOST)

As discussed in Chapter 1, much can be learned about a dwarf galaxy's formation and evolution through the study of its resolved stellar populations (SPs). Through photometry and astrometry alone, present-day properties of the system can be constrained − such as its stellar mass, distance, age, and bulk motion on the sky. Some evolutionary properties, such as the star-formation history, can also be derived from these observations (i.e., studying the colour-magnitude of its collective SPs). However, it is through spectroscopic observations of these stars that a more complete understanding of the dwarf's evolution can be understood, through chemical abundance analyses paired with internal kinematics (e.g., Walker et al. 2006, del Pino et al. 2017, Tolstoy et al. 2023, Tolstoy et al. 2025, among many more). While the bulk of this thesis has focused on the astrometric and photometric properties of stars in dwarf galaxies, this chapter highlights the spectroscopic follow-up studies made possible from the data published in Jensen et al. (2024). It is in these works in which the dwarf's evolutionary properties can ultimately be derived, through a detailed chemo-dynamic analysis of the system.

With the conclusion of work in Chapter 2, I produced a uniform catalogue of candidate member stars for every MW dwarf (excluding Sgr and the Magellanic Clouds) within ∼450 kpc of Galactic Centre. These lists, complete for every dwarf in Jensen et al. (2024) down to a limiting magnitude of $G < 21$ mag, formed the basis for a variety of follow-up efforts. The most significant of these projects involved the commissioning of a newly deployed, high-resolution spectrograph at the Gemini South Observatory. I contributed to these efforts by developing target lists for both the spectrograph's commissioning and Guaranteed Time Observations (GTO), as will be discussed below.

4.1.1 GHOST Instrumentation Overview

The Gemini High-resolution Optical SpecTrograph (GHOST) is a fibre-fed, optical spectrograph designed for the 8.1-meter Gemini South telescope (McConnachie et al. 2024). It operates across a broad wavelength range (348 − 1061 nm) and supports both a standard ($R \sim 56{,}000$) and high ($R \sim 75{,}000$) resolution mode for spectral

observations. Although GHOST was designed to support a wide variety of science cases, it is particularly well-suited for the study of faint resolved stellar populations in ultra-faint dwarf galaxies (UFDs), where high spectral resolution and wide wavelength coverage are essential. Here, I describe GHOST's state-of-the-art design features that make this spectrograph a staple for future studies of UFDs.

There are three main components to GHOST: the Cassegrain unit that is mounted on the telescope itself, a connecting fibre cable, and the bench spectrograph located inside Gemini South's pier lab. Light first enters the spectrograph through the two integral field units (IFUs) housed within the Cassegrain unit. These IFUs can be positioned independently within a 7.5-arcminute FOV, allowing for up to two science targets to be observed simultaneously in the standard resolution mode. In this instance, a single IFU is centred on the science target while the second can be used for acquisition, guiding, or measuring the noise contribution of the background sky. This setup is extremely efficient for obtaining spectra of very faint ($G \sim 19$ mag) stars that − in typical spectral observations − are too dim to guide on, particularly during the lengthy exposures required for good signal-to-noise. Alternatively, a single (smaller) IFU can be used to achieve high-resolution observations.

Once collected by the IFUs, the light is transmitted through a fibre optic cable that runs from the Cassegrain unit down to the bench-mounted spectrograph located inside Gemini South's pier lab. To optimize both the resolution and wavelength coverage, the bench spectrograph features an échelle configuration. Unlike conventional spectrographs that operate at low diffraction orders, échelle spectrographs by design access many high diffraction orders via a large blaze angle. In these high orders, the wavelength differences ($\Delta\lambda$) of spectral features are very fine, such that each pixel on the CCD can sample a more narrow wavelength range; thus, it maximizes the resolution of the observations. The spectral orders are then fed to a beam splitter that channels the wavelengths of each order into a blue and red arm of the spectrograph (respective to the selected wavelength range).

The blue and red arms are units that are optimized for either blue or red wavelength ranges. As an example, blue-sensitive coatings were applied to the blue camera to enhance the throughput of shorter wavelengths. Once the orders are limited in wavelength, they are each fed to an individual cross-disperser in each arm that is used to spread the overlapping orders in a vertically stacked pattern across the corresponding CCD. By design, the cross-disperser and CCD in the blue arm are oriented to only capture blue wavelengths (specifically those from half of the highest

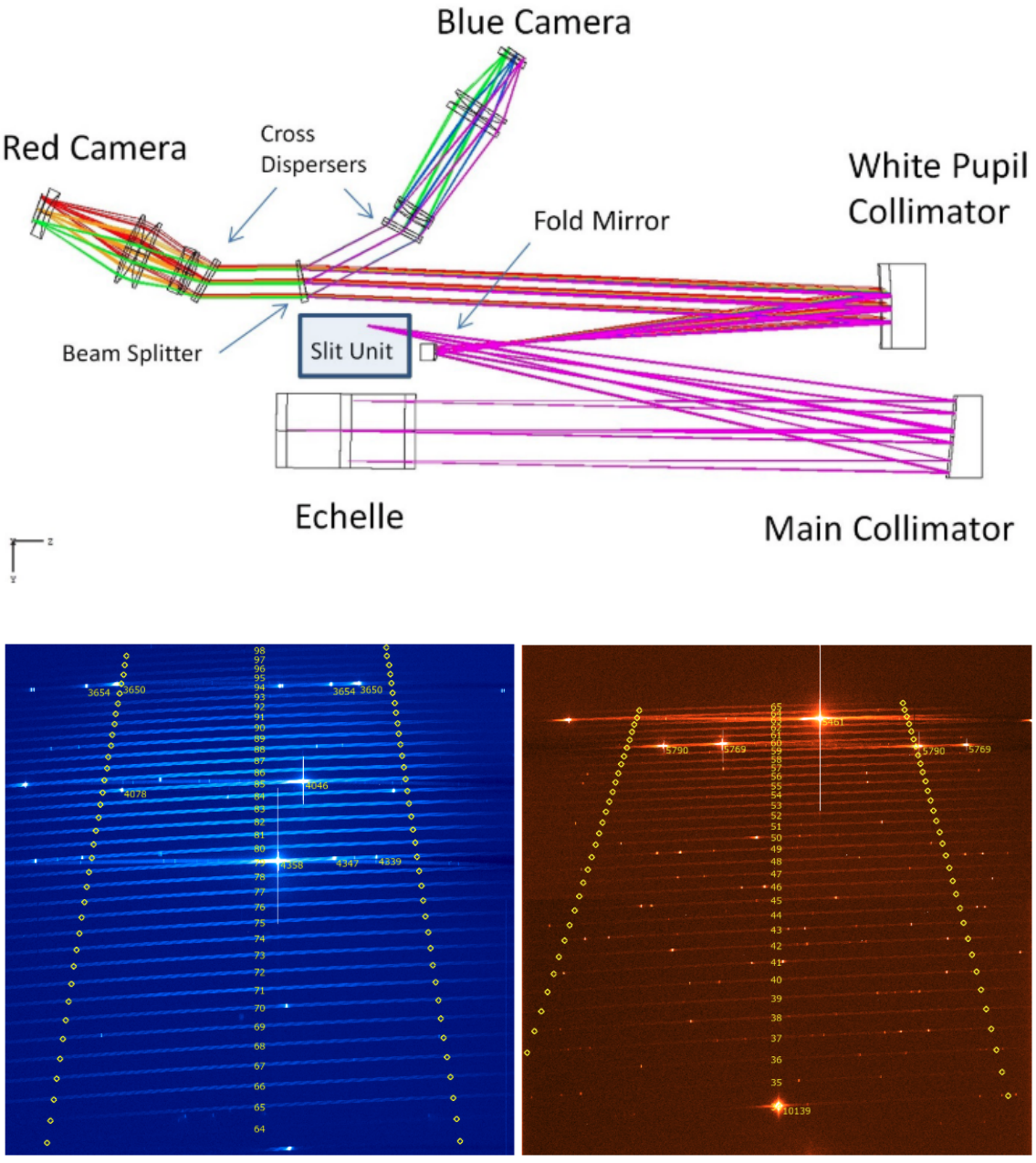

Figure 4.1: Graphical layout of GHOST's bench spectrograph (top) and example spectral images from the blue (bottom left) and red (bottom right) cameras. In the bottom panels, each spectral order and significant Hg emission lines are labelled. Source: McConnachie et al. (2024).

orders; $95 - 64$) and the cross-disperser in the red arm is oriented to only capture red wavelengths (from the lower half orders; $63 - 34$).

In Figure 4.1, the top graphic represents the layout of GHOST's bench spectrograph, and an example of the "ladder" (i.e., "échelle") pattern of overlapping spectral orders in the bottom panels. Utilizing this configuration allows the entire optical spectrum to be captured while maximizing the signal-to-noise, thereby enhancing GHOST's ability to extract weak absorption features in faint ($G \sim 19$ mag) stars.

4.1.2 Commissioning Publications

Two initial observing runs were carried out as part of the commissioning of GHOST at Gemini South Observatory, taking place from $20 - 30$ June and $12 - 16$ September of 2022. These observations were designed to test the on-sky performance of the instrument across its full range of capabilities, including resolution, guiding stability, and sensitivity on faint stellar sources. As part of this effort, I provided a list of targets that met the observing criteria of the instrument and telescope. To optimize the scientific return of these observations, members of our group directly involved with commissioning identified specific dwarfs that have high scientific interest. Of these, a final subset of data were drawn and submitted as part of the commissioning program.

When developing these target lists, I selected stars that (i) had reasonable probability of membership ($P_{max} \geq 20\%$), (ii) satisfied criteria for good astrometric measurements, (iii) had magnitudes $G \leq 19.5$ mag, and (iv) are from systems that are observable by Gemini South (Declination $\leq +30°$). As a reminder, the algorithm is particularly efficient at correctly categorizing MW foreground stars as sources with low probabilities ($P_{max} \sim 0\%$; see Figure 2.9). Our group additionally took the opportunity to test the success of the algorithm in correctly identifying dwarf galaxy member stars, by targeting sources with probabilities as low as $P_{max} = 20\%$. As discussed in the following sections, every star we have ever observed has turned out to be a member of the constituent dwarf, further solidifying the power of this algorithm.

Although I was not directly involved in the observation or subsequent spectroscopic analysis of these studies, I am a co-author on these works due to my contributions that initiated the project. In addition to the provided target lists, I calculated the tangent plane coordinates (ξ, η) for every star in each field, centred on each respective dwarf galaxy. I also estimated the radial distance of every target in units of

the dwarf's half-light radii (r_h). And finally, I provided useful comments and revisions to each manuscript prior to its acceptance.

Some of the commissioning observations were taken of stars that were indeed at large radial distances to their host dwarf (e.g., Tucana 2), though the current publications of GHOST commissioning papers included stars within $3r_h$. While many of the selected stars were used to validate the instrument's performance, several were chosen due to their compelling scientific potential. These stars have contributed to a number of early GHOST publications, which are summarized in the sections below.

A Chemically Peculiar Star in Reticulum 2: Hayes et al. (2023)

Reticulum 2 (Ret2) is a relatively nearby (∼30 kpc; Koposov et al. 2015b) MW UFD that has been found in recent works to host intriguing chemical properties. It is believed to have experienced very little star formation early on in its formation resulting in a stellar population that is chemically pristine, making it one of the most metal-poor galaxies known ([Fe/H] = −2.4 dex; Simon et al. 2015). Notably, Ret2 is the first UFD found to exhibit significant (i.e., 2 − 3 orders of magnitude higher) r-process enrichment (Ji et al. 2016b). Recently, Ji et al. (2016a) argued that this chemical pattern in Ret2 is likely produced by a rare, singular event, such as a neutron star merger.

Given this dwarf's unique past, high-resolution spectroscopic observations have been conducted for all of Ret2's bright RGBs. However, in examining the target lists I compiled for this system, Dr. Christian Hayes of our group identified one candidate that did not already have detailed chemistries published in the literature. Interestingly, this missed RGB had a significant membership probability ($P_{max} \sim 99\%$) due to its consistent proper motions and central location ($<2r_h$). Previous studies (e.g., Ji et al. 2023) had identified it as a potential Ret2 member given its consistent metallicity and RV, but had largely ignored it due to its reddened colour (see CMD panel in Figure 4.2) compared to the CMD of other stars in Ret2. As part of the GHOST commissioning program, our group aimed to test its membership and confirm the hypothesis that its colour may be due to an excess of Carbon. The results of this work are published in Hayes et al. (2023).

The spectral analyses conducted in Hayes et al. (2023) found that this particular star is indeed a member of the Ret2 dwarf galaxy. This conclusion was based on its consistency to Ret2 in radial velocity (RV), metallicity ([Fe/H]), and its abundance

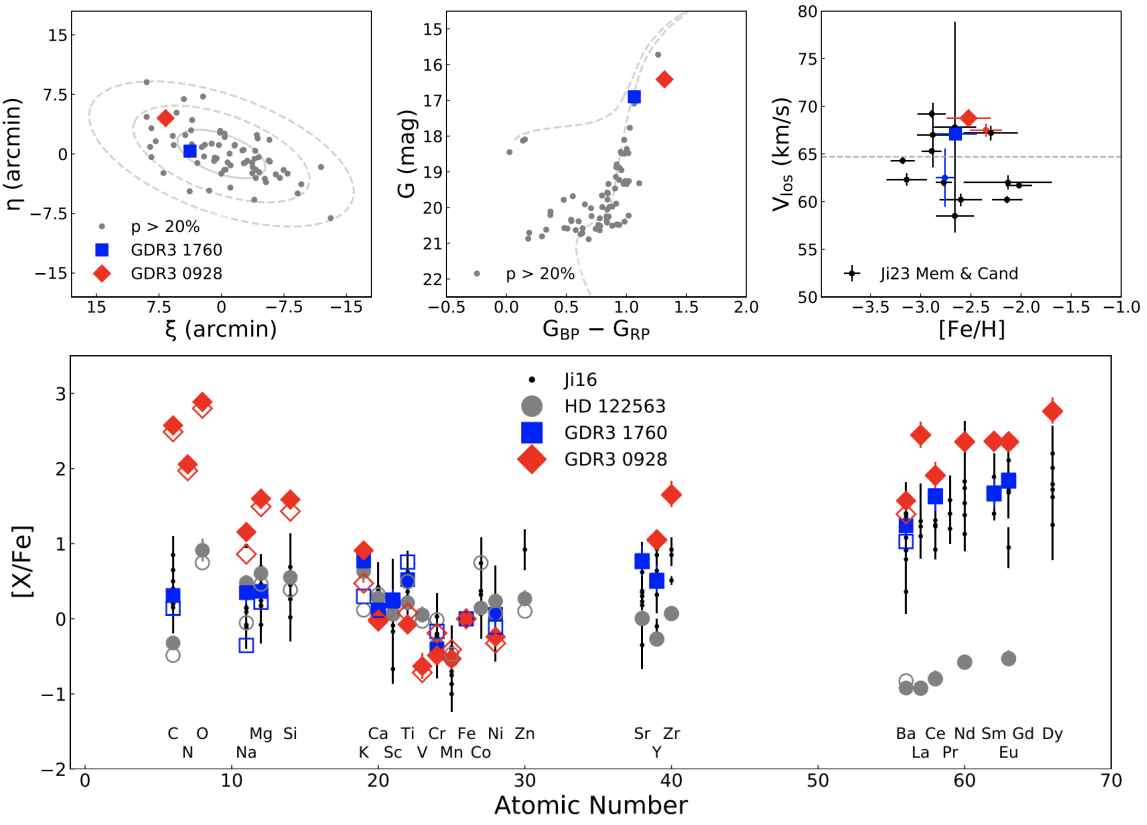

Figure 4.2: Observational properties of the 2 Ret2 stars studied during GHOST commissioning, reproduced from Hayes et al. (2023) and created by Dr. Christian Hayes. In all panels, the blue square and red diamond represent the 2 targets observed in this work, and black data are previously identified spectroscopic members of Ret2. **Top:** Tangent plane positions, CMD, and radial velocity vs metallicity trends of Ret2 stars. Candidates from Jensen et al. (2024) are highlighted in grey for comparison. **Bottom:** Chemical abundance trends of Ret2 stars, as a function of atomic number. Grey circles in this panel represent the chemical trends of HD 122563, which serves as a bright, metal-poor MW benchmark star. Open shapes indicate the solutions when accounting for non-LTE (non-Local Thermodynamic Equilibrium) in the spectral analysis conducted by Dr. Hayes.

trends in r-process elements. Hayes et al. (2023) furthermore determined that the star's light elements (C, N, O, Na, Mg, and Si) are enhanced compared to other Ret2 stars, shown in the bottom panel of Figure 4.2. These trends, in conjunction with the enhancement in r-processed elements, indicates that this star is a particularly rare subtype of Carbon-enriched star. Not only is this source a Carbon-Enhanced Metal-Poor (CEMP) star, but its unusual enhancement in r-process elements indicates it is classified as a CEMP-r star. Previous stellar evolution studies argue that these types of stars may have imprints from faint supernovae (SNe) arising from the earliest generations of stars. Hayes et al. (2023) claim that identifying more of these rare sources may better constrain the yields produced by faint SNe, allowing us to better understand the chemical traits of the earliest stars.

Chemodynamical Analyses of Sagittarius 2 and Aquarius 2: Zaremba et al. (2025)

Two additional systems – Aquarius 2 (Aq2) and Sagittarius 2 (Sgr2) – were also selected as targets for GHOST commissioning. These specific satellites were chosen for GHOST follow-up by Dr. Alan McConnachie and Dr. Kim Venn, as neither of these systems had pre-existing high-resolution observations in the literature. Additionally, the faintness of these targets offered a prime test for the resolution limits of GHOST at high magnitudes (targets ranged between 17 to 18.8 mag in G). In total, five stars (2 stars in Aq2 and 3 in Sgr2) were observed during commissioning. Due to the fact that all targets in this study had been previously observed with low-resolution spectroscopy, the objectives of this work were to namely to (i) examine epoch observations to explore the potential influence of binaries, and (ii) provide detailed chemistries for these two stellar systems for the first time. The analysis of these stars were conducted by MSc student Dasha Zaremba and published by Zaremba et al. (2025).

Using these new commissioning observations, Zaremba et al. (2025) first derived RVs and metallicities for each target and confirmed that these 5 stars are indeed members of Aq2 and Sgr2. To confirm consistency across epochs, Zaremba et al. (2025) compared their RV and [Fe/H] measurements of our new (high-resolution) observations to the pre-existing (low-resolution) values cited in the literature. In concluding that the new estimates were reliable and consistent, Zaremba et al. (2025) combined the total spectral samples to evaluate the mean and spread (i.e., dispersion)

of each satellite's RV and [Fe/H] distributions.

As discussed in Zaremba et al. (2025), it is often the system's dispersions in RV and [Fe/H] that are utilized as proxies to determine whether it is a UFD or globular cluster (GC). For a system in dynamic equilibrium, the RV dispersion (σ_{RV}) is correlated to the amount of mass in the system (referred to as dynamical mass; Walker et al. 2009a). Therefore, a larger σ_{RV} indicates the system is dark matter-dominated. Similarly, the metallicity dispersion ($\sigma_{[Fe/H]}$) for a dwarf galaxy is typically higher than that of star clusters of the same luminosity (Willman & Strader 2012; Leaman 2012). Dwarfs, as systems containing more mass than observed by starlight alone, naturally have deeper potential wells that allow them to retain gas more efficiently than star clusters. Though Aq2 and Sgr2 have been presented in the literature as confirmed dwarf galaxies, Zaremba et al. (2025) revisited this conclusion by first refining the current estimates of σ_{RV} and $\sigma_{[Fe/H]}$. With new high-resolution GHOST observations, these categorizations can then be further solidified by examining the chemistries of these stars in detail.

For Aq2, Zaremba et al. (2025) concluded that the dispersions in RV and metallicity indicate that this system is indeed a dwarf galaxy ($\sigma_{RV} \approx 5.68$ km s^{-1}; $\sigma_{[Fe/H]} \approx 0.47$ dex). Furthermore, the chemical abundances derived in this work indicate that Aq2 experienced very inefficient star formation (SF; see Figure 4.3). Zaremba et al. (2025) find that the abundances of Aq2 stars are deficient in Odd-Z elements (explicitly, [Na/Fe]) that trace yields from core-collapse supernovae, as well as deficiencies in neutron-capture elements ([Sr/Fe] and [Ba/Fe]) that arise from specific neutron-capture events (e.g., neutron star mergers). Zaremba et al. (2025) argue that these combined trends indicate that only the earliest, massive stars enriched the dwarf's interstellar medium before Aq2's SF shut down. These specific abundances are shown to be largely produced from Asymptotic Giant Branch (AGB) stars. In systems with efficient SF, it is expected that the chemical trends would show a positive gradient in [Na/Fe] vs [Fe/H] and the general abundances for [Sr/Fe] and [Ba/Fe] would be more enhanced than observed in this work. The suppressed abundances of all three elements indicate that Aq2 likely experienced a very limited number of enrichment events, consistent with a system that formed only a small number of stars before quenching early in its evolution.

In the case of Sgr2, the chemo-dynamic analysis appeared to be much less conclusive. Zaremba et al. (2025) examined the RV and metallicity dispersions and found that, while an estimate could be determined, the solutions to these parameters are not

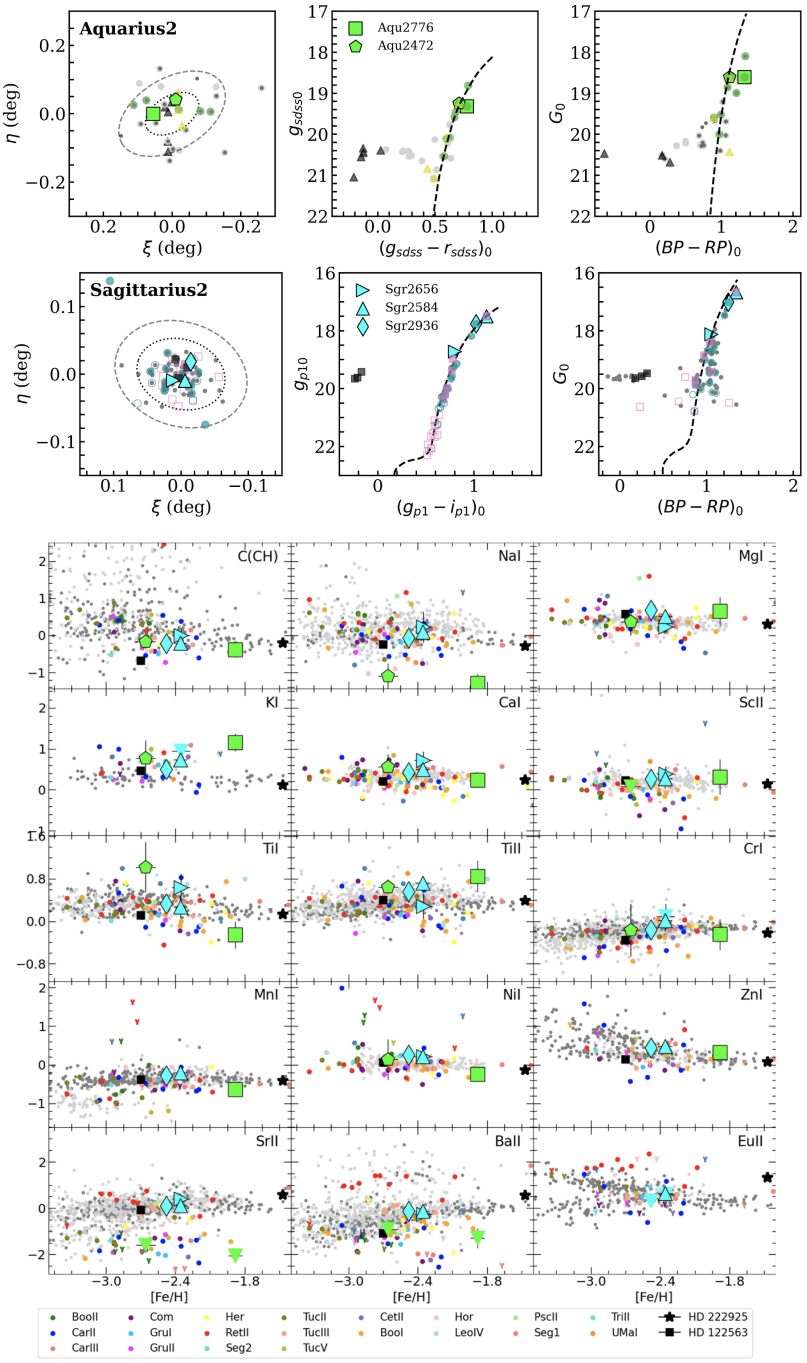

Figure 4.3: Observational properties of the 5 Aq2 (lime green) and Sgr2 (cyan) stars studied during GHOST commissioning, reproduced from Zaremba et al. (2025) and created by Dasha Zaremba. **Top 2 rows:** Tangent plane positions and CMDs of stars in Aq2 and Sgr2. Candidates from Jensen et al. (2024) are highlighted as grey points for comparison. **Bottom:** Chemical abundances for the 5 stars observed during GHOST commissioning discussed in this work. Stellar abundances of MW halo stars are plotted in grey, while coloured points are literature abundances derived from other MW UFDs.

indicative of the presence (or lack thereof) of dark matter. Zaremba et al. (2025) argue that Sgr2's RV ($\sigma_{RV} \approx 1.73$ km s^{-1}) and metallicity ($\sigma_{[Fe/H]} \approx 0.13$ dex) dispersions are only just barely resolved, and in both cases, only slightly higher than expected of a GC. The chemical abundance patterns measured in Sgr2 indicate that this satellite is largely chemically typical for a low-mass stellar system, with no strongly unusual trends (see cyan icons in Figure 4.3). Zaremba et al. (2025) find that most of the abundances, including α-elements and Fe-peak elements, fall within the expected ranges for metal-poor stars in UFDs. The only notable exception is one Sgr2 star that was observed to have a moderate r-process enhancement, indicated by elevations in [Eu/Fe], [Sr/Fe], and [Ba/Fe]. Though r-process enhancement is a rare detection in UFDs, Zaremba et al. (2025) show that the [Eu/Fe] abundances in these enriched UFDs have similar trends to other r-process enriched GCs from the literature. Thus, Zaremba et al. (2025) argue that the level of [Eu/Fe] in this Sgr2 star does not provide a clear diagnostic to distinguish the satellite as a UFD or star cluster.

In summary, these GHOST commissioning observations demonstrate the power (and limitations) of high-resolution spectroscopy in revealing the true nature of the MW's stellar satellites. The combination of precise RVs and metallicities are useful observables that confirmed Aq2's classification as a UFD while also enabling a comprehensive analysis of its star formation history through its chemical abundance patterns. This study presented an equally detailed analysis of Sgr2 that, in contrast, leaves open questions about its true nature. This ambiguous system sits near the boundary in size and luminosity between confirmed dwarfs and confirmed globular clusters (see Figure 1 from Zaremba et al. 2025), making it a compelling subject for continued study. As discussed in Zaremba et al. (2025), additional diagnostics – such as determining the degree of segregation between low and high mass stars in the satellite (induced by internal dynamical interactions) – may provide more conclusive insights into the nature of Sgr2. Future works seeking to better constrain the nomenclature of this system may be able to do so using (i) epoch spectroscopic studies to confirm/deny the presence of binaries that may inflate Sgr2's velocity dispersion, in addition to (ii) deeper photometric surveys from facilities like LSST and Euclid that will allow for mass segregation to be better established.

4.1.3 GHOst Ultra-faint Legacy Survey (GHOULS)

With each new photometric survey release, additional MW satellites are discovered. Yet the spectroscopic follow-up of these systems − particularly at high resolution − is nonuniform across the population. Therefore, the aim of the GHOst Ultra-faint Legacy Survey (GHOULS) is to provide, in conjunction with existing observations, a uniform high-resolution census of all accessible stars in all observable UFDs with the GHOST instrument (McConnachie et al., in prep).

In this survey, target systems are selected based on several observational factors. The primary focus is the UFD population, defined broadly as galaxies with absolute magnitudes $M_V \leq -7.0$ mag. At fainter luminosities however, the boundary between star clusters and dwarfs becomes ambiguous. Additional selection criteria were applied in order to help mitigate this issue. To approximately limit the selection of star clusters, compact systems with physical sizes $r_h \geq 10$ pc were removed. To a similar end, the sample is limited by surface brightnesses of $\mu_{eff} \geq 26$ mag/arcsec^2; this broad restriction is to limit to systems with surface brightnesses fainter than any confirmed MW globular cluster in the literature. Because GHOULS will rely on observations using the newly commissioned GHOST spectrograph on Gemini-South, targets are further restricted to declinations $\leq+28°$. The final sample of systems totals 46 MW satellites.

Within each system, target stars are chosen by the PI's of the program (Dr. Alan McConnachie and Dr. Kim Venn) to maximize membership probability and observability. Stars must have $P_{max} > 10\%$ (from Jensen et al. 2024) and apparent magnitudes $G \leq 18.5$ mag. Horizontal branch stars are avoided by applying a broad colour cut of $(B_P - R_P) \geq 0.8$ mag. Existing high-resolution data are carefully cross-checked in the literature, and only previously unobserved candidates are retained for the survey. The final GHOULS sample thus consists of all qualifying stars across the 46 satellites that lack prior high-resolution spectroscopy. Figure 4.4 shows CMDs for all UFD targets, where black points mark candidate members within $<3r_h$ and open circles mark those in the outskirts ($>3r_h$). Stars with previous high-resolution follow-up are indicated as red squares, while star icons in the figure denote new or ongoing GHOULS/GHOST observations. For comparison, a metal-poor ([Fe/H] = −2.19) Padova isochrone shifted to each system's distance modulus is also plotted.

A number of these satellites (i) have not yet been spectroscopically confirmed as dwarf galaxies, (ii) have no prior high-resolution observations, or (iii) lack spec-

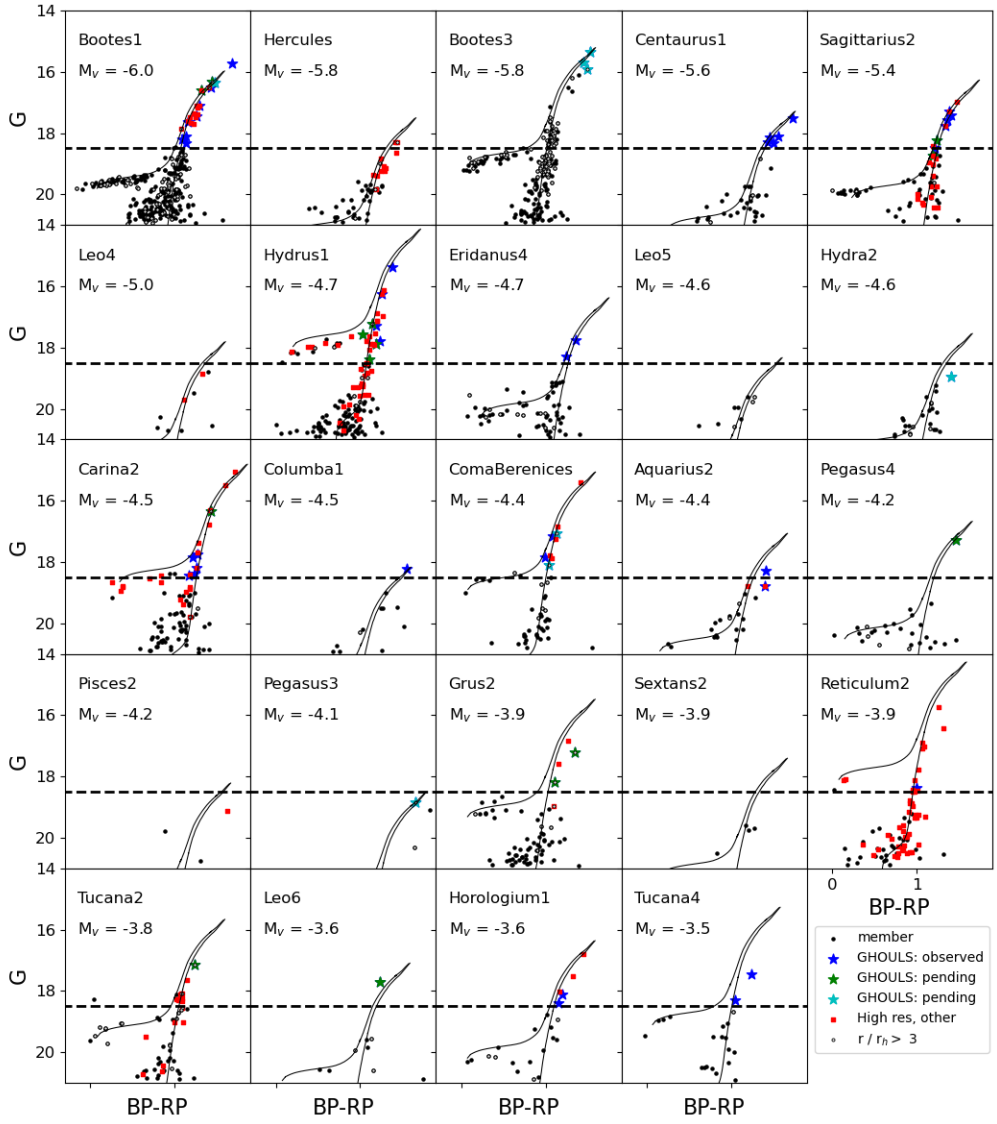

Figure 4.4: CMDs for all UFDs submitted as part of GHOULS, organized from brightest (Boötes 1) to faintest (Cetus 2; continued in next figure). In each panel, star icons indicate GHOULS targets while red points represent candidates with existing high-resolution follow-up in the literature. Data plotted with white points circled in black indicate that its radial distance is $>3r_h$. All data are candidates from Jensen et al. (2024) with $P_{max} \geq 0.1$. An old (12 Gyr) PADOVA isochrone is also plotted in each panel, shifted by the distance modulus and reddening of each corresponding dwarf. This figure (and the subsequent set of CMDs) are created by Dr. Alan McConnachie using data supplied by my target lists.

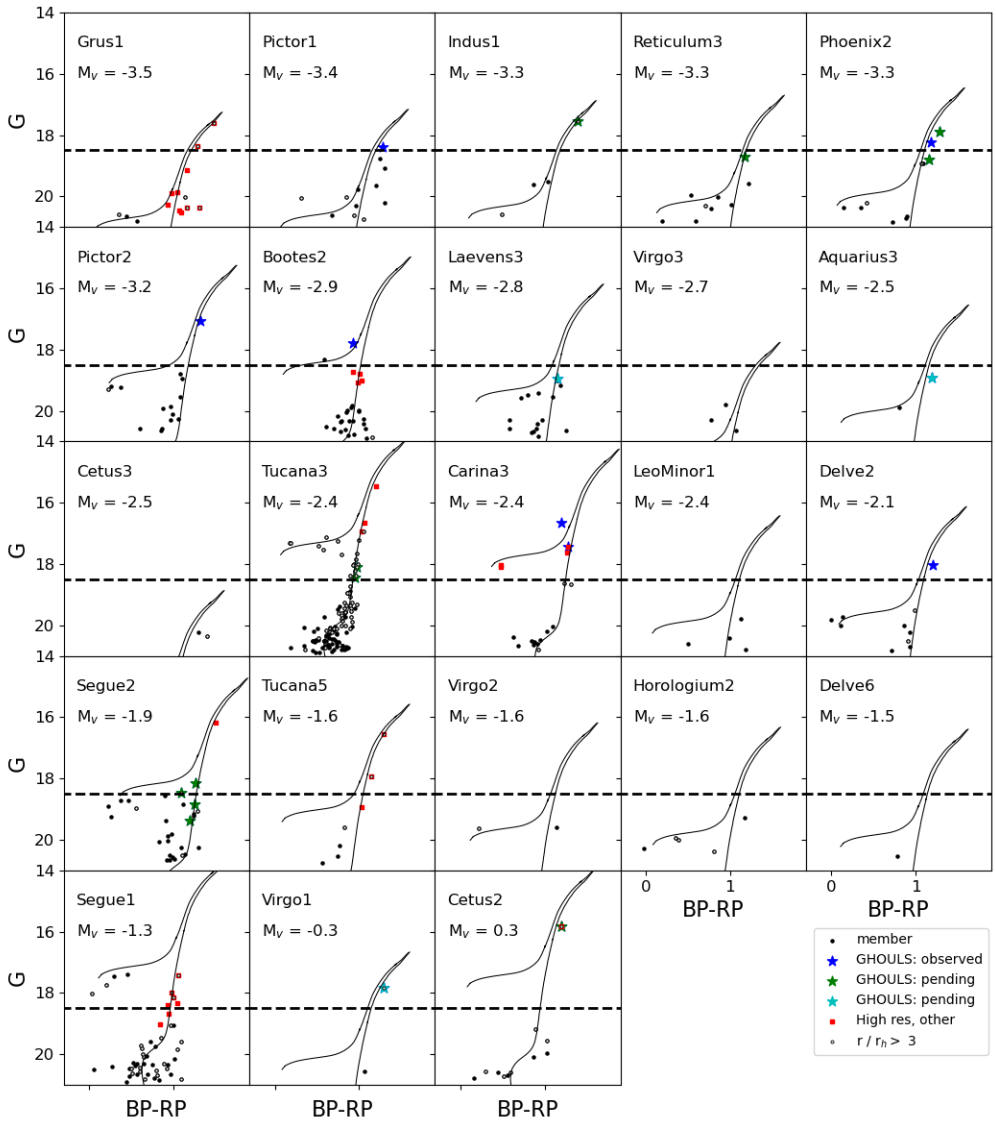

Figure 4.4: *continued.*

troscopic follow-up observations altogether. GHOULS will deliver a transformative dataset, providing critical benchmarks for the chemical and dynamical properties of the faintest galaxies and enabling a wide range of future studies.

4.2 Independent Spectroscopic Programs

In addition to the more wide-scale observations carried out in GHOST commissioning and the future survey proposed in GHOULS, multiple individual follow-up campaigns using various observing facilities were also conducted. In contrast to the GHOST-based campaigns discussed in the previous section, the works presented here involve independent programs that either (i) predate the commissioning of GHOST, (ii) directly test the algorithm's fidelity in identifying member stars at large radii, or (iii) apply the algorithm to confirm newly detected stellar systems in combination with *Gaia* data. Below, I discuss the results of these various projects.

As with the GHOST targets, my contributions included creating the target lists for these systems based on membership probabilities derived with the algorithm. Additionally, I calculated the tangent plane coordinates and half-light radial distances to all stars in their respective catalogues. Any additional contributions are also specified where relevant.

4.2.1 Dwarf Galaxy Outskirts: Confirming Stellar Membership

In the works below, Dr. Federico Sestito applied for independent spectroscopic follow-up for two Classical dwarfs. These systems were specifically identified in Jensen et al. (2024) as having an outer stellar excess. For both satellites, the brightest and most radially distant stars were targeted to test the fidelity of the algorithm in the outskirts, to confirm the presence of an extended outer component.

In these works, my contributions included the preparation and writing of the Scientific Justifications in these proposals and participating in the observations as co-Investigator. Furthermore, I provided code to translate the proper motion vectors of the satellites themselves into the true transverse velocity vectors, by correcting them for solar-reflex motion. In these works, I also contributed to the interpretation of results, though the final conclusions are the first author's. And finally, I also provided manuscript revisions during the publication process.

Galactic Tides and the Outskirts of Sculptor: Sestito et al. (2023a)

As discussed in Chapter 2, I found a handful of MW dwarfs where the algorithm identifies an extended stellar component in Jensen et al. (2024). The Sculptor (Scl) dwarf galaxy is one such system whose candidates extend out to distances of $\gtrsim 10 r_h$. Prior to this study, the most radially distant spectroscopic member of Scl was identified at $6r_h$. In Sestito et al. (2023a), we aimed to test the fidelity of this detection by investigating whether the farthest stars in our sample are indeed members of the Scl dwarf.

The targets selected for follow-up in this work are the two most radially distant ($9.7r_h$ and $10.1r_h$) and relatively bright (17.6 and 17.9 mag in G, respectively) stars in the sample of candidates ($P_{max} > 20\%$; membership probabilities were 46% and 45% respectively). Since only RVs and metallicities are required in order to confirm/deny their membership, Dr. Sestito opted to obtain low-resolution spectroscopic observations. As this work preceded the commissioning of GHOST, the targets were observed with the Gemini Multi-Object Spectrograph (GMOS; Hook et al. 2004) at the Gemini South Observatory through the Gemini Fast Turnaround (FT) program.

Analysis conducted in Sestito et al. (2023a) confirmed that the two targets indeed had consistent RVs and metallicities to Scl. In fact, Sestito et al. (2023a) noted that archival observations of the more distant target (Target 2) published by Westfall et al. (2006) had reported similar RVs to our analysis. Given the star's radial distance from Scl, and that this observation precedes the advent of *Gaia*, Westfall et al. (2006) ruled it out as a Scl member. However, the analysis in Sestito et al. (2023a) now officially confirms the membership of both targets to Scl. This conclusion is born about from the stars' (i) RVs, (ii) metallicities, (iii) proper motions. As an additional statistical confirmation, Sestito et al. (2023a) ran a Besançon Milky Way statistical model (Robin et al. 2003) to explore the possibility of observing stars from the MW foreground population whose properties are the same as previously confirmed Scl members. Sestito et al. (2023a) find that, out of the 230 mock stellar particles, there are only 55 that populate the same region of metallicity and RV space as Scl stars. Of these, only one particle has proper motions similar to that of the dwarf; however, its statistically-interpreted magnitude is more than a dex from Scl stars of the same colour. Given that the Besançon model does not produce any particles reproducing all Scl member star properties at once, and that the spectroscopic values and probabilities are consistent with membership to the dwarf, Sestito et al. (2023a)

conclude that the two RGBs observed in this study are indeed members of the Scl dwarf galaxy.

Based on this finding, Sestito et al. (2023a) argue that Scl's stellar extent reaches as far as (if not more than) $\sim 10 r_h$, or approximately $\sim$3 kpc. By confirming the membership of a few of the most radially distant stars in Scl, it is reasonable to assume that the candidates interior to this distance are also member of Scl. As discussed in Jensen et al. (2024), I argue that the outer excess of stars in satellite dwarf galaxies are most likely caused by either (i) MW tides acting to strip the satellite, or (ii) a stellar halo of stars accreted from a dwarf in a merger. Using the candidate members I supplied, Sestito et al. (2023a) aimed to test whether tides can explain the stellar distribution of Scl by exploring its density profile.

In Sestito et al. (2023a), Dr. Sestito created stellar density profiles of both Scl and Fornax (Fnx, a system that has been arguably unaffected by tides due to its large pericenter; see Borukhovetskaya et al. 2022) as a control sample to highlight the outer excess of stars in Scl (see density profiles in Figure 4.5). To broadly compare to a dynamical interpretation, these profiles were also compared to the those of simulations conducted by Peñarrubia et al. (2008). These N-body models explored the distributions of stellar particles in tidally perturbed satellites (including Scl), assumed to start as a King isothermal profile (King 1962) in a static MW potential. Sestito et al. (2023a) then directly compared the observed density profile to those of the simulated initial King particle distribution and the final distribution of particles at the end of the simulation.

Sestito et al. (2023a) find that the observed stellar density excess appears to closely match that of the tidally perturbed Scl model in Peñarrubia et al. (2008). Furthermore, Sestito et al. (2023a) argue that imprints of tidal effects do not only appear in the stellar density profile (Σ(r)), but can also be identified in the logarithmic slope of this function (Γ(r)). In examining Γ(r), the observed Scl data appears to approximately follow the same trends of the tidal example. In striking contrast, Sestito et al. (2023a) observe that Fnx's stellar density largely follows an exponential function in Σ(r) and a nearly linear trend in Γ(r). Although this dwarf has a relatively large pericentric distance in its orbit around the MW ($\sim$55 kpc; see Pace et al. 2022 and Battaglia et al. 2022) and previous works do not predict strong tidal influence on Scl, it would seem that tides cannot be completely ruled out as an origin for the stellar distribution excess observed in the outskirts of this system. More detailed simulations catered to match the observed properties of Scl will have to be conducted

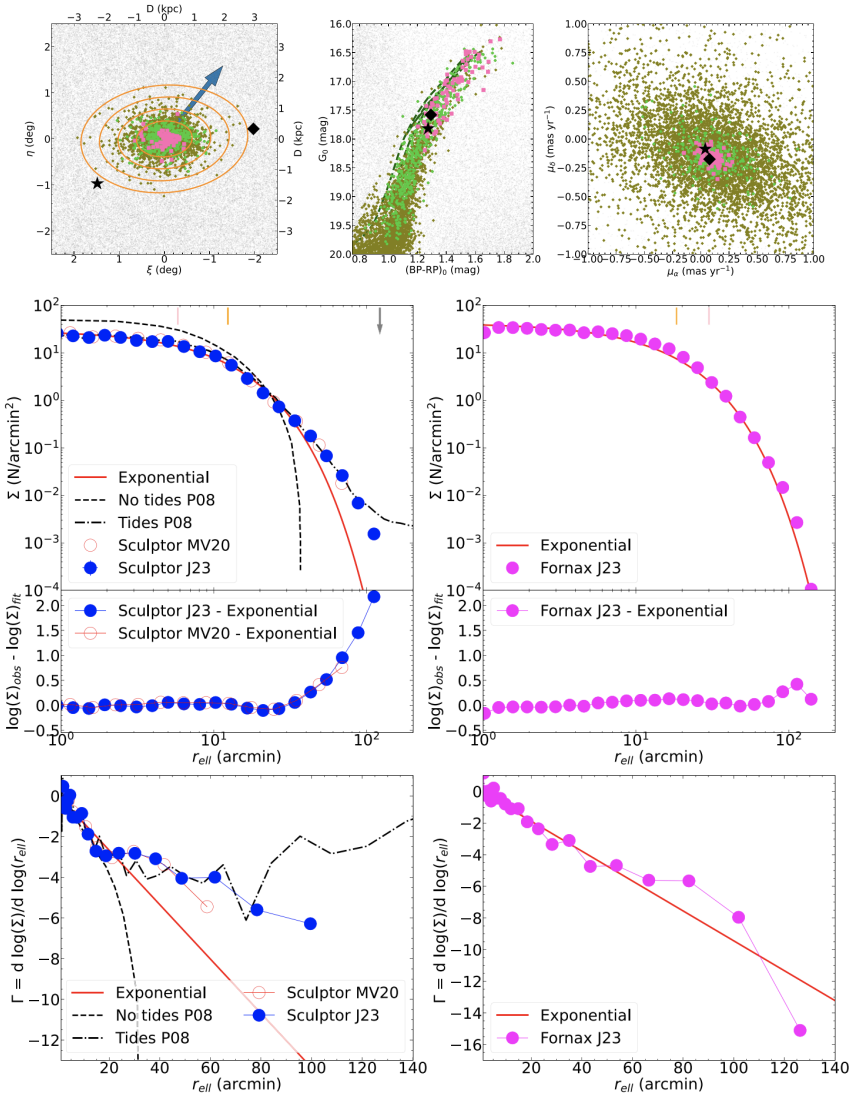

Figure 4.5: Observational properties of Scl stars reproduced from Sestito et al. (2023a), created by Dr. Sestito using the candidate stars provided by my work. **Top:** Tangent plane coordinates, CMD, and proper motions of all *Gaia* stars in the Scl field. Candidates from Jensen et al. (2024) are plotted in olive, while spectroscopically confirmed members are shown in lime green and pink. Targets 1 and 2 are highlighted as the black diamond and star icon, respectively. MW foreground stars are shown in grey. **Bottom:** Stellar density profiles (Σ(r)) and the logarithmic derivative (Γ(r)) of Scl (left) and Fnx (right) using stellar candidates from Jensen et al. (2024). Both are plotted against an exponential profile (red solid line). For comparison to the tidal models in Peñarrubia et al. (2008), the data are also plotted against the assumed density profiles at the beginning (black dashed lines) and end (black dashed dotted lines) of the N-body simulations to highlight the influence of tides in the distribution.

to make more concrete conclusions.

The findings in this study not only highlight the success of the algorithm in detecting extended stellar excesses in MW dwarf galaxy satellites, but additionally showcases the varied science that is achievable with these observations. Scl will remain an interesting dwarf for future works to study, as even this relatively isolated system may be influenced by tidal effects.

The Extended "Stellar Halo" of Ursa Minor: Sestito et al. (2023b)

Of the nine systems I identified in Jensen et al. (2024), Dr. Sestito also submitted an independent proposal to study the outskirts of Ursa Minor (UMi). Prior to these observations, UMi's most radially distant spectroscopic member was at $6.8r_h$. In Sestito et al. (2023b), five new targets (selected from my target lists) are confirmed to be members of UMi. The most distant of these is located at $11.7r_h$.

Similar to the work conducted in Sestito et al. (2023a), Dr. Sestito was awarded spectroscopic follow-up for a number of bright targets in the outskirts of the dwarf in order to test whether the stellar excess detected in Jensen et al. (2024) was indeed part of the system. Five relatively bright (G from 17.4 to 18.3 mag) radially distant targets (ranged from $5.2r_h - 11.7r_h$) that did not currently have any spectroscopic observations in the literature were selected to be observed in this program. Though each star's membership probability was particularly high (P_{max} between 80% and 97%), none of these stars had previous spectroscopic follow-up. Dr. Sestito submitted a proposal through the Gemini Semester Program to obtain spectroscopic observations using the Gemini Remote Access to CFHT ESPaDOnS Spectrograph (GRACES; Chene et al. 2014; Pazder et al. 2014). For four of the targets, low-resolution spectroscopy was requested in order to derive RVs and metallicities and confirm their membership. However, Dr. Sestito requested high-resolution observations of the final (most radially distant) star in order to obtain detailed chemical abundances. While RVs and metallicities, in addition to the high membership probabilities indicating similar tangential motions and consistent stellar populations, all are parameters indicating membership to UMi, the detailed chemical abundances allowed Sestito et al. (2023b) to additionally explore whether the presence of this exceptionally distant star was motivated by tidal or merging effects.

Analysis presented in Sestito et al. (2023b) shows that all five observed stars have RVs and metallicities consistent with UMi membership, thus extending the UMi's

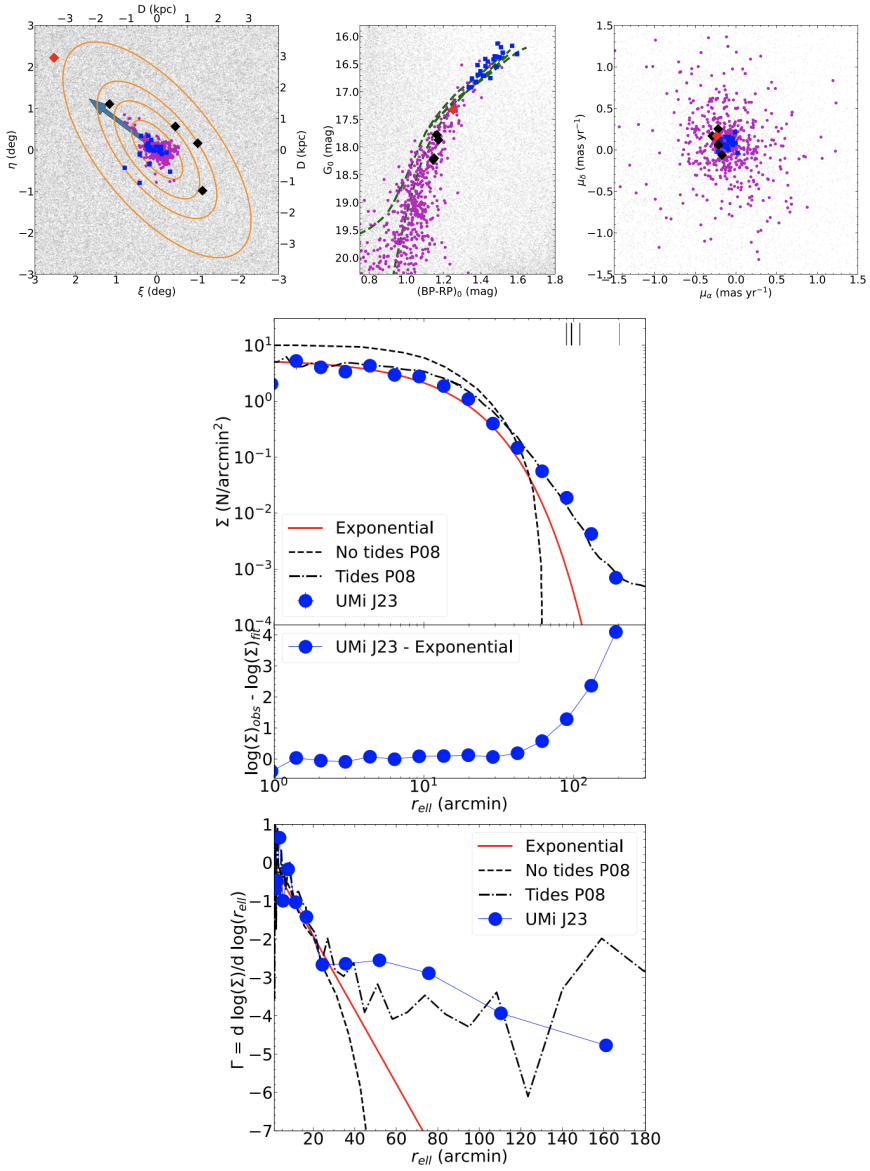

Figure 4.6: Observational properties of UMi stars reproduced from Sestito et al. (2023b) and created by Dr. Sestito using candidate stars that I had supplied. **Top:** Tangent plane coordinates, CMD, and proper motions of all *Gaia* stars in the Scl field. Spectroscopically confirmed UMi members are plotted in purple and blue. Targets analyzed in this work are shown as diamonds (black and red). High-resolution observations for the star indicated with a red diamond were also obtained. MW foreground stars are shown in grey. **Bottom:** Stellar density profile (Σ(r)) and the logarithmic derivative (Γ(r)) of UMi, using stellar candidates from Jensen et al. (2024). An exponential profile is plotted as the red solid line. For comparison to the tidal models in Peñarrubia et al. (2008), the data are also plotted against the assumed density profiles at the beginning (black dashed lines) and end (black dashed dotted lines) of the N-body simulations to highlight the influence of tides in the distribution.

known stellar extent out to ∼4.5 kpc. In the same manner of analysis as the preceding work, Sestito et al. (2023b) also compare the statistical probability of these stars being members of the MW foreground population using the Besançon MW model (Robin et al. 2003). Only 39 out of 300 stellar particles populate the same region in RV and metallicity space as UMi, and of these only three have consistent proper motions to the dwarf. Similar to Sestito et al. (2023a), these data are much brighter than any star in UMi (at that particular colour). Sestito et al. (2023b) conclude that no star particles properly represent all observed properties presented in this work; therefore, these stars are conclusively members of the UMi dwarf galaxy.

Assuming that the algorithm performs equally well at identifying dwarf member stars at positions interior to these radii, Sestito et al. (2023a) attempted to test for tides in the same manner of analysis as the work in the previous subsection. Sestito et al. (2023b) argue that this is a reasonable assumption, especially when considering that the distances of these confirmed GRACES targets range from $\sim 5 - \sim 12 r_h$, vastly covering UMi's outskirts. Here, UMi's radial profiles of stellar density and the logarithmic derivative appear to follow the same trends as UMi's tidally perturbed model in Peñarrubia et al. (2008). The interpretation is thus that UMi's stellar density in the outskirts may be affected by MW tides.

In contrast to Sestito et al. (2023a), the follow-up observations included high-resolution spectroscopy of the most radially distant star. Using the detailed abundances, Sestito et al. (2023b) aimed to conclude whether stars in the outskirts may be an accreted population from a dwarf-dwarf merger, or are more consistent with an in *in situ* formation and tidal migration scenario. The abundances reported in Sestito et al. (2023a), which are all observations of stars at $>5 r_h$, do appear to be consistent to other high-resolution observations of UMi reported in the literature. As the data are chemically similar within $<5 r_h$ and in the outskirts, Sestito et al. (2023b) concluded that the newly confirmed members are most likely originated from the dwarf itself and have radially migrated. The chemical deficiencies observed in [Ca/Mg], [Na/Mg] and [Ba/Fe] (which are lower than all the other UMi observations) indicated that the most radially distant member was born in an environment polluted by low-mass Type II SNe. In conjunction with the conclusions from other observations that suggest UMi had an inefficient SFH, this finding corroborates the notion that this star formed in UMi originally and must have migrated.

Based on these findings, Sestito et al. (2023b) conclude that UMi's stellar population extends at least to $\sim 12 r_h$, or 4.5 kpc. The presence of the extended stellar

component of UMi appears to have a tidal origin, even though there does not appear to be evidence of unbound stars from the dwarf forming a stellar stream. As with Scl in Sestito et al. (2023a), the confirmation of these distant members supports the interpretation that extended stellar populations identified by the algorithm are genuine, and highlights the intriguing science that can be achieved with follow-up observations of this data.

4.2.2 Newly Discovered Milky Way Satellites in UNIONS

A further application of the Jensen et al. (2024) algorithm enables the confirmation of the presence of co-moving groups of stars in newly detected MW satellites. Below are summaries of two works in which an independent satellite detection was made by PhD student Simon Smith using the UNIONS photometric catalogue that I then confirmed as a co-moving group of stars via the algorithm. Together, these data led to additional spectroscopic follow-up in which Simon Smith was Principal Investigator, and I participated as a co-Investigator. With these follow-up observations, the entire parameter space of each satellite could be derived and published for the utility of future studies.

In these projects, I contributed as co-author by providing an independent confirmation of these detections. Furthermore, I provided the code to derive orbit properties in both of the following works, such as pericentre, apocentre, and orbital time, in addition to the system's trajectory in Galactocentric coordinates (X, Y, Z). Finally, I also assisted in the interpretation of these orbit results and provided feedback on the final manuscripts. The conclusions of these works is ultimately attributed to Simon Smith.

The Discovery of Boötes 5: Smith et al. (2023)

Detecting new dwarf galaxies is an important observational objective in the field of Galactic Archaeology. The "missing satellites problem" for example, suggests that significantly less satellites in the MW are observed compared to what is predicted in large-scale hydrodynamic simulations for a MW-mass galaxy (Klypin et al. 1999; Moore et al. 1999). The variation of the galaxy luminosity function between observational and cosmological perspectives has proven difficult to merge, though multiple theories have been offered to explain these discrepancies. Observational biases, for example, may play a role in the limited detections of dwarf galaxies in the ultra-faint

regime. Indeed, detection limits of photometric surveys have greatly increased the number of MW satellites observed over the years (see Figure 1 in Simon 2019) and will hopefully continue with newer and deeper surveys. These detections not only assist in tying together observation and theory, but furthermore may be useful to answer the type of dark matter governing the Universe (Lovell & Zavala 2023) since WDM suppresses small-scale halo formation.

Recently, Smith et al. (2023) reported on the detection of a new MW satellite known as Boötes 5 (Boo5). This system was detected using a matched filter technique applied to the CFIS r- and Pan-STARRS i-bands of UNIONS. In this work, Smith et al. (2023) estimated Boo5's structural properties (such as r_h, position angle, and ellipticity), distance, and luminosity. Interestingly, Boo5 appears to fall precisely in the "valley of ambiguity" (Gilmore et al. 2007) of the size-luminosity plane, where the boundary between globular clusters and dwarf galaxies becomes muddled. At this time, Boo5 can only be classified as a dwarf galaxy candidate, but its observational properties derived in this work suggest it is more likely a dwarf.

Once the structural properties of Boo5 had been assessed, I applied the Jensen et al. (2024) algorithm to a 2° field in *Gaia* to search for stellar members. This serves to not only estimate, for the first time, a proper motion for this dwarf, but simultaneously allows for a comparison of stellar samples from two independent detections. The algorithm identified five high probability members (>90%) in Boo5 from *Gaia*, all of which were also considered members using the matched filter method.

With the confirmation of a stellar overdensity in UNIONS and a separate detection of a co-moving group in *Gaia*, there was ample justification to obtain follow-up observations of Boo5. Simon Smith applied for GMOS low-resolution spectroscopic observations through Directors Discretionary Time at Gemini North to constrain the radial velocity and metallicity of the brightest (and highest probability; 99.9%) stellar member. In obtaining these observations, Smith et al. (2023) were then able to publish all necessary properties of Boo5. These included its structure (equatorial position, half-light radius, absolute magnitude, position angle, ellipticity), kinematic information (distance, proper motions, RV), and metallicity.

With only one star's RV and metallicity observed, it must be noted that this information is not enough to conclude whether Boo5 is a dwarf or cluster. Indeed, further spectroscopic observations must be conducted to at least explore the system's velocity and metallicity dispersions, and additionally study the detailed chemistry of its stellar population. Though it is reasonably considered ambiguous, Smith et al. (2023) argue

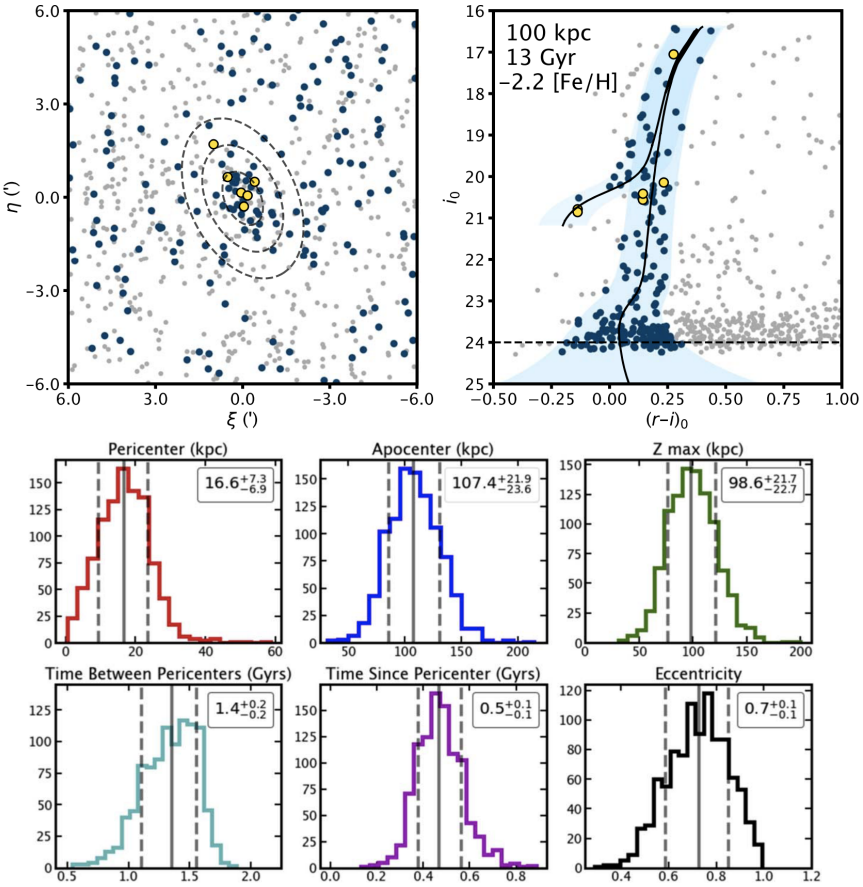

Figure 4.7: Observational properties of Boo5, reproduced from Smith et al. (2023) and created by Simon Smith using my *Gaia* stellar candidates and orbit analysis code. **Top:** UNIONS-selected (blue points) and *Gaia*-selected co-moving members (yellow) of Boo5, compared to the MW foreground (grey). The left panel shows the tangent plane positions of these stars while the right is their positions in colour and magnitude, compared to the isochrone selection used in Smith et al. (2023). **Bottom:** Distributions of Boo5's orbital properties derived from 1000 MC sampled realizations of the satellite, within 1-σ observational errors.

that its properties in size, metallicity, and distance favour a dwarf categorization. Compared to other confirmed MW globular clusters, Boo5's physical size ($\sim$27 pc) would make it the third largest in the Galaxy. Its distance ($\sim$100 kpc) would make it the fourth most distant. And finally, its metallicity ([Fe/H] ≈ -2.85 dex) would place it 0.5 dex *below* the most metal-poor *intact* (i.e., not tidally disrupted) globular cluster in the MW. As all these properties are mostly typical of our LG dwarf galaxy population (save metallicity), Boo5 is either an enigmatic globular cluster outlier, or a very metal-poor dwarf galaxy. Only additional spectroscopic follow-up will be able to constrain this system better in the future.

A brief orbit analysis of Boo5 was also conducted, by modelling the orbit of 1000 Monte Carlo realizations of Boo5. Orbit properties such as the system's pericentre, apocentre, maximum height above the MW disk, time since pericentre, orbital time, and eccentricity were also estimated; the distributions of these are provided in the bottom panels of Figure 4.7. Smith et al. (2023) found that Boo5 is a system approaching apocentre in a very polar and eccentric orbit. Given that it only takes $\sim$1.4 Gyrs for Boo5 to complete an orbit, it has likely experienced many since its accretion. Since there are no clear tidal features of this system in the matched filter (let alone that this is not a satellite where the algorithm detects the presence of an outer profile), Smith et al. (2023) argue that this is further indication that Boo5 is a stellar system enveloped in a protective dark matter halo. The conclusions drawn from the orbit analysis further solidifies the interpretation that this newly discovered satellite is very likely a dwarf galaxy.

Discovery of the Faintest Known MW Satellite, UNIONS-1/Ursa Major 3: Smith et al. (2024)

Applying a matched filter technique to the UNIONS catalogue has proven highly effective in uncovering new MW and M31 dwarf galaxy candidates. Using the same methodology as the previously discussed work, Smith et al. (2024) reported the discovery of the faintest MW satellite observed to date − a result that pushes the observational frontier into the extreme low-luminosity regime. This work is significant not only for setting a new detection benchmark, but also for confronting a fundamental theoretical question: *what is the smallest galaxy that can possibly form?* To address this question, the discovery space of faint stellar systems must continue to expand to ever fainter and more distant regimes. These observations are key to understanding

fundamental properties of galaxy formation at the smallest scales, and have direct implications for our cosmological perspective.

This new stellar system detected by Smith et al. (2024) goes by two names, UNIONS-1 if it is a cluster or Ursa Major 3 (UMa3) if it is a dwarf galaxy, as its categorization remains ambiguous. Its structural parameters indicate it is a very nearby (10 kpc), compact ($r_h \approx 3$ pc), and extremely faint ($M_V \approx +2.2$ mag) satellite. Smith et al. (2024) furthermore estimate that its stellar mass is only $16 M_\odot$ and composed of only a handful of sparsely populated MS stars.

To independently detect a co-moving group of stars, I utilized the structural parameters obtained from Simon Smith's UNIONS detection and applied the Jensen et al. (2024) algorithm to a 2° *Gaia* field. In addition to the identification of stellar members, this allowed me to also determine the satellite's proper motion for orbit analysis. Simon Smith led a follow-up spectroscopic program to obtain observations for as many stars in the field as possible, using the DEep Imaging Multi-Object Spectrograph (DEIMOS; Faber et al. 2003) on the Keck II telescope. 59 stars were observed, 11 of which showed internal consistency in their RVs (seven of these 11 have $P_{max} > 99.9\%$). Metallicity of these stars unfortunately could not be calibrated, as all 11 targets are MS and subgiant branch stars[1]. Regardless, the RVs derived from these low-resolution observations permitted Smith et al. (2024) to determine the systemic RV of the system in addition to the velocity dispersion. Indeed, the RV analysis confirmed that all members from the algorithm are consistent with the hypothesis that they form a co-moving group.

As previously discussed, the velocity dispersion is often used as a metric indicating the presence of dark matter in a system. Smith et al. (2024) attempted to derive the velocity dispersion, finding a preliminary estimate of $\sim$3.7 km s^{-1}. At face value, this estimate is large enough to suggest that UNIONS-1/UMa3 is a dwarf galaxy. However, Smith et al. (2024) note that the removal of one RV outlier decreases the estimate to $\sim$1.9 km s^{-1}, a value that is more consistent with the interpretation that this system is a stellar cluster. Removing a second RV outlier actually makes the velocity dispersion be unresolved. Thus, this current work (especially without a metallicity or dispersion to further constrain this system) is unable to confirm/deny

[1]The metallicities in this study are calibrated using the Ca II triplet, whose Equivalent Widths (EW) have an empirical relationship to metallicity (e.g., Armandroff & Zinn 1988; Armandroff & Da Costa 1991; Starkenburg et al. 2010). However, these absorption features are sensitive to surface gravity and temperature and thus have only been calibrated for giants for which log(g) and effective temperature (T_{eff}) only vary in a narrow range with respect to luminosity.

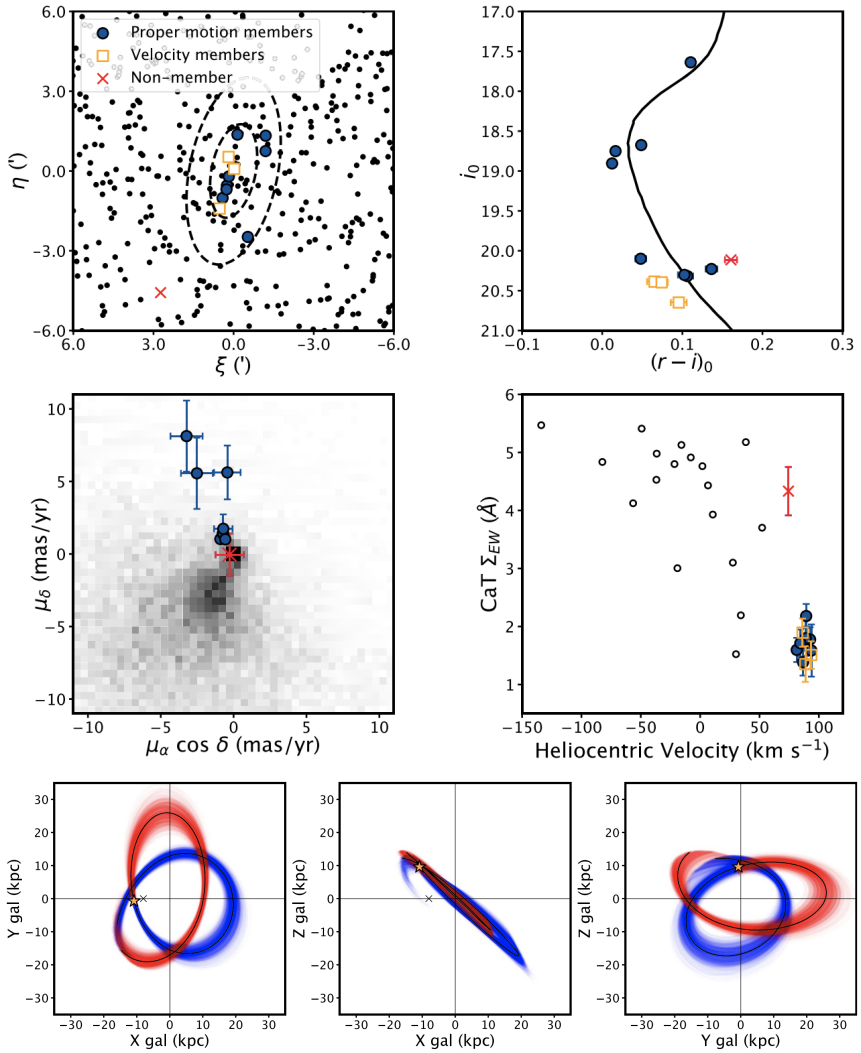

Figure 4.8: Observational properties of UMa3/UNIONS-1, reproduced from Smith et al. (2024) and created by Simon Smith using my *Gaia* stellar candidates and orbit analysis code. **Top and Middle:** UNIONS-selected (black points) and *Gaia*-selected co-moving members (blue) of UMa3/UNIONS-1, compared to the *Gaia*-selected MW foreground (grey; only present in the middle left panel). Orange square markers indicate sources that do not have good astrometric measurements, but given their RVs and metallicity they are also considered members of this system. **Bottom:** Orbit of UMa3/UNIONS-1 in Galactocentric coordinate derived from 1000 MC sampled realizations of the satellite, within 1-σ observational errors.

the presence of dark matter in this ambiguous faint satellite.

The dynamic analysis for UNIONS-1/UMa3 (implemented in the same manner as Smith et al. 2023) indicates that this system has a relatively polar, eccentric, and prograde orbit. Though this information is not enough to classify the system in entirety, Smith et al. (2023) argue that it is more likely a dwarf galaxy given that it does not share many orbit properties with other *in situ* formed clusters. With a pericentre of ∼13 kpc and a very short orbital timescale (∼375 Myrs), this system would have experienced many pericentric passages through the disk that would have had substantial tidal influence. The presence (or lack thereof) of a stellar stream would also be indicative that this system is a tidally disrupted remnant of a globular cluster. However, future work photometrically (to examine mass segregation) and spectroscopically (to obtain metallicities and better calibrate the metallicity and RV dispersions) will be necessary in order to fully categorize this system.

4.3 Summary

The candidate catalogues produced in Jensen et al. (2024) have laid the foundation for a diverse suite of spectroscopic follow-up programs aimed at probing the structure, dynamics, chemistry, and membership of MW dSph satellites. This chapter has presented the broad range of science enabled by those catalogues, from programs that leveraged early commissioning time on GHOST to those carried out independently with Gemini/GMOS, Gemini/GRACES, and Keck/DEIMOS. Together, these efforts span multiple scientific objectives, allowing us to (i) test the algorithm's performance in the low-density outskirts of known systems, (ii) validate new satellite discoveries with *Gaia*-based kinematics, (iii) obtain homogeneous high-resolution coverage for all Southern-sky MW dwarfs, and (iv) derive detailed chemistries for chemically pristine systems, for the first time in some cases. Collectively, the programs highlighted in this chapter demonstrate the lasting scientific utility of the algorithm and candidate selection framework established in Chapter 2, and underscore the inherently collaborative nature of follow-up observations enabled by these data.

Chapter 5

Conclusions & Outlook

5.1 In Summary

The aim of this thesis has been to investigate the Milky Way (MW) dwarf galaxy satellites in search of faint substructures. As all the dwarfs studied in this work are pressure-supported systems, such features are most likely the result of external effects such as tidal stripping from the host MW or alternatively a stellar halo populated with previously accreted debris from a smaller dwarf. Determining which scenario is most feasible requires an interpretation of both dynamical and chemical analyses. As each dwarf's history is appreciably unique, these studies − from the initial detection of faint features, to target selection and proposal submission for follow-up observations, to analyzing new data and cross-referencing existing observations, and finally drawing conclusions based on the entire picture − requires effective collaboration in order to study every system with equal care. In this thesis, each chapter builds from Chapter 2 where I presented the development of the algorithm used to detect faint extended features in MW dwarfs and identify stellar candidates. This work built the foundation for the targeted analyses of individual systems and observing campaigns in the subsequent chapters. Together, these contributions have advanced our ability to detect, interpret, and understand the chemo-dynamics of nearby dwarfs, significantly impacting ongoing research in the field of Galactic Archaeology.

Studying the faint outskirts of dwarf galaxies is inherently challenging, particularly in the case of ultra-faint dwarfs (UFDs). In Chapter 2, I addressed this problem by updating a Bayesian-based algorithm that simultaneously (i) distinguishes high-confidence dwarf members from the dominant MW foreground and (ii) identifies

systems hosting an outer excess of stars. The analysis uncovered nine dwarfs (spanning both the classical and UFD mass regimes) that exhibit evidence of extended substructure. This work represented the first systematic census of extended stellar halos in the MW dwarf population, producing robust candidate catalogues that have since served as the foundation for multiple spectroscopic follow-up campaigns in our collaboration.

Building on this foundation, Chapter 3 examined one of the most peculiar systems identified in the previous analysis: Boötes 3 (Boo3). Boo3 has long been proposed as the progenitor of the ∼50°-long Styx stellar stream, which − if confirmed − would be a significant structure with which to derive the MW's underlying dark matter (DM) halo. Using the *Gaia*-selected members from Jensen et al. (2024), new CFHT CaHK narrow-band photometry, and a matched filter analysis with SDSS and DELVE, I searched for any evidence of Boo3's putative tidal debris, including exploring the alleged link to Styx. Instead, I found no evidence for a kinematic connection between these structures, nor any detection of extended Boo3 debris beyond $\gtrsim$5 half-light radii (or $\gtrsim \pm 2.75°$). This result not only challenges the presumed Boo3-Styx association, but also underscores the need to verify the linkage between progenitor and stream when only a photometric detection exists. As the MW is full of numerous substructures − $\gtrsim$100 individual streams (Mateu 2023), ∼65 dwarf galaxies (McConnachie 2012), and ∼150 globular clusters (GCs; Harris 2010) − there may inevitably be overlap between structures that are not in fact affiliated. As photometric observations alone do not provide a comprehensive view, it is necessary to obtain additional data of both the progenitor and stream in order to physically connect the structures.

The absence of clear tidal features in Boo3 does not rule out past disruption, and in fact multiple findings (including my own regarding a stellar excess in Boo3's density profile, using our *Gaia*-selected members) strongly suggest this system is disrupting. If indeed Boo3 has undergone strong tidal disruption as previously suggested, the lack of extended features may be explained by the dispersion of stream stars through an interaction with the Galactic bar. However, testing this scenario will require more complex dynamical models than were conducted in this work. This chapter highlights both the difficulty of probing the lowest surface brightness regimes (such as the distant outskirts of Boo3) with currently available facilities, and also illustrates the importance of confirming substructure associations beyond photometric evidence alone.

Chapter 4 presented the wide-ranging science that has been achieved as a di-

rect result of the algorithm in Chapter 2, in which I had a variety of roles. The candidate catalogues I produced provided the foundation for multiple spectroscopic campaigns, including those used to test and commission the Gemini High-resolution Optical SpecTrograph (GHOST) and be part of the homogeneous Southern-sky study in the GHOst Ultra-faint Legacy Survey (GHOULS). Additional independent programs in which I participated as co-Investigator and was involved with the writing of the observing proposals, were also conducted to target the most radially distant stars in two classical dwarfs. In these programs, I identified both the targets for follow-up and the systems themselves as those hosting an extended stellar excess. I also provided a secondary method to verify the detection of new dwarf galaxy candidates in UNIONS, by confirming the presence of a co-moving group in *Gaia*. Using the candidates that were shared between the UNIONS-*Gaia* detections, I also participated as co-Investigator of these spectroscopic follow-up campaigns, which were used to calibrate radial velocities and confirm membership. I also determined the systemic proper motion of the system using the algorithm. For these newly discovered satellites, the complete dwarf parameters were reported (e.g., structural parameters, positions, distances, and luminosities). My specific contributions facilitated the estimates for the dwarfs' systemic proper motions, velocities (by way of providing targets for observation), and a complete orbit analysis in which I determined various orbital parameters from the integrations (pericentre, apocentre, and orbital period). Collectively, these works demonstrate how the candidate lists I developed have enabled substantial science beyond the initial purpose of Jensen et al. (2024). Each work has helped to deepen our understanding of the chemo-dynamics of our MW dwarf galaxies, providing substantial impact in the field of Galactic Archaeology.

Together, the results of Chapters 2 − 4 establish a coherent framework for understanding the chemo-dynamics of MW dwarf galaxies. Studying the structure and evolution of dwarfs, particularly their outskirts which remains largely unexplored territory, has profound implications for cosmology and astrophysics. For example, the observed frequency of dwarf stellar haloes is a useful, indirect statistic for constraining the type of DM that governs our Universe. Though the flavour of DM remains inconclusive, the total number of simulated DM galaxy subhaloes (later evolving into dwarf galaxies) are significantly suppressed in Warm Dark Matter cosmologies (Deason et al. 2022; Lovell & Zavala 2023). Consequently, the decreased number of subhaloes reduces the number of possible mergers and therefore the ubiquity of observed dwarf stellar haloes formed from previously accreted stars. By building a

census of MW dwarfs that host these extended features and determining their likely origin, this thesis illustrates the cosmological importance of these structures and how they provide insight into the formation of the smallest galaxies.

5.2 Future Directions

The number of scientific endeavours enabled by the work in this thesis, even with the data currently in hand, is already substantial. As discussed in Chapter 4, the candidate lists produced by my algorithm provide a critical resource for future studies. These lists form the foundation of large-scale homogeneous programs such as GHOULS, which is targeting the inner ($<3r_h$) stellar candidates of all Southern MW UFDs. Yet, the potential of these data extends well beyond this scope.

One natural next step is to design programs that specifically target stars at larger radii ($\gtrsim 4r_h$), where the frequency of contaminants is higher, but so is the scientific payoff. Smaller, dedicated spectroscopic campaigns could focus on the most distant bright candidates in dwarfs with well-defined radial profiles, particularly those lying beyond the transition radius (r_{trans}) where an outer profile begins to dominate. Confirming members in this regime would be especially valuable, as such stars may trace the remnants of intermediate dwarf–dwarf mergers (Deason et al. 2022), populating an extended stellar halo in the surviving system. This type of study directly tests the limits of hierarchical merging at the smallest galactic scales.

Another avenue is to compare the stellar distributions revealed by my algorithm to tailored N-body simulations. Previous work has broadly compared and contrasted our observed density profiles of Sculptor (Scl) and Ursa Minor (UMi) with tidally disrupted models of Peñarrubia et al. (2008). However, these models aimed for a broad study of MW dwarfs rather than attempting to reproduce as many observable properties (per dwarf) as possible, and also did not include the influence of the Large Magellanic Cloud which has been shown to influence the orbit of Scl in particular (Battaglia et al. 2022). Previous N-body simulations of Scl showed that, while a large proportion of its DM may be stripped during its orbit, Scl's stellar component is minimally affected at present-day (Iorio et al. 2019). Conducting our own N-body simulations matched to the density profiles from Jensen et al. (2024) would provide a direct test into whether tides alone can explain the stellar excess that is observed. Currently, research in this direction is already underway in the study of Scl and UMi (Boyea et al., in prep), but other promising cases such as Boötes 1 (Boo1) and Boötes

3 (Boo3) for which I identify many stellar candidates may yield equally interesting results. In the case of Boo1, tides are speculated to influence the stellar distribution but have not been proven, and the influence of the Galactic bar on the stellar density of Boo3 would be an intriguing case to study.

Finally, the methodology developed here can be extended to the ∼150 GCs in the MW. Unlike dwarfs, GCs lack a protective dark matter halo and are therefore far more susceptible to tidal disruption. Applying the same framework to this population could provide a wide-scale, homogeneous census of extended tidal features across the MW GC systems. Such a study would not only refine our understanding of the dynamics of individual clusters, but even identifying singular GCs with extra-tidal stars may offer additional data to constrain the effect of MW tides across the Galaxy. Since any irregularity in the morphology of GCs is most likely tidal in origin, this application would provide a clean and influential test of MW tides across a wide range of environments.

In summary, the existing data products of this thesis already enable a wealth of follow-up opportunities, ranging from targeted programs of individual dwarfs, to detailed simulation comparisons, to systematic studies of the MW GC population. These varied avenues can extend the impact of this work well beyond the results presented here, thus enabling advancements in the detection and subsequent study of MW substructures.

5.3 Looking Ahead: Future Data

The current era in astronomy presents unprecedented opportunities to explore our Galaxy (and its satellites) in exquisite detail, with new data emerging from a new generation of facilities, particularly the Rubin Observatory's *Legacy Survey of Space and Time* (LSST; Ivezić et al. 2019; Bianco et al. 2022) and Euclid's *Wide Survey* (Euclid Collaboration et al. 2025). In conjunction with the methods of Jensen et al. (2024), it may yet be possible to utilize these upcoming catalogues to extend to *even fainter* detection limits to identify extended stellar structures of our MW dwarfs.

LSST is a ground-based survey that, in January 2028, will deliver the first data release of its deep multi-band photometry (*ugrizy*) across the southern sky (declination $< +15°$). This catalogue will prove exceptionally useful for detecting faint stellar features in our MW dwarfs, as LSST's deep *u*-band coverage can be exploited to isolate specific stellar populations (Ivezić et al. 2008). Currently, the algorithm assign

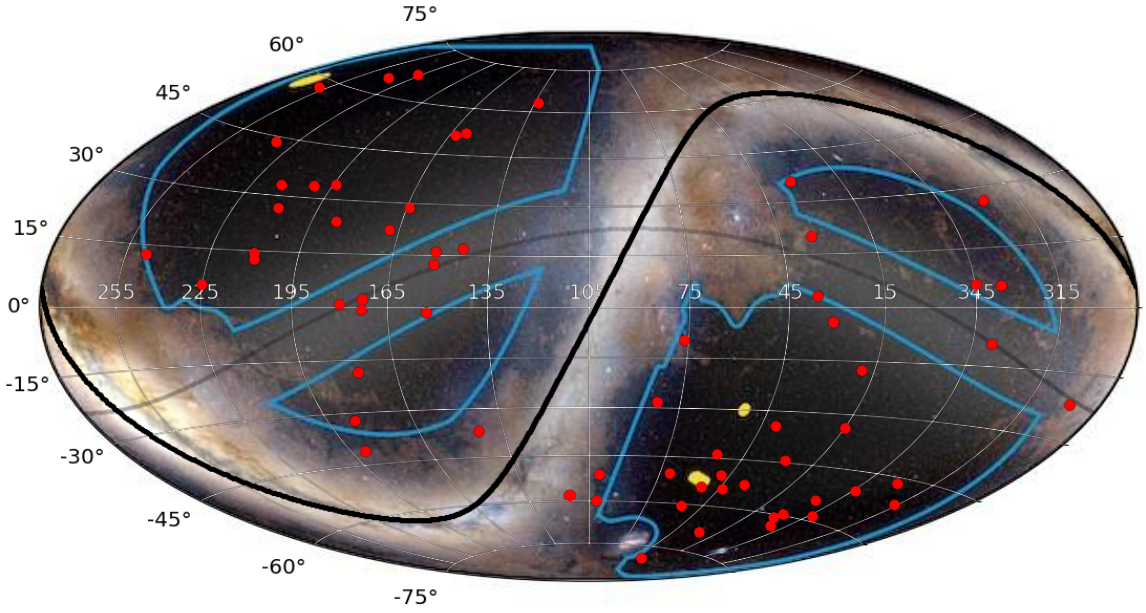

Figure 5.1: Equatorial positions of MW dwarf satellites (shown as red points) in an Aitoff projection, overlain on the proposed Euclid Wide Survey coverage highlighted as blue polygons (image credit: Euclid Consortium Survey Group/J.-C. Cuillandre). Note the synergy between LSST (limited to Dec $< +15°$) in the south and UNIONS (Dec $> +15°$) in the north, producing nearly all-sky coverage of MW dwarf galaxies (excluding the Galactic disk).

membership probabilities for stars in a field around a given dwarf, using the three aforementioned likelihood models. The present implementation of the algorithm relies solely on *Gaia* astrometry and photometry, thereby limiting detections to *Gaia*'s magnitude threshold. In future iterations of this technique, I will incorporate LSST's much deeper *ugriz* photometry into the algorithm to optimize the filtering of the dwarf's stellar populations. Refining the CMD model to factor in LSST's complete optical coverage will enable more precise identification of stars in dwarf galaxies by (i) probing deeper magnitudes and uncover even fainter substructures, and (ii) improving the selection of metal-poor stars, which will reduce contamination from the more metal-rich MW foreground.

An important consideration when exploring fainter regimes is contamination from inadequate star-galaxy separation. At deeper magnitudes, particularly in later LSST releases, accurate classification of point sources will be essential for comprehensive study of dwarf stellar populations and planning follow-up observations. To mitigate this issue, I can utilize Euclid's space-based imaging which will effectively remove faint galaxy contaminants. Euclid's superior imaging capabilities (such as its well-constrained point-spread functions, absence of atmospheric turbulence, and high photometric precision) make it well-suited for disentangling stellar sources. Figure 5.1 highlights the on-sky coverage of Euclid's *Wide Survey* (blue polygons), highlighting the overlap of the survey with our MW dwarf galaxy population (red points). The extensive coverage of Euclid will thereby enable effective star-galaxy separation at the faintest regimes for *most* MW dwarfs.

A promising test of this methodology can already be conducted using existing *ugriz*-band data from UNIONS (Gwyn et al. 2025; declination $> +15°$). As a member of the UNIONS collaboration, I can currently access these photometric catalogues and use them to test the updated algorithm on northern dwarf galaxies. Previous studies have already demonstrated that UNIONS *ugriz*-bands are effective to isolate specific stellar populations (Thomas et al. 2018, 2019), given particularly the enhanced depth in the *u*-band which is $\approx$3 magnitudes deeper than that of SDSS and similar in forcasted depth of the first LSST data release. With UNIONS as a playground for the northern dwarfs, paired with LSST's coverage in the south, my research will enable an *even deeper* census of faint dwarf substructures than currently possible with available wide-field data.

In the coming decade, the field of Galactic Archaeology will be again transformed by the absolute wealth of new data from next-generation telescopes. Between

LSST/UNIONS and Euclid, nearly every (currently known) MW satellite will soon be mapped to unprecedented detail that will allow us to uncover the faintest stellar substructures. Combined with the methods developed in this thesis, these surveys will facilitate a systematic census of small-scale stellar haloes and dwarf galaxy tidal debris across the full MW satellite population. Simultaneously, the rapid discovery of new dwarf candidates will continue to expand the total inventory of dwarf satellites itself, ensuring a multitude of new systems to explore. The work presented here only marks the starting point in a field where the smallest galaxies provide the largest insights.

Appendix A

Additional Information for Chapter 3

Equations from Stoughton et al. (2002) used to convert from SDSS survey coordinates to equatorial:

$$\cos(\alpha - 95^\circ)\cos(\delta) = -\sin(\lambda_{SDSS}) \tag{A.1}$$

$$\sin(\alpha - 95^\circ)\cos(\delta) = \cos(\lambda_{SDSS})\cos(\eta_{SDSS} + 32.5^\circ) \tag{A.2}$$

$$\sin(\delta) = \cos(\lambda_{SDSS})\sin(\eta_{SDSS} + 32.5^\circ) \tag{A.3}$$

where the origin $(\lambda, \eta)_{SDSS} = (0^\circ, 0^\circ)$ and pole $(\lambda, \eta)_{SDSS} = (0^\circ, 90^\circ)$ in SDSS survey coordinates are located at (RA, Dec) = (185°, 32.5°) and (RA, Dec) = (275°, 0°), respectively. The equatorial pole (RA, Dec) = (0°, 90°) is located at $(\lambda, \eta)_{SDSS} = (5.57^\circ, 0^\circ)$ in this frame of reference.

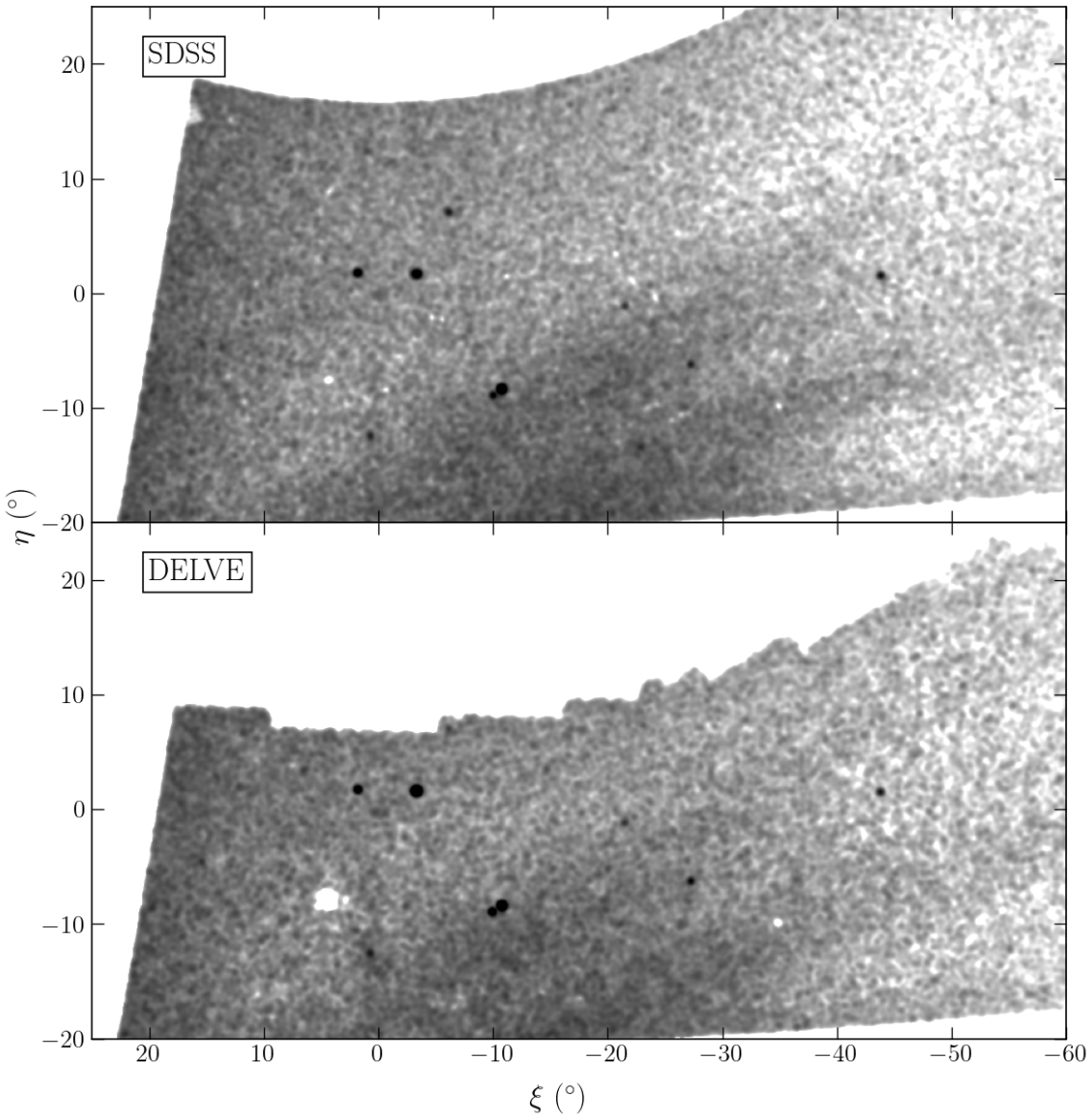

Figure A.1: Matched filter maps of SDSS and DELVE, spanning a wider area to highlight the presence of the Sagittarius stellar stream. This feature is clearly observed in both maps as the overdensity ranging from $0° \lesssim \xi \lesssim -40°$. These two features are known as the stream's upper and lower bifurcations, caused by the second wrap of the stream around the Galaxy.

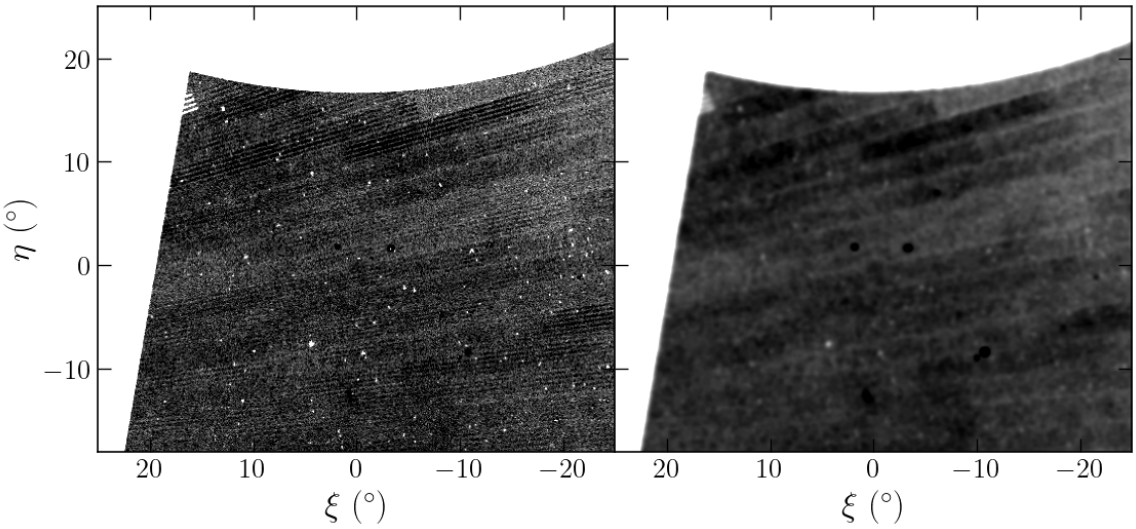

Figure A.2: Tangent plane density maps of the matched filter likelihoods (left; pixel size of 0.1°) and the same map smoothed with a Gaussian kernel of 0.2° (right) using the SDSS catalogue. The photometric limits of this data are only the 5-σ point source depth determined in this work. As shown in both panels, the streaking observation pattern is oriented in the same direction as the faint feature seen in the SDSS panels of Figure 3.15. This feature is therefore likely an artifact caused by the SDSS observing pattern that, when smoothed, appears to grow in size when summed together. As it is a feature that does not appear in DELVE MF maps, it is not likely a real MW substructure.

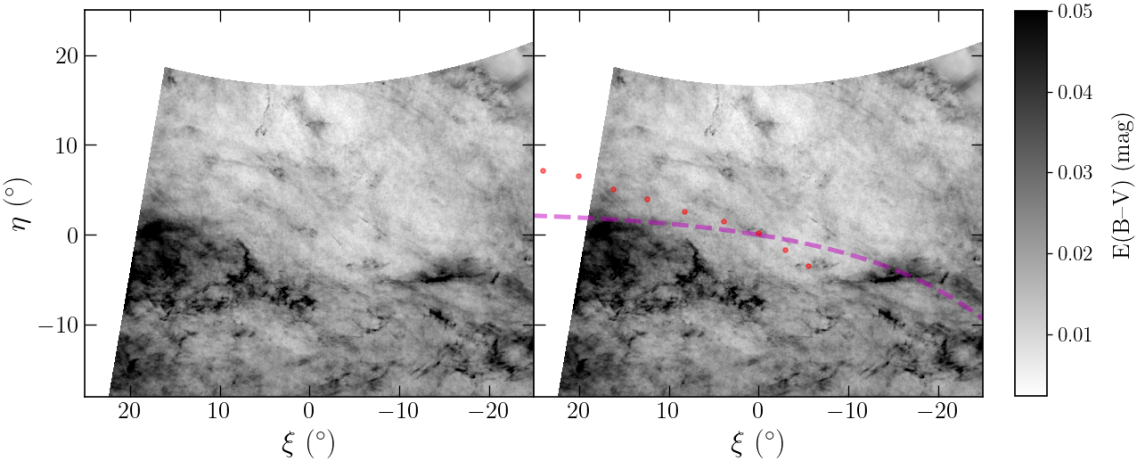

Figure A.3: Extinction maps of the vicinity of Boo3, converted to tangent plane coordinates. Boo3's orbit and the approximate location of Styx are indicated in the magenta dashed line and red nodes, respectively, in the right panel for comparison.

Bibliography

Abbott T. M. C., et al., 2018, ApJS, 239, 18

Abdurro'uf et al., 2022, ApJS, 259, 35

Adén D., et al., 2009, A&A, 506, 1147

Amorisco N. C., Evans N. W., van de Ven G., 2014, Nature, 507, 335

Ardern-Arentsen A., Kane S. G., Belokurov V., Matsuno T., Montelius M., Monty S., Sanders J. L., 2025, MNRAS, 537, 1984

Armandroff T. E., Da Costa G. S., 1991, AJ, 101, 1329

Armandroff T. E., Zinn R., 1988, AJ, 96, 92

Astropy Collaboration et al., 2013, A&A, 558, A33

Astropy Collaboration et al., 2018, AJ, 156, 123

Battaglia G., Helmi A., Tolstoy E., Irwin M., Hill V., Jablonka P., 2008, ApJL, 681, L13

Battaglia G., Taibi S., Thomas G. F., Fritz T. K., 2022, A&A, 657, A54

Baumgardt H., Hilker M., Sollima A., Bellini A., 2019, MNRAS, 482, 5138

Beaton R. L., et al., 2021, AJ, 162, 302

Bechtol K., et al., 2015, ApJ, 807, 50

Bellazzini M., Ferraro F. R., Origlia L., Pancino E., Monaco L., Oliva E., 2002, AJ, 124, 3222

Belokurov V., 2013, NewAR, 57, 100

Belokurov V., et al., 2006, ApJL, 642, L137

Belokurov V., et al., 2007a, ApJ, 654, 897

Belokurov V., et al., 2007b, ApJ, 658, 337

Belokurov V., et al., 2009, MNRAS, 397, 1748

Belokurov V., Erkal D., Evans N. W., Koposov S. E., Deason A. J., 2018, MNRAS, 478, 611

Benítez-Llambay A., Navarro J. F., Abadi M. G., Gottlöber S., Yepes G., Hoffman Y., Steinmetz M., 2015, MNRAS, 450, 4207

Benítez-Llambay A., Navarro J. F., Abadi M. G., Gottlöber S., Yepes G., Hoffman Y., Steinmetz M., 2016, MNRAS, 456, 1185

Benson A. J., 2010, Physics Reports, 495, 33

Bettinelli M., Hidalgo S. L., Cassisi S., Aparicio A., Piotto G., Valdes F., Walker A. R., 2019, MNRAS, 487, 5862

Bianco F. B., et al., 2022, ApJS, 258, 1

Bland-Hawthorn J., Gerhard O., 2016, ARA&A, 54, 529

Blanton M. R., et al., 2017, AJ, 154, 28

Bonaca A., Price-Whelan A. M., 2025, NewAR, 100, 101713

Bonaca A., et al., 2020, ApJ, 889, 70

Borukhovetskaya A., Errani R., Navarro J. F., Fattahi A., Santos-Santos I., 2022, MNRAS, 509, 5330

Bovy J., Rix H.-W., 2013, ApJ, 779, 115

Bowen I. S., Vaughan A. H. J., 1973, Applied Optics, 12, 1430

Boylan-Kolchin M., Bullock J. S., Kaplinghat M., 2011, MNRAS, 415, L40

Bullock J. S., Boylan-Kolchin M., 2017, ARA&A, 55, 343

Bullock J. S., Johnston K. V., 2005, ApJ, 635, 931

Bullock J. S., Kravtsov A. V., Weinberg D. H., 2000, ApJ, 539, 517

Caldwell N., et al., 2017, ApJ, 839, 20

Callingham T. M., et al., 2019, MNRAS, 484, 5453

Cantu S. A., et al., 2021, ApJ, 916, 81

Carlin J. L., Sand D. J., 2018, ApJ, 865, 7

Carlin J. L., Grillmair C. J., Muñoz R. R., Nidever D. L., Majewski S. R., 2009, ApJL, 702, L9

Cautun M., et al., 2020, MNRAS, 494, 4291

Cerny W., et al., 2021a, ApJ, 910, 18

Cerny W., et al., 2021b, ApJL, 920, L44

Cerny W., et al., 2023a, ApJ, 942, 111

Cerny W., et al., 2023b, ApJ, 953, 1

Chambers K. C., et al., 2016, arXiv e-prints, p. arXiv:1612.05560

Chene A.-N., et al., 2014, in Navarro R., Cunningham C. R., Barto A. A., eds, Society of Photo-Optical Instrumentation Engineers (SPIE) Conference Series Vol. 9151, Advances in Optical and Mechanical Technologies for Telescopes and Instrumentation. p. 915147 (arXiv:1409.7448), doi:10.1117/12.2057417

Chiti A., Frebel A., Ji A. P., Jerjen H., Kim D., Norris J. E., 2018, ApJ, 857, 74

Chiti A., et al., 2021, Nature Astronomy, 5, 392

Chiti A., et al., 2023, AJ, 165, 55

Cicuéndez L., Battaglia G., 2018, MNRAS, 480, 251

Conselice C. J., Wilkinson A., Duncan K., Mortlock A., 2016, ApJ, 830, 83

Cooper A. P., et al., 2010, MNRAS, 406, 744

Correnti M., Bellazzini M., Ferraro F. R., 2009, MNRAS, 397, L26

Dall'Ora M., et al., 2006, ApJL, 653, L109

DeBuhr J., Ma C.-P., White S. D. M., 2012, MNRAS, 426, 983

Deason A. J., Belokurov V., Evans N. W., 2011, MNRAS, 416, 2903

Deason A. J., Belokurov V., Evans N. W., Watkins L. L., Fellhauer M., 2012, MNRAS, 425, L101

Deason A., Wetzel A., Garrison-Kimmel S., 2014, ApJ, 794, 115

Deason A. J., et al., 2021, MNRAS, 501, 5964

Deason A. J., Bose S., Fattahi A., Amorisco N. C., Hellwing W., Frenk C. S., 2022, MNRAS, 511, 4044

Dekel A., Silk J., 1986, ApJ, 303, 39

Drlica-Wagner A., et al., 2015, ApJ, 813, 109

Drlica-Wagner A., et al., 2022, ApJS, 261, 38

Eilers A.-C., Hogg D. W., Rix H.-W., Ness M. K., 2019, ApJ, 871, 120

Erkal D., et al., 2018, MNRAS, 481, 3148

Erkal D., et al., 2019, MNRAS, 487, 2685

Errani R., Navarro J. F., 2021, MNRAS, 505, 18

Errani R., Navarro J. F., Ibata R., Peñarrubia J., 2022, MNRAS, 511, 6001

Euclid Collaboration et al., 2025, A&A, 697, A1

Faber S. M., et al., 2003, in Iye M., Moorwood A. F. M., eds, Society of Photo-Optical Instrumentation Engineers (SPIE) Conference Series Vol. 4841, Instrument Design and Performance for Optical/Infrared Ground-based Telescopes. pp 1657–1669, doi:10.1117/12.460346

Fardal M. A., Huang S., Weinberg M. D., 2015, MNRAS, 452, 301

Farrow D. J., et al., 2014, MNRAS, 437, 748

Ferguson P., Shipp N., 2025, arXiv e-prints, p. arXiv:2506.05469

Filion C., Wyse R. F. G., 2021, ApJ, 923, 218

Foreman-Mackey D., Hogg D. W., Lang D., Goodman J., 2013, PASP, 125, 306

Frebel A., Norris J. E., 2015, ARA&A, 53, 631

Frebel A., Lunnan R., Casey A. R., Norris J. E., Wyse R. F. G., Gilmore G., 2013, ApJ, 771, 39

Frebel A., Simon J. D., Kirby E. N., 2014, ApJ, 786, 74

Frebel A., Norris J. E., Gilmore G., Wyse R. F. G., 2016, ApJ, 826, 110

Frenk C. S., White S. D. M., Davis M., Efstathiou G., 1988, ApJ, 327, 507

Fritz T. K., Carrera R., Battaglia G., Taibi S., 2019, A&A, 623, A129

Fu S. W., et al., 2018, ApJ, 866, 42

Gaia Collaboration et al., 2016, A&A, 595, A1

Gaia Collaboration et al., 2018a, A&A, 616, A1

Gaia Collaboration et al., 2018b, A&A, 616, A10

Gaia Collaboration et al., 2018c, A&A, 616, A12

Gaia Collaboration et al., 2021, A&A, 649, A1

Gaia Collaboration et al., 2023, A&A, 674, A1

Geha M., Willman B., Simon J. D., Strigari L. E., Kirby E. N., Law D. R., Strader J., 2009, ApJ, 692, 1464

Gilmore G., Wilkinson M. I., Wyse R. F. G., Kleyna J. T., Koch A., Evans N. W., Grebel E. K., 2007, ApJ, 663, 948

Girardi L., Bertelli G., Bressan A., Chiosi C., Groenewegen M. A. T., Marigo P., Salasnich B., Weiss A., 2002, A&A, 391, 195

Goater A., et al., 2024, MNRAS, 527, 2403

Gravity Collaboration et al., 2019, A&A, 625, L10

Green G., Edenhofer G., Krughoff S., Smith A., Lenz D., Malanchev K., conornally 2024, gregreen/dustmaps: v1.0.13, doi:10.5281/zenodo.10517733

Grillmair C. J., 2009, ApJ, 693, 1118

Grillmair C. J., Carlin J. L., 2016, in Newberg H. J., Carlin J. L., eds, Astrophysics and Space Science Library Vol. 420, Tidal Streams in the Local Group and Beyond. p. 87 (arXiv:1603.08936), doi:10.1007/978-3-319-19336-6_4

Grillmair C. J., Dionatos O., 2006, ApJL, 643, L17

Gunn J. E., Gott III J. R., 1972, ApJ, 176, 1

Gunn J. E., et al., 2006, AJ, 131, 2332

Gwyn S., et al., 2025, arXiv e-prints, p. arXiv:2503.13783

Hansen T. T., et al., 2017, ApJ, 838, 44

Hargreaves J. C., Gilmore G., Irwin M. J., Carter D., 1994, MNRAS, 271, 693

Harris W. E., 1996, AJ, 112, 1487

Harris W. E., 2010, arXiv e-prints, p. arXiv:1012.3224

Hastings W. K., 1970, Biometrika, 57, 97

Hattori K., Erkal D., Sanders J. L., 2016, MNRAS, 460, 497

Hayes C. R., et al., 2023, ApJ, 955, 17

Helmi A., 2020, ARA&A, 58, 205

Helmi A., White S. D. M., de Zeeuw P. T., Zhao H., 1999, Nature, 402, 53

Helmi A., Babusiaux C., Koppelman H. H., Massari D., Veljanoski J., Brown A. G. A., 2018, Nature, 563, 85

Hidalgo S. L., et al., 2011, ApJ, 730, 14

Higgs C. R., McConnachie A. W., Annau N., Irwin M., Battaglia G., Côté P., Lewis G. F., Venn K., 2021, MNRAS, 503, 176

Hill V., et al., 2019, A&A, 626, A15

Hook I. M., Jørgensen I., Allington-Smith J. R., Davies R. L., Metcalfe N., Murowinski R. G., Crampton D., 2004, PASP, 116, 425

Ibata R. A., Lewis G. F., Irwin M. J., Cambrésy L., 2002, MNRAS, 332, 921

Ibata R. A., et al., 2017, ApJ, 848, 128

Ibata R. A., Malhan K., Martin N. F., 2019, ApJ, 872, 152

Ibata R., Bellazzini M., Thomas G., Malhan K., Martin N., Famaey B., Siebert A., 2020, ApJL, 891, L19

Ibata R., et al., 2024, ApJ, 967, 89

Iorio G., Nipoti C., Battaglia G., Sollima A., 2019, MNRAS, 487, 5692

Irwin M., Hatzidimitriou D., 1995, MNRAS, 277, 1354

Ivezić Ž., et al., 2008, ApJ, 684, 287

Ivezić Ž., et al., 2019, ApJ, 873, 111

Jensen J., et al., 2021, MNRAS, 507, 1923

Jensen J., Hayes C. R., Sestito F., McConnachie A. W., Waller F., Smith S. E. T., Navarro J., Venn K. A., 2024, MNRAS, 527, 4209

Ji A. P., Frebel A., Chiti A., Simon J. D., 2016a, Nature, 531, 610

Ji A. P., Frebel A., Simon J. D., Chiti A., 2016b, ApJ, 830, 93

Ji A. P., Frebel A., Ezzeddine R., Casey A. R., 2016c, ApJL, 832, L3

Ji A. P., et al., 2021, ApJ, 921, 32

Ji A. P., et al., 2023, AJ, 165, 100

Johnston K. V., Bullock J. S., Sharma S., Font A., Robertson B. E., Leitner S. N., 2008, ApJ, 689, 936

Jurić M., et al., 2008, ApJ, 673, 864

Kacharov N., et al., 2017, MNRAS, 466, 2006

Kado-Fong E., et al., 2022, ApJ, 931, 152

Kallivayalil N., van der Marel R. P., Besla G., Anderson J., Alcock C., 2013, ApJ, 764, 161

Kim D., et al., 2016, ApJ, 833, 16

King I., 1962, AJ, 67, 471

Kirby E. N., Boylan-Kolchin M., Cohen J. G., Geha M., Bullock J. S., Kaplinghat M., 2013, ApJ, 770, 16

Kirby E. N., Simon J. D., Cohen J. G., 2015a, ApJ, 810, 56

Kirby E. N., Cohen J. G., Simon J. D., Guhathakurta P., 2015b, ApJL, 814, L7

Kirby E. N., Cohen J. G., Simon J. D., Guhathakurta P., Thygesen A. O., Duggan G. E., 2017, ApJ, 838, 83

Kleyna J. T., Wilkinson M. I., Evans N. W., Gilmore G., 2005, ApJL, 630, L141

Klypin A., Kravtsov A. V., Valenzuela O., Prada F., 1999, ApJ, 522, 82

Koch A., et al., 2009, ApJ, 690, 453

Koposov S. E., et al., 2011, ApJ, 736, 146

Koposov S. E., Belokurov V., Torrealba G., Evans N. W., 2015a, ApJ, 805, 130

Koposov S. E., et al., 2015b, ApJ, 811, 62

Koposov S. E., et al., 2018, MNRAS, 479, 5343

Koposov S. E., et al., 2019, MNRAS, 485, 4726

Koposov S. E., et al., 2023, MNRAS, 521, 4936

Kroupa P., 2001, MNRAS, 322, 231

Laevens B. P. M., et al., 2015, ApJ, 813, 44

Law D. R., Majewski S. R., Johnston K. V., 2009, ApJL, 703, L67

Leaman R., 2012, AJ, 144, 183

Li T. S., et al., 2017, ApJ, 838, 8

Li T. S., et al., 2018a, ApJ, 857, 145

Li T. S., et al., 2018b, ApJ, 866, 22

Licquia T. C., Newman J. A., 2015, ApJ, 806, 96

Lindegren L., et al., 2018, A&A, 616, A2

Lindegren L., et al., 2021a, A&A, 649, A2

Lindegren L., et al., 2021b, A&A, 649, A4

Longeard N., et al., 2018, MNRAS, 480, 2609

Longeard N., et al., 2020, MNRAS, 491, 356

Longeard N., et al., 2021, MNRAS, 503, 2754

Longeard N., et al., 2022, MNRAS, 516, 2348

Longeard N., et al., 2023, MNRAS, 525, 3086

Lovell M. R., Zavala J., 2023, MNRAS, 520, 1567

Magnier E. A., Cuillandre J. C., 2004, PASP, 116, 449

Majewski S. R., Skrutskie M. F., Weinberg M. D., Ostheimer J. C., 2003, ApJ, 599, 1082

Majewski S. R., et al., 2017, AJ, 154, 94

Malhan K., Ibata R. A., 2018, MNRAS, 477, 4063

Malhan K., Ibata R. A., Martin N. F., 2018, MNRAS, 481, 3442

Mao Y.-Y., et al., 2024, ApJ, 976, 117

Marshall J. L., et al., 2019, ApJ, 882, 177

Martin N. F., Ibata R. A., Chapman S. C., Irwin M., Lewis G. F., 2007, MNRAS, 380, 281

Martin N. F., de Jong J. T. A., Rix H.-W., 2008, ApJ, 684, 1075

Martin N. F., et al., 2016a, MNRAS, 458, L59

Martin N. F., et al., 2016b, ApJ, 818, 40

Martin N. F., et al., 2024, A&A, 692, A115

Martínez-García A. M., del Pino A., Aparicio A., 2023, MNRAS, 518, 3083

Martínez-Vázquez C. E., et al., 2019, MNRAS, 490, 2183

Martínez-Vázquez C. E., et al., 2021, AJ, 162, 253

Martinez G. D., Minor Q. E., Bullock J., Kaplinghat M., Simon J. D., Geha M., 2011, ApJ, 738, 55

Mateo M., Olszewski E. W., Walker M. G., 2008, ApJ, 675, 201

Mateu C., 2023, MNRAS, 520, 5225

Mau S., et al., 2020, ApJ, 890, 136

McConnachie A. W., 2012, AJ, 144, 4

McConnachie A. W., Venn K. A., 2020a, Research Notes of the American Astronomical Society, 4, 229

McConnachie A. W., Venn K. A., 2020b, AJ, 160, 124

McConnachie A. W., et al., 2024, PASP, 136, 035001

McMillan P. J., 2017, MNRAS, 465, 76

Mo H., van den Bosch F. C., White S., 2010, Galaxy Formation and Evolution

Moehler S., Landsman W. B., Sweigart A. V., Grundahl F., 2003, A&A, 405, 135

Monelli M., et al., 2010, ApJ, 720, 1225

Moore B., Ghigna S., Governato F., Lake G., Quinn T., Stadel J., Tozzi P., 1999, ApJL, 524, L19

Moskowitz A. G., Walker M. G., 2020, ApJ, 892, 27

Muñoz R. R., Carlin J. L., Frinchaboy P. M., Nidever D. L., Majewski S. R., Patterson R. J., 2006, ApJL, 650, L51

Muñoz R. R., Côté P., Santana F. A., Geha M., Simon J. D., Oyarzún G. A., Stetson P. B., Djorgovski S. G., 2018, ApJ, 860, 66

Nagasawa D. Q., et al., 2018, ApJ, 852, 99

Naidu R. P., Conroy C., Bonaca A., Johnson B. D., Ting Y.-S., Caldwell N., Zaritsky D., Cargile P. A., 2020, ApJ, 901, 48

Navarro J. F., Frenk C. S., White S. D. M., 1996, ApJ, 462, 563

Nidever D. L., et al., 2015, AJ, 150, 173

Niederste-Ostholt M., Belokurov V., Evans N. W., Gilmore G., Wyse R. F. G., Norris J. E., 2009, MNRAS, 398, 1771

Niederste-Ostholt M., Belokurov V., Evans N. W., 2012, MNRAS, 422, 207

Norris J. E., Gilmore G., Wyse R. F. G., Wilkinson M. I., Belokurov V., Evans N. W., Zucker D. B., 2008, ApJL, 689, L113

Norris J. E., Wyse R. F. G., Gilmore G., Yong D., Frebel A., Wilkinson M. I., Belokurov V., Zucker D. B., 2010, ApJ, 723, 1632

Olszewski E. W., Aaronson M., 1985, AJ, 90, 2221

Pace A. B., 2024, arXiv e-prints, p. arXiv:2411.07424

Pace A. B., Li T. S., 2019, ApJ, 875, 77

Pace A. B., et al., 2020, MNRAS, 495, 3022

Pace A. B., Erkal D., Li T. S., 2022, ApJ, 940, 136

Palau C. G., Miralda-Escudé J., 2023, MNRAS, 524, 2124

Palma C., Majewski S. R., Siegel M. H., Patterson R. J., Ostheimer J. C., Link R., 2003, AJ, 125, 1352

Pazder J., Fournier P., Pawluczyk R., van Kooten M., 2014, in Navarro R., Cunningham C. R., Barto A. A., eds, Society of Photo-Optical Instrumentation Engineers (SPIE) Conference Series Vol. 9151, Advances in Optical and Mechanical Technologies for Telescopes and Instrumentation. p. 915124, doi:10.1117/12.2057327

Pazder J., Burley G., Ireland M. J., Robertson G., Sheinis A., Zhelem R., 2016, in Evans C. J., Simard L., Takami H., eds, Society of Photo-Optical Instrumentation Engineers (SPIE) Conference Series Vol. 9908, Ground-based and Airborne Instrumentation for Astronomy VI. p. 99087F, doi:10.1117/12.2234366

Peñarrubia J., Navarro J. F., McConnachie A. W., 2008, ApJ, 673, 226

Peñarrubia J., Navarro J. F., McConnachie A. W., Martin N. F., 2009, ApJ, 698, 222

Pearson S., Price-Whelan A. M., Johnston K. V., 2017, Nature Astronomy, 1, 633

Piatek S., Pryor C., Bristow P., Olszewski E. W., Harris H. C., Mateo M., Minniti D., Tinney C. G., 2005, AJ, 130, 95

Plummer H. C., 1911, MNRAS, 71, 460

Portail M., Gerhard O., Wegg C., Ness M., 2017, MNRAS, 465, 1621

Price-Whelan A. M., Sesar B., Johnston K. V., Rix H.-W., 2016, ApJ, 824, 104

Qi Y., Zivick P., Pace A. B., Riley A. H., Strigari L. E., 2022, MNRAS, 512, 5601

Ramos P., et al., 2022, A&A, 666, A64

Read J. I., Wilkinson M. I., Evans N. W., Gilmore G., Kleyna J. T., 2006, MNRAS, 367, 387

Rees M. J., Ostriker J. P., 1977, MNRAS, 179, 541

Reines A. E., Greene J. E., Geha M., 2013, ApJ, 775, 116

Robin A. C., Reylé C., Derrière S., Picaud S., 2003, A&A, 409, 523

Roderick T. A., Mackey A. D., Jerjen H., Da Costa G. S., 2016, MNRAS, 461, 3702

Roederer I. U., Pace A. B., Placco V. M., Caldwell N., Koposov S. E., Mateo M., Olszewski E. W., Walker M. G., 2023, ApJ, 954, 55

Santana F. A., et al., 2021, AJ, 162, 303

Santos-Santos I. M. E., Fattahi A., Sales L. V., Navarro J. F., 2021, MNRAS, 504, 4551

Schechter P., 1976, ApJ, 203, 297

Schlafly E. F., Finkbeiner D. P., 2011, ApJ, 737, 103

Schlegel D. J., Finkbeiner D. P., Davis M., 1998, ApJ, 500, 525

Schönrich R., Binney J., Dehnen W., 2010, MNRAS, 403, 1829

Sestito F., Roediger J., Navarro J. F., Jensen J., Venn K. A., Smith S. E. T., Hayes C., McConnachie A. W., 2023a, MNRAS, 523, 123

Sestito F., et al., 2023b, MNRAS, 525, 2875

Shapley H., 1938, Harvard College Observatory Bulletin, 908, 1

Shipp N., et al., 2018, ApJ, 862, 114

Shipp N., et al., 2021, ApJ, 923, 149

Shipp N., et al., 2025, MNRAS, 542, 1109

Simon J. D., 2019, ARA&A, 57, 375

Simon J. D., Geha M., 2007, ApJ, 670, 313

Simon J. D., et al., 2011, ApJ, 733, 46

Simon J. D., et al., 2015, ApJ, 808, 95

Simon J. D., et al., 2017, ApJ, 838, 11

Simon J. D., et al., 2020, ApJ, 892, 137

Sirko E., et al., 2004, AJ, 127, 899

Skillman E. D., et al., 2014, ApJ, 786, 44

Smith S. E. T., et al., 2023, AJ, 166, 76

Smith S. E. T., et al., 2024, ApJ, 961, 92

Sollima A., 2020, MNRAS, 495, 2222

Somerville R. S., Davé R., 2015, ARA&A, 53, 51

Spencer M. E., Mateo M., Walker M. G., Olszewski E. W., 2017, ApJ, 836, 202

Spencer M. E., Mateo M., Olszewski E. W., Walker M. G., McConnachie A. W., Kirby E. N., 2018, AJ, 156, 257

Starkenburg E., et al., 2010, A&A, 513, A34

Starkenburg E., et al., 2017, MNRAS, 471, 2587

Stierwalt S., Besla G., Patton D., Johnson K., Kallivayalil N., Putman M., Privon G., Ross G., 2015, ApJ, 805, 2

Stoughton C., et al., 2002, AJ, 123, 485

Tarumi Y., Yoshida N., Frebel A., 2021, ApJL, 914, L10

Thomas G. F., Battaglia G., 2022, A&A, 660, A29

Thomas G. F., et al., 2018, MNRAS, 481, 5223

Thomas G. F., et al., 2019, ApJ, 886, 10

Tolstoy E., et al., 2004, ApJL, 617, L119

Tolstoy E., Hill V., Tosi M., 2009, ARA&A, 47, 371

Tolstoy E., et al., 2023, A&A, 675, A49

Tolstoy E., et al., 2025, A&A, 698, A53

Torrealba G., et al., 2016, MNRAS, 463, 712

Torrealba G., et al., 2019, MNRAS, 488, 2743

Valenti E., et al., 2016, A&A, 587, L6

Vargas L. C., Geha M., Kirby E. N., Simon J. D., 2013, ApJ, 767, 134

Vasiliev E., 2018, arXiv e-prints, p. arXiv:1802.08255

Vasiliev E., Belokurov V., Erkal D., 2021, MNRAS, 501, 2279

Walker M. G., Mateo M., Olszewski E. W., Bernstein R., Wang X., Woodroofe M., 2006, AJ, 131, 2114

Walker M. G., Mateo M., Olszewski E. W., 2009a, AJ, 137, 3100

Walker M. G., Belokurov V., Evans N. W., Irwin M. J., Mateo M., Olszewski E. W., Gilmore G., 2009b, ApJL, 694, L144

Walker M. G., Mateo M., Olszewski E. W., Bailey John I. I., Koposov S. E., Belokurov V., Evans N. W., 2015, ApJ, 808, 108

Walker M. G., et al., 2016, ApJ, 819, 53

Waller F., et al., 2023, MNRAS, 519, 1349

Wan Z., et al., 2020, Nature, 583, 768

Wang J., Hammer F., Yang Y., 2022, MNRAS, 510, 2242

Webster D., Frebel A., Bland-Hawthorn J., 2016, ApJ, 818, 80

Weiler M., 2018, A&A, 617, A138

Weisz D. R., Dolphin A. E., Skillman E. D., Holtzman J., Gilbert K. M., Dalcanton J. J., Williams B. F., 2014, ApJ, 789, 147

Westfall K. B., Majewski S. R., Ostheimer J. C., Frinchaboy P. M., Kunkel W. E., Patterson R. J., Link R., 2006, AJ, 131, 375

Wheeler C., et al., 2019, MNRAS, 490, 4447

White S. D. M., Rees M. J., 1978, MNRAS, 183, 341

Willman B., Strader J., 2012, AJ, 144, 76

Willman B., Geha M., Strader J., Strigari L. E., Simon J. D., Kirby E., Ho N., Warres A., 2011, AJ, 142, 128

Wilson A. G., 1955, PASP, 67, 27

Wilson J. C., et al., 2019, PASP, 131, 055001

Wolf J., Martinez G. D., Bullock J. S., Kaplinghat M., Geha M., Muñoz R. R., Simon J. D., Avedo F. F., 2010, MNRAS, 406, 1220

Xue X.-X., et al., 2011, ApJ, 738, 79

Yang Y., Hammer F., Jiao Y., Pawlowski M. S., 2022, MNRAS, 512, 4171

Yanny B., et al., 2000, ApJ, 540, 825

Yanny B., et al., 2009, AJ, 137, 4377

York D. G., et al., 2000, AJ, 120, 1579

Youakim K., et al., 2017, MNRAS, 472, 2963

Zaremba D., et al., 2025, ApJ, 987, 217

Zasowski G., et al., 2013, AJ, 146, 81

Zasowski G., et al., 2017, AJ, 154, 198

de Blok W. J. G., 2010, Advances in Astronomy, 2010, 789293

de los Reyes M. A. C., Kirby E. N., Ji A. P., Nuñez E. H., 2022, ApJ, 925, 66

del Pino A., Aparicio A., Hidalgo S. L., Łokas E. L., 2017, MNRAS, 465, 3708